The Dissertation Committee for Minh Tu Nguyen Certifies that this is the approved version of the following dissertation:

Electronic Materials Based on Conducting Metallopolymers and Self-Assembly

Committee:

Bradley J. Holliday, Supervisor

Brian A. Korgel

Michael J. Rose

Simon M. Humphrey

David A. Vanden Bout

Electronic Materials Based on Conducting Metallopolymers and Self-Assembly

by

Minh Tu Nguyen, B.S. CH.

Dissertation

Presented to the Faculty of the Graduate School of

The University of Texas at Austin

in Partial Fulfillment

of the Requirements

for the Degree of

Doctor of Philosophy

The University of Texas at Austin

December 2014

Dedication

- *Gửi tặng ba mẹ, những người đã chịu nhiều vất vả để chăm lo cho tụi con đi học. Luận văn cho học vị cao nhất này chính là một trong những thành quả mà ba mẹ đã cố gắng lo cho anh em con.*
- *Gửi tặng hia, người đã định hướng để em đạt được kết quả tốt như hôm nay và đã lo lắng cho em suốt những năm đại học; Gửi đến chế Mén (Tố Tâm) cho những sự yêu thương, lo lắng hết lòng của chế dành cho em ngay từ lúc còn bé xíu.*
- *Gửi tặng "vợ mèo", người đã luôn yêu thương, chăm sóc, sát cánh bên nikon suốt những năm tháng cô đơn, vất vả trên đất Mẽo này.*

Acknowledgements

First, I would like to acknowledge my advisor, Prof. Bradley J. Holliday for all of his support, guidance, and mentorship. Beginning with his sponsorship for me to come to UT, he has unwaiveringly supported me during the last five years. I would like to express my sincere appreciation to him for everything he has done to help me be successful in my graduate school and career development.

I would also like to thank my committee members, Prof. Michael Rose, Prof. Simon Humphrey, Prof. David Vanden Bout, and Prof. Brian Korgel for their helpful discussions and support. Additionally, I would like to thank Dr. Jiping Zhou and Prof. Jianshi Zhou for their assistance and advice with TEM and SQUID magnetic property measurements. I also acknowledge Lauren Avery (Mitchell) in the Holliday Group and Dr. Vince Lynch for teaching and introducing me to the world of X-ray crystallography.

In addition, I would like to acknowledge the members of the Holliday group, both past and present, for their support and friendship. I would like to thank Jennifer Caraway, Kory Muller, and Dan Strohecker for their countless time spent revising my "unpleasure" writing.

Finally, I would like to thank my family for unconditionally supporting me and always being there. Especially, I would like to express my deepest appreciation to my wife Ha Do for her love, understanding, encouragement, and support during my five years of being away from her.

Electronic Materials Based on Conducting Metallopolymers and Self-Assembly

Minh Tu Nguyen, Ph.D.

The University of Texas at Austin, 2014

Supervisor: Bradley J. Holliday

Conducting metallopolymers (CMPs) have been extensively studied due to their potential for various applications in sensing, catalysis, light-emitting diodes, and energy harvesting and storage. The incorporation of metal centers into conjugated organic polymer backbones not only makes these materials multi-functional, but also changes the properties, such as electroactivity and conductivity. In this work, we aim to take advantage of the direct electronic interaction between metal centers and polymer backbones in these metallopolymers to make novel materials that could be used for photovoltaic and spintronic applications. Furthermore, a fundamental study on the interactive role of transition metals in conducting metallopolymers has been conducted, which could help to provide insights for the rational design of metallopolymers for certain applications.

Charge transfer in hybrid photovoltaics is often inhibited by the capping ligands on inorganic semiconductors. To bypass the ligand effect, my study was focused on preparing a conducting metallopolymer, in which metal ions are directly bound to the conjugated organic backbone. These metal ions will serve as nucleation or seed points upon which the inorganic semiconductor can grow directly within the polymer matrix. This fabrication method provides materials with direct bonds between the inorganic

semiconductor and the conducting polymer backbone and therefore results in direct electronic communication between the donor and acceptor. With this material, the charge transfer limited by capping ligands could be overcome and can result in highly efficient devices when utilized in solar cells.

Besides the efforts to harvest energy form renewable resources, changing the way that we use energy (e.g., in lighting and information storage) could also help to reduce our energy demand. The bistability offered by spin-crossover (SCO) complexes has resulted in sustained research interest due to potential applications in molecular electronics such as memory storage. Interested in making memory devices with a bottom up approach, we have designed and prepared CMPs that are not only conductive but also possess spin-crossover behavior. The novelty of this study lies in the fact that spin-switching could be possibly obtained by changing the oxidation states of metal centers, which could be done at room temperature, offering a new method for spin switching compared to conventional methods for SCO such as in thermal-induced spin transition.

To study the charge delocalization and charge transport in CMPs, a series of conducting polymers of Schiff-base ligands and metal complexes have been prepared and characterized. Our successful syntheses of ligand polymers allows for full characterization and direct comparison of these polymers to the corresponding metal-containing polymers, from which the role of the metal centers is elucidated. The effects of conjugation length on electrochemical and spectroscopic properties are also investigated and discussed.

Table of Contents

List of Tables

List of Figures

List of Schemes

Chapter 1: Conducting Metallopolymers: Functional Materials with Emerging Applications

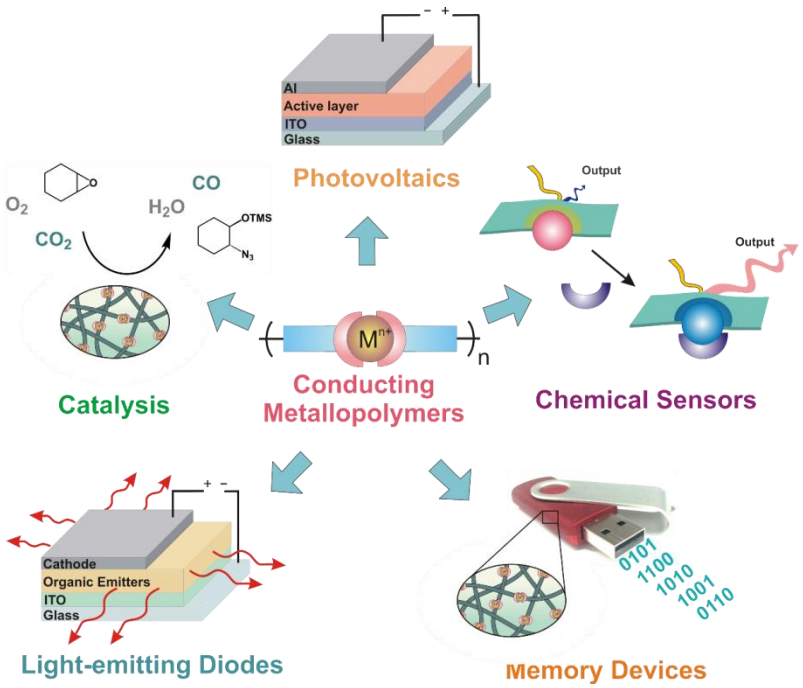

1.1. INTRODUCTION

1.1.1. Conducting metallopolymers (CMP): Combination of conducting polymer and metal complexes?

The development of π-conjugated conducting polymers (CPs) has been well-established over the past several decades.[1,2] Semiconducting behavior is a key feature of the materials to be used in optoelectronics (photovoltaics, light-emitting diodes) or traditional electronic devices (conductors, field effect transistors, memory devices, etc.). However, the application of conducting polymers is not limited to these fields due to the ease of structural modification of the polymers. A large amount of work has been devoted to increasing the functionality of CPs by not only changing the polymer main-chain structures but also by attaching new functional components to the polymer chains.[1] Among the added functionalities, metal complexes are the most common and promising due to the various advantageous applications of metal centers such as in catalysis,[3] sensing,[4] pure-colored light-emission,[5] etc. The properties of CMPs not only are inherited from their individual components (i.e. polymer backbone and metal complexes) but also depend on the interaction between these two components. Depending on the strength of the interaction, which may be controlled by structural design, the inter-influences will be strong or weak and the optical and electronic properties of both the organic backbone and the metal sites can be tuned by modifying one of the other element.[6] In addition, electron or energy transfer between the polymer backbone and the metal centers is more effective when they are covalently bound to each other. Therefore, CMPs have become a unique class of materials that allow for accessible tuning of optical and electronic properties than can be realized by simply combined materials.

1.1.2. Molecular architecture of CMPs

A well-accepted classification of CMPs was reported by Wolf based on how the metal centers are attached to polymer backbones.[7,8] Building upon this classification, we suspected that the way that metal coordinates to ligand centers is also important to the polymer structures and strongly affects the properties of CMPs. Therefore, subclasses of CMPs have been introduced as seen in Figure 1.1. In Wolf Type-I CMPs, the metal centers are tethered to the polymer backbone by an insulating linker, usually an alkyl chain. In this type, there is very little to no interaction between the metal center and the organic backbone. As a result, the CMPs have almost the same properties that would result from simply combining the two components. From a coordination aspect, the metal center may coordinate to ligand centers of two organic linkers or from one linker with auxiliary ligands filling out the coordination sphere (Figure 1.1A). The latter case is usually found for lanthanide and emissive metal ions while the former subclass is utilized in ion separation or sensing.

In Wolf Type-II CMPs, metal centers are covalently bound to the polymers conjugated backbone and the properties of each component are influenced by each other. However, the influence is sometimes not significant if there is a conjugated-buffer linker between the metal and the polymer main chain (Figure 1.1B). This allows a way to control the inter-influences but still maintain the electronic communication for effective electron and/or energy transfer. For example, in some cases it is necessary to dope the polymer backbone to achieve higher conductivity without affecting the electronic properties of metal centers.

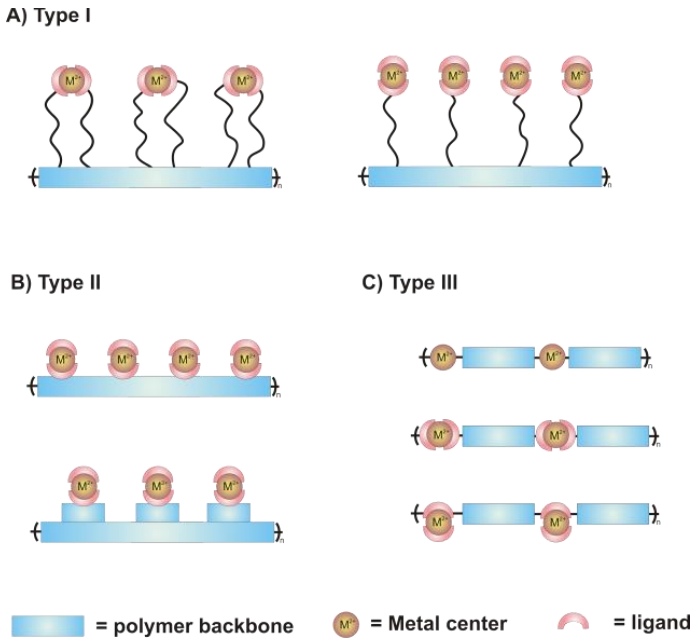

Figure 1.1. Illustration of Wolf Type I-III CMPs based on the interaction between the metal centers and the conjugated backbone. Subclasses in each type are introduced based on metal-ligand coordination.

In Wolf Type-III CMPs, the metal centers act as a part of the polymer backbone. In addition to structurally supporting the CMPs, the metal centers also have a strong electronic interaction with the organic bridges. Therefore, optical and electronic properties of these metal centers are highly sensitive to the electronic changes of the polymer backbone. Additionally, the properties of CMPs are dependent on the coordination types and the geometry around the metal centers. The metals can directly bind to the conjugated backbone by covalent bonding or *via* coordination to a ligand center with and without auxiliary ligands (Figure 1.1C). In most cases, the square planar geometry around the metal centers helps to extend the π-conjugated system. For octahedral metal complexes and other coordination geometries, the metal centers can either extend or interrupt the conjugation of the polymer backbone depending on the arrangement of ligand around the metal centers. Due to the strong electronic interaction

and extensive tunability of Wolf Type-III CMPs, this class has received a great deal of interest and has been extensively studied. Figure 1.2 shows some examples of this CMP type with different sub-classes.

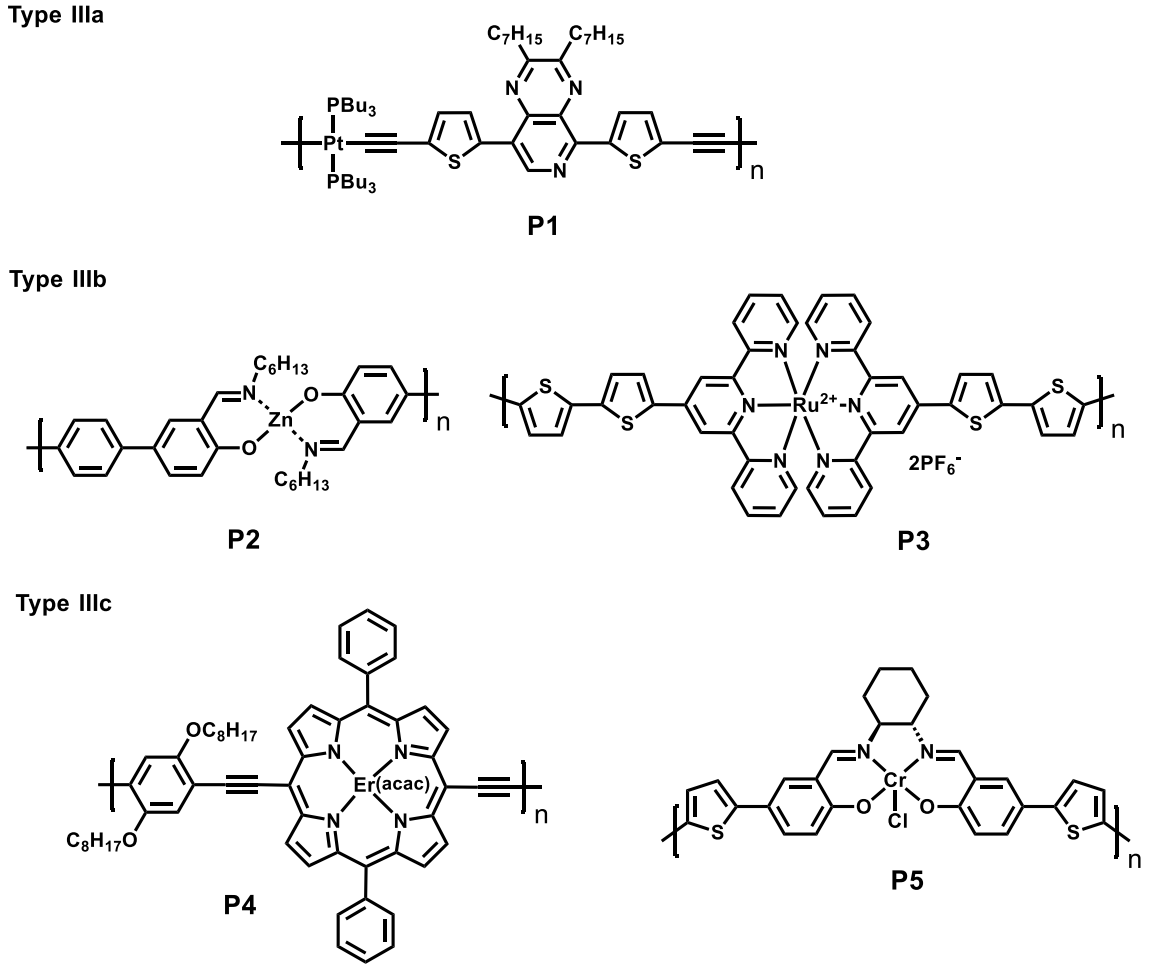

Figure 1.2. Examples of subclasses Wolf Type-III CMPs: (IIIa) metal centers directly bind to and are in conjugation to organic backbone (**P1**);[9] (IIIb) metal centers connected to organic bridges *via* coordination in square planar (**P2**)[10] or octahedral (**P3**)[11] geometry; (IIIc) CMPs that have metal center with auxiliary ligands (**P4**[12] and **P5**[13]).

1.1.3. Preparation of CMPs

One of the advantages of polymeric materials is the ease of processing them into thin films *via* solution processing. Metal complexes, however, usually are not very soluble in organic solvents and, when incorporated to polymer, the resulting CMPs usually have poor solubility as well making characterization and processing difficult. With the development of modern chemistry of aromatic coupling reactions, novel synthetic approaches have been developed to prepare CMPs. In general, CMPs could be obtained by four methods: electropolymerization, chemical coupling polymerization, coordinating polymerization, and polymer metallation (Figure 1.3). (i) In electropolymerization method, metal complex monomers are subjected to an external electric current/potential. The monomers undergo oxidation or reduction to form activated species, the radical cations or anions, which then couple to each other to form oligomers and polymers. Details of the mechanistic aspects, conditions, and examples of CMP electropolymerization could be found elsewhere.[14,15] (ii) Coupling polymerization is based on the reaction between a metal-complex-bearing monomer and another aromatic moiety *via* aromatic coupling reactions, of which Suzuki, Stille, and Sonogashira couplings are among the three most common used. (iii) Another polymerization process used to make CMPs is coordination polymerization in which CMPs are formed upon the metallation process of bis-ligand-center organic linkers. CMPs obtained by this method may have a dynamic binding manner between the metal ions and the organic likers offering possible switching between dynamic and static forms upon changing the oxidation state of the metal centers.[16] (iv) CMPs could also be obtained by first preparing a metal-free polymer followed by the metallation process. This method, however, requires the ligand polymers being soluble in organic solvents and, in some cases, the complexation process may not go to completion.

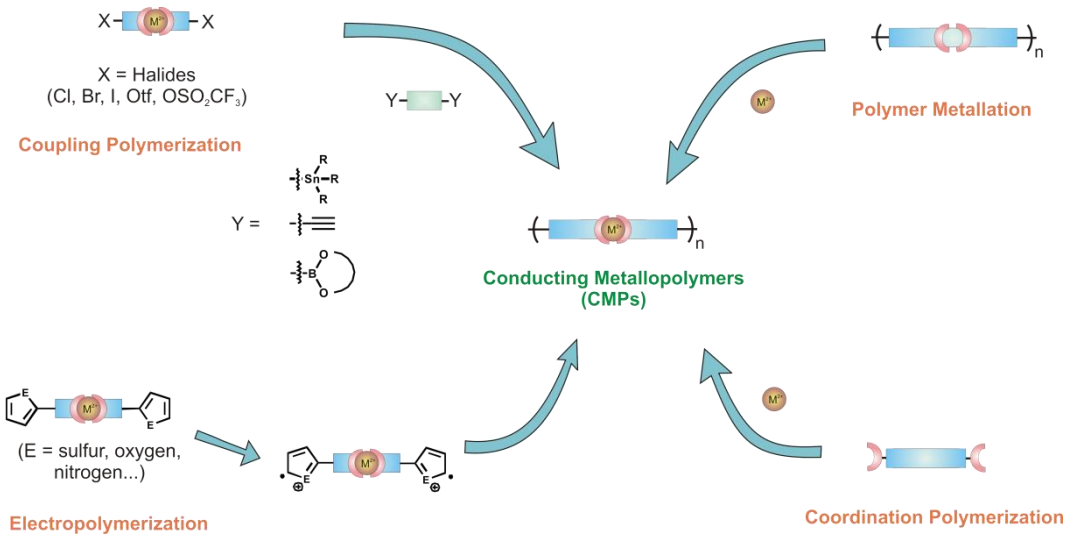

Figure 1.3. Synthetic strategies for the preparation of conducting metallopolymers.

1.1.4. Scope of this review

A good number of reviews have been reported on the development of metallopolymers with both conjugated and non-conjugated polymer chains.[6-8,15-20] In this review, we focus on applications of π-conjugated conducting metallopolymers that utilize the electrical conductivity of polymer in conjunction with the functionality of metal complexes. The applications of CMPs in light-emitting diode, which is likely the most extensively explored in CMPs, have been recently reviewed based on the category of metal types (iridium,[20,21] platinum,[20] and zinc[20], and lanthanides[22]) and will not be covered. Recent advances in applications of π-conjugated CMPs in the fields of chemical sensors, memory devices, catalysis, and organic photovoltaics will be highlighted. Additionally, we also address, when possible, the current challenges of these fields and how the use of CMPs could possibly fulfill the requirements to be a promising material.

1.2. Application of CMPs in Chemical Sensors

Chemical sensing is not only an important process in biological systems but also an essential tool in environmental studies.[23] In order to detect an analyte, a chemical

sensor needs to contain two main components: the recognition site (receptor) and a signaling unit. These two elements need to be in communication with each other so that when a molecule/ion of interest binds to the receptor, it changes the output of the signaling units. As addressed in the previous section, metal centers and organic backbone in CMPs could possibly be in electronic communication and influence the optical and electrochemical properties of each other. In addition, each of the two components could be able to serve as either the binding site or a signaling unit. These characteristics offer promisingly sensing potential of CMPs for chemical sensors.

Research on chemosensing applications of CMPs has been focused on utilizing the two primary properties of CMPs as output signals: photoluminescence (PL) and conductivity. Molecule/ion detection is often based either on a "turn-on" or "turn-off" mechanism (Figure 1.4).[6] In the former case, the output signal of sensing devices is increased when a small molecule/ion binds to the recognition sites. "Turn-off" chemosensors, on the other hand, have the output of response signal decrease upon the binding of analytes. In this section, research progress and current advances using CMPs as chemical sensors limited to the use of PL and conductivity as response signals will be presented.

1.2.1. Chemosensors based on photoluminescence (PL)

Photoluminescence chemosensors are some of the most common chemical sensors due to the high sensitivity of PL signals as well as the ease of the PL technique.[24] The detection of analytes in PL chemosensors could be based on the increasing/decreasing of PL intensity, the change in emission color, and/or the PL lifetime.

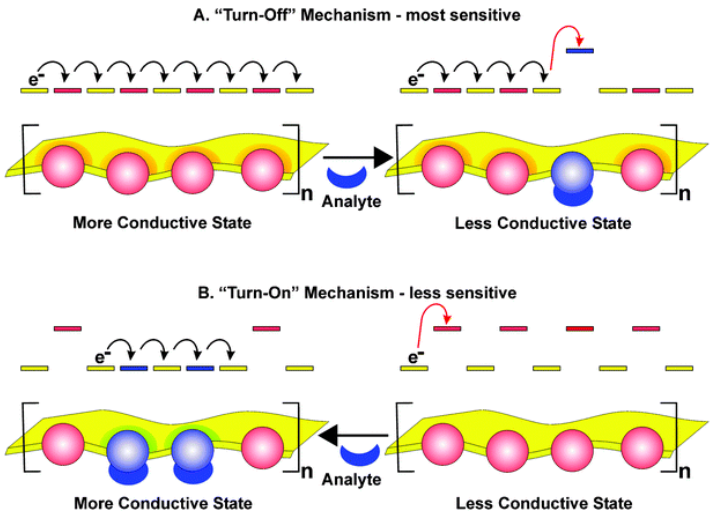

Figure 1.4. Schematic representation of two sensing mechanisms in small molecule/ion sensors based on the increasing (turn-on) and decreasing (turn-off) of conductivity. Reproduced with permission.[6]

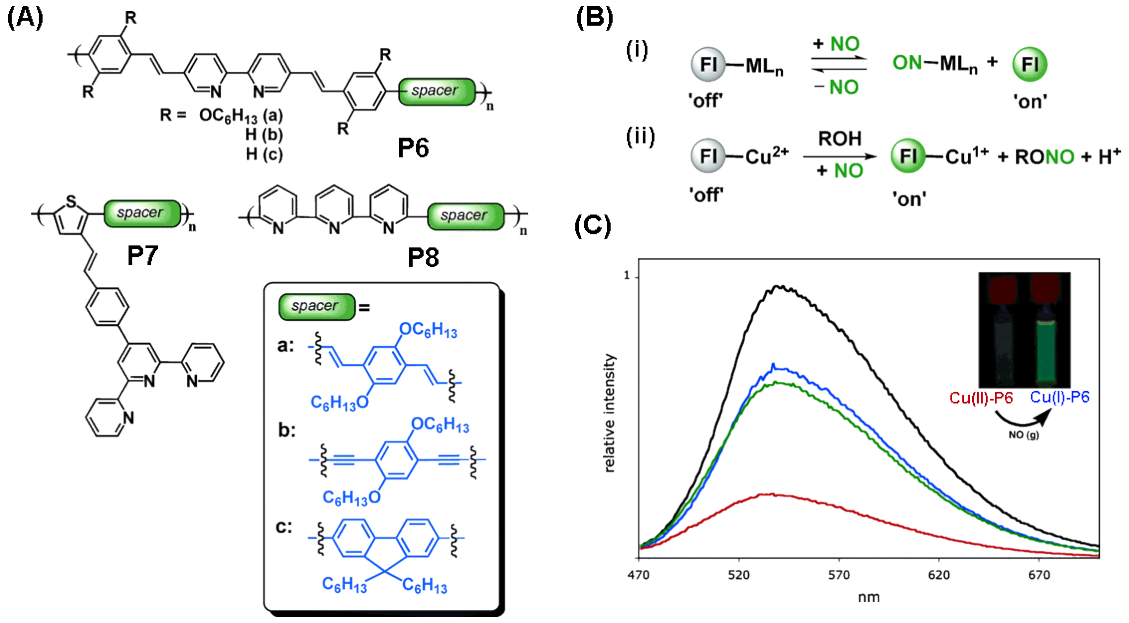

Figure 1.5. (A) Conjugated backbones (**P6-8**) used to prepare copper-containing CMPs for NO detection (B) Two mechanisms of PL "turn-on" for NO detection by Cu-CMPs (c) PL response upon treating Cu(II)-**P6** with NO: Emission spectra of **P6** (black), Cu(I)-**P6** (green), Cu(II)-**P6** (red), and Cu(II)-**P6** immediately following addition of 300 equivalents of NO gas (blue). Adapted with permission.[25,26] Copyright 2006 American Chemical Society.

1.2.1.1. Nitric oxide detection

Nitric oxide (NO) is an important bio-signaling molecule involving in many biological processes and the detection of this molecule is of interest to the biochemical scientific community.[27] Lippard and co-workers have developed a series of Wolf Type-II copper-containing CMPs (Cu(II)-**P6-8**, Figure 1.5A) for the detection of NO using the PL "turn-on" mechanism.[25,26,28,29] The increase in PL intensity was reported to happen by either phosphore replacement or reductive nitrosylation (Figure 1.5B). In the prior process, the phosphore that binds to metal centers is replaced by NO molecule forming a metal nitrosyl. The free phosphore now is PL active due to the removal of PL-quenching metal ions resulting in a "turn-on" effect. The latter case involves the reduction of the paramagnetic, PL-quenching Cu(II) ion, to the diamagnetic, non-quenching Cu(I) ion and, therefore, turning the PL signal of polymer back on. Cu-containing CMPs Cu(II)-**P6-8** reported by Lippard *et al.* exhibit an approximate 3-fold increase in PL intensity when treated with NO.[25,26] Sensing mechanism was found to occur *via* the reduction of Cu(II) centers by NO molecules. The suggested mechanism was proposed as the PL intensity of Cu(II)-**P6** after treatment with NO gas is observed to be almost the same as in the PL spectrum of the CMP from **P6** and Cu(I) ions (Figure 1.5C). The diminution of electron paramagnetic resonance (EPR) signal of Cu(II) centers in Cu(II)-**P6** after exposure to NO further confirms the argument. Using this mechanism, Lippard and co-workers have also prepared water-soluble CMPs for NO sensing by replacing alkyl chains with hydrophilic groups.[28] The sensing activity of the obtained CMPs remains almost the same as for **P6-8** with 3.2-fold PL increase upon adding excess NO. The results exhibit promising application of these Cu-CMPs for use to detect NO in biological systems in aqueous media.[28]

The quenching effect of Cu(II) ions to the PL signal of organic backbone as well as PL "turn-on" effect for NO detection are also observed when the Cu(II) ions do not strongly interact to the organic backbone. The use of a weakly coordinating center, bithiophene, in place of the bipyridine in **P6-8** also resulted in CMPs with similar sensing behavior.[29] Zhu *et al.* reported another Wolf Type-I Cu-CMP (Cu(II)-**P9**, Figure 1.6), in which Cu(II) ions weakly coordinate to imidazole moieties that are linked to a conjugated backbone by a hexyl chain.[30] Although there is little interaction between metal ions and conjugated backbone as typically found in Wolf Type-I CMPs, a 75% PL quenching is observed when **P9** coordinate to Cu(II) ions; 70% of which was recovered when the resulting CMP was exposed to NO.[30]

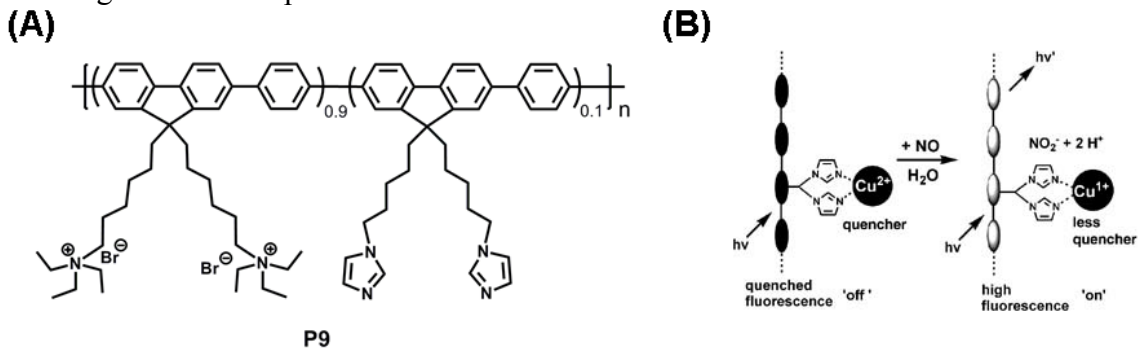

Figure 1.6. (A) Chemical structure of metal-free polymer **P9**. (B) Sensing mechanism of weakly coordinated Cu-CMP (Cu(II)-**P9**) for NO detection. Reproduced with permission.[30]

1.2.1.2. Oxygen detection

The detection of molecular oxygen using metal complexes is typically based on the quenching of phosphorescence by oxygen molecule. The ground state of O_2 facilitates triplet-triplet energy transfer from the triplet excited state of the metals.[31] Late-transition-metal complexes, such as those of Ru, Ir, and Pt, are commonly used in oxygen sensing due to the highly efficient phosphorescence of these metals. CMPs of these metals also

inherit combined advantages from the polymer backbone, such as the π-conjugated delocalization, fast electron or energy transfer, and the high luminescence efficiencies. Swager *et al.* have demonstrated that the use of a cyclometalated Pt-CMP (**P10**) could increase the sensitivity for oxygen detection by 30-40% compared to the molecular model complex **M10** (Figure 1.7).[32] The results suggest that the mixing of the excited state of metal complexes with the conjugated conducting polymers could be a potentially viable means towards improving oxygen sensing materials.

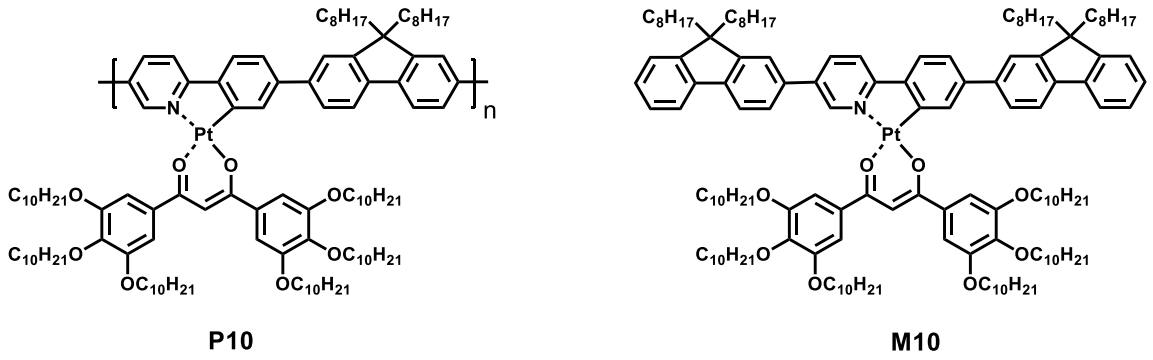

Figure 1.7. Chemical structure of cyclometalated Pt-CMP, **P10**, and the corresponding model complex **M10** for O_2 sensing.

Recently, Huang and co-workers reported the use of polymer dots (Pdots) of an Ir-CMP (**P11**) as an oxygen-sensing material (Figure 1.8).[33] The reported material not only has the beneficial properties from highly phosphorescent complexes and a conjugated polymer system but also takes advantage of small, nano-size polymer particles for biological compatibility. These polymer dots exhibit low cytotoxicity and can pass through cell membranes to reach into the cytoplasm. The formation of singlet oxygen from the irradiation of polymer dots with 488 nm light can effectively induce the apoptosis and death of tumor cells. Moreover, the authors also demonstrated that Ir-CMP Pdots can also be used in cellular imaging by laser scanning microscopy indicating a

multi-functional application of the material in oxygen sensing, cellular imaging, and photodynamic cancer therapy.

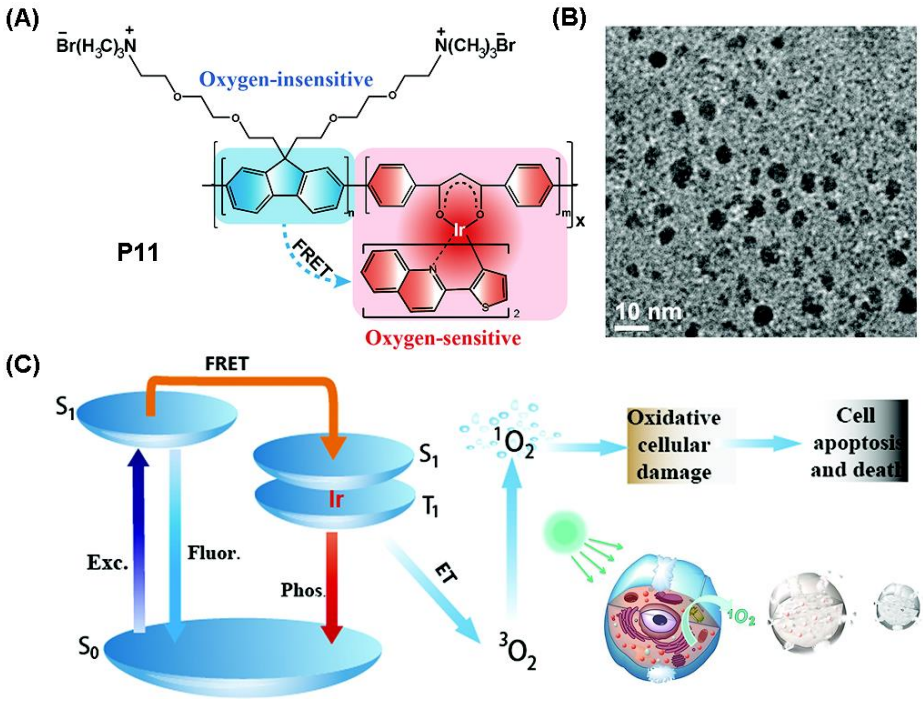

Figure 1.8. (A) Chemical structure phosphorescent Ir(III)-CMP **P11**. (B) TEM of **P11** polymer dots. (C) mechanisms of oxygen sensing and photodynamic therapy. Reproduced with permission.[33]

1.2.1.3. Anion detection

Many toxic anions, such as cyanide or sulfide, are used and found in water from industrial processes and the detection of these ions has become important from industrial, environmental, and biological points of view. Because of their exceptionally low lethal dosage, chemosensors for those anions need to be highly sensitive to sub-ppm levels, creating challenges in searching for effective sensing materials. Chemosensors from CMPs utilizing the PL output signal have become a potentially promising technique to sense toxic anions due to the strong affinity of these anions to metal centers combined with the high sensitivity and ease of PL measurements.

In general, the use of CMPs as PL chemosensors to detect anions are primarily based on two steps: (i) the PL quenching of organic backbone by metal centers and (ii) the PL "turn on" due to decomplexation of the metal centers from the CMPs upon exposure to anions, which usually have higher affinity to metal centers than the ligand centers in CMPs. As an effective PL quenching ion, Cu(II) is commonly used in CMP systems to detect toxic or biologically important anions.

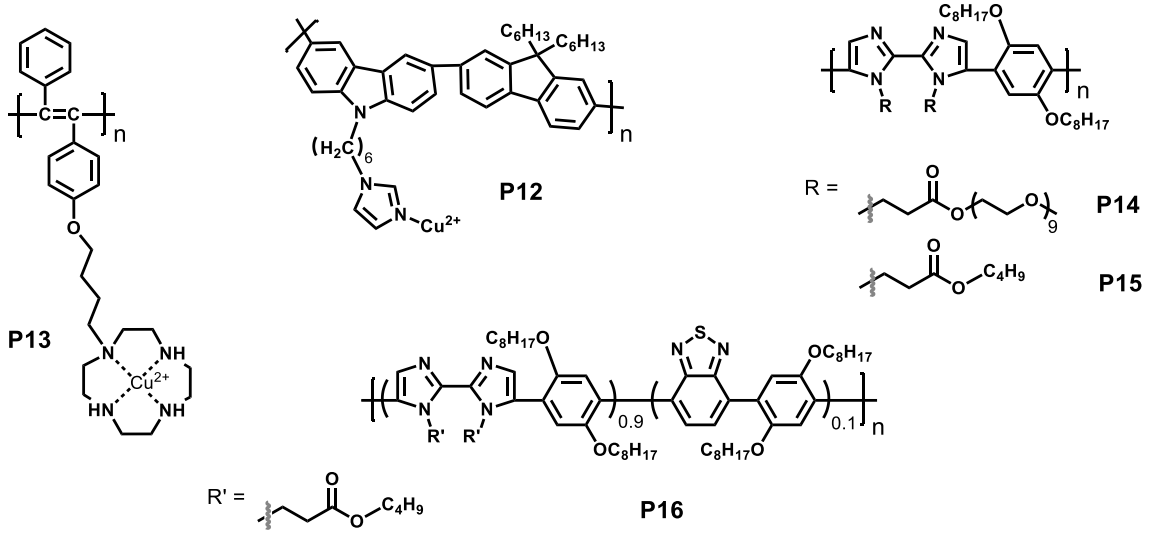

Figure 1.9. Chemical structure of CMPs (**P12-P16**) used in anion sensing.

Qin and coworkers reported a Wolf Type-I copper-containing CMP (**P12**) synthesized by the complexation of an imidazole-bearing ligand polymer with copper (II) ions.[34] The addition of Cu(II) ions quenches the PL of the conducting polymer. However, when treated with cyanide (CN^-) ions, the PL signal turns back on allowing for the sensitive detection of CN^-. The CMP showed a high selectivity to CN^- over 11 other tested anions with the detection limit as low as 0.31 ppm. However, though **P12** showed high selectivity and sensitivity toward the CN^- anion, further investigations on sensing selectivity may be necessary. As previously mentioned, a imidazole-bearing Cu-CMP system reported by Zhu *et al.* also displayed a high response to NO detection although

employing a different mechanism (Figure 1.6).[30] A recent report from the same group was focused on the detection of sulfide (S^{2-}) anions using a polyacetylene backbone bearing cyclen moieties (**P13**).[35] The detection limit for S^{2-} by PL quenching was reported at 2.0 x 10^{-7} mol·L^{-1} and the material showed high selectivity over 26 other anions including cyanide. Bai *et al.* reported a series of 2,2'-biimidazole-bearing Cu-CMPs (Cu(II)-**P14-16**) that showed excellent sensing properties for the pyrophosphate anion, a byproduct of ATP hydrolysis under cellular conditions, with a 0.17 ppm detection limit.[36]

1.2.1.4. Transition metal detection

Transition metals, such as Fe(II), Cu(II), and Ni(II), etc., are reputedly known as PL "killers" and, consequently, the use of PL could become an effective mean to detect these metals. However, it is required that sensing materials need to have a high selectivity in addition to good sensitivity to a certain metal.

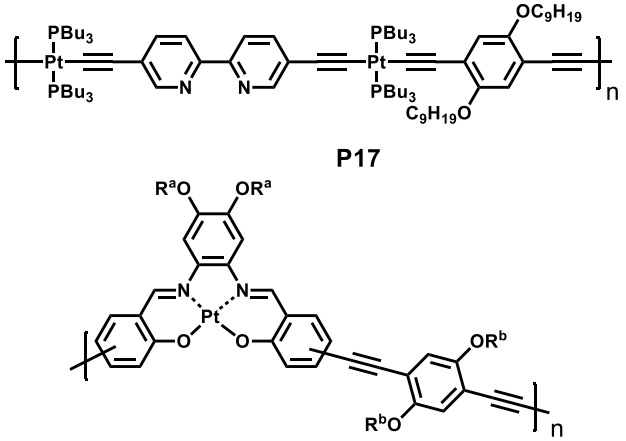

P17

P18 (*m*-O) **P19** (*p*-O)

P20 (*m*-O) **P21** (*p*-O)

$R^a = R^b =$

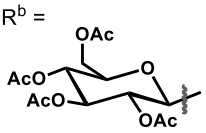

$R^a = C_{12}H_{25}$ $R^b = C_{16}H_{33}$

Figure 1.10. Chemical structure of CMPs (**P17-P21**) for Cu(II) detection.

Schanze *et al.* initiated the use of CMPs as sensing materials for transition metal cation detection.[37] They reported the use of a platinum acetylide polymer (**P17**), a Wolf Type-III CMP, for cation sensing of six different transition metals. Although the material displayed effective PL quenching, this polymer system did not show very good selectivity due to the strong coordination tendency of the 2,2'-bipyridine acceptor site. However, as reported in oxygen sensing by Swager and co-workers,[32] the extension of the conjugated backbone in the polymer shows a much higher sensitivity in PL quenching with Cu(II) and Ni(II) compared to model complexes.[37] These results, again, suggest an "amplified quenching effect" of CMPs in sensing activity.

A highly selective sensing polymer for Cu(II) detection has been reported for Pt-salen CMPs, **P18-21**.[38] The authors reported effective Cu(II) selectivity by PL quenching to 9 other metal cations including Pb^{2+} and Hg^{2+}. However, further testing with other reputed PL-quenching transition metal cations such as Fe^{2+} or Ni^{2+} was not reported.

In addition to the "turn-off" mechanism in the PL quenching of metal cations, detection of metal cations can also be based on the change in emission color of sensing materials. An Ir-containing CMP (**P22**) was reported by Huang and co-workers that could detect trace amounts of Hg^{2+} as low as 0.5 ppb.[39] Exposure of **P22** solution to a low content of Hg^{2+} changes the emission color from red to yellow-green corresponding to a shift of emission wavelength from 618 nm to 519 nm (Figure 1.11). The shifting was assigned to the decomposition of Ir-complex due to the coordination of Hg^{2+}. Moreover, the detection of Hg^{2+} can also be noticed by the change in polymer color which could be visibly noticed and monitored by the absorption spectra.

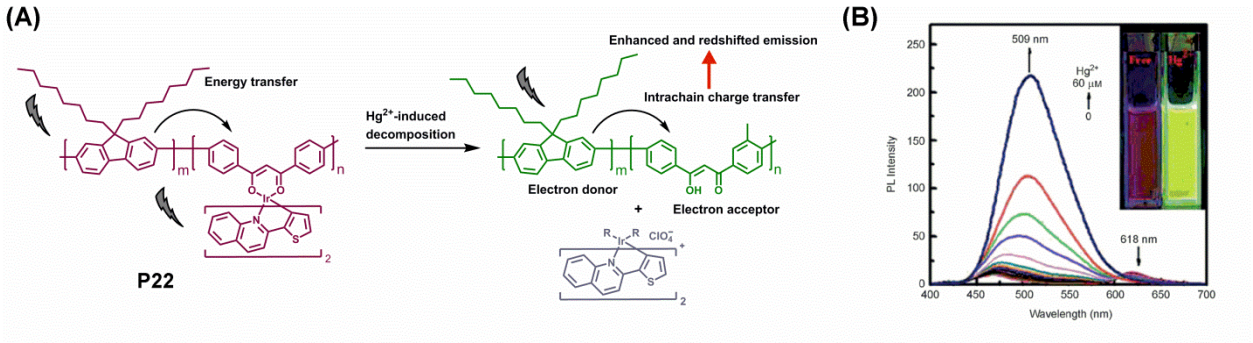

Figure 1.11. (A) Chemical structure of **P22** and sensing mechanism using **P22** for Hg^{2+} detection. (B) Emission spectra of **P22** as increasing concentration of Hg^{2+}. Inset shows the polymer emission color before and after exposure to Hg^{2+}. Adapted with permission.[33]

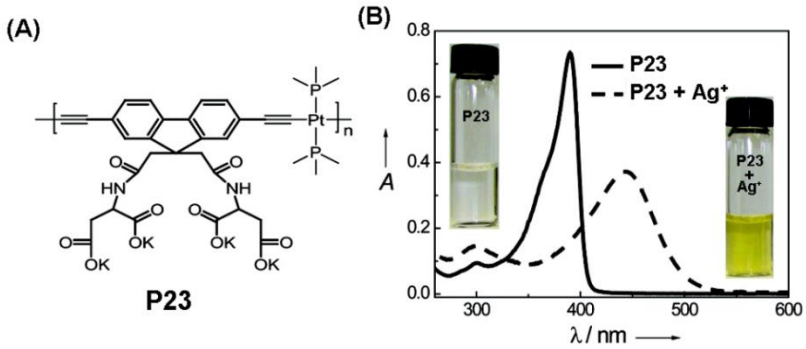

Figure 1.12. (A) Chemical structure of **P23**. (B) Absorption spectra and color changes of **P23** solution before and after exposure to Ag^{+}. Reproduced with permission.[40] Copyright 2010 American Chemical Society.

Another example of cation sensing by change in polymer color was reported by Wang and coworkers.[40] A water-soluble fluorescence-based Pt acetylide CMP (**P23**) was synthesized *via* Sonogashira coupling reaction and the resulting CMP demonstrated remarkably high sensitivity and selectivity to Ag^{+}. In the presence of Ag^{+} ions, the polymer exhibits a clear visual color change from colorless to yellow along with a 25-nm shift of emission peak. With a distinctive color change visible to the naked eye, this system demonstrates a quick, simple, and highly practical procedure for Ag^{+} detection.

1.2.2. Chemosensors based on conductivity

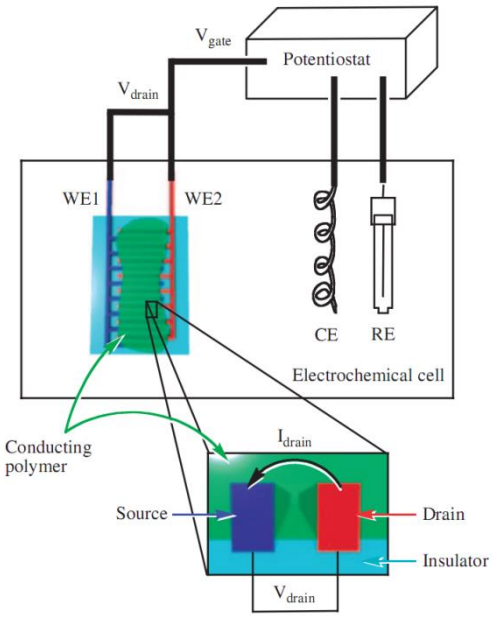

Figure 1.13. Schematic representation of an electrochemical diagram for the determination of polymer's conductivity as a function of analyte and applied potential. Reproduced with permission.[41]

The key feature of a chemical sensor is the change of an output signal upon binding of the analytes of interest. The detection limits are dependent on the type of signal and the influence of analytes on the signal output. In practice, the signal can be monitored optically or electrically based on the PL intensity and color change or the material conductivity, respectively. Conductometric sensors, which will be reviewed in this section, monitor the flowing charge between two electrodes that are covered with the sensing materials. These sensory devices were developed in Swager's laboratory using interdigitated electrodes (Figure 1.13).[41] The devices function in a transistor mode in which a drain current (I_{drain}) flows between the two working electrodes (WE1 and WE2) that have a small offset potential (V_{drain}). By scanning the electrochemical potential of both the source and drain electrodes, a profile of I_{drain}, which is proportional to the

conductivity of the polymers, is determined. Conductometric chemosensors using CMPs are based on the binding of analytes to metal centers or a receptor site that will influence the electrochemical properties of CMPs and therefore increases (turn-on) or decreases (turn-off) the polymer redox conductivity.

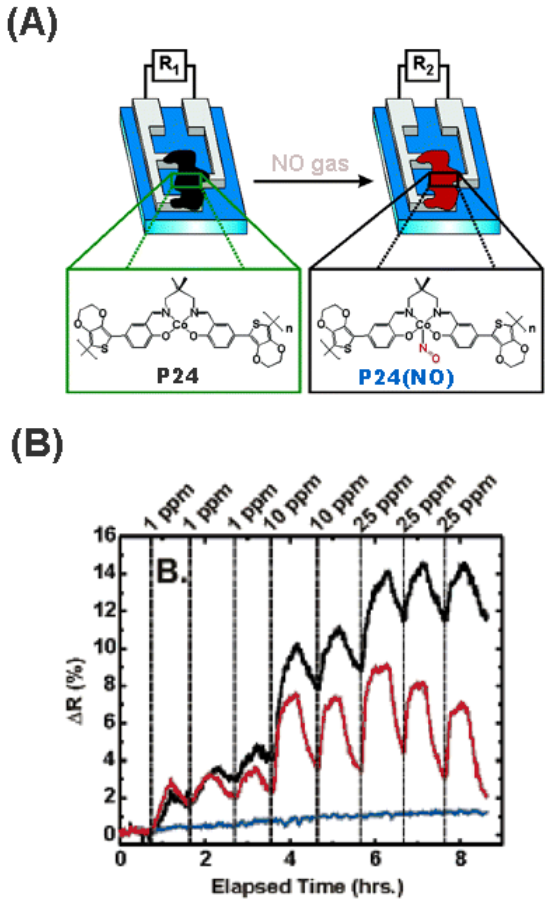

Figure 1.14. (A) Schematic illustration of chemosensing device utilizing CMP **P24**. (B) Relative variations of resistance of **P24** films to increasing concentrations of NO gas. Adapted with permission.[42] Copyright 2006 American Chemical Society.

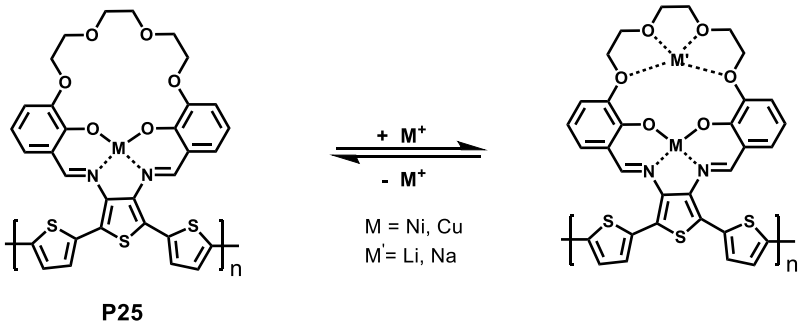

Figure 1.15. Chemical structure of **P25** and mechanism for cation sensing.

1.2.2.1. Small molecule sensing

Swager and Holliday have reported a sensory device for the detection of nitric oxides (NO_x) using a Co-containing CMP (**P24**) in the solid state.[42] A cobalt salphen [*N,N'*-propylene*bis*(salicylidenimine)] complex bearing 3,4-ethylenedioxythiophene (EDOT) was synthesized and electropolymerized onto an interdigitated electrode (Figure 1.14). The coordinatively unsaturated cobalt center serves as a receptor site for analyte binding. Furthermore, redox matching of the metal centers and polymer backbone, poly(EDOT), resulted in the amplification of the influence of an analyte on the polymer conductivity upon binding to the metal units. The authors demonstrated that this polymer-film sensor system could selectively detect NO gas over other small molecules (O_2, NO_2, CO, and CO_2) with a detection limit below 1 ppm.

1.2.2.2. Metal cation sensing

The change in the electrochemical behavior of CMPs is caused not only by the bonding of small molecules to metal centers but also by metal cations as reported by Reynolds and co-workers.[43] In their study, crown-ether-containing CMPs (**P25**) have been synthesized *via* electropolymerization. These polymers possess two sensory sites; the metal SALOTH unit and the crown-ether center (Figure 1.15). The former site allows the binding of small donor molecules (i.e. pyridine, DMF, DMSO) to oxidized metal

centers resulting in the change of polymer electroactivity. The latter sensory site, the crown-ether moiety, exhibits electrochemical shifting in the present of Li^+, Na^+, Mg^{2+}, and Ba^{2+} cations. Depending on type of ions, the process is reversible (Li^+ and Na^+) or irreversible (Mg^{2+} and Ba^{2+}).

1.3. APPLICATION OF CMPS IN MEMORY DEVICES

The rapid development of information technology has put an urgent demand on the search for new materials and/or methods for high-capacity data storage. In order to be used in data storage devices, a material should be able to be switched between two states that have different properties, which may be recorded as a "0" or "OFF" mode and the "1" or "ON" mode. Based on how the ON/OFF mode is resisted after a stimulus is turned off, memory devices are divided into two classes: volatile and non-volatile. In volatile devices, an external stimulation (electric bias or magnetic field) needs to be maintained to keep the "1" mode on otherwise it will relax to the "0" state. DRAM (dynamic random access memory) and SRAM (static random access memory) belong to this device class. Non-volatile memory devices, on the other hand, can maintain the ON mode after the stimulus is removed. This type of data storage devices is used in WORM (write-one read-many-time) and flash (rewritable) memory devices.[44]

With respect to working principle, there are two main types of memory devices: resistive memory devices and magnetic memory devices. In the former device type, a voltage bias or pulse is used to switch between the non-conductive (high-resistance, OFF) and the conductive (low-resistance, ON) states. The ON/OFF states in magnetic data storage devices, however, are determined by localized magnetization directions in the materials, which are modified by a relatively weak magnetic field *via* a head read/writer. Magnetic memory devices are usually permanent data storage devices while resistive

memory devices could be volatile or non-volatile depending on the properties of the materials used.

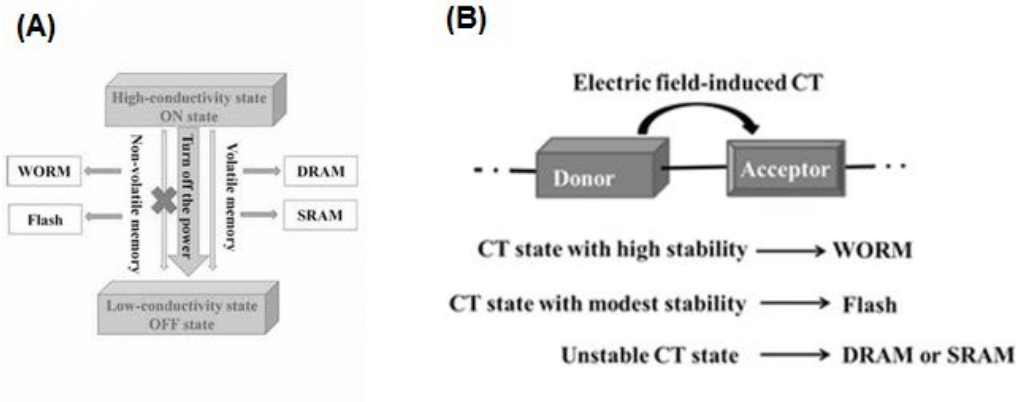

Figure 1.16. (A) Schematic representation of memory device classification. (B) Memory behavior of materials with various stabilities of charge transfer (CT) state. Reproduced with permission.[44]

Conjugated conducting polymers are usually non-conductive in the neutral state and become conductive upon chemical or electrochemical doping.[1,2] This bistable behavior makes them promising candidates for use in memory devices. Conducting metallopolymers (CMPs), moreover, display beneficial properties of both conducting polymers and metal complexes. In addition to the resistance-bistability of conducting polymers, the redox and magnetic properties of metal centers contained therein also offer a two-state system for use in data storage devices. In this section, we review some of the current advances in using CMP materials for non-volatile memory devices that operate using both resistance- and magnetization-based manners.

1.3.1. Resistive memory devices

There are several possible mechanisms to switch between the neutral non-conductive (OFF) state of a conducting polymer and the conductive (ON) state such as electrical-field-induced charge transfer, conformation change, charge trapping,

filamentary conduction, etc.[44] The use of CMPs in memory devices usually employ a charge transfer mechanism, in which the organic backbone acts as electron donors and metal complexes act as electron acceptors and charge holders. Additionally, the metal centers in CMPs may be switched between two redox states (low and high oxidation states). Switching between these two states can result in the change in conductivity of CMPs, and thus may be utilized in information storage devices.

1.3.1.1. Memory devices based on donor-acceptor charge transfer

In conducting polymers, the charge transfer (CT) process happens as electronic charge is partially transferred from a charge-donor moiety of the polymer to a charge-acceptor one upon the application of an electronic voltage bias. This CT process usually results in a significant increase in polymer conductivity. Depending on the stability of the CT states generated, the materials could be used for different types of memory devices (Figure 1.16). Due to varying arrangements between the polymer backbones and metal complexes in CMPs, the efficiency of the CT process and stability of CT state are dependent on the CMP types. This section will discuss the use of CMPs in memory devices based on CMP types. The chemical structures of Wolf Type I-III CMPs which have been used in resistive memory devices are shown in Figure 1.17 and their device characteristics are summarized in Table 1.1.

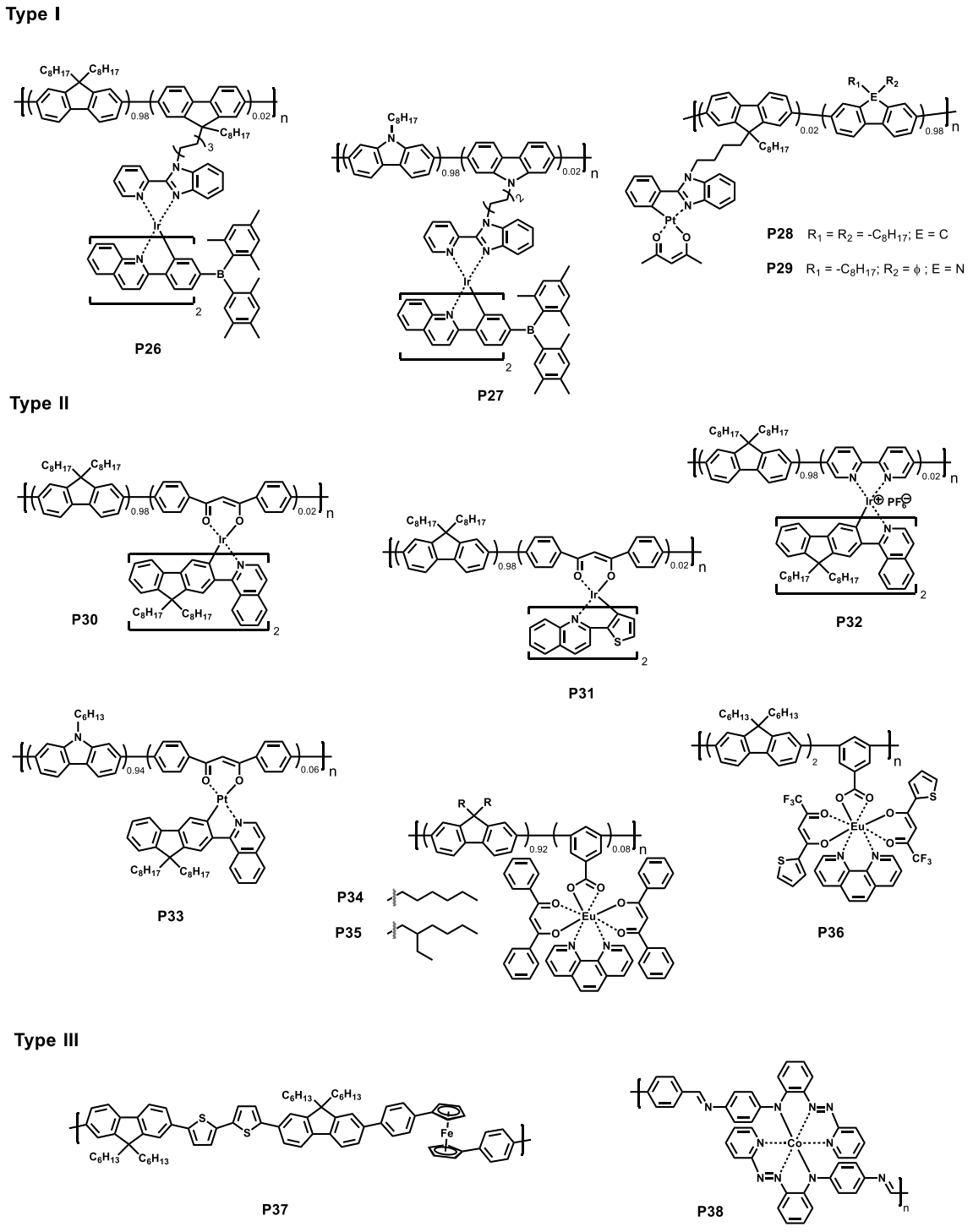

Figure 1.17. Chemical structures of conducting metallopolymers (**P26-P38**) used in resistive memory devices.

In Wolf Type-I CMPs, the metal complexes and organic backbone are separated by an insulating organic linker and ON/OFF conductivity switching is based on through-space charge-transfer. Huang and co-workers reported the synthesis and investigation of memory effect behaviors of Wolf Type-I CMPs incorporating Ir (III) complexes.[45] Two different polymer backbones, polyfluorene (**P26**) and polycarbazole (**P27)**, were used to clarify the effect of polymer backbones on the device performance. Both polymers exhibit flash memory behaviors with low voltages for writing, reading, and erasing. The ON/OFF ratio, which reflects the ratio of passing currents through the device between the conductive and non-conductive states, is higher than 10^3, indicating a good device function for minimal misreading errors. Both ON and OFF states are stable up to 10^7cycles at reading voltage of 1.0 V (Figure 1.18).

To explain the memory effect behaviors of the polymers, the authors proposed that under an applied field (-1.2 and -1.4 V for **P26** and **P27**, respectively), charges are transferred from the polymer backbone to the Ir(III) complex moieties, resulting in the formation of a stable CT complex. These CT complexes make the migration of charge carriers among different polymer chains easier, resulting in an abrupt increase in conductivity of the CMPs. Thus, the device is switched from the OFF state to the ON state, which persists even with the removal of the driving power due to the high stability of the generated CT complex. To switch the device back to the OFF state, a reverse bias (3. 7 and 4. 1 V for **P26** and **P27**, respectively) is applied leading to the dissociation of CT complex. This reversible switching of the ON/OFF states demonstrates the flash (rewritable) memory behavior of these two Ir(III) CMPs. The use of different polymer backbones was found to lead to a difference in the “switch-on” or “writing” voltages due to the difference in energy level between polyfluorene and polycarbazole to those of the same Ir(III) complexes.

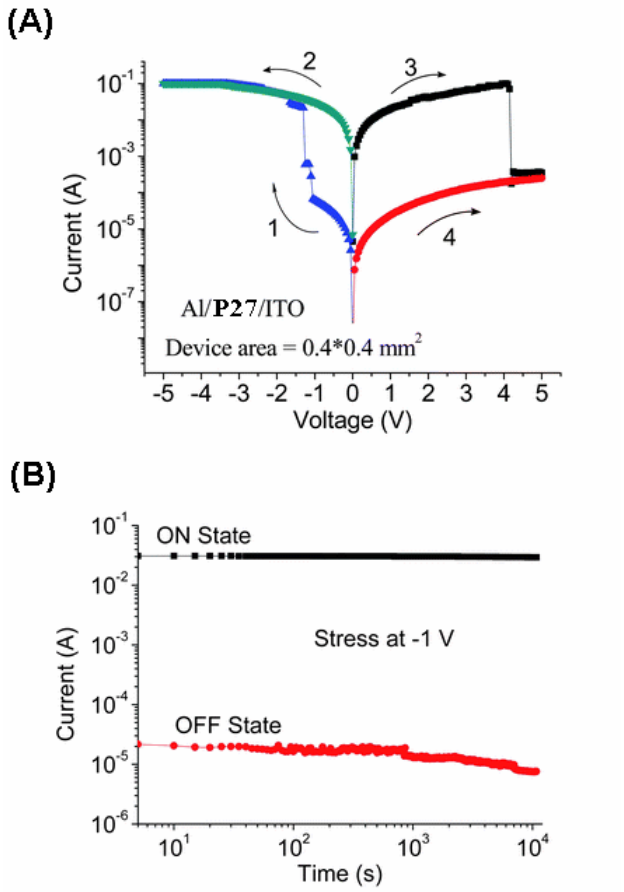

Figure 1.18. (A) *I-V* characteristics of the ITO/**P27**/Al device, showing the "write-read-erase-read" cycle. (B) Stability of a memory device from **P27** in either ON or OFF state under a constant stress (-1.0 V). Adapted with permission.[45]

A similar effect was observed and reported by the same group on Wolf Type-I CMPs of Pt(II) complexes (**P28** and **P29**).[46] These two Pt(II) CMPs also exhibit excellent memory effect behaviors in ITO/polymer/Al devices (Figure 1.19). When changing the polymer backbone from polyfluorene to polycarbazole, the authors observed a significant decrease for the "switch-on" voltage, from -2.6 V for **P28** to -1.6 V for **P29**. Compared to the previously-mentioned Ir(III) CMPs, the applied bias of Pt(II) CMPs is more negative; this is likely due to the different nature of the metal centers and auxiliary ligands.

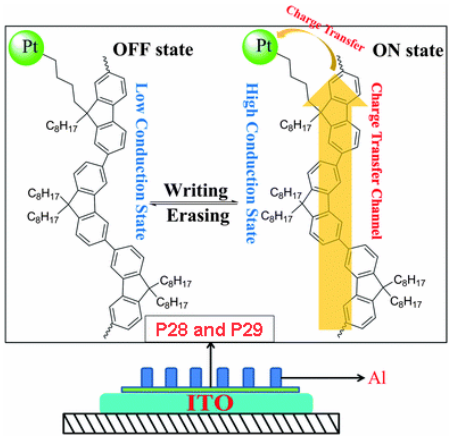

Figure 1.19. Device structure and memory-effect mechanism for Wolf Type-II Pt(II) CMPs (**P28** and **P29**). Reproduced with permission.[46]

In Wolf Type-II CMPs, the metal centers are bound directly to the polymer backbones, leading to direct electronic communication between the two components. Therefore, charge transfer between the donor (polymer backbone) and the acceptor (metal complex), in principle, is easier, resulting in a lower required bias voltage to "switch-on" the conductivity of Wolf Type-II CMPs compared to that of Wolf Type-I polymers. This is an important characteristic for memory devices with respect to energy consumption, especially concerning mobile devices that have limited energy storage capacities such as cell phones and laptops.

Most reported studies on using Wolf Type-II CMPs in data storage devices are based on hybrid polymers of Ir(III),[47] Pt(II),[48] and Eu(III)[49-51] complexes and polyfluorene or polycarbazole backbones. The chemical structures and device characterization of those polymers may be found in Figure 1.17 and Table 1, respectively. A series of Wolf Type-II Ir(III) CMPs (**P30-32**) has been synthesized and investigated for memory storage behavior by Huang *et al.*[39] These three polymers show excellent memory effects when fabricated into ITO/polymer/Al devices. Compared to memory devices fabricated from **P26**,[45] a polyfluorene Ir(III) Wolf Type-I CMP, devices obtained from

Table 1.1. Characteristics of resistive memory devices that use conducting metallopolymers.

Polymer	Metal	CMP type	Device type	Writing bias (V)	Erasing bias (V)	ON/OFF ratio	Stability (cycles)[a]
P26	Ir	I	Flash	-1.4	3.7	10^3	10^7
P27	Ir	I	Flash	-1.2	4.1	10^3	10^7
P28	Pt	I	Flash	-1.6	2.9	$5x10^3$	10^7
P29	Pt	I	Flash	-2.6	3.0	10^3	10^7
P30	Ir	II	Flash	-0.9	3.4	10^3	-
P31	Ir	II	Flash	-1.1	3.8	10^3	-
P32	Ir	II	Flash	-1.6	2.8	10^5	10^8
P33	Pt	II	Flash	-1.5	4.1	10^7	10^7
P33	Eu	II	WORM	3	n/a	10^7	10^8
P35	Eu	II	WORM	3	n/a	10^6	10^7
P36	Eu	II	WORM	4	n/a	$2x10^2$	-
P37	Fe	III	Flash	-1.9	1.4	10^3	$> 10^2$
P38	Co	III	Flash	-3	3	10^2	-

[a] by applying a constant stress at reading voltage ~ 1.0 V.

P30 and **P31** display a much lower "switch-on" voltages (-1.1 and -0.9 V, respectively). This behavior may be due to a more accessible on-chain charge-transfer process. However, it may be too early to conclude this without further investigations into structure and device performance relationships of CMPs. A better understanding of the effects of the metals, ligand centers, auxiliary ligands, coordination manner, and organic backbones is necessary in order to be able to rationally design systems with excellent memory effect

and efficiency. For example, in spite of belonging to the Wolf Type-II CMPs, **P33** gives devices that still exhibit a higher "switch-on" bias voltage than those from **P29**, a Wolf Type-I CMP with the same polycarbazole backbone, which may be due to the use of different on-chain ligands, as well as auxiliary ligands.

In resistive memory devices that employ charge transfer processes as the switching mechanism for memory behaviors, the stability of the CT complex will determine the device type. When the CT complex is highly stable, which is usually found in polymers with high electron affinities with regard to the metal complex moieties, the reverse process to turn the ON state back to the OFF mode is not likely to occur, and the materials are used for write-once-read-many-time (WORM) memory devices. Kang and co-workers reported the synthesis and fabrication into memory devices of a Eu(III)-containing CMP series (**P34-36**).[49-51] Devices fabricated from these polymers exhibit WORM memory behaviors with a CT mechanism, in which the backbone, polyfluorene, acts as the electron donor and Eu(III) complex act as the electron acceptor. Polymers **P34** and **P35** show excellent memory effect at ~ 3 V writing voltages. The ON/OFF ratios of memory devices from these two CMPs are as high as 10^6-10^7, and the stabilities of the ON and OFF states allow for up to 10^7-10^8 reading cycles.[49,50] Changing the auxiliary ligands that are bound to the Eu(III) metal centers in these polymers from a dibenzoylmethanido ligand in **P34** to a 2-thenoyltrifluoroacetonato one in **P36** significantly reduced the ON/OFF ratio to 200 at "switch-on" voltage around 4 V.[51] This further confirms the influence of auxiliary ligands on device performance as observed in Ir(III) CMPs.

1.3.1.2. Memory devices based on metal redox bistability

Besides the "switch-on" mechanism by charge transfer between the donor and acceptor moieties in CMPs, the bistability offered by redox-active metal centers may also be used to induce a memory effect. In Wolf Type-III CMPs, metal centers act as an intergrated component of the polymer backbone and therefore have significantly strong interactions with the conjugated organic segments. The change in electronic properties of the embedded metal centers, such as the oxidation states, could greatly affect the properties of the whole polymer chain. The transition between the low and high oxidation states of metal centers usually significantly influences the charge transport properties of the materials and can be used to switch between the non-conductive and conductive states of the CMPs; this bistability behavior may potentially be taken advantage of for use in memory devices.

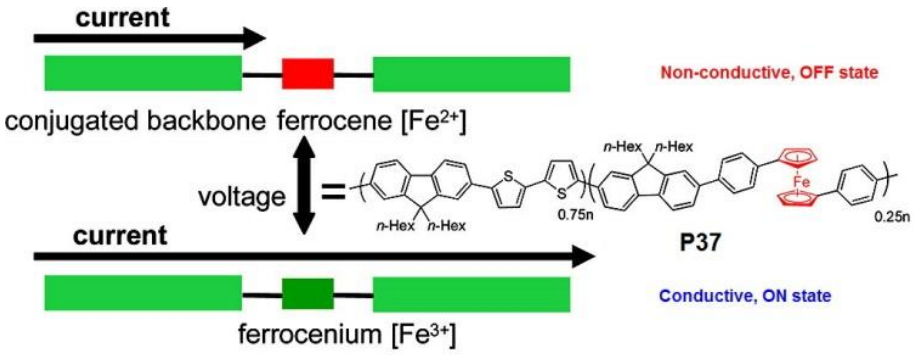

Figure 1.20. Chemical structure and memory effect mechanism of the iron-containing CMP **P37**. Adapted with permission.[52] Copyright 2007 American Chemical Society.

Choi and co-workers have prepared a ferrocene-containing CMP with fluorene and bithiophene as conjugated segments (**P37**).[52] This Wolf Type-III CMP has been successfully applied to memory devices using sandwich structure ITO/polymer/LiF/Al. The initial device exhibits a low-conducting state (OFF state) at low voltages and has an

abrupt increase in conductivity under a -1.9 V bias, showing a "switch-on" transition with an ON/OFF current ratio on the order of 10^3. The conductive state persisted under the reverse scan until a 1.4 V bias was applied, which reverted the CMP back to the low-conductive state. The reversible switching of the ON/OFF states indicates a flash (rewritable) memory effect of this Fe-CMP. The switching mechanism was assigned to the oxidation of ferrocene groups to ferocenium moieties. Ferrocene can be viewed to act like a voltage-dependent *in-situ* dopant resulting in the increase in the conductivity of the polymer film (Figure 1.20). Devices made from conducting polymers of the same organic conjugated backbone without ferrocene groups did not show any memory-effect behavior, an indication of the crucial role of ferrocene moieties and the redox-bistability of the iron metal centers for the observed memory effect. In addition, memory devices fabricated with **P37** exhibit a much lower "erasing" voltage compared to other CMPs (Table 1), an indication of a promising material for memory devices with low energy consumption.

Another example of memory devices using metal redox bistability switching was reported by Hugichi *et al.* using a cobalt-containing Wolf Type-III CMP.[53] In this study, the authors investigated the memory effect of both non-conjugated and conjugated polymers bearing Co(III) complexes of an aromatic azo ligand (**NP38** and **P38**, Figure 1.21). The conjugated polymer, a Wolf Type-III CMP (**P38**), gives a facile memory effect when incorporated into memory devices. The current-voltage (I-V) curve characteristic of the devices shows a "switch-on" voltage from the low-conducting to the high-conducting states at -3 V, and a reversed bias of 3 V is needed to turn the device back to the OFF state. The authors have conducted different studies on the I-V characteristics to confirm that this memory effect is expressly based on the redox activity of cobalt centers, apart from other mechanisms. The non-conjugated metallopolymer

(**NP38**) also exhibits a memory effect, however, with a much lower ON/OFF ratio and higher leakage current, which is the current passing through the device in the OFF state (Figure 1.21). Devices fabricated with **P38** have leakage currents that are 100 times lower than that of devices made with **NP38**, resulting in devices that have leakage currents 10^3 times lower than standard devices and therefore produce 10^6 times less heat.[53] The remarkable control of leakage current is attributed to the more extended conjugation in **P38**, allowing for more efficient current flow in the polymer film.

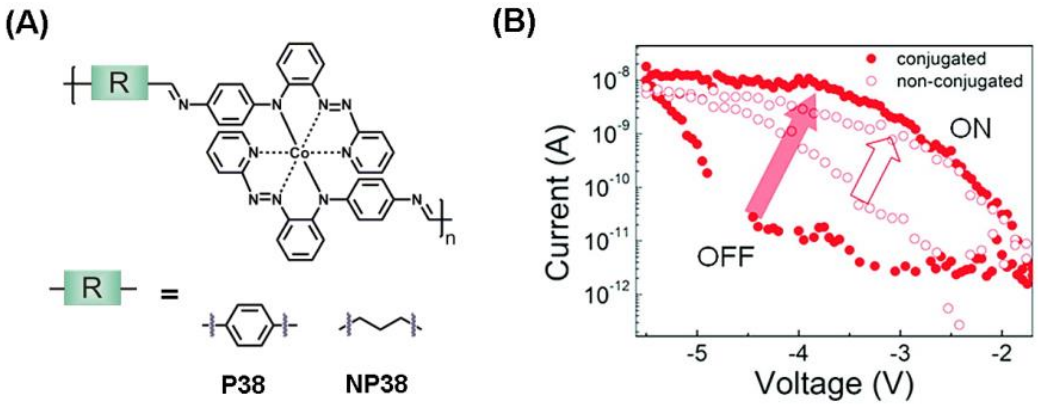

Figure 1.21. (A) Structure of non-conjugated (**NP38**) and conjugated (**P38**) cobalt-containing metallopolymers. (B) The comparative logarithmic current in flash memory devices fabricated with **NP38** and **P38**. Adapted with permission.[53] Copyright 2007 American Chemical Society.

Overall, CMPs of Wolf Types I-III have been successfully fabricated into resistive memory devices. These polymers exhibit excellent memory effects in WORM and flash memory devices based on either a donor-acceptor charge-transfer mechanism or the redox-bistability of metal centers. The control of device performance based on the rational design of polymer backbones, metal ions, on-chain and auxiliary ligands as well as coordination manner is still unexplored and opened for researchers interested in this field.

1.3.2. Magnetic memory devices

Nowadays, magnetic and optical hard disk drives (HDDs) are taking a primary role in storing, retrieving, and distributing the world information and knowledge. The data storage process in those devices involves a magnetic writing and an optical reading of encoded areas (bits) on the disks. Depending on the magnetization direction of a bit, it is detected as "1" or "0" for a binary storage system. The fast growth of the information industry is placing an increasing demand on the search for new materials or methods that allow for data storage devices with higher capacities than current technology. The use of resistive memory devices mentioned in the previous section is one of these fast-growing new technologies for memory storage devices used in solid-state drives (SSD). In this section, we discuss a new class of CMP materials that could be potentially applied in magnetic memory devices.

It is well-known that transition metals with d^4-d^7 electron configurations can exist in either low-spin or high-spin states. The transition between these two states in a metal complex is known as spin crossover (SCO) and usually results in a change in color, volume, and magnetic property of the material.[54,55] The magnetic bistability of SCO complexes could be utilized for use in memory devices, with the low-spin state acting as the "0" mode and the high-spin state being the "1" mode.

Being hybrid materials of conjugated conducting polymers and metal complexes, conducting metallopolymers (CMPs) inherit the beneficial properties from both components. When bearing metal complexes with SCO behavior, CMPs not only exhibit a magnetic bistability effect, but also are electrically conductive, fulfilling the requirements for many electronic devices. The low-/high-spin states offered from the metal centers exhibit memory effects and may be used in data storage devices.

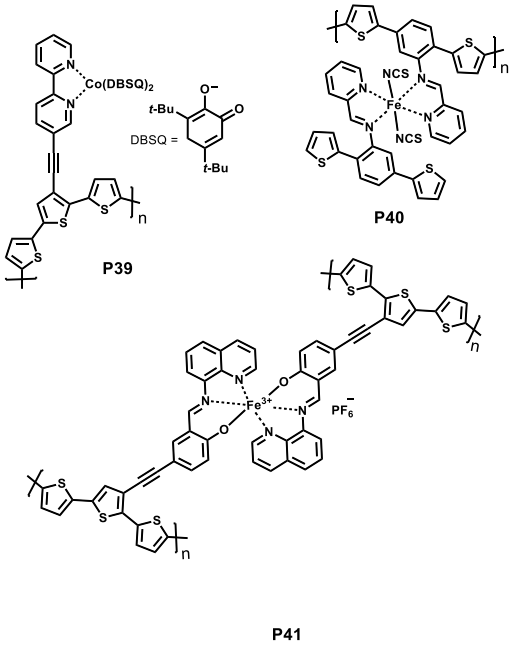

Figure 1.22. Chemical structure of CMPs (**P39-41**) that exhibit spin crossover (SCO), allowing for their potential use in magnetic memory devices.

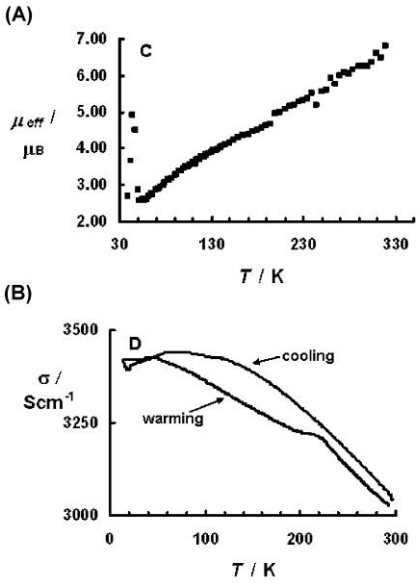

Figure 1.23. Variable-temperature magnetic properties (A) and conductivity (B) of a **P41** film on ITO-coated glass. Adapted with permission.[56] Copyright 2007 American Chemical Society.

Lemaire and co-workers have reported the synthesis and magnetic study of a series of CMPs bearing cobalt and iron complexes (**P39-41**, Figure 1.22).[56-58] Cobalt and iron were used in these polymers as the spin transition of their complexes is usually accompanied with a large change in magnetic moment. Hence, if applied in memory devices, the ON/OFF signal ratio should be remarkably high, resulting in fewer misreading errors. These polymers are obtained by electropolymerization of thiophene units on the complexes, and show remarkably high conductivity,[56] which is significantly higher than other reported SCO conductors. Variable-temperature magnetic studies of **P39-41**, however, showed only gradual spin transition across a large temperature range, which may not be favorable to be applied in data storage devices.[54] Therefore, the development of CMPs or metal complexes that exhibit spin crossover behaviors with abrupt transition and hysteresis still remains a challenge for the SCO scientific community. In addition to the resistive memory effect resulting from for high- and low-oxidation states of the metal center, such as in **P37-38**, CMPs bearing SCO metal complexes may also exhibit magnetic memory behavior. Although there still remain many challenges to be overcome before practical memory devices can be made, the use of CMPs as materials for magnetic memory devices could result in the new era in the information technology not only because of the potential high capacity of devices from molecular levels but also due to the "multiple-memory-effect-behavior" from both resistance-based and magnetic effects.

1.4. Application of CMPs in Catalysis

1.4.1. Chemical reaction catalysis

Metal complexes have been known for their catalytic properties in many chemical transformation reactions.[3] They have been applied widely in chemical industry as well as

in research laboratories in both homogeneous and heterogeneous forms. Modern chemical catalysis requires not only high activity but also high selectivity for a certain product, especially in asymmetric syntheses where stereochemistry is highly important for aspects such as biological activity. For large scale production, heterogeneous catalysts are usually preferable over homogeneous analogues due to the ease of catalyst recovery and thereby lowering the manufacturing costs.[59]

In efforts to make highly efficient heterogeneous asymmetric catalysts, Schulz and co-workers have prepared a series of CMPs and tested their catalytic activity for various reactions.[13,60-63] A thiophene-based Cr-salen CMP (**P5**, a Wolf Type-III CMP) has been synthesized from an electropolymerizable complex *via* electrodeposition. The insoluble chiral polymer was first investigated for catalytic activity in hetero-Diels-Alder (HDA) reactions and has shown good efficiency and high enantioselectivity (up to 88%).[13] When engaged in successive HDA reactions, **P5** still afforded the high yield and stereoselectivity of expected products with no loss in efficiency for up to 15 successive runs for the same substrate, and 20 successive runs in multi-substrate reactions.[60] The reproducibility of this high catalytic activity and selectivity reveals the high stability and versatility of the Cr-CMP. Interestingly, this particular CMP has demonstrated that the same catalyst batch could be used with high activity and selectivity to promote different types of reactions including HDA, Henry reactions, dialkylzinc addition to aldehyde, and epoxides ring opening reactions for up to 9 cycles.[61] Although the yield and selectivity of some reactions were not high, this has shown the first example of the same catalyst batch is involved in multiple asymmetric reactions.

In the studies shown by Schulz *et al.*, the "conducting" polymer backbone does not directly contribute to the catalytic application but is rather simply a "prerequisite" for preparing the polymers by electropolymerization. The polymers were easily recovered by

simple filtration and could be reused in a successive transformation, indicating their high stability. Changing the number of thiophene rings on the polymer backbone did not result in a large change in catalytic activity, and the resulted polymer still exhibit high durability in subsequent chemical reactions.[62] Recently, studies from the same research group showed that CMPs composed of a cobalt-salen core substituted with electropolymerizable thiophene or pyrrole groups also display good catalytic activities in the hydrolytic kinetic resolution of epoxides in high yield and with up to 85% ee.[63,64] These results indicate that CMPs could be used as promising heterogeneous asymmetric catalysts.

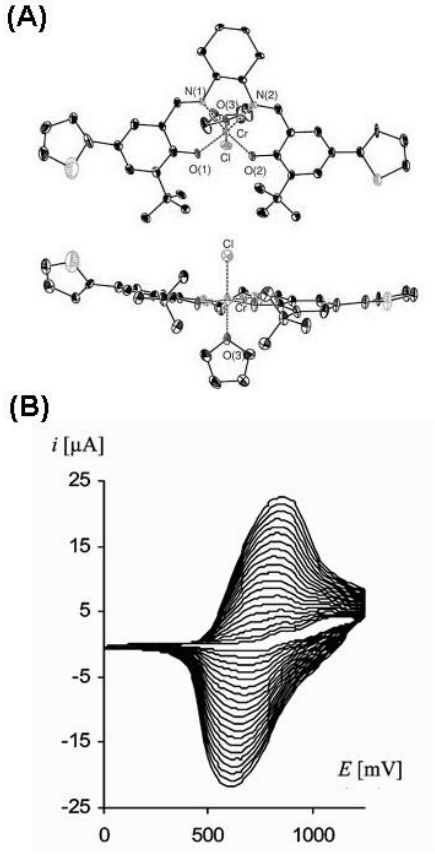

Figure 1.24. (A) Crystal structure of monomer **M5**. (B) Electropolymerization to form **P5** from **M5** for use as a catalyst in various chemical reactions. Reproduced with permission.[60]

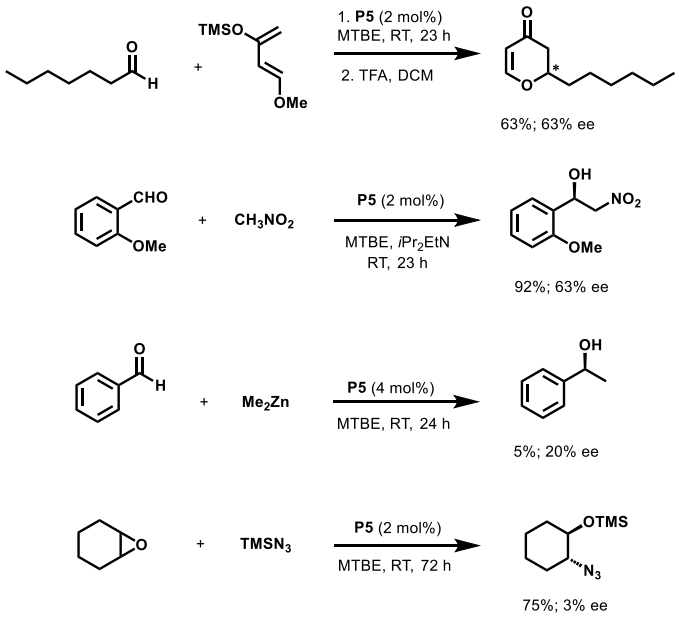

Figure 1.25. Chemical reactions that use **P5** as the same catalyst batch for multiple reactions.

1.4.2. Electrocatalysis

Unlike normal catalytic reactions, electrocatalytic reactions involve an electrochemical process at an electrode surface to convert the catalyst to its active forms.[65] Therefore, charge transport is an important process in electrocatalysis especially in heterogeneous reactions where the catalyst is also the electrode surface itself. In this case, the catalyst has to be a conductive material for efficient charge transfer. Bearing metal complexes in the backbone, CMPs could have metal centers act as catalytic centers and organic backbone serve as the conducting medium for charge transport. Additionally, it is possible to tune the catalytic properties of metal complexes in CMPs by structural modification of organic backbone. These attributes have made CMPs become highly attractive candidates for use in electrocatalysis. Due to metal center-organic backbone interactions in CMPs, in some cases, the redox properties of the polymer backbones could be utilized to enhance or retard catalytic properties of the materials as desired. In

this section, the use different CMPs for some important electrocatalytic reactions will be highlighted.

1.4.2.1. Oxygen (O_2) reduction

The reduction of O_2 to H_2O *via* electrocatalytic reaction is a crucial process in fuel cells.[65] Current technology, however, is dominated by Pt-based catalysts, which are too expensive to be widely applied in an industrial setting.[66] Therefore, much effort has been focused on seeking alternative electrocatalysts that can efficiently catalyze oxygen reduction. Swager *et al.* have reported the synthesis of a Co-containing conducting metallopolymer (**P45**, a Wolf Type-III CMP) and investigated the electrocatalytic properties of this CMP in O_2 reduction.[67] The polymer was obtained by electropolymerization of an EDOT-bearing Co-salen complex. Electrocatalytic study of **P45** show a high catalytic activity for oxygen reduction with a current density of 2.6 $mA/(cm^2(V/s)^{1/2})$. The near complete conversion of oxygen to water (theoretical value of current density is 3.2 $mA/(cm^2(V/s)^{1/2})$ is attributed to the high conductivity of the CMP backbone, allowing rapid electron transfer to the active metal centers. In addition, rotating disk voltammetry has shown that water is the sole product with no trace of hydrogen peroxide detected.

Recently, our group has developed a novel method to prepare a palladium nanoparticle/conducting polymer hybrid material for oxygen-reduction applications.[68] This method was initiated by the synthesis of a Pd-CMP (**P43**) by electropolymerization of a palladium-salen complex with electropolymerizable bithiophene groups. Then, the Pd(II) metal centers on the polymer matrix were used as seed points (nucleation points) to grow Pd metal nanoparticles (NPs), which act as catalytic centers for oxygen reduction to water. The NP growth process involves the exposure of Pd-CMP films to a nitrogen-

sparged mixture of $PdCl_2$ in water and $Na_2CO_3/NaHCO_3$ buffer solution. The treated polymer films were subsequently exposed to a five-minute treatment with aqueous ascorbic acid solution, which acts as the reductant to form Pd metal from Pd(II) ions. The NP growth was monitored by TEM and the size of Pd-NPs could be controlled by adjusting the distance between Pd(II) seed points in the co-polymer using various lengths of polythiophene spacers. Electrocatalytic experiment demonstrated that the Pd-NP/CMP hybrid material exhibits catalytic behavior toward oxygen reduction with peak current density up to 0.714 $mA/(cm^2(V/s)^{1/2})$.

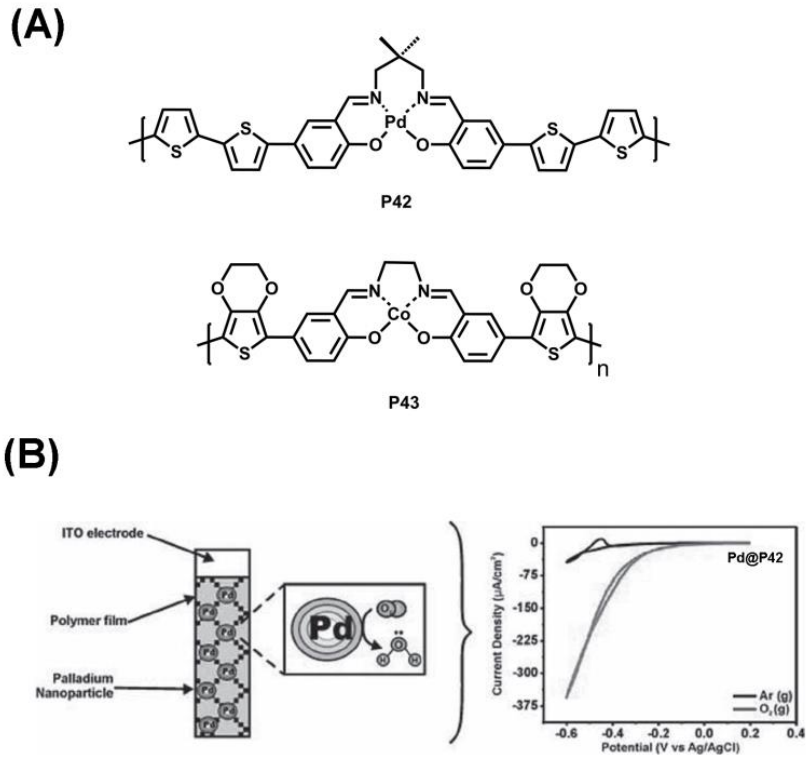

Figure 1.26. (A) Chemical structures of CMPs (**P42-43**) used in O_2 reduction. (B) Palladium nanoparticle-**P42** composite and electrocatalytic activity of the NP-CMP in CO2 reduction. Reproduced with permission.[68]

1.4.2.2. CO_2 reduction

The recycling of CO_2 to fuels by electrocatalytic reduction is an important process with beneficial effects concerning both energy consumption and environmental impact. It not only involves the production of renewable fuels but also helps balance the carbon cycle and therefore may reduce the global warming process and other environmental issues caused by CO_2 evolution.[69,70] The electrocatalytic activity for CO_2 reduction is usually identified by two factors: the reduction potential and the increase of reductive current upon the presence of CO_2 gas. Carbon monoxide (CO) is an important intermediate product in the CO_2 conversion process and can be used to produce H_2 *via* the water-gas shift reaction or methanol as a liquid fuel through the Fischer-Tropsch process.[71] The conversion of CO_2 to CO by electrocatalysis has been studied with high efficiency in homogeneous systems of Re(I) halotricarbonyl complexes.[72] However, the use of heterogeneous catalysts is preferable over these small molecules due to advantages such as ease of catalyst recovery as well as product separation, lower catalytic loading amounts, and the stability of electrocatalysts.

The first heterogeneous electrocatalyst for CO_2 reduction to CO from Re(I) CMPs was reported by Meyer and co-workers.[73,74] The Re-containing CMP (**P44**) was obtained by cathodic electropolymerization of a $ReCl(vbipy)(CO)_3$ (vbipy = 4-vinyl-4'-methyl-2,2'-bipyridine) complex onto a Pt disc electrode. Electrocatalytic study of the metallopolymer showed a 92.3% current conversion efficiency and 516 turnover cycles, which is remarkably higher than the 20-30 cycles achieved for the corresponding monomer solution in the same conditions.[73] Moreover, the polymer exhibited a much higher selectivity with CO as the sole product, while homogeneous reaction with the monomer complex revealed equal amount of CO and CO_3^{2-}. This result exhibits the magnification of electrocatalytic activity of this CMP over its complex monomer.

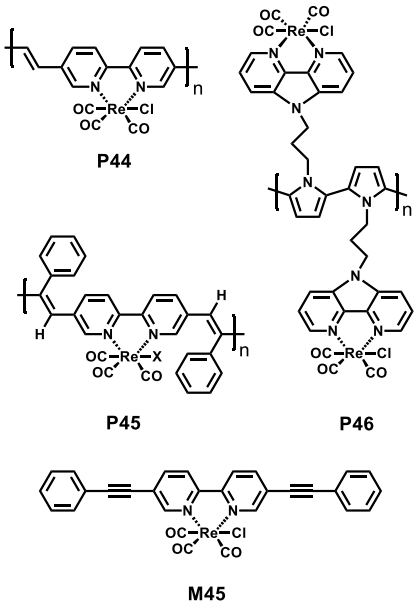

Figure 1.27. Chemical structures of Re(I) CMPs (**P44-46**) used as electrocatalysts for CO_2 reduction.

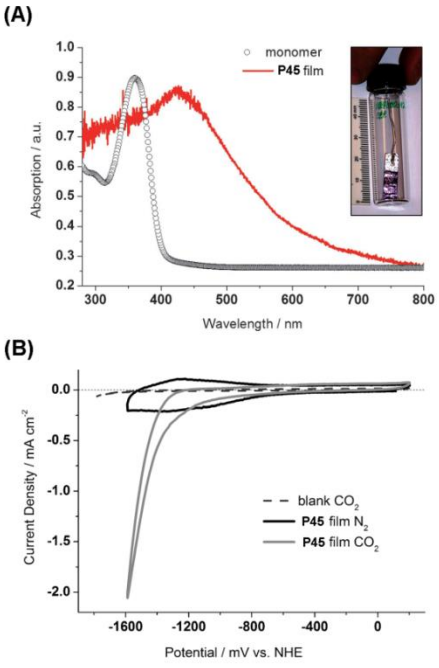

Figure 1.28. (A) UV-Vis of **P45** film formed by cathodic electropolymerization. (B) Electrocatalytic activity of **P45** film in CO_2 reduction. Reproduced with permission.[75]

Another Re(I)-CMP cathodic electropolymerization was prepared and reported by Sariciftci *et al.*[75] Although the reductive current does not increase with number of scans in cyclic voltammetry for the polymerization, a deep purple film observed on a Pt-plate electrode and a red-shift in the UV-Vis absorption of the film indicate the formation of a polymer (Figure 1.28). The proposed structure of the polymer (**P45**) is shown in Figure 1.27 was suggested by the authors. When applied in electrocatalytic reduction of CO_2, polymer **P45** exhibits an approximate 33% current efficiency, which is a little lower than that of the corresponding monomers with 45% efficiency.[76] However, the number of turnover cycles for the polymer was estimated to be about 1400, which is significantly higher than that of the monomer.

For CMPs containing heterocylic 5-member rings (thiophene, pyrole, and furan) as conductive backbones, electropolymerization is realized *via* the oxidation of monomers at the cathode. The oxidized radical cation species, then couple to each other to form oligomers and polymers. Wong and co-workers have recently reported the anodic (oxidative) electropolymerization of a chlorotricarbonyl Re(I) complex with a pendant pyrrole group as an electropolymerizable moiety.[77] The electrode-confined films of **P46** show electrocatalytic activity towards the reduction of CO_2. *In-situ* FTIR spectroelectrochemical studies suggest CO formation due to the increase of a carbonyl stretch at 2138 cm^{-1}. No other signals of alternative reduction products, such as formate, were detected, indicating the selective electroreduction of CO_2 to CO of **P46**.

1.5. APPLICATION OF CMPS IN ORGANIC BULK-HETEROJUNCTION PHOTOVOLTAICS

Organic photovoltaics (OPVs) based on π-conjugated conducting polymers have attracted much research attention in the past two decades. Tremendous efforts focused on synthesis of novel materials and new fabrication methods to improve power conversion efficiency (PCE) as well as the stability of OPVs have been reported.[78-80] The necessary processes to generate electric current from OPV devices are described in Figure 1.29, involving (i) the generation of excitons (the electron-hole pairs) upon photoexcitation, (ii) the diffusion of excitons to the donor-acceptor interface, (iii) the separation of excitons into free charge carriers at the interface, and (iv) the charge transport of electrons and holes to the electrodes, where current can be collected.[81] Each of these four processes is crucial to the performance of OPVs and need to happen effectively in order to obtain devices with high efficiencies. While the band gap and charge mobility of the materials in active layers are important, respectively, to the exciton generation and charge transport processes, the structures of OPV devices significantly affect the exciton diffusion and charge separation. Excitons in OPVs are known to diffuse only 10-20 nm before recombination.[82] Thus, in order to obtain high PCEs, OPV devices must have structures that allow the generated excitons to reach the interface, where charge separation occurs, within this diffusion-length limit. Another way to reduce the recombination of the generated excitons is to facilitate the formation of triplet-state excitons, which are usually formed in the presence of metal centers.[83] These triplet-state excitons have longer lifetimes and diffusion lengths than singlet-state excitons found in solely-organic conducting polymers. Therefore, the use of metal complexes could help increase the efficiency of OPVs based on the extension of exciton lifetimes, thus reducing charge recombination and increasing free-charge-carrier separation.

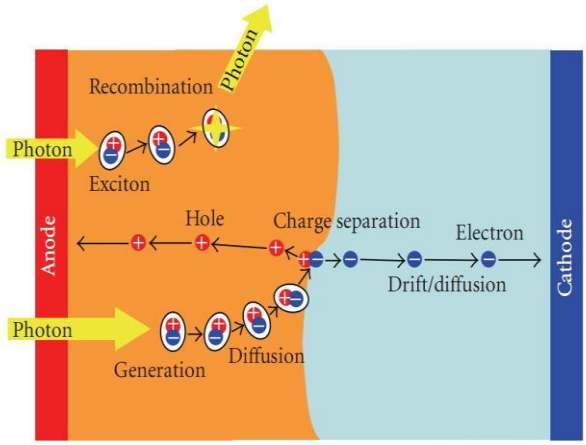

Figure 1.29. Processes necessary for generating electric current from OPV devices. Reproduced with permission.[81]

CMPs with metal complexes connected to CPs have become promising materials for OPVs not only due to the presence of metal centers facilitating triplet-state excitons, but also because of the direct electronic communication between the metal centers and the organic backbone, allowing effective charge transfer (CT). Additionally, as previously mentioned in the memory device section, the organic backbone and metal complexes result in the formation of donor-acceptor (D-A) polymers, which are found to have low band gaps due to the orbital mixing of the donor and acceptor units.[84] Due to these promising features of CMPs for use in OPVs, a significant number of CMPs has been prepared and successfully fabricated into OPV devices.[20,85-88] Huang and co-workers reviewed the application of CMPs in OPVs up to 2012 based on the metal type present in CMPs.[86] In this section, we highlight some CMP systems that have been applied in OPVs with devices that have a PCE > 1% and recent breakthroughs in CMP-based OPVs with excellent device performance (up to 8.6% PCE as an active material and 9.1% PCE as a cathode interlayer). However, it is worth noting that PCEs of OPV

devices are strongly dependent on the engineering of the device structures in addition to the intrinsic properties of the active materials used.

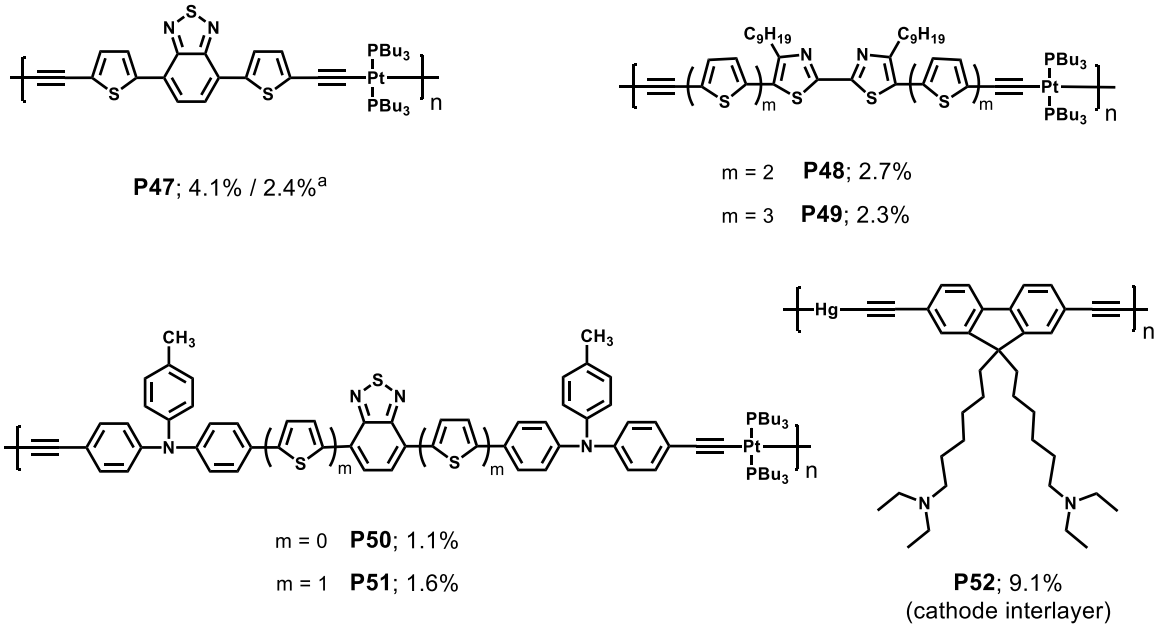

Figure 1.30. Chemical structures of selected metallopolyyne CMPs used in OPVs with high PCEs. The presented PCEs are for OPV devices that use either **$PC_{61}BM$** or **$PC_{71}BM$** as n-type semiconductors, except for **P52**, which acts as a cathode interlayer. [a] The two PCEs were reported by different research groups with the same CMP and device structure but different PCBM derivatives.

1.5.1. Metallopolyyne CMPs

Wolf Type-III CMPs are among the most common CMPs used in OPVs, which is likely due to the strong interactions between the metal centers and the organic backbone in this type of CMP. These interactions may cause effective diffusion of triplet-state excitons, when formed on metal centers, to the organic backbone and then to donor-acceptor interface, thus increasing the PCE of these OPV devices. The initial work that

showed CMPs as OPV-promising materials was reported by Wong and coworkers.[89] A Wolf Type-III platinum polyyne-based CMP (**P47)** that has Pt centers covalently bound to the conjugated backbone, was prepared and fabricated into OPV devices with **$PC_{61}BM$**. Device performance show an average PCE of 4.1% without any annealing or spacer layers, which are usually needed to get comparable PCEs with the well-known OPV system, **P3HT** and **$PC_{61}BM$**. However, there was a controversy on the PCEs of OPV devices from **P47**. Janssen *et al.* has argued, based on theoretical calculations, that the PCE of OPV devices from **P47** could not exceed 2.2% for a 70-nm-thin active-layer film, reported by Wong.[90] Jenekhe and coworkers later reported 2.4% PCE for OPV devices from **P47** and **$PC_{71}BM$**, a material that usually results in higher PCEs compared to devices from **$PC_{61}BM$** and the same p-type polymer.[9] Nevertheless, **P47** still remains a promising material for OPVs.

Since the report by Wong *et al.*, many investigations of structural modifications of the polymer backbone, focusing on changing the 2,1,3-benzothiadiazole unit to other groups, have been conducted.[86] However, there are only a few CMP systems that display remarkable PCEs, presented in Figure 1.30 (**P48-52**). The replacement of the 2,1,3-benzothiadiazole moiety in **P47** with the bithiazole unit, reported by Wong and Djurisic, results in CMPs (**P48-49**) that give OPV devices with high PCEs.[91] The authors also observed that the number of thiophene units in the polymer main chain significantly affect the performance of OPV devices made from these CMPs. This observation is attributed to the difference in absorption features of these CMPs, suggesting that, though present in the polymer main chain, Pt centers may not fully extend the conjugation of the organic backbone to the whole polymer. Another structural modification of Pt polyyne-based CMPs that yields OPV devices with promising PCEs was recently reported by Wong and Wang.[92] By inserting an electron donating unit, triphenylamine, into the **P47**

polymer chain, two low-band gap CMPs (**P50-51**) with internal donor-acceptor-donor π-conjugated fragments were obtained and have been fabricated into OPV devices with **$PC_{61}BM$** as n-type semiconductor. The best PCE of 1.6% was achieved for OPV devices of **P51**, which has a lower band gap than **P50** due to the additional thiophene units along the polymer chain. The results again indicate that metal centers in this type of CMP do not help extend the conjugation from one organic linker to another. This argument is further confirmed with the observation that there is very little difference between the band gap of monomers and polymers of **P50** and **P51**.[92]

Besides being utilized as materials in active layers of OPVs, CMPs could also be used as charge injecting layers. The ability to increase device performance of these layers in some cases is highly appealing. Huang *et al.* reported a Hg-containing metallopolyyne CMP that has on-chain fluorene moieties and pendant amino groups (**P52**).[93] This CMP has been applied as a cathode interlayer in OPV devices with a blend of **$PC_{71}BM$** and **PTB7**.[94] Interestingly, the OPV devices with **P52** as a cathode interlayer exhibited a significantly improved PCE; from 3.2% for unmodified devices to 9.1% for devices with **P52** as the interlayer, which is among the highest PCEs for single-junction OPV devices to date. The PCE improvement is also observed when using a cathode interlayer from an organic conducting polymer of similar structure, though with less improvement.[93] However, the benefit of using **P52** is that high PCEs could be achievable in a wider range of film thicknesses, making large-area device processing possible.

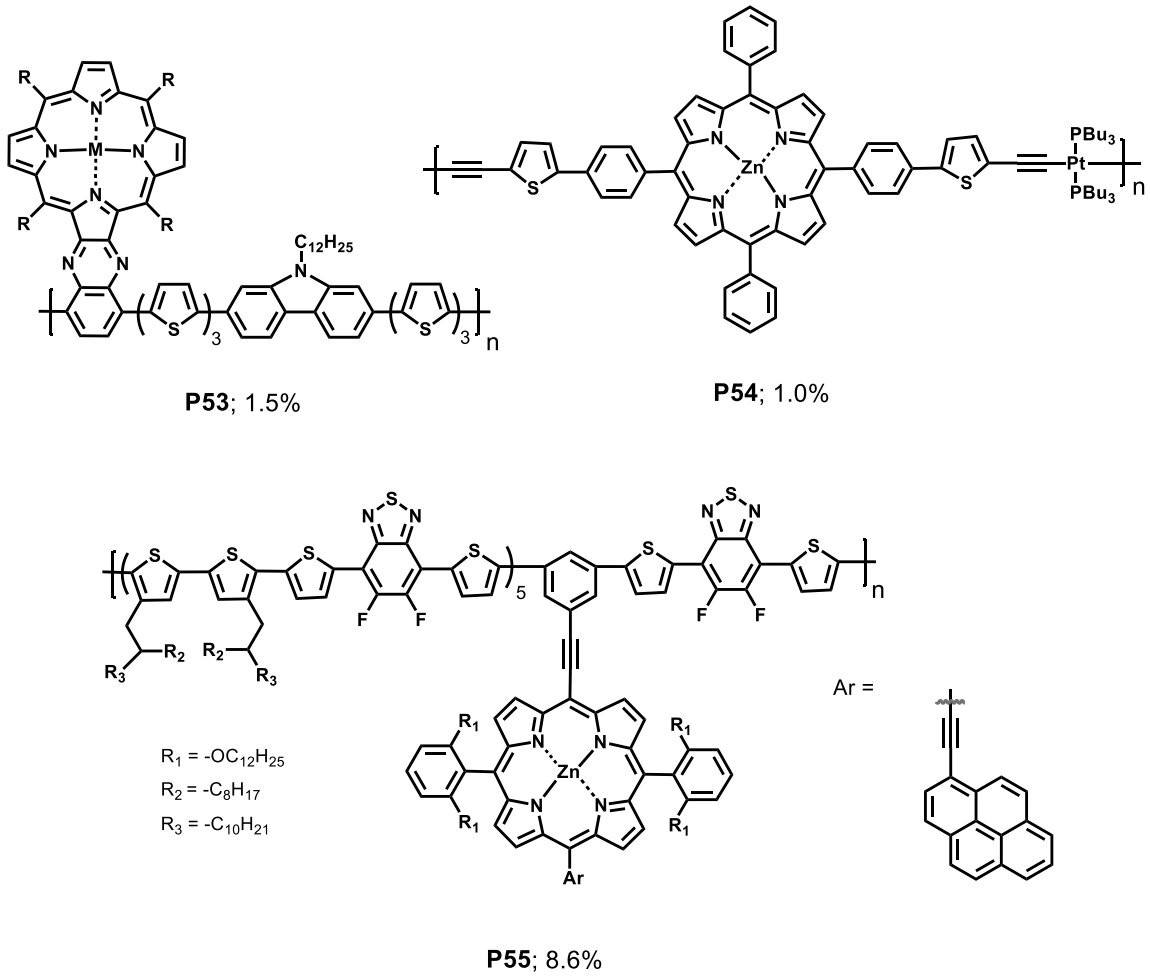

Figure 1.31. Chemical structures of selected metalloporphyrin CMPs used in OPVs with high PCEs. The presented PCEs are for OPV devices that use either **$PC_{61}BM$** or **$PC_{71}BM$** as n-type semiconductors.

1.5.2. Metalloporphyrin CMPs

The next class of CMPs that are extensively studied for photovoltaic performance is metalloporphyrin CMPs. Playing an important role in the photosynthesis of plants, porphyrins with strong optical absorption, good thermal stability, and high charge mobility are promising materials for OPVs. Many efforts to incorporate Zn-porphyrin into CPs for use in OPVs have been reported. However, many of these systems show poor performance in OPV devices. Wang and coworkers reported a Wolf Type-II CMP,

P53, that has quinoxalino[2,3-*b*′]-porphyrinatozinc in the backbone showing a promising OPV device performance.[95] Devices made from **P53** and **$PC_{71}BM$** exhibit a 1.5% PCE, which was the highest PCE for OPV devices from Zn-porphyrin CMPs at the reported time. However, although showing higher hole mobility and wider absorption range, **P53** exhibits a decrease in PCE compared to the metal-free polymer. The result is attributed to the morphology of the **P53**/**$PC_{71}BM$** blend film, which is not beneficial for exciton dissociation and charge carrier transport. Wong, Harvey and Djurisic *et al.* reported a series of CMPs that have a mixed-metal system of Pt-metallopolyyne and Zn-porphyrin in the polymer chain.[96] A maximum PCE of only 1.0% was obtained for a polymer with one bridged thiophene unit between the two moieties (**P54**).

A Zn-porphyrin CMP that displays excellent device performance in OPVs was reported by Hsu *et al.* in 2014.[97] By introducing a Zn-porphyrin-pyrene as a complementary light harvest unit (LHU) into a donor-acceptor CP, these authors have prepared a CMP (**P55**) that exhibits a maximum PCE of 8.0 % in OPV devices. Devices with even higher PCEs of 8.6% were achieved when processed with 1-chloronaphathalene as an additive and cross-linked [6,6]-phenyl-C_{61}-butyric styryl dendron ester as cathode interlayer.[97] The excellent performance of OPV devices obtained from **P55** is attributed to the wide absorption of the CMP. The authors argued that although modification of donor and acceptor units in D-A polymers effectively shifts the absorption of these polymers toward longer wavelengths, the absorption band is not broadened due to the weak absorption of shorter wavelength photons. Through adding a complementary LHU, **P55** becomes a panchromatic absorber therefore increasing the amount of absorbed photons in the solar spectrum and resulting in high performance OPV devices.

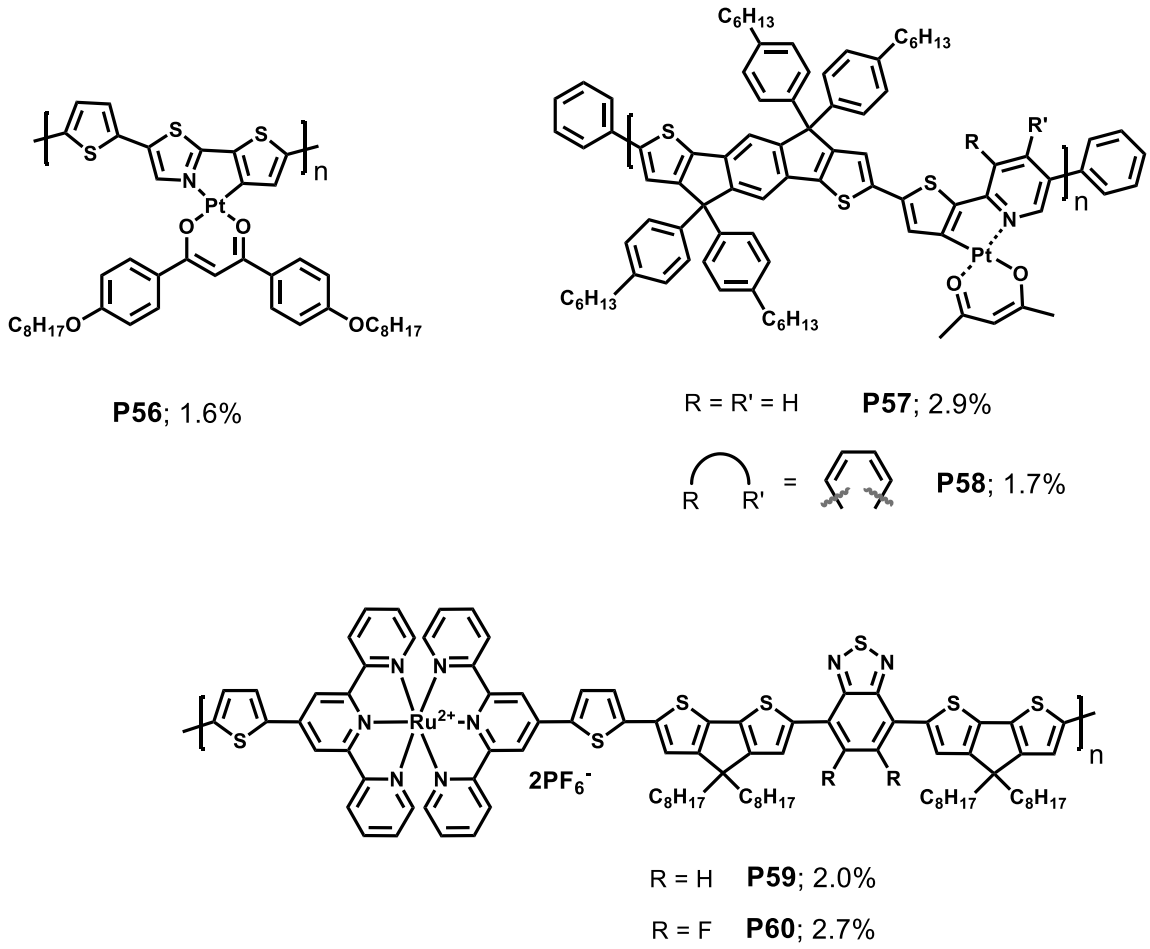

Figure 1.32. Chemical structures of other CMPs used in OPVs with high PCEs. The presented PCEs are for OPV devices that use either **$PC_{61}BM$** or **$PC_{71}BM$** as n-type semiconductors

1.5.3. Other CMP systems

Frechet *et al.* reported a Wolf Type-II cyclometalated Pt-containing CMP that has Pt(II) centers coordinating to a 2-(2'-thienyl)thiazole C^N ligand site on the backbone and an O^O diketonate auxiliary ligand (**P56**).[98] OPV devices made from **P56** and **PCBM** display a 1.3% PCE. Followed this work, Cheng and coworkers prepared a more complicated cyclometalated Pt-CMP system utilizing a 4,4,9,9-*tetrakis*(4-hexylphenyl)-4,9-dihydro-*s*-indaceno[1,2-*b*:5,6-*b*']dithiophene (**TPT**) moiety in the polymer

backbone.[99] The resulted CMPs (**P57-58**) were fabricated with **$PC_{71}BM$** to OPV devices with remarkable PCEs up to 2.9%, which is the highest value for OPV devices from cyclometalated CMPs.

Aside from CMPs of platinum and zinc metals, the only other transition metal CMP system that was reported to exhibit promising PCEs in OPV devices for Ru-containing CMPs. A recent report by Peng and coworkers focused on the preparation and fabrication of OPV devices with two Ru-CMPs that have metal centers dynamically bound to a bis(terpyridine)-organic linker (**P59-60**).[100] OPV devices from these two CMPs reveal a maximum PCE of 2.7% for **P60**, which is attributed to the effect of the fluorine atoms on the band gap, mobility and fine phase separation compared to those in **P59**.

In summary, a large number of CMPs incorporating various transition metals including Pt, Zn, Ru, Ir, Re, and Hg have been successfully investigated for OPV device performance. Of these CMPs, metallopolyyne and metalloporphyrin polymers have been extensively studied and have resulted in OPV devices with promisingly high PCEs up to 9.1%, which is among the highest PCE for current single-junction OPV devices.

1.6. SUMMARY AND OUTLOOK

The field of conducting metallopolymers has witnessed tremendous growth since the late 1990s. Specifically, the incorporation of metal centers to π-conjugated organic backbone both increases the functionalities of new materials and also influences the two components, which can be utilized to tune the optical and electronic properties of each or both moieties. These multi-functional properties along with their tunability make this class of materials unique with a potential for a wide range of applications. In this review, we have highlighted recent advances in the use of CMPs in catalysis and

(opto)electronics such as chemical sensors, memory storage devices, and photovoltaics. Significant progress and breakthroughs have been observed in these fields utilizing CMPs. However, some fundamental aspects and challenges regarding CMPs are remain unexplored for researchers interested in this field. For example, in spite of many reported studies on the potential applications of CMPs, reports on the structure-property and/or structure-device performance relationships of CMPs have been limited. Better understanding of the roles of metal centers and organic backbones, as well as the electronic interactions between them, on the optical and electronic properties of the materials is necessary for the rational designs of materials with desired features. In addition, more novel materials should be explored to meet the requirements of certain electronic devices such as SCO behavior for memory devices. In summary, CMPs have emerged as a research field worth further exploration in both their properties and application potential.

REFERENCES

(1) Skotheim, T. A.; Reynolds, J. *Handbook of Conducting Polymers, Third Edition* **2007**.

(2) Hadziioannou, G.; Malliaras, G. G. *Semiconducting Polymers: Chemistry, Physics and Engineering, 2nd Edition* **2006**.

(3) Savéant, J.-M. *Chem. Rev.* **2008**, *108*, 2348.

(4) Rogers, C. W.; Wolf, M. O. *Coord. Chem. Rev.* **2002**, *233–234*, 341.

(5) Kido, J.; Okamoto, Y. *Chem. Rev.* **2002**, *102*, 2357.

(6) Holliday, B. J.; Swager, T. M. *Chem. Commun.* **2005**, 23.

(7) Wolf, M. O. *Adv. Mater.* **2001**, *13*, 545.

(8) Wolf, M. *J. Inorg. Organomet. Polym. Mater.* **2006**, *16*, 189.

(9) Wu, P.-T.; Bull, T.; Kim, F. S.; Luscombe, C. K.; Jenekhe, S. A. *Macromolecules* **2009**, *42*, 671.

(10) Peng, Q.; Xie, M.; Huang, Y.; Lu, Z.; Cao, Y. *Macromol. Chem. Phys.* **2005**, *206*, 2373.

(11) Hjelm, J.; Handel, R. W.; Hagfeldt, A.; Constable, E. C.; Housecroft, C. E.; Forster, R. J. *Inorg. Chem.* **2005**, *44*, 1073.

(12) Pizzoferrato, R.; Ziller, T.; Paolesse, R.; Mandoj, F.; Micozzi, A.; Ricci, A.; Lo Sterzo, C. *Chem. Phys. Lett.* **2006**, *426*, 124.

(13) Mellah, M.; Ansel, B.; Patureau, F.; Voituriez, A.; Schulz, E. *J. Mol. Catal. A: Chem.* **2007**, *272*, 20.

(14) Heinze, J.; Frontana-Uribe, B. A.; Ludwigs, S. *Chem. Rev.* **2010**, *110*, 4724.

(15) Friebe, C.; Hager, M. D.; Winter, A.; Schubert, U. S. *Adv. Mater.* **2012**, *24*, 332.

(16) Whittell, G. R.; Hager, M. D.; Schubert, U. S.; Manners, I. *Nat Mater* **2011**, *10*, 176.

(17) G. Pickup, P. *J. Mater. Chem.* **1999**, *9*, 1641.

(18) Whittell, G. R.; Manners, I. *Adv. Mater.* **2007**, *19*, 3439.

(19) Eloi, J.-C.; Chabanne, L.; Whittell, G. R.; Manners, I. *Mater. Today* **2008**, *11*, 28.

(20) Ho, C.-L.; Wong, W.-Y. *Coord. Chem. Rev.* **2011**, *255*, 2469.

(21) Zhao, Q.; Liu, S.-J.; Huang, W. *Macromol. Rapid Commun.* **2010**, *31*, 794.

(22) Stanley, J. M.; Holliday, B. J. *Coord. Chem. Rev.* **2012**, *256*, 1520.

(23) Fan, L.-J.; Zhang, Y.; Murphy, C. B.; Angell, S. E.; Parker, M. F. L.; Flynn, B. R.; Jones Jr, W. E. *Coord. Chem. Rev.* **2009**, *253*, 410.

(24) Lodeiro, C.; Capelo, J. L.; Mejuto, J. C.; Oliveira, E.; Santos, H. M.; Pedras, B.; Nunez, C. *Chem. Soc. Rev.* **2010**, *39*, 2948.

(25) Smith, R. C.; Tennyson, A. G.; Lim, M. H.; Lippard, S. J. *Org. Lett.* **2005**, *7*, 3573.

(26) Smith, R. C.; Tennyson, A. G.; Won, A. C.; Lippard, S. J. *Inorg. Chem.* **2006**, *45*, 9367.

(27) Bryan, N. S.; Grisham, M. B. *Free Radical Biol. Med.* **2007**, *43*, 645.

(28) Do, L.; Smith, R. C.; Tennyson, A. G.; Lippard, S. J. *Inorg. Chem.* **2006**, *45*, 8998.

(29) Tennyson, A. G.; Do, L.; Smith, R. C.; Lippard, S. J. *Polyhedron* **2007**, *26*, 4625.

(30) Xing, C.; Yu, M.; Wang, S.; Shi, Z.; Li, Y.; Zhu, D. *Macromol. Rapid Commun.* **2007**, *28*, 241.

(31) Papkovsky, D.; Zhdanov, A. V.; Fercher, A.; Dmitriev, R. I.; Hynes, J. *Phosphorescent Oxygen-Sensitive Probes* **2012**.

(32) Thomas Iii, S. W.; Yagi, S.; Swager, T. M. *J. Mater. Chem.* **2005**, *15*, 2829.

(33) Shi, H.; Ma, X.; Zhao, Q.; Liu, B.; Qu, Q.; An, Z.; Zhao, Y.; Huang, W. *Adv. Funct. Mater.* **2014**, *24*, 4823.

(34) Li, Z. a.; Lou, X.; Yu, H.; Li, Z.; Qin, J. *Macromolecules* **2008**, *41*, 7433.

(35) Huang, Y.; Ou, D.; Wang, C.; Huang, C.; Li, Q.; Li, Z. *Polym. Chem.* **2014**, *5*, 2041.

(36) Bao, Y.; Wang, H.; Li, Q.; Liu, B.; Li, Q.; Bai, W.; Jin, B.; Bai, R. *Macromolecules* **2012**, *45*, 3394.

(37) Ogawa, K.; Guo, F.; Schanze, K. S. *J. Photochem. Photobiol. A: Chem.* **2009**, *207*, 79.

(38) Sun, S.; Tong, W.-L.; Chan, M. C. W. *Macromol. Rapid Commun.* **2010**, *31*, 1965.

(39) Shi, H.-F.; Liu, S.-J.; Sun, H.-B.; Xu, W.-J.; An, Z.-F.; Chen, J.; Sun, S.; Lu, X.-M.; Zhao, Q.; Huang, W. *Chem. Eur. J.* **2010**, *16*, 12158.

(40) Qin, C.; Wong, W.-Y.; Wang, L. *Macromolecules* **2010**, *44*, 483.

(41) Sugiyasu, K.; Swager, T. M. *Bull. Chem. Soc. Jpn.* **2007**, *80*, 2074.

(42) Holliday, B. J.; Stanford, T. B.; Swager, T. M. *Chem. Mater.* **2006**, *18*, 5649.

(43) Reddinger, J. L.; Reynolds, J. R. *Chem. Mater.* **1998**, *10*, 3.

(44) Lin, W.-P.; Liu, S.-J.; Gong, T.; Zhao, Q.; Huang, W. *Adv. Mater.* **2014**, *26*, 570.

(45) Liu, S.-J.; Lin, W.-P.; Yi, M.-D.; Xu, W.-J.; Tang, C.; Zhao, Q.; Ye, S.-H.; Liu, X.-M.; Huang, W. *J. Mater. Chem.* **2012**, *22*, 22964.

(46) Wang, P.; Liu, S.-J.; Lin, Z.-H.; Dong, X.-C.; Zhao, Q.; Lin, W.-P.; Yi, M.-D.; Ye, S.-H.; Zhu, C.-X.; Huang, W. *J. Mater. Chem.* **2012**, *22*, 9576.

(47) Liu, S.-J.; Lin, Z.-H.; Zhao, Q.; Ma, Y.; Shi, H.-F.; Yi, M.-D.; Ling, Q.-D.; Fan, Q.-L.; Zhu, C.-X.; Kang, E.-T.; Huang, W. *Adv. Funct. Mater.* **2011**, *21*, 979.

(48) Lin, W.; Sun, H.; Liu, S.; Yang, H.; Ye, S.; Xu, W.; Zhao, Q.; Liu, X.; Huang, W. *Macromol. Chem. Phys.* **2012**, *213*, 2472.

(49) Ling, Q.-D.; Song, Y.; Teo, E. Y. H.; Lim, S.-L.; Zhu, C.; Chan, D. S. H.; Kwong, D.-L.; Kang, E.-T.; Neoh, K.-G. *Electrochem. Solid-State Lett.* **2006**, *9*, G268.

(50) Song, Y.; Tan, Y. P.; Teo, E. Y. H.; Zhu, C.; Chan, D. S. H.; Ling, Q. D.; Neoh, K. G.; Kang, E. T. *J. Appl. Phys.* **2006**, *100*.

(51) Li, L.; Ling, Q.-D.; Lim, S.-L.; Tan, Y.-P.; Zhu, C.; Chan, D. S. H.; Kang, E.-T.; Neoh, K.-G. *Org. Electron.* **2007**, *8*, 401.

(52) Choi, T.-L.; Lee, K.-H.; Joo, W.-J.; Lee, S.; Lee, T.-W.; Chae, M. Y. *J. Am. Chem. Soc.* **2007**, *129*, 9842.

(53) Bandyopadhyay, A.; Sahu, S.; Higuchi, M. *J. Am. Chem. Soc.* **2011**, *133*, 1168.

(54) Gülichi, P.; Goodwin, H. A. *Spin Crossover in Transition Metal Compounds I–III, Top. Curr. Chem.* **2004**.

(55) Halcrow, M. A. *Spin-Crossover Materials: Properties and Applications* **2013**.

(56) Djukic, B.; Lemaire, M. T. *Inorg. Chem.* **2009**, *48*, 10489.

(57) O'Sullivan, T. J.; Djukic, B.; Dube, P. A.; Lemaire, M. T. *Chem. Commun.* **2009**, 1903.

(58) Djukic, B.; Seda, T.; Gorelsky, S. I.; Lough, A. J.; Lemaire, M. T. *Inorg. Chem.* **2011**, *50*, 7334.

(59) Baleizão, C.; Garcia, H. *Chem. Rev.* **2006**, *106*, 3987.

(60) Zulauf, A.; Mellah, M.; Guillot, R.; Schulz, E. *Eur. J. Org. Chem.* **2008**, *2008*, 2118.

(61) Zulauf, A.; Mellah, M.; Schulz, E. *Chem. Commun.* **2009**, 6574.

(62) Zulauf, A.; Hong, X.; Brisset, F.; Schulz, E.; Mellah, M. *New J. Chem.* **2012**, *36*, 1399.

(63) Hong, X.; Mellah, M.; Bordier, F.; Guillot, R.; Schulz, E. *ChemCatChem* **2012**, *4*, 1115.

(64) Hong, X.; Billon, L.; Mellah, M.; Schulz, E. *Catal. Sci. Technol.* **2013**, *3*, 723.

(65) Koper, M. T. M.; Iwasawa, Y. *PCCP* **2014**, *16*, 13567.

(66) Marković, N. M.; Schmidt, T. J.; Stamenković, V.; Ross, P. N. *Fuel Cells* **2001**, *1*, 105.

(67) Kingsborough, R. P.; Swager, T. M. *Chem. Mater.* **2000**, *12*, 872.

(68) Edelman, K. R.; Stevenson, K. J.; Holliday, B. J. *Macromol. Rapid Commun.* **2012**, *33*, 610.

(69) Sullivan, B. P.; Krist, K.; Guard, H. E. *Electrochemical and Electrocatalytic Reaction of Carbon Dioxide*; Elsevier: New York, 1993.

(70) Halman, M. M.; Steinberg, M. *Greenhouse Gas Carbon Dioxide Mitigation: Science and Technology*; CRC Press LLC: Boca Raton, 1999.

(71) Underwood, A. J. V. *Ind. Eng. Chem.* **1940**, *32*, 449.

(72) Benson, E. E.; Kubiak, C. P.; Sathrum, A. J.; Smieja, J. M. *Chem. Soc. Rev.* **2009**, *38*, 89.

(73) O'Toole, T. R.; Margerum, L. D.; Westmoreland, T. D.; Vining, W. J.; Murray, R. W.; Meyer, T. J. *J. Chem. Soc., Chem. Commun.* **1985**, 1416.

(74) O'Toole, T. R.; Sullivan, B. P.; Bruce, M. R. M.; Margerum, L. D.; Murray, R. W.; Meyer, T. J. *J. Electroanal. Chem. Interfacial Electrochem.* **1989**, *259*, 217.

(75) Portenkirchner, E.; Gasiorowski, J.; Oppelt, K.; Schlager, S.; Schwarzinger, C.; Neugebauer, H.; Knör, G.; Sariciftci, N. S. *ChemCatChem* **2013**, *5*, 1790.

(76) Portenkirchner, E.; Oppelt, K.; Ulbricht, C.; Egbe, D. A. M.; Neugebauer, H.; Knör, G.; Sariciftci, N. S. *J. Organomet. Chem.* **2012**, *716*, 19.

(77) Cheung, K.-C.; Guo, P.; So, M.-H.; Lee, L. Y. S.; Ho, K.-P.; Wong, W.-L.; Lee, K.-H.; Wong, W.-T.; Zhou, Z.-Y.; Wong, K.-Y. *J. Organomet. Chem.* **2009**, *694*, 2842.

(78) Cao, W.; Xue, J. *Energy Environ. Sci.* **2014**, *7*, 2123.

(79) Cao, H.; He, W.; Mao, Y.; Lin, X.; Ishikawa, K.; Dickerson, J. H.; Hess, W. P. *J. Power Sources* **2014**, *264*, 168.

(80) Jørgensen, M.; Norrman, K.; Gevorgyan, S. A.; Tromholt, T.; Andreasen, B.; Krebs, F. C. *Adv. Mater.* **2012**, *24*, 580.

(81) Kietzke, T. *Adv. OptoElectronics* **2007**, *2007*, 15.

(82) Ewbank, P. C.; Laird, D.; McCullough, R. D. *Organic photovoltaics* **2009**.

(83) Guo, F.; Kim, Y.-G.; Reynolds, J. R.; Schanze, K. S. *Chem. Commun.* **2006**, 1887.

(84) Kularatne, R. S.; Magurudeniya, H. D.; Sista, P.; Biewer, M. C.; Stefan, M. C. *J. Polym. Sci., Part A: Polym. Chem.* **2013**, *51*, 743.

(85) Mak, C. S. K.; Chan, W. K. In *Macromolecules Containing Metal and Metal-Like Elements*; John Wiley & Sons, Inc.: 2010, p 159.

(86) Liu, S.-J.; Chen, Y.; Xu, W.-J.; Zhao, Q.; Huang, W. *Macromol. Rapid Commun.* **2012**, *33*, 461.

(87) Xu, H.; Chen, R.; Sun, Q.; Lai, W.; Su, Q.; Huang, W.; Liu, X. *Chem. Soc. Rev.* **2014**, *43*, 3259.

(88) Asatkar, A. K.; Bedi, A.; Zade, S. S. *Isr. J. Chem.* **2014**, *54*, 467.

(89) Wong, W.-Y.; Wang, X.-Z.; He, Z.; Djurisic, A. B.; Yip, C.-T.; Cheung, K.-Y.; Wang, H.; Mak, C. S. K.; Chan, W.-K. *Nat. Mater.* **2007**, *6*, 521.

(90) Gilot, J.; Wienk, M. M.; Janssen, R. A. J. *Nat. Mater.* **2007**, *6*, 704.

(91) Wong, W.-Y.; Wang, X.-Z.; He, Z.; Chan, K.-K.; Djurišić, A. B.; Cheung, K.-Y.; Yip, C.-T.; Ng, A. M.-C.; Xi, Y. Y.; Mak, C. S. K.; Chan, W.-K. *J. Am. Chem. Soc.* **2007**, *129*, 14372.

(92) Wang, Q.; Wong, W.-Y. *Polym. Chem.* **2011**, *2*, 432.

(93) Liu, S.; Zhang, K.; Lu, J.; Zhang, J.; Yip, H.-L.; Huang, F.; Cao, Y. *J. Am. Chem. Soc.* **2013**, *135*, 15326.

(94) *poly[4,8-bis(2-ethylhexyloxyl)benzo[1,2-b:4,5-b']dithiophene-2,6-diyl-alt-ethylhexyl-3-uorothithieno[3,4-b]thiophene-2-carboxylate-4,6-diyl]*.

(95) Shi, S.; Jiang, P.; Chen, S.; Sun, Y.; Wang, X.; Wang, K.; Shen, S.; Li, X.; Li, Y.; Wang, H. *Macromolecules* **2012**, *45*, 7806.

(96) Zhan, H.; Lamare, S.; Ng, A.; Kenny, T.; Guernon, H.; Chan, W.-K.; Djurišić, A. B.; Harvey, P. D.; Wong, W.-Y. *Macromolecules* **2011**, *44*, 5155.

(97) Chao, Y. I. H.; Jheng, J.-F.; Wu, J.-S.; Wu, K.-Y.; Peng, H.-H.; Tsai, M.-C.; Wang, C.-L.; Hsiao, Y.-N.; Wang, C.-L.; Lin, C.-Y.; Hsu, C.-S. *Adv. Mater.* **2014**, *26*, 5205.

(98) Clem, T. A.; Kavulak, D. F. J.; Westling, E. J.; Fréchet, J. M. J. *Chem. Mater.* **2009**, *22*, 1977.

(99) Liao, C.-Y.; Chen, C.-P.; Chang, C.-C.; Hwang, G.-W.; Chou, H.-H.; Cheng, C.-H. *Sol. Energy Mater. Sol. Cells* **2013**, *109*, 111.

(100) Feng, K.; Shen, X.; Li, Y.; He, Y.; Huang, D.; Peng, Q. *Polym. Chem.* **2013**, *4*, 5701.

Chapter 2: Seeded Growth of Seeded Growth of CdSe Nanocrystals within a Conducting Polymer Matrix

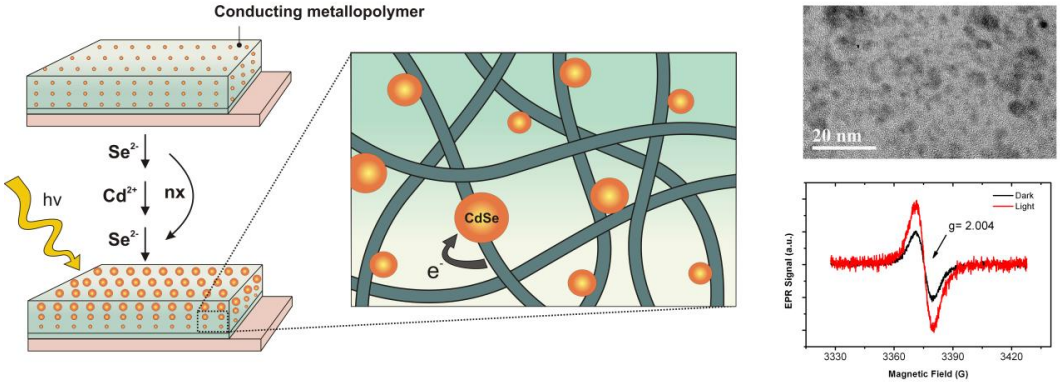

2.1. INTRODUCTION

Hybrid solar cells based on conjugated polymers and inorganic nanocrystals (NCs) have attracted a large amount of attention recently due to the advantages of the tunable absorption properties of nanocrystals coupled with the ease of device processing offered by polymeric systems.[1] Device performance depends not only on the geometries of the nanocrystals but also on the interactions at the polymer-nanocrystal interface. Although the use of elongated nanocrystals has shown some positive effects on device performance, efficiencies of hybrid solar cells are still too low (approaching 4%) for commercialization.[2-5] The main limiting factors seem to be related to film morphologies and trap states, both related to the surface chemistry of the nanocrystals.[6]

Inorganic nanocrystals used in hybrid solar cells are usually capped by surfactants or ligands such as trioctylphosphine oxide (TOPO) after synthesis. These surfactants act as stabilizers to prevent aggregation and passivate surface states.[7] However, long alkyl chains in the TOPO ligand act as insulators and inhibit charge transfer between the nanocrystal and polymer, as well as the charge transport between nanocrystals. Exchanging the long chain ligands with pyridine or other shorter chain surfactants can induce more effective charge transfer, and thus improve device efficiency.[8-12] On the other hand, the exchange of ligands has some disadvantages, such as a lack of control over morphology, the requirement of post-preparation treatment, and incomplete exchange processes.[6] In addition, coordination between nanoparticles and the end-functional amine groups in a modified conductive polymer was observed to give higher device efficiency.[13] This observation, along with the aforementioned effects of ligand exchange, shows that polymer-nanocrystal interface interactions play a crucial role in improving efficiencies in hybrid solar cells. Thus, forming direct bonds between nanocrystals and polymers could offer a promising strategy to bypass the effects of

capping ligands. Some research groups have focused on the use of polymers as stabilizers to synthesize NCs directly into polymers.[14,15] Dayal *et al.* have reported the synthesis of CdSe particles directly from poly-3-hexylthiophene (P3HT).[15] Photoinduced charge separation, observed in these CdSe-P3HT composites, indicates potential application for hybrid solar cells. However, the synthesis uses a highly toxic precursor, dimethyl cadmium, and high temperature conditions, which might introduce limitations in this system as a photovoltaic device.

Previous reports from our group have demonstrated the formation of CdS[16] and Ga_2S_3[17] within the matrix of a Wolf Type III polymer, in which the metal ions interrupt the conjugation of the polymeric backbone.[18,19] However, extending the conjugation of the system could lead to a polymer with a higher charge-carrier mobility, which is an important factor for materials in electronic devices. With this in mind, we prepared a Wolf Type II metallopolymer in which the metal centers still maintain communication with the polymer but do not interrupt the conjugation. In considering the n-type material for the hybrid systems, we have taken into account several factors, including the band gaps of different semiconductors. The relatively small band gap of CdSe (1.73 eV) better complements that of most polymers and broadens the absorption of the material across the solar spectrum.

Herein, we report the direct synthesis of CdSe NCs from a conducting metallopolymer at room temperature using a seeded growth technique. This method employs the multi-functional properties of metallopolymers, a system in which metal ions interact with the conjugated system of a conducting polymer. From these metal ions, CdSe NCs were grown by sequentially treating with cadmium and selenium precusors. The size of the NCs can be controlled by altering the number of growth cycles. Since the metal centers are in direct electronic communication with the conjugated polymer chains,

similar interaction between the polymers and the resulting NCs is expected. Charge separation between the polymer and CdSe NCs, studied by light-induced electron paramagnetic resonance (L-EPR), shows a successful charge transfer between the NCs and polymer, indicating potential application in optoelectronic devices.

Scheme 2.1. Synthesis of the cadmium-containing Wolf Type-II conducting metallopolymer.

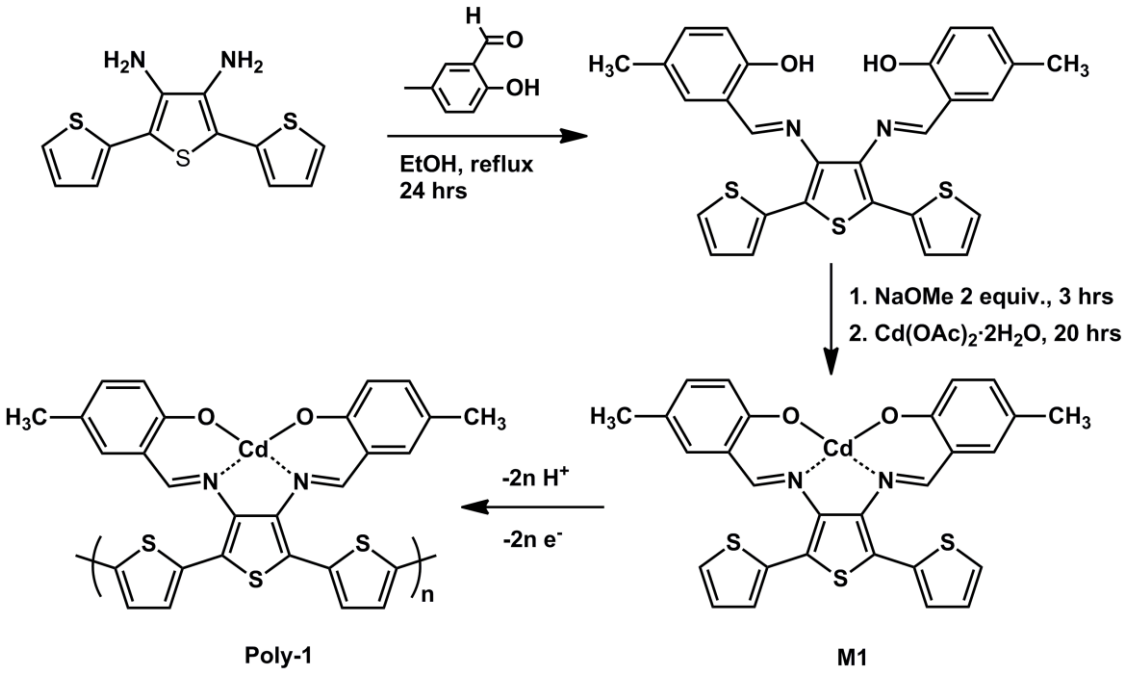

2.2. RESULT AND DISCUSSION

2.2.1 Synthesis of Cadmium Complex Monomer

The synthesis of the cadmium complex monomer and the corresponding metallopolymer is outlined in Scheme 2.1. The electropolymerizable ligand was synthesized using a literature procedure reported by Reynolds *et al*.[20] The novel cadmium complex monomer (**M1**) was prepared by first deprotonating the two phenol groups with sodium methoxide (NaOMe), followed by reaction of the deprotonated ligand with

cadmium acetate ($Cd(OAc)_2 \cdot H_2O$) in the mixture of methylene chloride and methanol at room temperature for 20 hours. The cadmium complex monomer has been fully characterized by mass spectrometry, nuclear magnetic resonance (NMR) spectroscopy, UV-Vis spectrocopy, and cyclic voltammetry. All the recorded data are fully consistent with the proposed structure (experimental section).

2.2.2. Synthesis and Characterization of Cd-containing Conducting Metallopolymer

Conducting metallopolymer (**poly-1**) films were formed *via* electropolymerization of monomer **M1** by cyclic voltammetry (CV) onto various working electrodes such as platinum button, stainless steel, ITO-coated glass, and gold transmission electron microscopy (TEM) grids. The monomer solutions of **M1** in CH_2Cl_2 were oxidatively polymerized by sweeping the potential of the working electrode between -0.75 and 1.25 V versus Fc/Fc^+ at a 100 mV/s scan rate. A typical electropolymerization of **M1** onto Pt button electrode is shown in Figure 2.1A. The linear increase in the polymer oxidation peak as the increase of number of CV scans indicates the growth progress of the metallopolymer after each electrochemical cycle. The electrode-confined films were characterized using electrochemical methods, X-ray photoelectron spectroscopy (XPS), UV-Vis-NIR spectroelectrochemistry, and electron paramagnetic resonance (EPR) spectroscopy. Study of the electrochemical scan-rate dependence of the polymer films (Figure 2.1B) in pure electrolyte solution revealed a linear relationship between the observed current and the scan rate in the range of 10-500 mV/s. This linear dependence is a characteristic observation of a strongly absorbed electroactive film in which current is not limited by the diffusion of counter ions. The free diffusion of counter ions is an important aspect for seeded growth of NCs as the ionic precusors need to diffuse into the film in order to nucleate at the metal seed points.

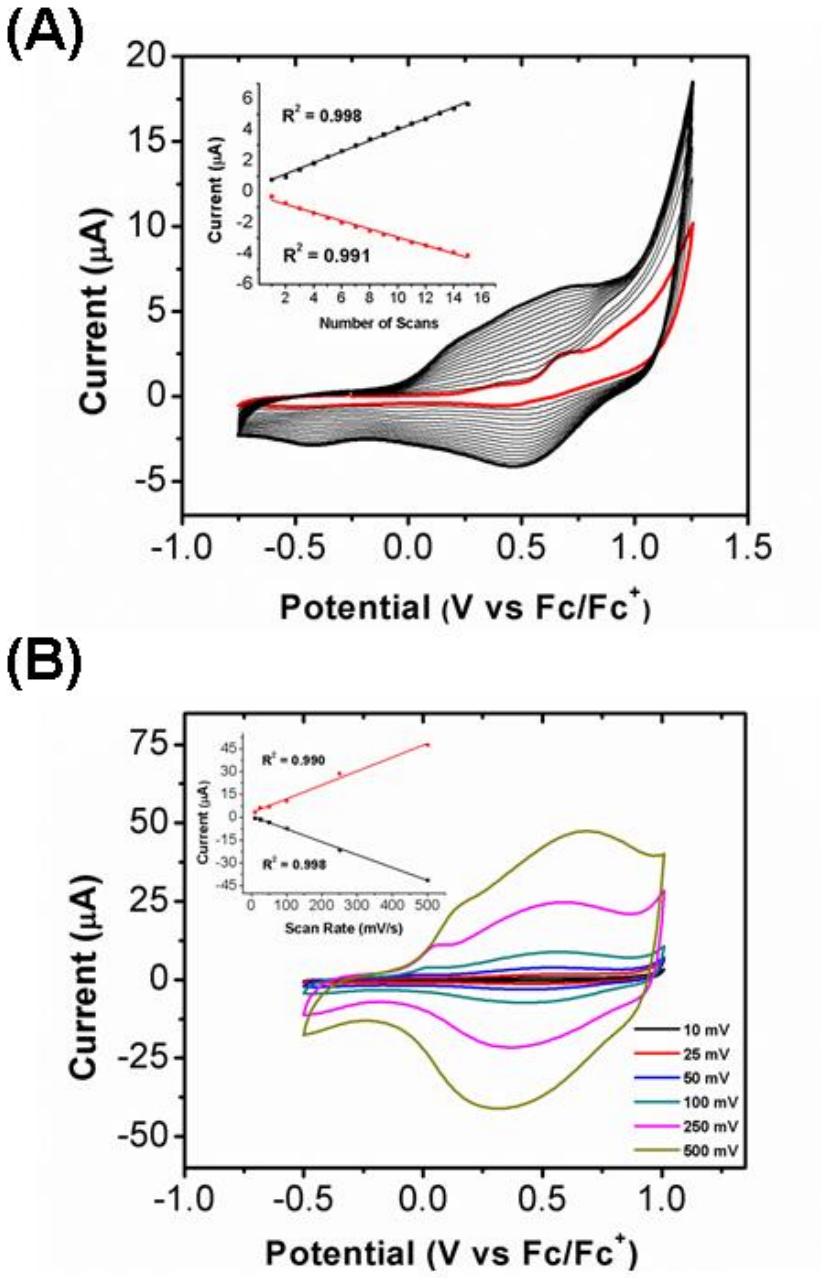

Figure 2.1. (A) Electropolymerization of **M1** from a 2×10^{-4} M CH_2Cl_2 solution, 0.1 M $TBAPF_6$, Pt button electrode. Inset shows the peak current versus the number of scans. (B) Scan rate dependence of an electrode-confined film of **Poly-1** using a 0.1 M $TBAPF_6/CH_2Cl_2$ electrolyte solution. Inset shows the peak current versus the scan rate.

The composition of the Cd-containing conducting metallopolymer (CMP) **poly-1** was determined by X-ray photoelectron spectroscopy (XPS). The data plots for **poly-1** films are shown in Figure 2.2. Cd $3d_{5/2}$ and $3d_{3/2}$ peaks are observed at 405.8 eV and 412.5 eV, respectively. The S $2p$ peak for **poly-1** is at 164.3 eV. Quantitative XPS analysis of **poly-1** yielded an atomic ratio of Cd:S = 1:3.46. This is consistent with the predicted stochiometric ratio of 1:3 in the proposed polymer structure.

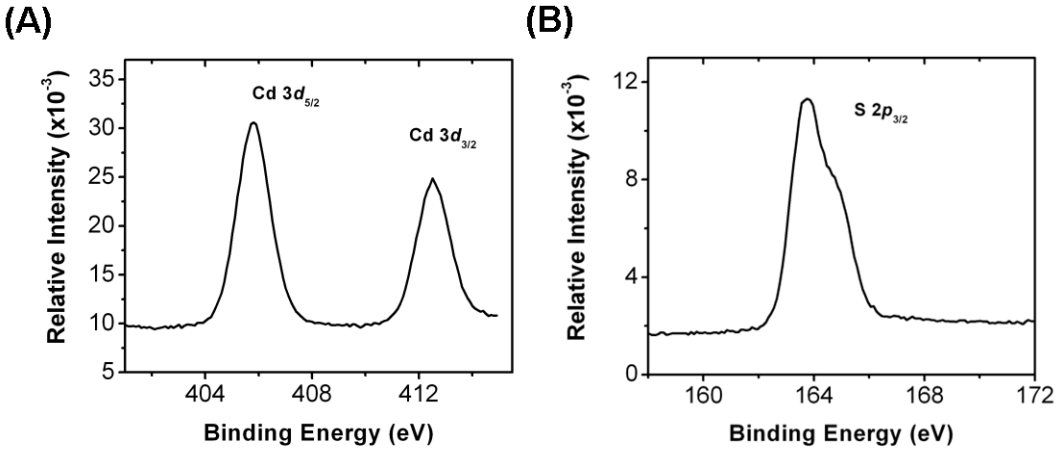

Figure 2.2. XPS data of **poly-1** (A) Cd 3*d* (B) S 2*p*.

The conjugated system of **poly-1** was investigated by UV-Vis-NIR spectroelectrochemistry. The structures and spectroelectrochemical data of **poly-1** (Wolf Type-II CMP) and a Cd-containing Wolf Type-III CMP, which has metal centers interrupting conjugated organic backbone as reported previously,[16] are presented in Figure 2.3. At 0 V, the Type II polymer exhibited strong absorption at wavelengths below 450 nm. Upon electrochemical oxidation of the polymer film, this absorption at 450 nm slightly decreased, while new bands at 700 nm and 1300 nm grew significantly (Figure 2.3A). Those bands are attributed to the formation of polarons and bipolarons, respectively, formed by partial oxidation of the neutral polymer. The absorption bands of

the polaron in the Type II polymer were not resolved in comparison to that of Type III. The broader absorption is due to the variety of delocalized states of the polaron species in the Type II metallopolymer. There was a significant shift from 1300 nm to 850 nm of the bipolaron peaks in the Type III polymer when increasing the applied potential. Howerver, very little shift was observed in the Type II metallopolymer. This blue shift is due to a reduction of delocalization length in the chromophores upon fomation of more bipolarons. The small shift in the Type II polymer revealed that the delocalization of bipolarons was not limited by the conjugation chain, an indication of a long conjugated system, which contributes to the mobility of a material.

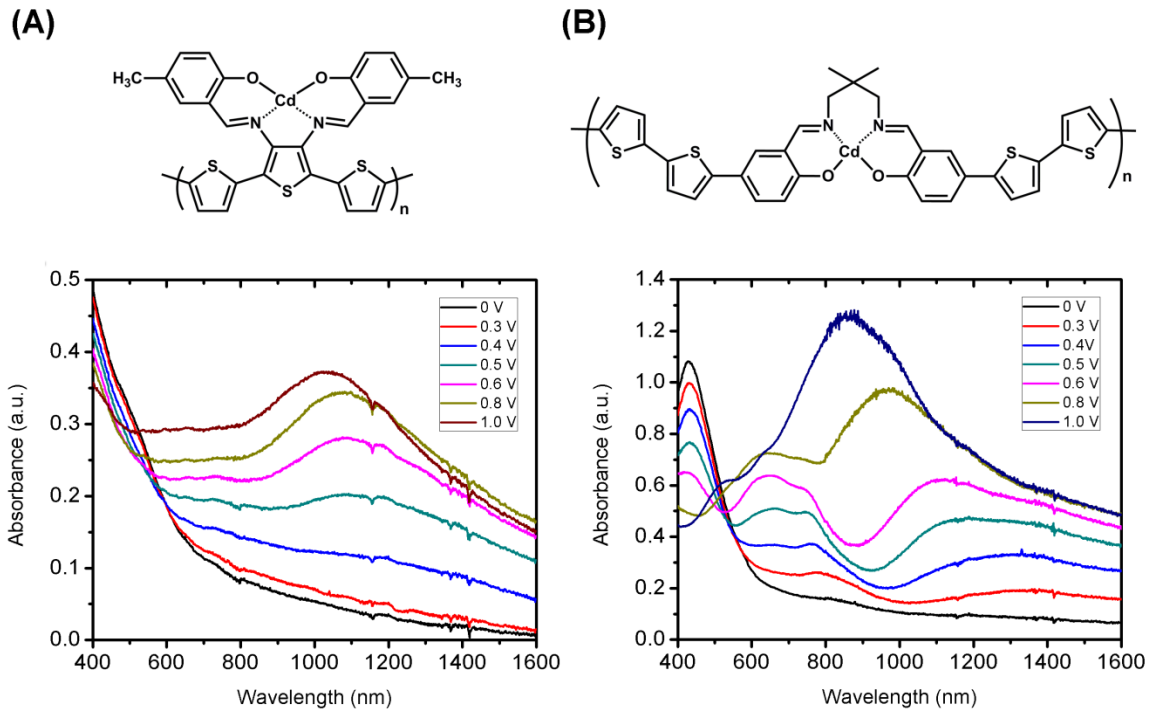

Figure 2.3. Structures and UV-Vis-NIR spectroelectrochemical spectra of metallopolymer films on ITO coated glass substrate at applied potential 0-1.0 (V) vs Fc/Fc^{+} of (A) Wolf Type II, **poly-1** and (B) Wolf Type III conducting metallopolymers.

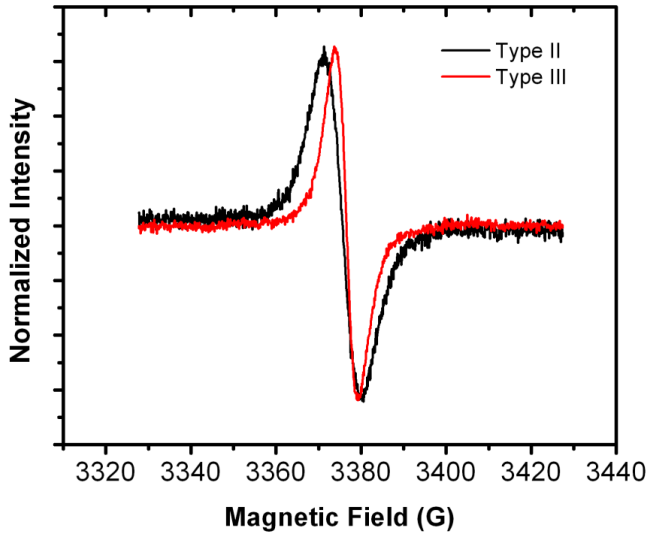

Figure 2.4. EPR spectra of the Wolf Type II (black line) and Type III (red line) conducting metallopolymers recorded at 100 K, microwave power: 2 mW, modulation amplitude: 2 G.

Spin properties of the oxidized polymers were studied by EPR spectroscopy. Polymer films were prepared and electrochemically oxidized to generate the paramagnetic centers. EPR spectra were recorded *ex-situ* at low temperature. The Wolf Type II metallopolymer gave a spectrum with a peak-to-peak linewidth of 8.3 G, while the Type III metallopolymer spectrum yielded a linewidth of 5.2 G (Figure 2.4). The linewidths of the EPR spectra reveal the kinds of interaction between the spins in the samples and can be decomposed into Gaussian and Lorentzian components. It is proposed that the broad Lorentzian EPR lines are generated by the less mobile polarons delocalized on the whole polymer matrix and highly mobile spins delocalized on isolated segments account for the narrow Gaussian lines.[21,22] Based on the linewidths of Gaussian and Lorentzian components obtained from the decomposition of the EPR spectra (Figure 2.5) of the Wolf Type II and III conducting metallopolymers, we propose that the paramagnetic centers in Type II metallopolymers are delocalized across the long

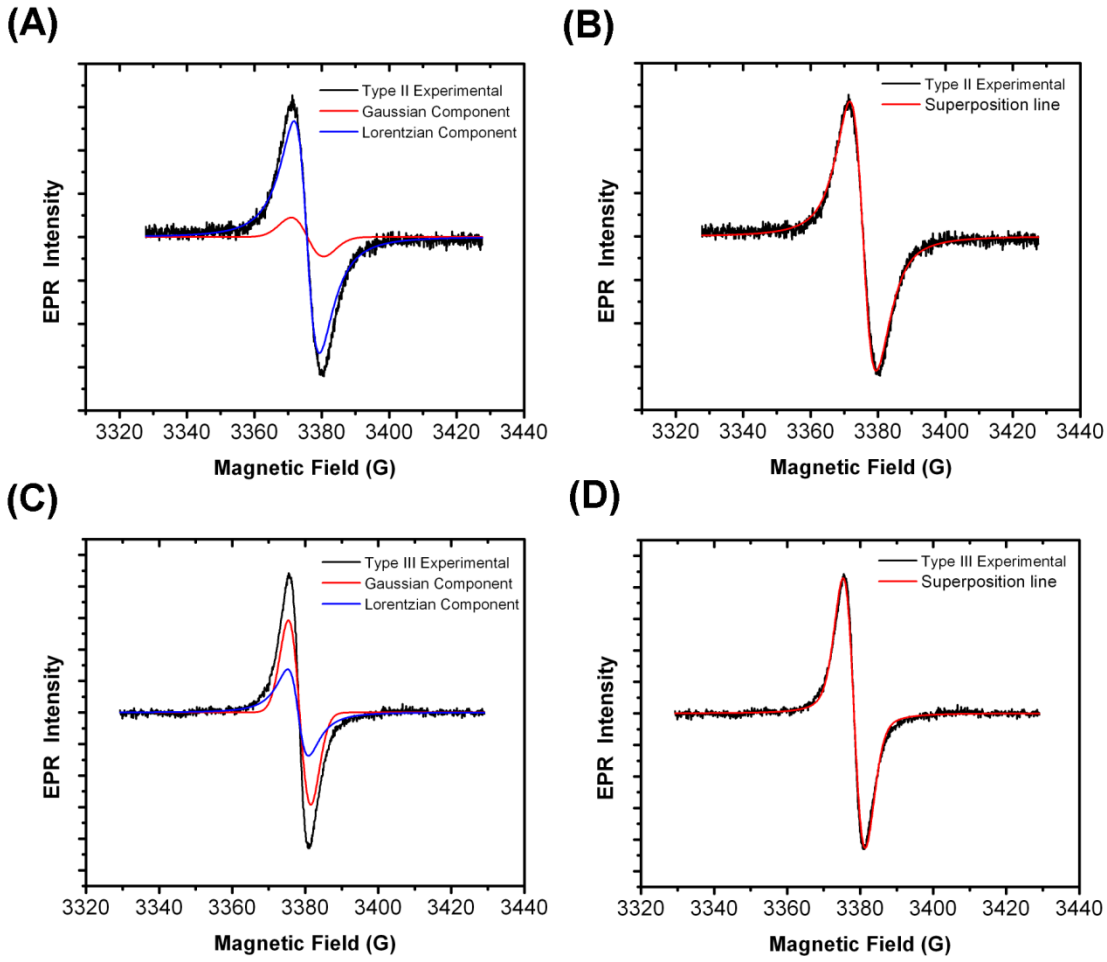

Figure 2.5. Decomposition of EPR spectra of the Wolf Type II and Type III conducting metallopolymers into Lorentzian and Gaussian components. (A) Type II polymer, Gaussian linewidth: 13.00 G, Lorentzian linewidth: 9.57 G (B) Gaussian/Lorentzian superpostion of Type II metallopolymer (C) Type III polymer, Gaussian linewidth: 9.84 G, Lorentzian linewidth: 6.13 G (D) Gaussian/Lorentzian superpostion of Type III metallopolymer.

conjugated chains resulting in broader EPR lines. Furthermore, the spins on the Type III polymer are more mobile on isolated segment with π-π stacking interactions giving a sharper EPR line. The spins of the Type II metallopolymer are not more mobile than in the Type III metallopolymer, as previously expected. This is likely due to the bulky salen centers of the polymer twisting out of the conjugation plane of the thiophene system,

which accounts for very weak or no interchain π-stacking interaction unlike as observed in the Type III metallopolymer. EPR results were consistent with UV-Vis-NIR spectroelectrochemical findings on the extension of spin delocalization on the two types of conducting metallopolymers. The results also reveal that the interchain interactions of these polymers play an important role in the spin mobility of the whole system. Detailed studies on the relationship between spin mobility and intra- and inter-chain interactions of conducting metallopolymers are needed to better understand the conduction mechanism of the metallopolymer and are under current investigation.

2.2.3. CdSe Nanocrystal Growth

CdSe NCs were synthesized directly within the aformentioned Cd-containing conducing metallopolymer matrix by sequentially treating the polymer films with Se^{2-} and Cd^{2+} solutions (Figure 2.6). To initiate NC growth at the Cd^{2+} metal seed points, the film was first dipped into a Se^{2-} solution, which was freshly prepared *in-situ* from the reduction of SeO_2 with $NaBH_4$.[23] The film was then immersed in a Cd^{2+} solution, followed by exposure to the Se^{2-} solution for a second time, completing one NC growth cycle. Each film was treated with 1 to 6 growth cycles and investigated by UV-Vis spectroscopy, transmission electron microscopy (TEM), and energy dispersive X-ray spectroscopy (EDS).

The growth of CdSe NCs could be visually confirmed by a color change from a yellow to a red hue. The absorption spectra of pure polymer film and films with 1 to 6 NC growth cycles further confirmed the formation of CdSe NCs (Figure 2.7). There were significant increases in the absorption coefficient at wavelengths less than 350 nm and a slight red-shift in the absorption onset. These features fall outside the absorption band of the pure polymer and are an indication of the growth of CdSe NCs after each cycle.

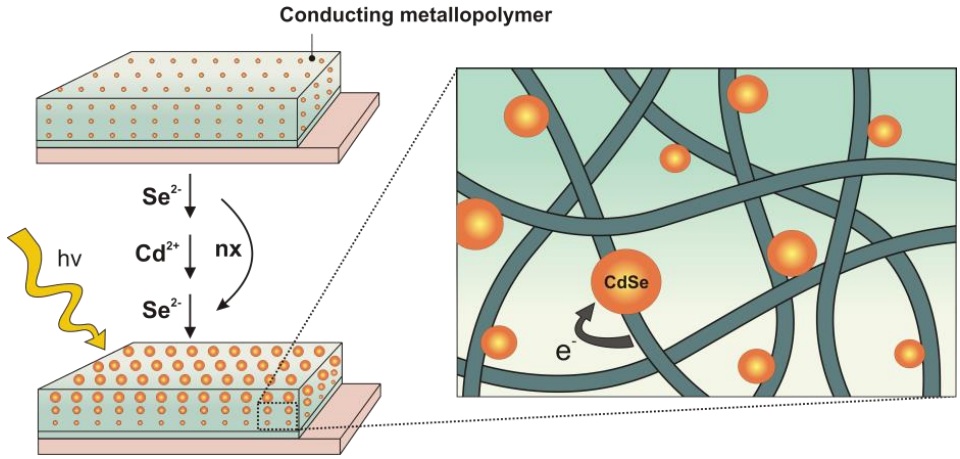

Figure 2.6. Illustration of seeded growth of CdSe NCs within the conducting metallopolymer. Inset showing the charge transfer between NCs and polymer upon illumination.

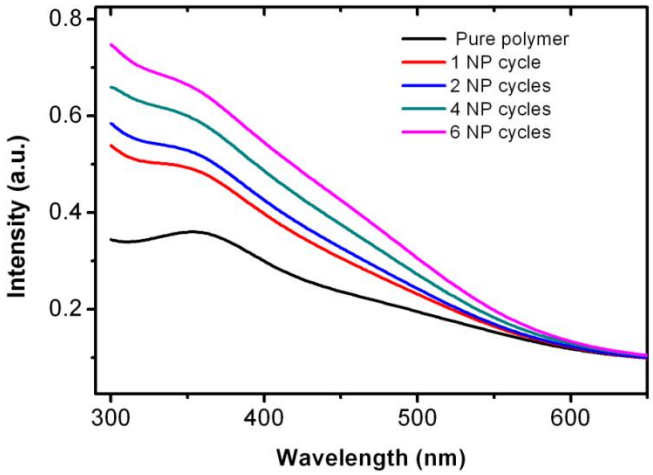

Figure 2.7. UV-Vis spectra of the Wolf Type II polymer films before and after treatment with 1-6 CdSe NC growth cycles.

By using the seeded growth technique,[9] the size of the nanocrystals can be controlled by varying the number of growth cycles. When increased from 2 to 4 growth cycles, CdSe NCs became larger in size and the distribution became denser, as shown in Figures 2.8A and 2.8B. CdSe NCs with an average size of 3.8 nm were observed in the polymer film with 2 NC growth cycles, while the mean NC size increased to 5.1 nm

when polymer films were treated with 4 NC growth cycles (Figure 2.9). Thickness of the polymer in these two films were kept the same.

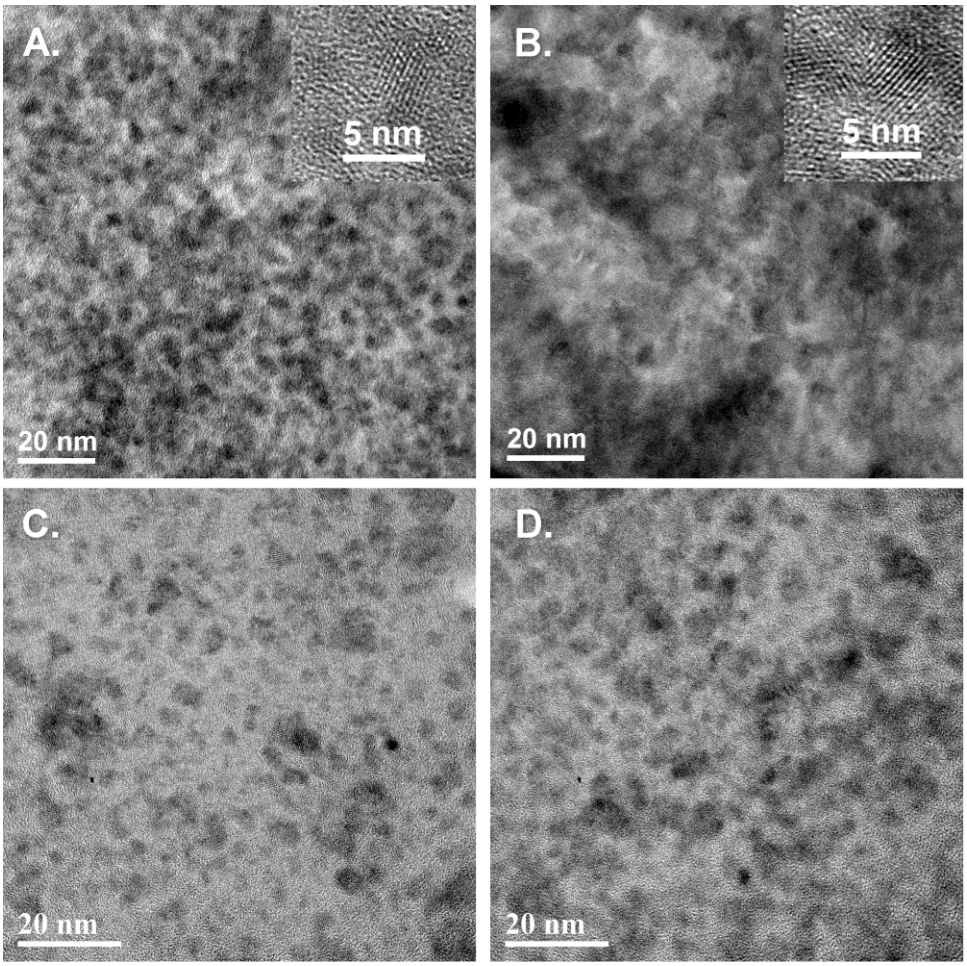

Figure 2.8. TEM images showing distribution of CdSe NCs in the Type II metallopolymer films. Films with the same polymer thickness treated with (A) 2x and (B) 4x NCs growth cycles. Polymer films treated with the same number of NC growth cycles grown at different thicknesses using (C) 1 CV scan and (D) 4 CV scans. Inset shows the crystallinity of NCs with HRTEM.

In our previous study,[16] a control experiment, in which bithiophene was used as the monomer to prepare a polymer film without seed points, was conducted in order to prove the role of metal centers in our seeded growth technique. The film was treated with

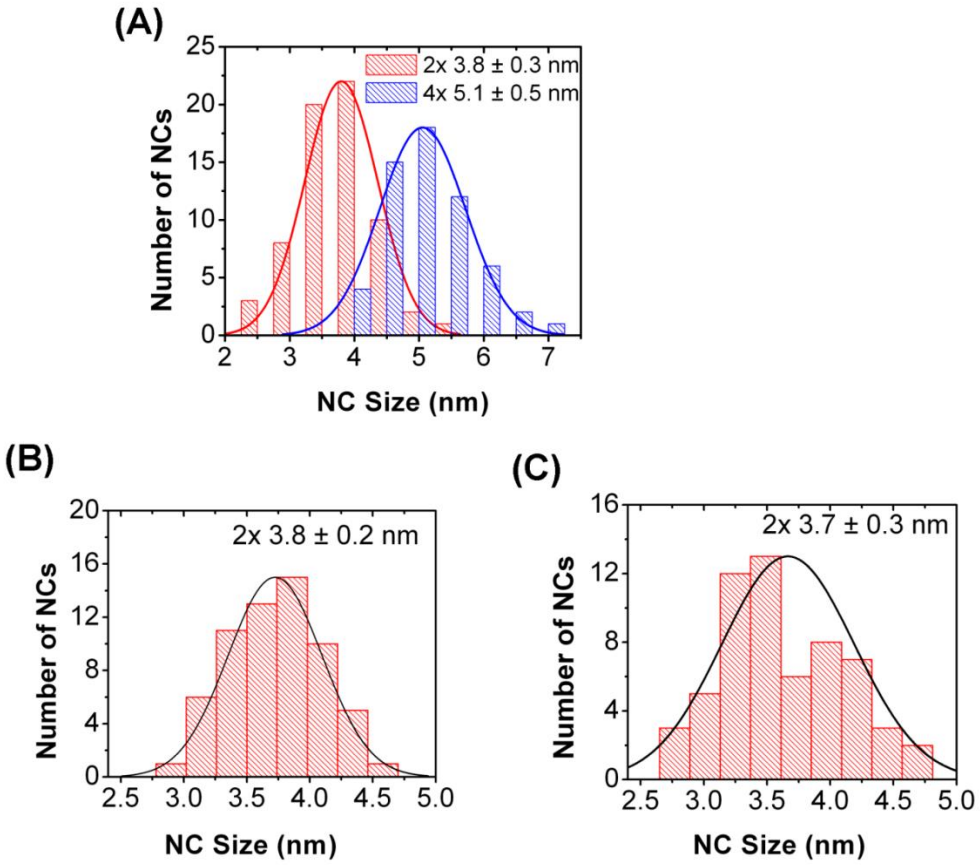

Figure 2.9. CdSe QDs size distribution in Type II metallopolymer films (A) with the same thickness and different QD growth cycles, 2x vs. 4x (B) film thickness: 1 CV scan, 2x QD growth cycles (C) film thickness: 4 CV scan, 2x QD growth cycles.

the same seeded growth procedure and TEM studies showed no nanocrystals present on the film. We further confirmed the importance of metal seed point for the formation of NCs by growing CdSe NCs from polymer films with different polymer thicknesses and metal seed point concentrations. Upon increasing the polymer film thickness, the number of Cd seed points in the film increased, which led to a higher population of NCs when the number of growth cycles was kept the same. As shown in Figures 2.8C and 2.8D, a denser distribution of NCs was found with a thicker polymer film, showing the

dependence of NCs on the number of seed points. Since the number of growth cycles remained unchanged, the average sizes of CdSe NCs in the two films were essentially equal (Figure 2.9).

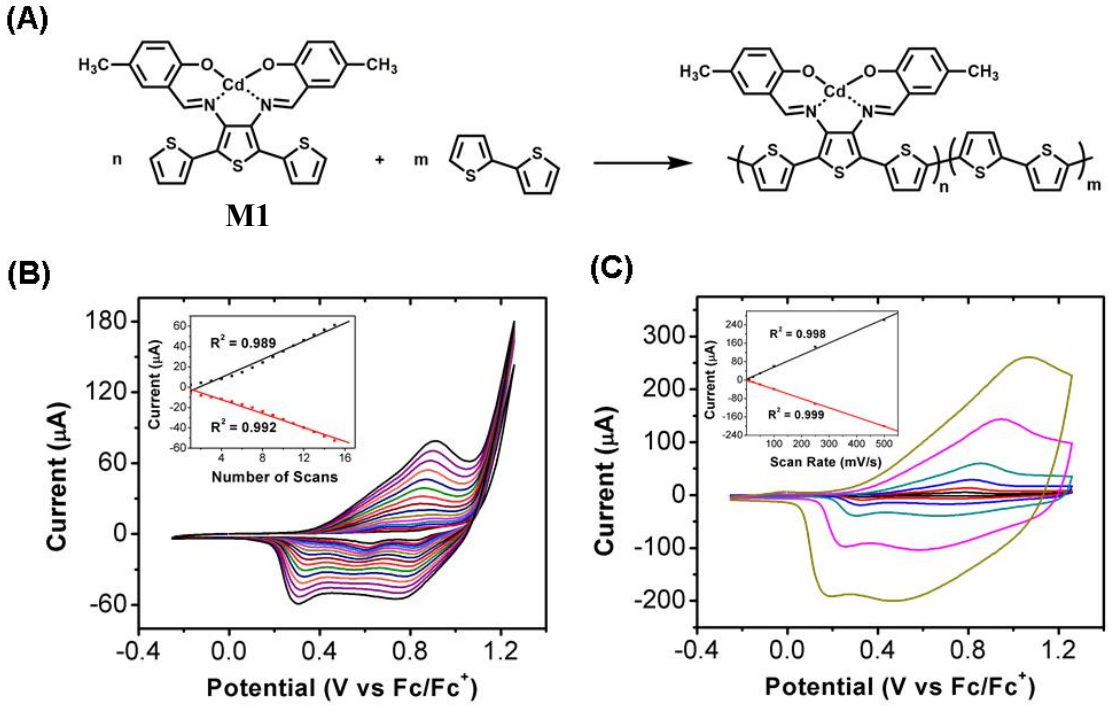

Figure 2.10. (A) Formation of copolymers from **M1** and BT (B) Electropolymerization of mixture of **M1** and BT of 1:5 ratio. Inset shows the peak current versus the number of scans. (C) Scan rate dependence of an electrode-confined film of **Poly-1** using a 0.1 M $TBAPF_6/CH_2Cl_2$ electrolyte solution. Inset shows the peak current versus the scan rates.

Distribution of CdSe NCs throughout the polymer film are also investigated with the changes in concentrations of Cd metal seed points. Polymer films composed of different concentrations of Cd seed points were prepared by the co-electropolymerization of **M1** with bithiophene (BT) at 1:0, 1:2, 1:5, and 0:1 ratios. These polymer films were then treated with the same NC growth cycles. The co-electropolymerization of **M1** and BT at 1:5 ratio and the scan rate dependence of resulted copolymer films are shown in

Figure 2.10. The distributions of CdSe NCs formed from polymer films with various metal seed point concentrations were studied by TEM. As shown in Figure 2.11, there are fewer CdSe NCs formed in polymer films composed of less seed points while no NCs are found in polybithiophene film with no metal seed points, indicating the crucial role of metal centers for the formation of CdSe NCs.

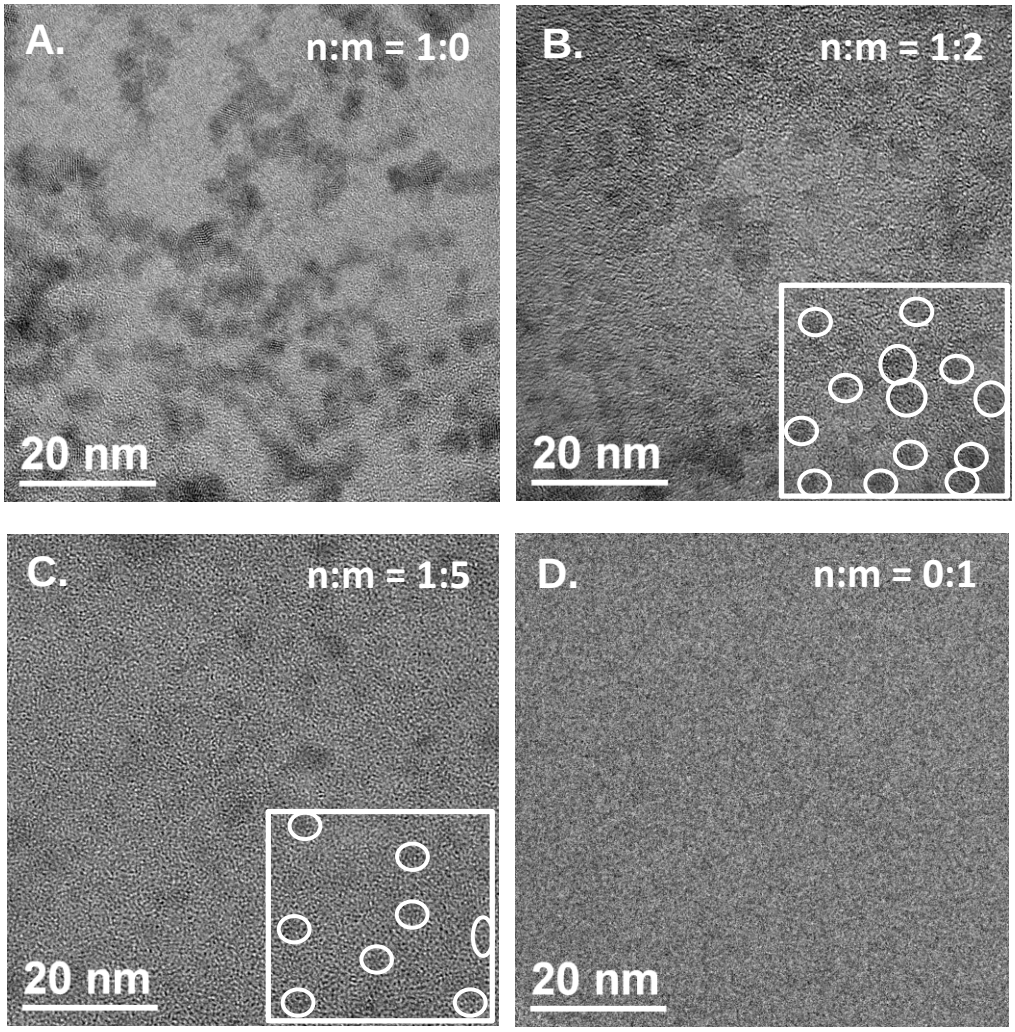

Figure 2.11. TEM images of $[M]_n[\text{bithiophene}]_m$ copolymer films at different ratios treated with 2x QD growth cycles (A) pure Type II metallopolymer, n:m = 1:0 (B) copolymer, n:m = 1:2 (C) copolymer, n:m = 1:5 (D) pure polybithiophene, n:m = 0:1.

2.2.4. Characterization of CdSe/CMP Hybrid Materials

The average composition of CdSe NCs, studied by energy-dispersive X-ray spectroscopy (EDS) analysis of the polymer film, reveals a ratio of Cd:Se that is consistent with that of the bulk structure. The ratios of Cd:Se in the films with 2x and 4x NC growth cycles were 1.0:1.1 and 1.0:1.0, respectively. Scanning transmission electron microscopy (STEM)-EDS elemental mapping of the polymer films after NC growth confirmed that Cd and Se are evenly distributed among the NCs (Figure 2.12).

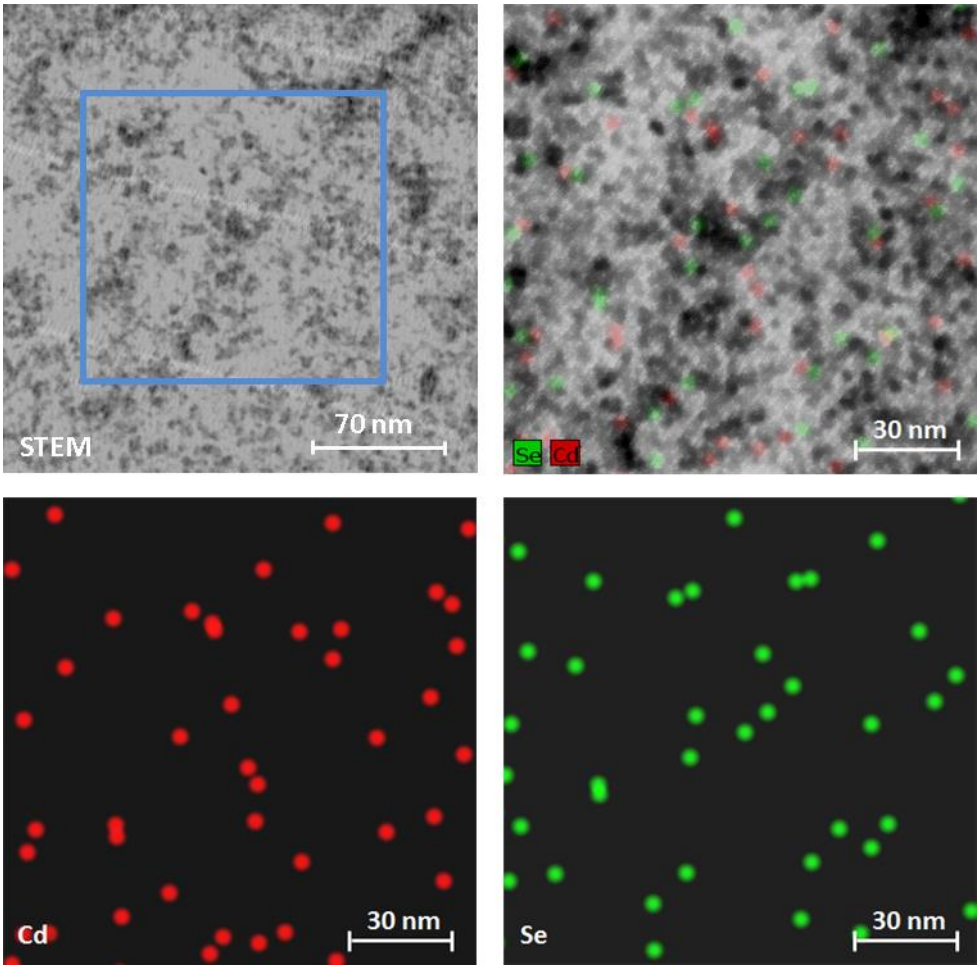

Figure 2.12. STEM-EDS elemental map of CdSe NCs within the Type II conducting metallopolymer.

Charge separation in metallopolymer-CdSe NCs systems was investigated by light-induced electron paramagnetic resonance (L-EPR). Figure 2.13 shows the L-EPR spectra of metallopolymer-CdSe NCs in the dark and under 543 nm laser excitation measured at 90 K. There was a primary resonance at g = 2.004 with a peak-to-peak width of 8.6 G. This resonance was attributed to the postive polaron formed from the polythiophene backbone of the metallopolymer, which was similar to the resonance of the polaron in poly-3-hexylthiophene (P3HT) for P3HT-CdSe blend systems.[9,24,25] No signal associated with electrons on NCs was found due to the high spin-lattice interaction from heavy elements Cd and Se. There was a weak resonance found in the dark due to a high number of defect states, which prevent charge recombination upon thermal annealing, as reported in literature.[24] The appearance of a high intensity resonance when illuminated indicates that polarons are generated from the polymer by photo-excitation and shows a successful photo-induced charge transfer between the metallopolymer and CdSe NCs.

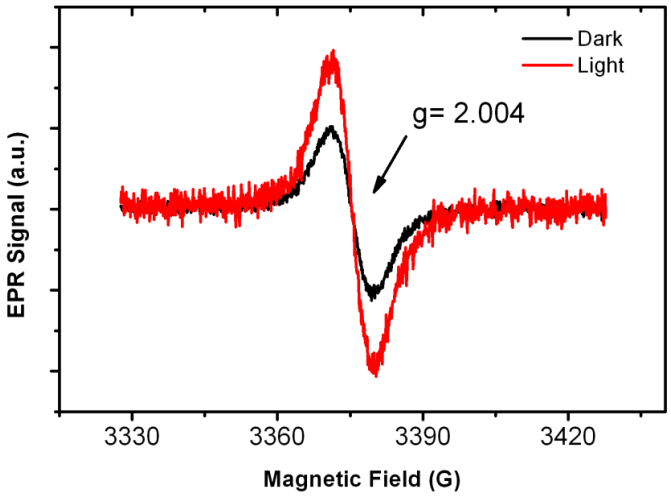

Figure 2.13. EPR spectra of metallopolymer-CdSe NCs synthesized by seeded growth technique at $P_{microwave}$ = 6 mW in the dark (black line) and under 5 mW laser excitation (red line).

2.3. CONCLUSION

In summary, we have demonstrated the synthesis of CdSe NCs within a Wolf Type II metallopolymer using a seeded growth technique. This is the first example of direct bonding of CdSe NCs to the backbone of a conducting polymer. By using our seeded growth method, the size and distribution of NCs can be controlled by altering the number of NC growing cycles, the thickness of polymer film, and the concentration of metal seed points. Since metal seed points are bonded directly to the polymer, the resulting NCs are in direct electronic communication with the polymer, allowing direct charge transfer between the donor and acceptor materials. L-EPR showed a successful charge separation between the metallopolymer and CdSe NCs demonstrating the potential of this system for application in hybrid solar cells. Photovoltaic devices developed based on this system will be the subject of future research.

2.4. EXPERIMENTAL

2.4.1. General Methods

Air- and moisture-sensitive reactions were carried out in flame-dried glassware using standard Schlenk techniques under an inert nitrogen atmosphere. All chemicals were purchased from commercial sources and used as received. Dry solvents were dried using an Innovative Technology, Pure Solv solvent purifier with a double purifying column. ^{1}H NMR (400 MHz) and ^{13}C $\{^{1}$H$\}$ NMR (100 MHz) spectra were obtained on a Varian (400 MHz) spectrometer and were referenced to residual solvent peaks. All peak positions are given in ppm and coupling constants are reported in Hz. Low-resolution and high-resolution mass spectrometry was carried out by a Thermo Finngan TSQ 700 and Waters Autospec Ultima, respectively. Melting points were recorded with an OptiMelt Automated Melting Point System with digital image processing technology from

Stanford Research System (SRS, Sunnyvale, CA). Elemental analysis was performed by QTI, Whitehouse, NJ (www.qtionline.com). Infrared spectra were recorded using a Nicolet IR 200 FTIR spectrometer. X-ray photoelectron spectroscopy (XPS) was carried out on a PHI 5700 XPS system equipped with dual Mg X-ray source and monochromatic Al X-ray source complete with depth profile and angle-resolved capabilities. 3',4'-dinitro-2,2':5',2''-terthiophene was prepared as reported in the literature.[26] The starting material, 2-hydroxy-4-methylbenzaldehyde (from Aldrich), and other commercially available reagents were used without further purification.

2.4.2. Electrochemistry

Electrochemical syntheses and studies were performed in a dry-box under an atmosphere of nitrogen using a GPES system from Eco. Chemie B. V. All the electrochemical experiments were carried out in a three-electrode cell with a $Ag/AgNO_3$ reference electrode (silver wire dipped in a 0.01 M silver nitrate solution with 0.1 M $[(n\text{-}Bu)_4N]^+[PF_6]^-$ in CH_3CN), a Pt working electrode, and a Pt wire coil counter electrode. Potentials were relative to this 0.01 M $Ag/AgNO_3$ reference electrode. Ferrocene was used as an external reference to calibrate the reference electrode before and after experiments were performed and that value was used to correct the measured potentials. All electrochemistry and electropolymerizations were performed in dichloromethane (DCM) or acetonitrile (ACN) solutions using 0.1 M $[(n\text{-}Bu)_4N]^+[PF_6]^-$ ($TBAPF_6$) as the supporting electrolyte. The $TBAPF_6$ was purified by recrystallization three times from hot ethanol before being dried for 3 days at 100-150 °C under active vacuum prior to use. Polymer films were prepared on Delta Technologies ITO-coated glass for spectroscopic measurement and on stainless steel for XPS. Electrosyntheses of the polymer films were performed from monomer solutions by continuous cycling between -0.5 and 1.5 V (vs.

Fc/Fc^+) at a scan rate of 100 mV/s. The films obtained were then washed with copious amounts of fresh DCM before further experiments.

2.4.3. UV-Vis-NIR Spectroelectrochemistry

The spectroelectrochemical measurements were performed using the previously described cell arrangement on a polymer film deposited on ITO coated glass substrate as working electrode, a platinum mesh as the counter electrode, and $Ag/AgNO_3$ as reference electrode. Experiments were carried out in an optical cuvette inside the glovebox. Absorption spectra were recorded on a Varian Cary 6000i UV-Vis-NIR spectrophotometer within the NIR/visible spectra ($1600 \geq \lambda \geq 400$ nm) under several applied potentials.

2.4.4. Electron Paramagnetic Resonance Spectroscopy (EPR)

EPR experiments were recorded on a Bruker EMX-Plus X-band spectrometer at 100 K. *Ex-situ* EPR of metallopolymer films were recorded by first depositing the polymer film on platinum mesh in the glovebox. In a pure electrolyte solution, a potential of 1.0 V was applied to the films for one minute. The polymer films were then put into EPR tubes and capped carefully. The samples were then taken out of the glove box and kept in liquid nitrogen until performing the EPR measurement. Decomposition of EPR spectra of two polymer types was done using the Bruker WinEPR Processing software.

Light-induced EPR was recorded for metallopolymers containing CdSe NCs. The film was put into an EPR tube and annealed at 90 ^oC for 30 seconds. The annealed tube was then introduced to the cavity and cooled to 90 K before the dark spectrum was recorded. Subsequently, the sample was excited with 543.5 nm laser light and the excited spectrum was recorded.

2.4.5. Se^{2-} Solution Preparation

An Se^{2-} solution was synthesized according to literature procedures.[23] Briefly, 0.1 g of SeO_2 is dissolved in 30 mL ethanol (30 mM), and purged with N_2, while stirring, for 15 minutes. Then 0.068 g of $NaBH_4$ (60 mM) was added quickly into the reaction flask containing SeO_2 and stirred under N_2 flow until the solution became clear. The flask was transfered to the glove box and the solution was diluted with dry acetonitrile to obtain the desired concentration.

2.4.6. CdSe Nanocrystal Growth

The electropolymerized thin films were treated with a 2 x 10^{-4} M Se^{2-} solution in acetonitrile for one minute then rinsed thoroughly with dry acetonitrile. The film was then treated with a solution of $Cd(NO_3)_2$ in acetonitrile (2 x 10^{-4} M) for one minute followed by another rinse with acetonitrile. The films were treated once more time with Se^{2-} solution, followed by rinsing. This process constitutes one cycle of the growth process, which was repeated up to six times.

2.4.7. Transmission Electron Microscopy (TEM)

TEM experiments were carried out on a JEOL 2010F microscope. Films were grown electrochemically onto 400 mesh carbon coated gold grids purchased from Electron Microscopy Sciences. Films were made by electropolymerization of **M1**, by cycling between -0.5 and 1.5 V four times. TEM grids containing the polymer film were kept in an air free environment and CdSe NCs were grown directly within the resulting polymer film. Analysis of the quantum dots was done using Gatan Digital Micrograph software.

2.4.8. Syntheses of Ligand L and Monomer M1

3',4'-diamino-2,2':5',2''-terthiophene. 3',4'-dinitro-2,2':5',2''-terthiophene (1.0 g), iron powder (250 mesh, 2.2 g), and acetic acid (45 mL) were mixed and heated at 60 °C for 30 minutes. The reaction mixture was cooled and poured into 100 mL deionized H_2O and extracted with diethyl ether. The organic layer was washed with a sodium bicarbonate solution and then rinsed 3 times with brine and water. After drying over anhydrous Na_2SO_4, the solvent was removed by rotary evaporation to afford the desired product as a brown-yellow solid (0.7 g, 84%). ^{1}H NMR ($CDCl_3$): δ 7.25 (dd, 2H, J = 1.6, 4.5), 7.07−7.01 (m, 4H), 3.80 (s, 4H); ^{13}C {^{1}H} NMR ($CDCl_3$) 135.9, 133.5, 127.8, 124.0, 123.9, 110.0.

***N,N'*-Bis(4-methylsalicylidene)-3',4'-diamino-2,2':5',2''-terthiophene (L).** To a solution of 3',4'-diaminoterthiophene (1.07 g, 5 mmol) in ethanol (20 mL) was added 2-hydroxy-4-methylbenzaldehyde (1.36 g, 10 mmol). The reaction mixture was brought to reflux for 20 hours. The mixture was cooled to room temperature, concentrated, and stored in a refrigerator overnight. The precipitate was collected by vacuum filtration to give the desired product (1.8 g, 71%). ^{1}H NMR (DMSO-d_6): δ 11.45 (s, 2H), 8.77 (s, 2H), 7.57 (dd, 2H, J = 1.1, 5.2), 7.41 (d, 2H, J = 2.2), 7.32 (dd, 2H, J = 1.1, 3.6), 7.20 (dd, 2H, J = 2.2, 8.4), 7.09 (dd, 2H, J = 3.6, 5.2), 6.82 (d, 2H, J = 8.4), 2.20 (s, 6H). ^{13}C {^{1}H} NMR: compound was not sufficiently soluble in any common organic solvent to obtain a spectrum. HRMS (CI^+) m/z calculated for $[C_{28}H_{22}N_2O_2S_3]^+$ ($[\mathbf{L}]^+$): 514.0843, found 514.0839.

***N,N'*-Bis(4-methylsalicylidene)-3',4'-diamino-2,2':5',2''-terthiophene cadmium(II) (M1).** To a solution of ligand **L** (0.206 g, 0.4 mmol) in methylene chloride (20.0 mL) was added a solution of NaOMe (0.046 g, 0.85 mmol) in 5 mL of methanol. The mixture was stirred for three hours before adding a solution of $Cd(OAc)_2{\cdot}2H_2O$

(0.106 g, 0.4 mmol) in 6 mL of methanol. The reaction mixture was stirred at room temperature for 20 hours then the methylene chloride was removed in vacuo, resulting in a suspension in methanol. The dark yellow solid were collected by filtration and dried to give the desired product (0.17 g, 68%). ^{1}H NMR (DMSO-d_6): δ 8.32 (s, 2H), 7.63 (d, 2H, J = 5.2), 7.29 (d, 2H, J = 3.6), 7.13 (dd, 2H, J = 3.6, 5.2), 6.95 (d, 2H, J = 8.4), 6.54 (s, 2H), 6.48 (d, 2H, J = 8.4), 2.07 (s, 6H). ^{13}C {^{1}H} NMR: compound was not sufficiently soluble in any common organic solvent to obtain a spectrum. HRMS (CI^{+}) m/z calculated for $[C_{28}H_{20}CdN_2O_2S_3]^{+}$ ([**M1**]$^{+}$): 625.9809, found 625.9807.

REFERENCES

(1) Huynh, W. U.; Dittmer, J. J.; Alivisatos, A. P. *Science* **2002**, *295*, 2425.

(2) Sun, B.; Marx, E.; Greenham, N. C. *Nano Letters* **2003**, *3*, 961.

(3) Sun, B.; Snaith, H. J.; Dhoot, A. S.; Westenhoff, S.; Greenham, N. C. *J. Appl. Phys.* **2005**, *97*, 014914.

(4) Gur, I.; Fromer, N. A.; Chen, C.-P.; Kanaras, A. G.; Alivisatos, A. P. *Nano Lett.* **2006**, *7*, 409.

(5) Dayal, S.; Kopidakis, N.; Olson, D. C.; Ginley, D. S.; Rumbles, G. *Nano Letters* **2009**, *10*, 239.

(6) Borchert, H. *Energy Environ. Sci.* **2010**, *3*, 1682.

(7) Kusum, K.; Umesh, K.; Shailesh, N. S.; Suresh, C.; Rita, K.; Vankar, V. D.; Vikram, K. *J. Phys. D: Appl. Phys.* **2008**, *41*, 235409.

(8) Lek, J. Y.; Xi, L.; Kardynal, B. E.; Wong, L. H.; Lam, Y. M. *ACS Appl. Mater. Interfaces* **2011**, *3*, 287.

(9) Lokteva, I.; Radychev, N.; Witt, F.; Borchert, H.; Parisi, J. r.; Kolny-Olesiak, J. *J. Phys. Chem. C* **2010**, *114*, 12784.

(10) Seo, J.; Kim, W. J.; Kim, S. J.; Lee, K.-S.; Cartwright, A. N.; Prasad, P. N. *Appl. Phys. Lett.* **2009**, *94*.

(11) Olson, J. D.; Gray, G. P.; Carter, S. A. *Sol. Energy Mater. Sol. Cells* **2009**, *93*, 519.

(12) Zhou, Y.; Riehle, F. S.; Yuan, Y.; Schleiermacher, H.-F.; Niggemann, M.; Urban, G. A.; Krüger, M. *Appl. Phys. Lett.* **2010**, *96*.

(13) Liu, J.; Tanaka, T.; Sivula, K.; Alivisatos, A. P.; Fréchet, J. M. J. *J. Am. Chem. Soc.* **2004**, *126*, 6550.

(14) Liao, H.-C.; Chen, S.-Y.; Liu, D.-M. *Macromolecules* **2009**, *42*, 6558.

(15) Dayal, S.; Kopidakis, N.; Olson, D. C.; Ginley, D. S.; Rumbles, G. *J. Am. Chem. Soc.* **2009**, *131*, 17726.

(16) Mejía, M. L.; Agapiou, K.; Yang, X.; Holliday, B. J. *J. Am. Chem. Soc.* **2009**, *131*, 18196.

(17) Mejia, M. L.; Reeske, G.; Holliday, B. J. *Chem. Commun.* **2010**, *46*, 5355.

(18) Wolf, M. O. *Adv. Mater.* **2001**, *13*, 545.

(19) Wolf, M. *J. Inorg. Organomet. Polym. Mater.* **2006**, *16*, 189.

(20) Reddinger, J. L.; Reynolds, J. R. *Macromolecules* **1997**, *30*, 673.

(21) Harima, Y.; Eguchi, T.; Yamashita, K.; Kojima, K.; Shiotani, M. *Synth. Met.* **1999**, *105*, 121.

(22) Zykwinska, A.; Domagala, W.; Czardybon, A.; Pilawa, B.; Lapkowski, M. *Chem. Phys.* **2003**, *292*, 31.

(23) Lee, H.; Wang, M.; Chen, P.; Gamelin, D. R.; Zakeeruddin, S. M.; Grätzel, M.; Nazeeruddin, M. K. *Nano Lett.* **2009**, *9*, 4221.

(24) Heinemann, M. D.; von Maydell, K.; Zutz, F.; Kolny-Olesiak, J.; Borchert, H.; Riedel, I.; Parisi, J. *Adv. Funct. Mater.* **2009**, *19*, 3788.

(25) Witt, F.; Kruszynska, M.; Borchert, H.; Parisi, J. *J. Phys. Chem. Lett.* **2010**, *1*, 2999.

(26) Kitamura, C.; Tanaka, S.; Yamashita, Y. *Chem. Mater.* **1996**, *8*, 570.

Chapter 3: Structure-property Relationships in Conducting Metallopolymers

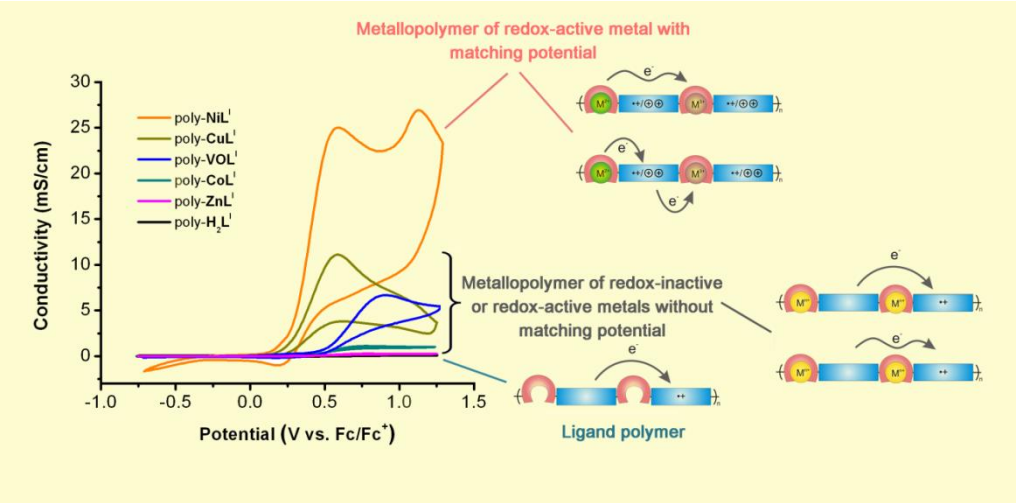

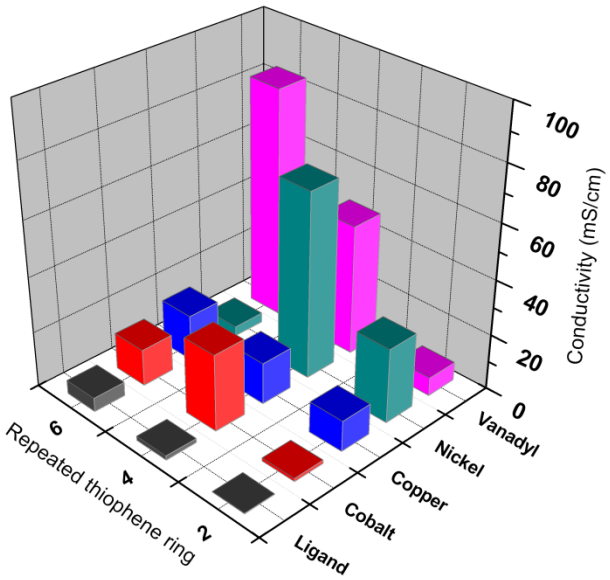

3.1. INTRODUCTION

Recently, conducting metallopolymers (CMPs) have been extensively studied due to their potential for various applications including sensing, catalysis, light-emitting diodes, energy applications, and memory storage.[1] The incorporation of metal centers into organic backbones not only makes the resulting materials multi-functional, but also lead to changes properties-such as electroactivity and conductivity-of the resulting materials compared to the individual inorganic and organic segments.[2-5] Therefore, understanding the interactive role of transition metals in those polymers will provide insight for rational design of metallopolymers tailored to certain applications, especially for those utilizing the polymer conductivity such as in gas sensors.[6,7]

Electronic conductivity of CMPs depends on the properties of three components: the organic backbone, metal centers, and the interaction between metal centers and organic backbone. In many cases, it is difficult to study the contribution of each element individually with regard to overall conductivity due to overlapping effects.[8] As a result, systematic studies on the charge transport of each component are necessary in order to understand their influence on electrochemical properties of metallopolymers. This requires an investigation of the charge transport property of an isolated organic backbone, the activity of metals, and charge transport caused by metal-backbone interaction. Specifically, systems containing redox-active metals that have oxidation potential lower, overlapping, and higher than that of the organic backbone are necessary to the study of metal-backbone interaction.

Kingsborough *et al.* reported that when the redox of the metal center matches that of the organic backbone of conducting polymers, the electroactivity of the metal center is greatly enhanced.[8] They also suggested that a redox potential of organic backbone that is lower than or equal to that of the metal redox potential should create materials with

enhanced electron mobility. Also, it is important to note that attempts to grow polymers from Schiff-base ligand monomers were reported to be unsuccessful, resulting in a lack of ligand-based polymer characterization.[8,9] For this reason, no direct comparison between ligand polymer and metallopolymer has been previously reported.

In this study, we aim to understand the effects of organic backbone, metal centers that are both redox-active and redox-inactive, and the interaction between metal and organic backbone on the charge delocalization and charge transport of conducting metallopolymers. A systematic study beginning with the syntheses of metal-free polymers and metallopolymers to characterization of those polymers and their optical and electrochemical properties has been investigated and will be presented. To our knowledge, this is the first time that a Schiff-based ligand polymer has been successfully prepared and characterized. The information obtained from the ligand polymer properties allows a direct comparison to those of the metallopolymer and helps elucidate the role of the metal centers.

3.2. Result and Discussion

3.2.1. Synthesis and Characterization of Electropolymerizable Ligands and Metal Complex Monomers.

Ligand monomers were prepared from the condensation reaction of 2,2-dimethylpropanediamine and a ligand-precursor aldehyde,[10] which were synthesized by a Stille coupling of 5-bromosalicylaldehyde with 2-(tributylstannyl)thiophenes (Scheme 3.1). The length of conjugated backbone in the conducting polymers was controlled by varying the number of thiophene units (n = 1-3, abriviated by $\mathbf{H_2L^{I\text{-}III}}$) attached to both sides of a Schiff-base ligand center. Consequently, polymers obtained from those ligands have a repeated oligomer chain of two, four, and six thiophene units, respectively. The

use of 2,2-dimethylpropanediamine helped increase the solubility of ligands and metal complexes compared with those prepared from ethylenediamine, a more commonly used diamine.

Scheme 3.1. Synthesis of electropolymerizable ligand and metal complex monomers.

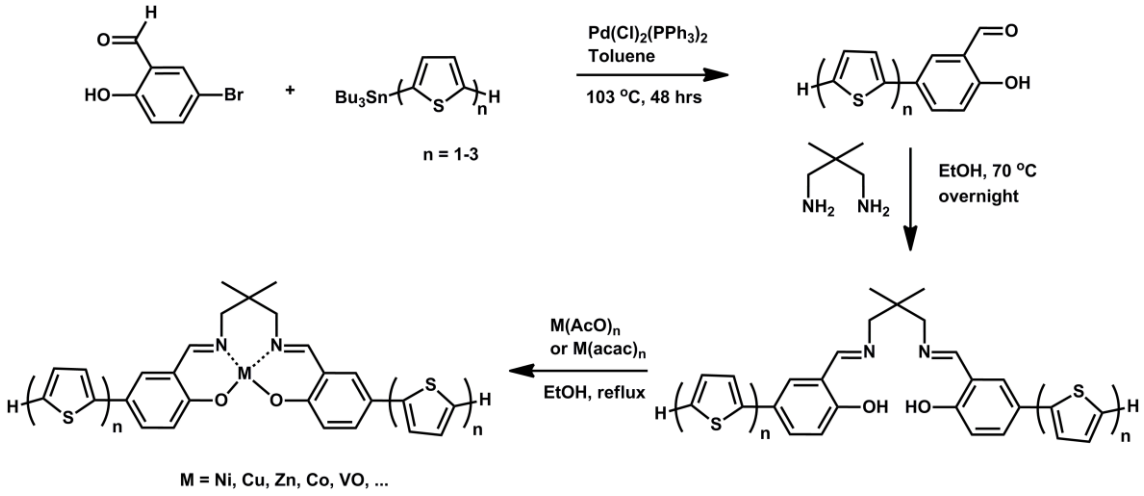

To understand the effects of both metal and the conjugated organic backbone on the charge transport and delocalization of CMPs, we have synthesized a series of metal complexes of aforementioned ligands and their corresponding polymers. The role of the metal centers emerges when the properties of metallopolymers and ligand polymers are compared. In addition, the effect of organic conjugation length can also be investigated when comparing the charge transport in polymers with different conjugation length of the same metal. Both redox-active (Co, Ni, V) and redox-inactive metals (Cu, Zn) were used to evaluate the interaction of metal to organic backbone. Metal complexes were prepared by reacting the ligands to metal acetate or acetylacetonate salts in chloroform/ethanol at 60 ^{o}C. In order to solve the very low solubility problem of the $\mathbf{H_2L^{III}}$, metal complexes of the terthiophene system have been prepared which contain the dialkyl chains on the

middle thiophene ring to increase the solubility of the corresponding metal complexes (Scheme 3.2). Both ethyl and *n*-butyl groups were used to synthesize the ligands and metal complexes. However, due to the higher solubility of metal complexes with *n*-butyl chain ($\mathbf{H_2L^{IIIC4}}$ series) compared to complexes with ethyl group ($\mathbf{H_2L^{IIIC2}}$ series), this system was used for further studies. Purity and structural information of the ligand and metal complex monomers were confirmed by elemental and single-crystal X-ray diffraction analyses, respectively.

Scheme 3.2. Structure of terthiophene series with different alkyl chain

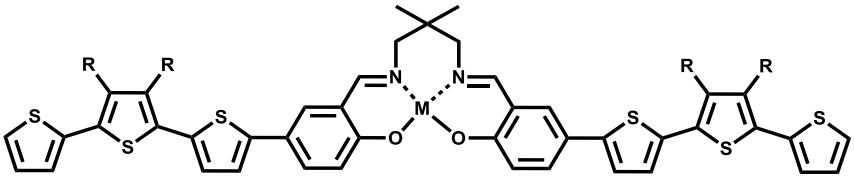

R = -H, $-C_2H_5$, $-C_4H_9$

M = Ni, Cu, Co, VO

3.2.2. Structure Determination

3.2.2.1. Ligand Monomers

Single-crystal X-ray diffraction was used to analyze the structural information of the ligands in the solid state. Crystals suitable for single-crystal X-ray diffraction analysis of these ligands were obtained by the slow evaporation from DCM/EtOH solutions. In the solid state, the two oxygen atoms of $\mathbf{H_2L^{I}}$ O1O2 are in the *trans*- configuration with respect to the two nitrogen atoms N1N2 (Figure 3.1). For the metallation process to occur, a reorganization of one of the half-salphen moieties is required, which could occur through the rotation of the C-N single bonds on the diamine. The two thiophene rings are highly planar to the connected iminophenol rings with a twist angle of 3.3^{o} and 0.26^{o} for

thiophene rings containing S1 and S2, respectively. The two iminophenol rings are found to twist at a 39.42° angle to each other.

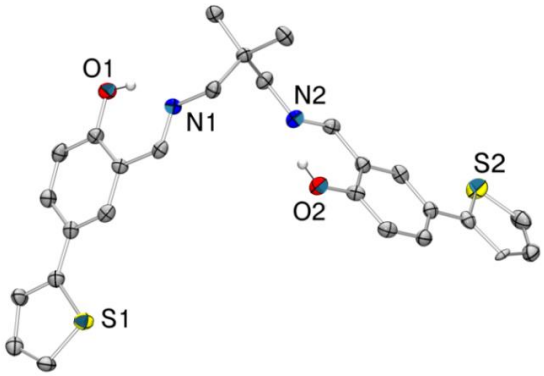

Figure 3.1. ORTEP view of molecule $\mathbf{H_2L^I}$, drawn with the thermal ellipsoids at the 50% probability level. Hydrogen atoms have been omitted for clarity.

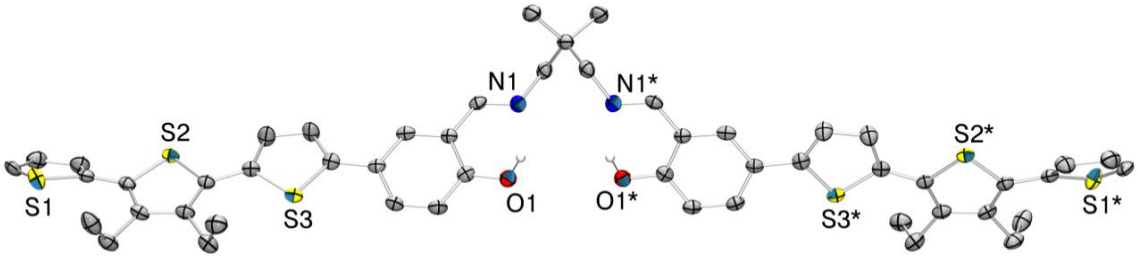

Figure 3.2. ORTEP view of molecule **LIIIC2**, drawn with the thermal ellipsoids at the 30% probability level. Hydrogen atoms have been omitted for clarity.

The conformation of ligand $\mathbf{H_2L^{IIIC2}}$ in the solid-state, on the other hand, is likely ready for complexation with the *cis*- configuration of the two hydroxyl groups with respect the two nitrogen atoms (Figure 3.2). There is a C_2 symmetry through the quaternary carbon resulting in equivelancy of the two organic segments. In addition, a twist angle of 45.72° between the two iminophenol groups is observed. The inner and the middle thiophene rings are nearly co-planar to the iminophenol ring with twist angles of 14.89° and 21.43°, respectively. The terminal thiophene ring, however, twists

significantly from the iminophenol ring (53.94°) and were modeled with static disorder over two sites.

3.2.2.2. Nickel(II) Complexes

We were able to obtain the single-crystal X-ray diffraction analysis of nickel(II) complexes with mono-, bi-, and dibutylter-thiophenes. Crystals suitable for single-crystal X-ray diffraction study of these ligands were obtained by the slow evaporation of DCM/EtOH solutions. The coordination environment around nickel (II) can be described as distorted square planar (Figure 3.3-3.5). The dihedral angle between the two iminophenol rings found in **NiL^{I}**, **NiL^{II}**, and **NiL^{IIIC4}** are 14.22°, 17.30°, 8.79°, respectively. The thiophene rings connected to the iminophenol rings in these complexes are near-planarity with regards to the core of the metal complexes while the terminal thiophene rings are twisted at a larger angle and accompanied by disorder over two sites.

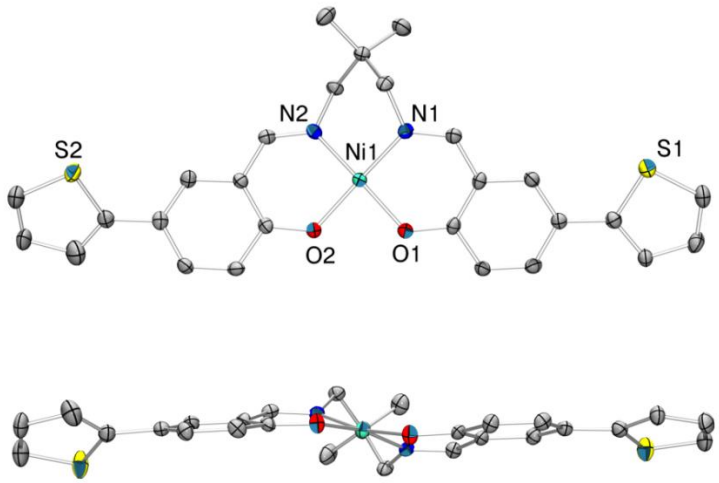

Figure 3.3. Top: ORTEP view of molecule **NiL^{I}**, drawn with the thermal ellipsoids at the 50% probability level. Hydrogen atoms and solvent molecules have been omitted for clarity. Bottom: Side view of the molecule **NiL^{I}**.

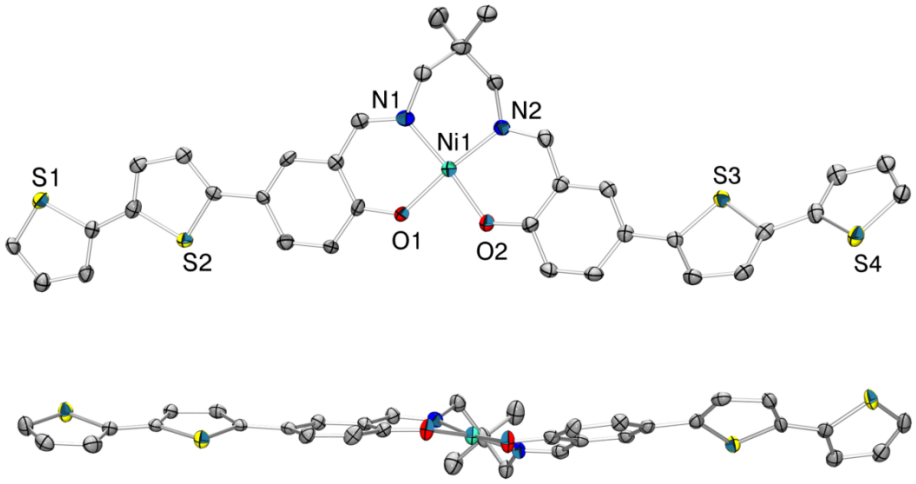

Figure 3.4. Top: ORTEP view of molecule **NiL^{II}**, drawn with the thermal ellipsoids at the 50% probability level. Hydrogen atoms have been omitted for clarity. Bottom: Side view of the molecule **NiL^{II}**.

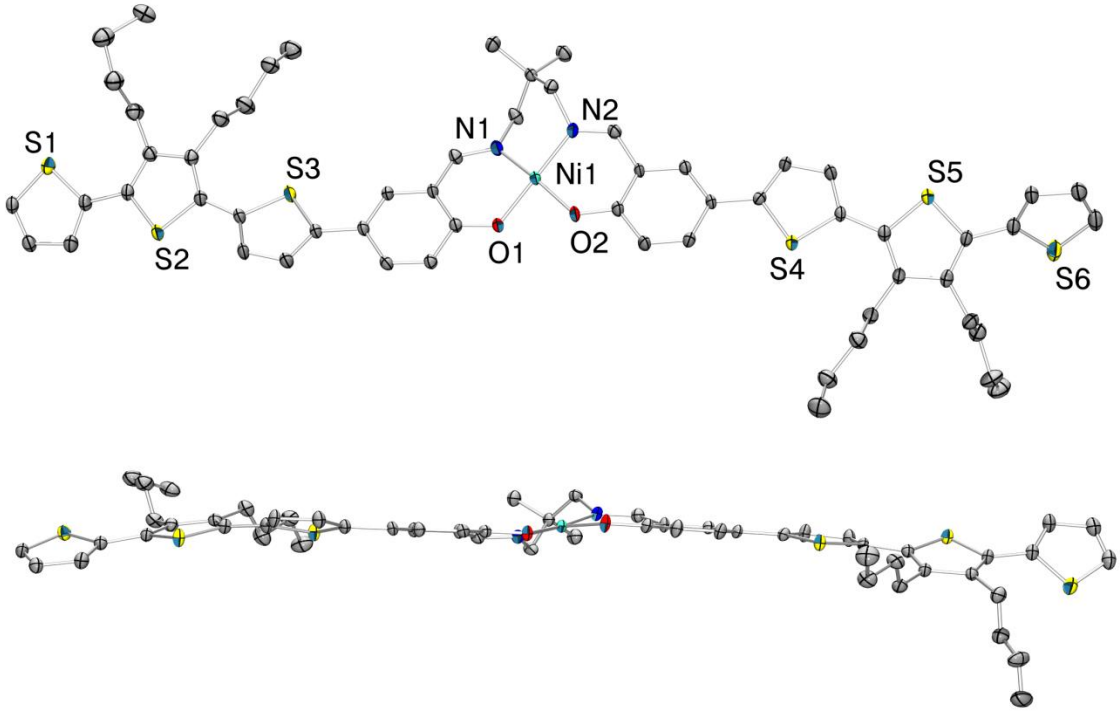

Figure 3.5. Top: ORTEP view of molecule **NiL^{IIIC4}**, drawn with the thermal ellipsoids at the 30% probability level. Hydrogen atoms and solvent molecules have been omitted for clarity. Bottom: Side view of the molecule **NiL^{IIIC4}**.

3.2.2.3. Copper(II) Complexes

X-ray quality crystals of copper(II) complexes were obtained by slow evaporation of DCM/EtOH solutions. The solid-state structure of **CuL^{II}** complex has been reported previously. The geometries around copper(II) centers are also distorted square planar as found in nickel(II) complexes, however, with more distortion (Figure 3.6 and 3.7). The dihedral angle between the two iminophenol rings in **CuL^{I}** and **CuL^{IIIC4}** are 35.03^{o} and 37.34^{o}, respectively. There is a C_2 symmetry through the quaternary carbon in both complexes as seen in ligand **H$_2$L^{IIIC2}**, making the two organic segmens equivalent. The thiophene rings connected to the iminophenol rings twist from these rings at an angle of 23.40^{o} and 31.00^{o} for **CuL^{I}** and **CuL^{IIIC4}**, respectively. Due the presence of *n*-butyl groups on the middle thiophene ring, there is a twist angle of this ring to the inner and terminal thiophene units of 23.40^{o} and 31.00^{o}, respectively.

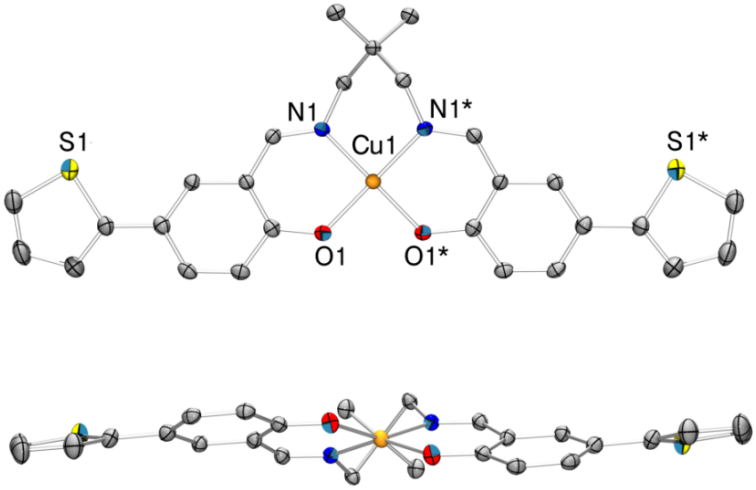

Figure 3.6. Top: ORTEP view of molecule **CuL^{I}**, drawn with the thermal ellipsoids at the 50% probability level. Hydrogen atoms and solvent molecules have been omitted for clarity. Bottom: Side view of the molecule **CuL^{I}**.

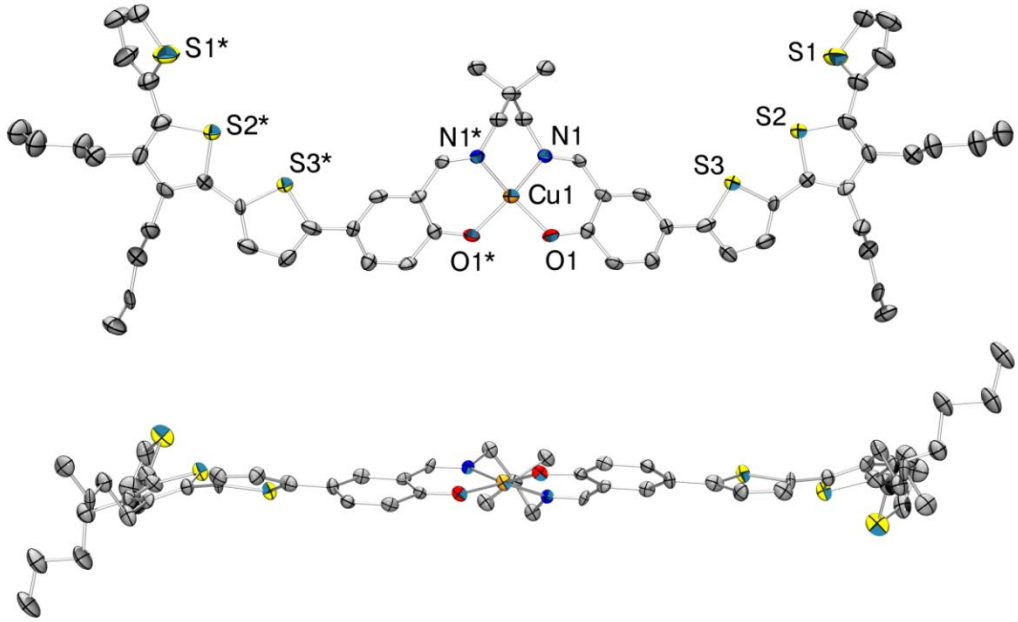

Figure 3.7. Top: ORTEP view of molecule **CuL^{IIIC4}**, drawn with the thermal ellipsoids at the 30% probability level. Hydrogen atoms and solvent molecules have been omitted for clarity. Bottom: Side view of the molecule **CuL^{IIIC4}**.

3.2.2.4. Vanadyl Complexes

Vanadyl complexes crystalize with geometry around the vanadium (IV) center distorted from octahedral by the presence of a solvent molecule, one oxygen atom in the vanadyl ion, and four coordination sites from the salen ligand (Figure 3.8 and 3.9). Depending on the crystallization conditions, the coordinating solvent could be dimethyl sulfoxide (DMSO) as found in **VOL^{I}** or acetonitrile (ACN) in **VOL^{II}** complex. The bond length of V1-O4 bond from the metal center to the oxygen atom of dimethylsulfoxide molecule in **VOL^{I}** is 2.29 Å, which is longer than the 1.96 Å of V-O single bonds with the oxygen atoms of the salen ligand and the V1-O3 double bond with the oxide oxygen. The V-N bond distance from the vanadium(IV) to the N atom of the acetonitrile in **VOL^{II}** is 2.3 Å, slightly longer than normal V-N bond (2.1 Å) with the neutral nitrogen atom in the salen ligand.

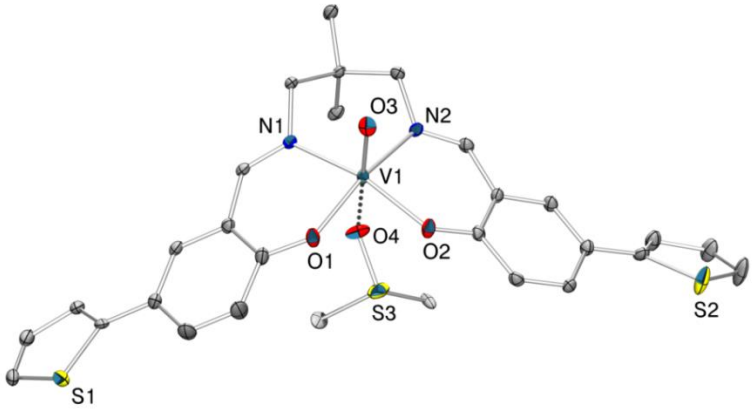

Figure 3.8. ORTEP view of molecule **VOL^{I}** with one DMSO coordinating molecule, drawn with the thermal ellipsoids at the 50% probability level. Hydrogen atoms and other solvent molecules have been omitted for clarity.

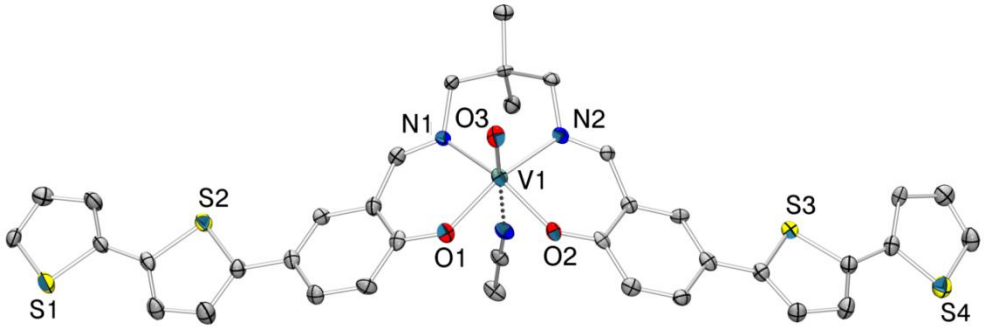

Figure 3.9. ORTEP view of molecule **VOL^{II}** with one ACN coordinating molecule, drawn with the thermal ellipsoids at the 30% probability level. Hydrogen atoms and other solvent molecules have been omitted for clarity.

3.2.2.5. Cobalt(II) Complexes

The structure of **CoL^{I}**, determined by X-ray crystallography, is a trinuclear complex with a metal-to-ligand ratio of 3:2 (Figure 3.10A). The two outer Co(II) ions have a distorted octahedral coordination geometry with the salen ligand occupying the four base coordination sites, one oxygen atom from a bridging acetate occupying one apical site, and one oxygen atom from a dimethylformaldehyde (DMF) solvent molecule

occupying the other apical site (Figure 3.10B). The Co1-O4 bond between the cobalt(II) ion and the oxygen atom in DMF molecule has a distance of 2.22 Å, only slightly longer than 2.02-2.10 Å of Co-O bond with the salen ligand or the bridging acetate. The small differences in these bond lengths make the coordination around Co(II) in **CoL^{I}** less distorted from octahedral geometry than that of V(IV) in **VOL^{I}**.

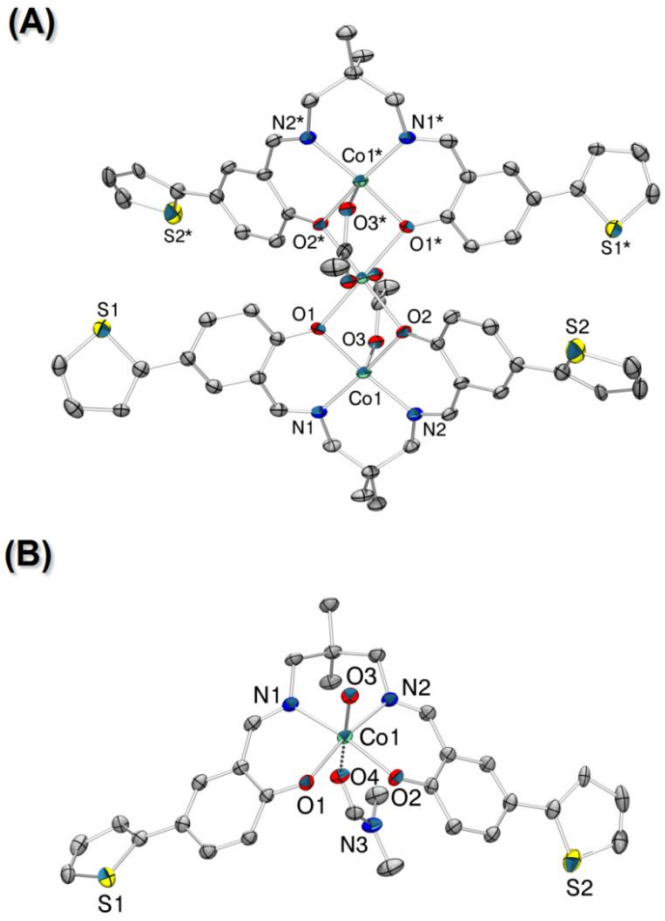

Figure 3.10. (A) ORTEP view of molecule **CoL^{I}**-trinuclear complex, drawn with the thermal ellipsoids at the 50% probability level. Hydrogen atoms and solvent molecules have been omitted for clarity. (B) ORTEP view of one **CoL^{I}** molecule in the **CoL^{I}**-trinuclear complex, showing the coordination around Co(II) ion with one DMF coordinating molecule.

The cobalt(II) complex of $\mathbf{H_2L^{II}}$ ligand ($\mathbf{CoL^{II}}$), on the other hand, forms a dinulear complex with two bridging water molecules to satisfy the 6-coordinate geometry around the metal centers (Figure 3.11). Unlike in $\mathbf{CoL^{I}}$, the salen ligand in $\mathbf{CoL^{II}}$ complex adapts the seesaw geometry and the two monomeric $\mathbf{CoL^{II}}$ molecules are almost parallel to each other. The bond distances between the cobalt(II) and water molecules in 1.91-1.94 Å range and are longer than the bonds of Co(II) to oxygen atoms in the salen ligand (1.89-1.90 Å).

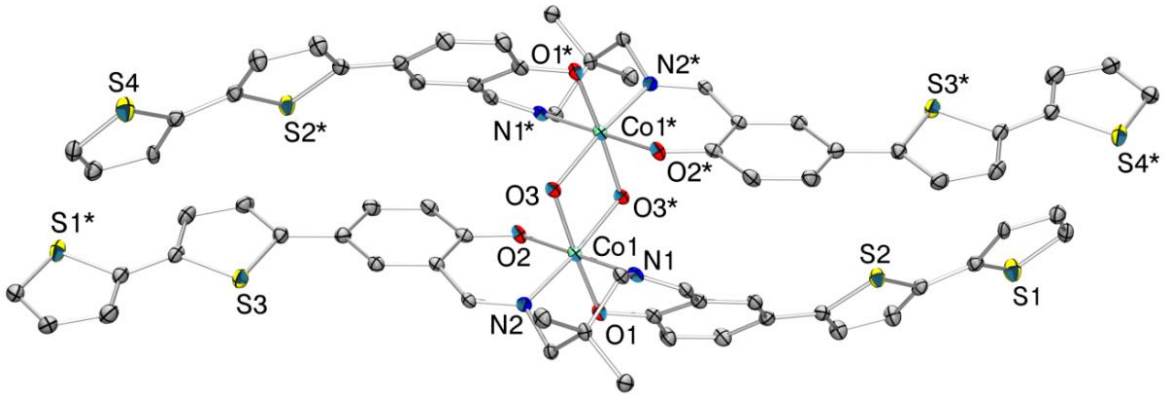

Figure 3.11. ORTEP view of molecule $\mathbf{CoL^{II}}$-dinuclear complex, drawn with the thermal ellipsoids at the 50% probability level. Hydrogen atoms have been omitted for clarity.

3.2.2.6. Zinc Complexes

For $\mathbf{ZnL^{I}}$ compounds, two crystal structures, a monomeric form with one coordinating water molecule and a trinuclear complex, were obtained (Figure 3.12 and 3.13). In $\mathbf{ZnL^{I}}$-monomeric form, the apical coordination site is occupied by a water molecule. The coordination geometry of zinc(II) ion in this complex is distorted square pyramidal, defined by two N atoms and two O atoms of the Schiff-base ligand as the basal plane and by an apical O atom of a water molecule. The zinc atom sits in the body

of the pyramid and 0.379 Å from the basal O1N1O2N2 plane. The bond distance between Zn(II) and oxygen atom of water molecule is 1.99 Å, which is slightly shorter than the bonds between Zn(II) and oxygen atoms in the salen ligand (2.02-2.03 Å).

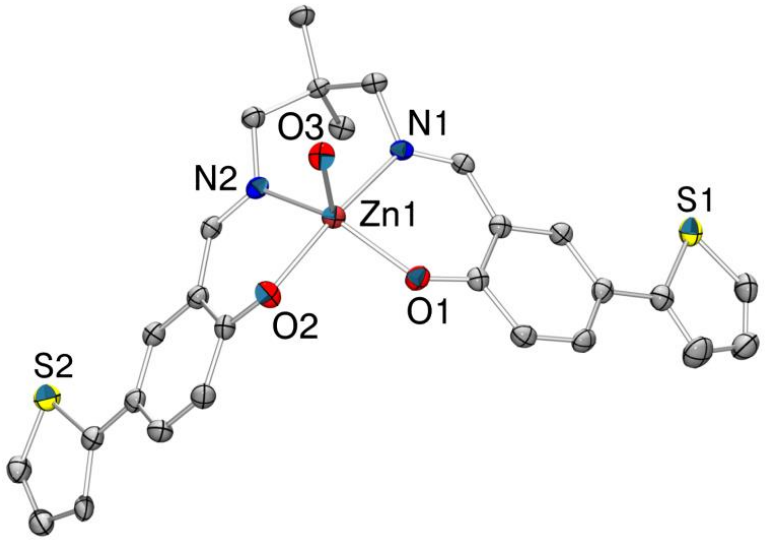

Figure 3.12. ORTEP view of molecule $\mathbf{ZnL^{I}\cdot H_2O}$, drawn with the thermal ellipsoids at the 50% probability level. Hydrogen atoms have been omitted for clarity.

The structure of $\mathbf{ZnL^{I}}$-trinuclear complex is similar to that of $\mathbf{CoL^{I}}$-trinuclear complex with two bridging acetate ligands except that there is no coordinating solvent molecule resulting in a square pyramidal geometry around two outer Zn(II) ions (Figure 3.13). The bond distance of 2.01 Å between Zn(II) ions and the apical oxygen from bridging acetate ligands is also shorter than the Zn-O bonds in the salen centers (2.07-2.11 Å) as found in the monomeric form. The trinuclear structures of $\mathbf{CoL^{I}}$ and $\mathbf{ZnL^{I}}$ are not uncommon for complexes of the two metal with salen-type ligands.[11-15]

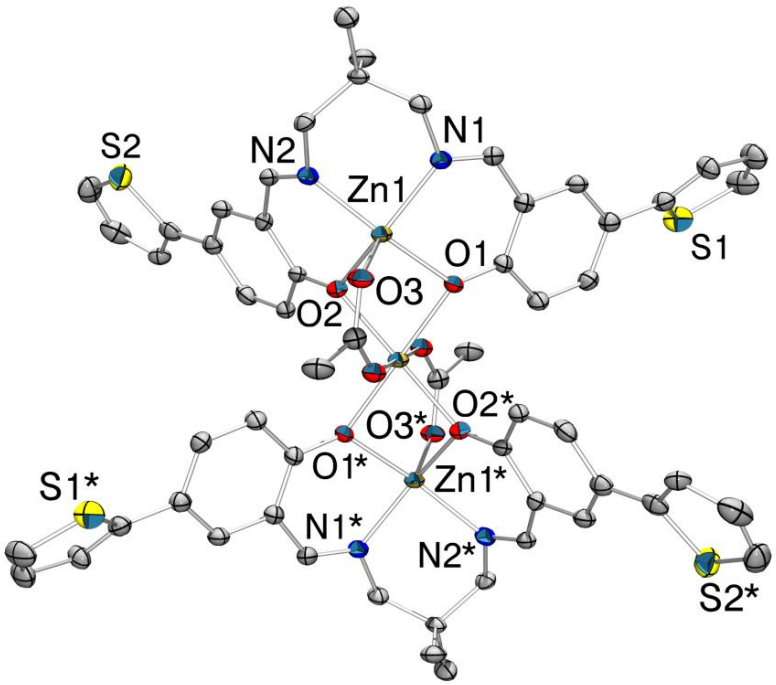

Figure 3.13. ORTEP view of molecule **ZnL^{I}**-trinuclear complex, drawn with the thermal ellipsoids at the 30% probability level. Hydrogen atoms and solvent molecules have been omitted for clarity.

Overall, there are various geometries around the metal centers in Schiff-base complexes of nickel(II), copper(II), vanadium(IV), cobalt(II), and zinc(II) ions. Coordination around nickel(II) and copper(II) is distorted squared planar with 4 coordinate while the geometry around vanadium(IV) and cobalt(II) is octahedral with 6 coordinate. Zinc(II) complexes, on the other hand, adopt a 5-coordinate environment with square pyramidal geometry. The structural information from these metal complexes suggests possible arrangements of those molecules in the metallopolymers upon electropolymerization. Copper(II) and nickel(II) metallopolymers may not have a major structural change upon polymerization while cobalt(II), vanaydyl(II), and zinc(II) polymers may undergo changes to satisfy the metal center coordination during

electropolymerization. A summary of geometries around metal centers and the metal-ligand bond lengths are presented in Figure 3.14 and Table 3.1.

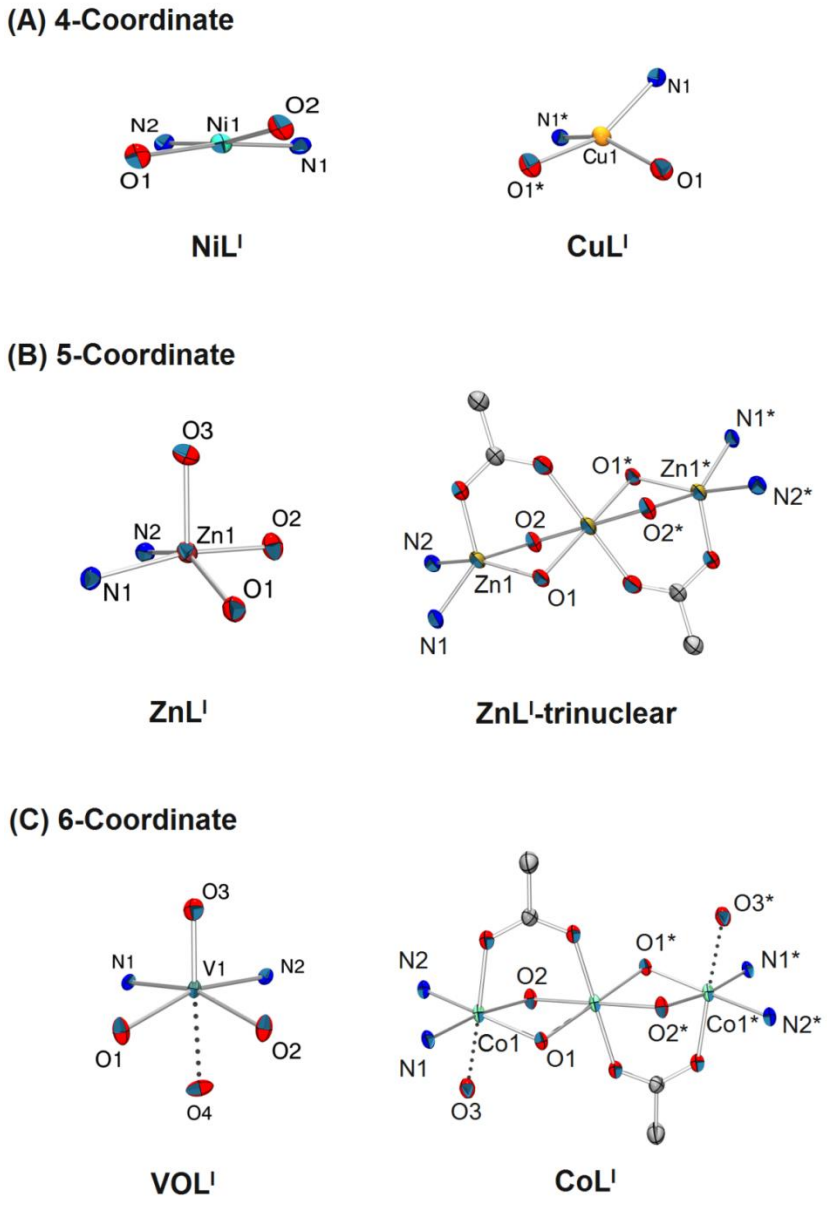

Figure 3.14. Coordination around metal centers in monothiophene series.

Table 3.1. Selected bond lengths and angles of metal complexes with $\mathbf{H_2L^I}$ ligand.

	$\mathbf{NiL^I}$	$\mathbf{CuL^I}$	$\mathbf{VOL^I}$	$\mathbf{CoL^I}$	$\mathbf{ZnL^I}$	$\mathbf{ZnL^I}$-trinuclear
Bond Length (Å)						
M(1)-O(1)	1.864	1.915	1.966	2.019	2.024	2.069
M(1)-O(2)	1.857	1.915	1.964	2.034	2.029	2.111
M(1)-N(1)	1.882	1.961	2.089	2.040	2.093	2.106
M(1)-N(2)	1.878	1.961	2.108	2.060	2.090	2.088
M(1)-O(3)	-	-	1.610	2.098	1.993	2.004
M(1)-O(4)	-	-	2.288	2.222	-	-
Angles (^{o})						
O(1)-M(1)-O(2)	84.67	91.10	85.89	82.89	94.64	80.58
O(1)-M(1)-N(1)	93.06	94.07	88.35	91.63	86.98	89.20
O(1)-M(1)-N(2)	169.70	154.76	163.50	170.84	169.07	156.90
O(2)-M(1)-N(1)	169.10	154.76	162.10	171.83	148.23	147.20
O(2)-M(1)-N(2)	93.30	94.07	89.69	89.02	86.76	87.21
N(1)-M(1)-N(2)	90.80	91.70	91.07	95.93	89.65	90.60

3.2.3. Polymer Syntheses and Characterization

3.2.3.1. Ligand Polymers

Ligand polymers were synthesized *via* electropolymerization onto various electrode surfaces using cyclic voltammetry. The monomer solutions of the ligands in CH_2Cl_2 were oxidatively polymerized by sweeping the potential of the working electrode between -0.75 and 1.25 V versus Fc/Fc^+ at a 100 mV/s scan rate. Typical electropolymerizations of the Schiff-base ligands $\mathbf{H_2L^I}$, $\mathbf{H_2L^{II}}$, $\mathbf{H_2L^{III}}$, and $\mathbf{H_2L^{IIIC4}}$ are shown in Figure 3.15. Interestingly, it was previously reported that Schiff-base ligand monomers with a mono-thiophene substitutent, were not electropolymerizable due to the high redox potential of the organic backbone.[8,16] However, our studies reveal that the growth of ligand polymers is a concentration-dependent process. When varying the concentration of the ligand monomers, we were able to obtain the corresponding

polymers grown onto various electrodes at low concentrations (ca. 10^{-4} M). The effect of concentration on electropolymerization was explained by nucleation and growth mechanisms. The increase in monomer concentrations favors the nucleation under diffusion control and decreases polymer growth rate.[17] To our best knowledge, this is the first time that Schiff-base ligand polymers were successful synthesized, allowing a direct comparison between the properties of metal-free polymers and metallopolymers. Therefore, the role of the metal centers in conducting metallopolymers can be elucidated unambiguously.

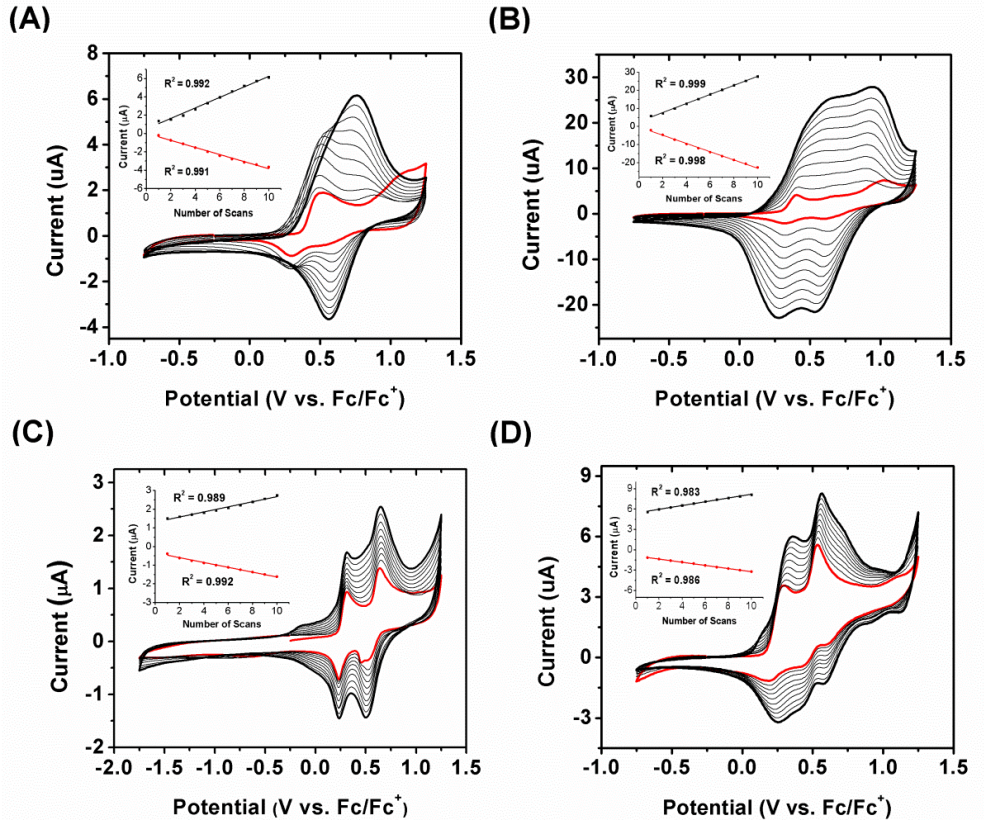

Figure 3.15. Electropolymerization of ligand monomers: (A) $\mathbf{H_2L^{I}}$, (B) $\mathbf{H_2L^{II}}$, (C) $\mathbf{H_2L^{III}}$, and (D) $\mathbf{H_2L^{IIIC4}}$. Insets show the linear relationship between peak polymer oxidation/reduction currents and number of scans.

3.2.3.2. Metallopolymers

Metallopolymers were obtained *via* electropolymerization of corresponding metal complex monomers in a dichloromethane (DCM) solution with 0.1 M tetra(*n*-butyl)ammonium hexafluorophosphate ($TBAPF_6$) as supporting electrolyte. The polymers were grown onto various electrode surfaces, including Pt button electrode, ITO-coated glass and stainless steel, using cyclic voltammetry (CV). Scheme 3.3 shows the electrochemical reactions to form the conducting metallopolymers of the metal complexes containing monothiophenes as electropolymerizable groups (**ML^{I}** series). All the metal complex monomers show a facile polymer growth during electropolymerization, indicated by the linear increase in the polymer oxidation current after each cyclic voltammetry scan. The electrode-confined polymer films were characterized using electrochemical methods, UV-Vis spectroscopy, X-ray photoelectron spectroscopy (XPS), UV-Vis-NIR spectroelectrochemistry, and *in-situ* conductivity measurements.

Scheme 3.3. Electropolymerization of Schiff-base ligand and metal complex monomers in the monothiophene series (**ML^{I}**).

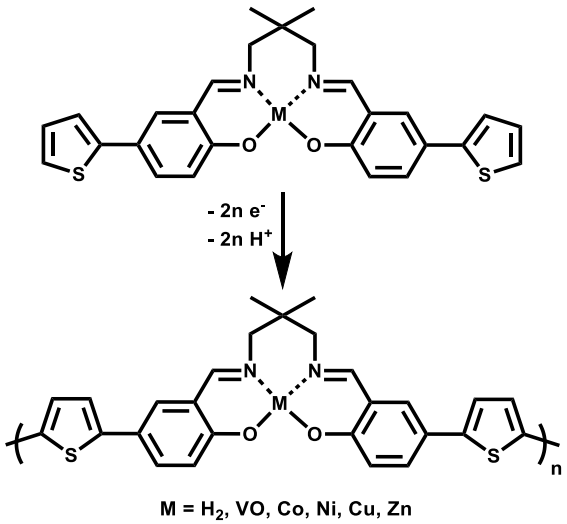

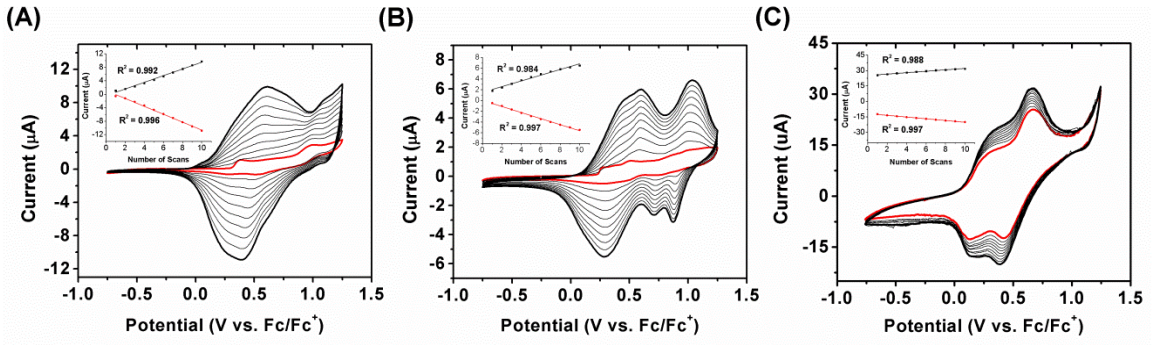

Figure 3.16. Electropolymerization of ligand monomers: (A) **NiL^{I}**, (B) **NiL^{II}**, and (C) **NiL^{IIIC4}**. Insets show the linear relationship between polymer peak oxidation/reduction currents and number of scans.

The presence of metal centers as well as the elemental composition of ligand and metallopolymers were confirmed by XPS analysis. XPS survey scans of ligand polymer and metallopolymers are shown in Figure 3.18. Relative atomic ratio of M : N : S in **ML^{I}** polymer series are listed in Table 3.2, which is in agreement with the theoretical ratios in proposed polymer structures. The absorption coefficient (α) of these polymers was determined from thin films deposited on ITO using eq 1,[18]

$$\alpha = \frac{-10^{-\ln(A)}}{T} \qquad (1)$$

where A is polymer absorbance and T is thickness measured by profilometry. All the metallopolymers show a much higher absorption coefficient than that of the ligand polymer (Table 3.2), which is a favorable characteristic for applications in optoelectronics, such as in photovoltaic devices.

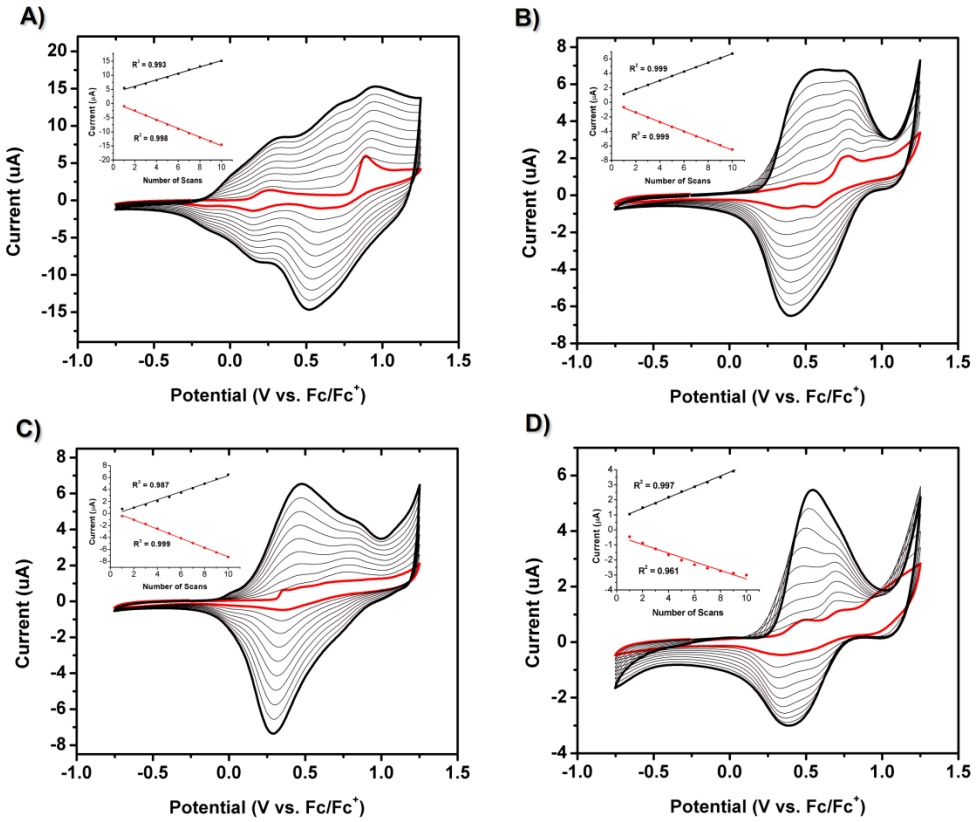

Figure 3.17. Electropolymerization of metal complexes in $\mathbf{ML^I}$ series: (A) $\mathbf{VOL^I}$, (B) $\mathbf{CoL^I}$, (C) $\mathbf{CuL^I}$, and (D) $\mathbf{ZnL^I}$. Insets show the linear relationship between polymer peak oxidation/reduction currents and number of scans.

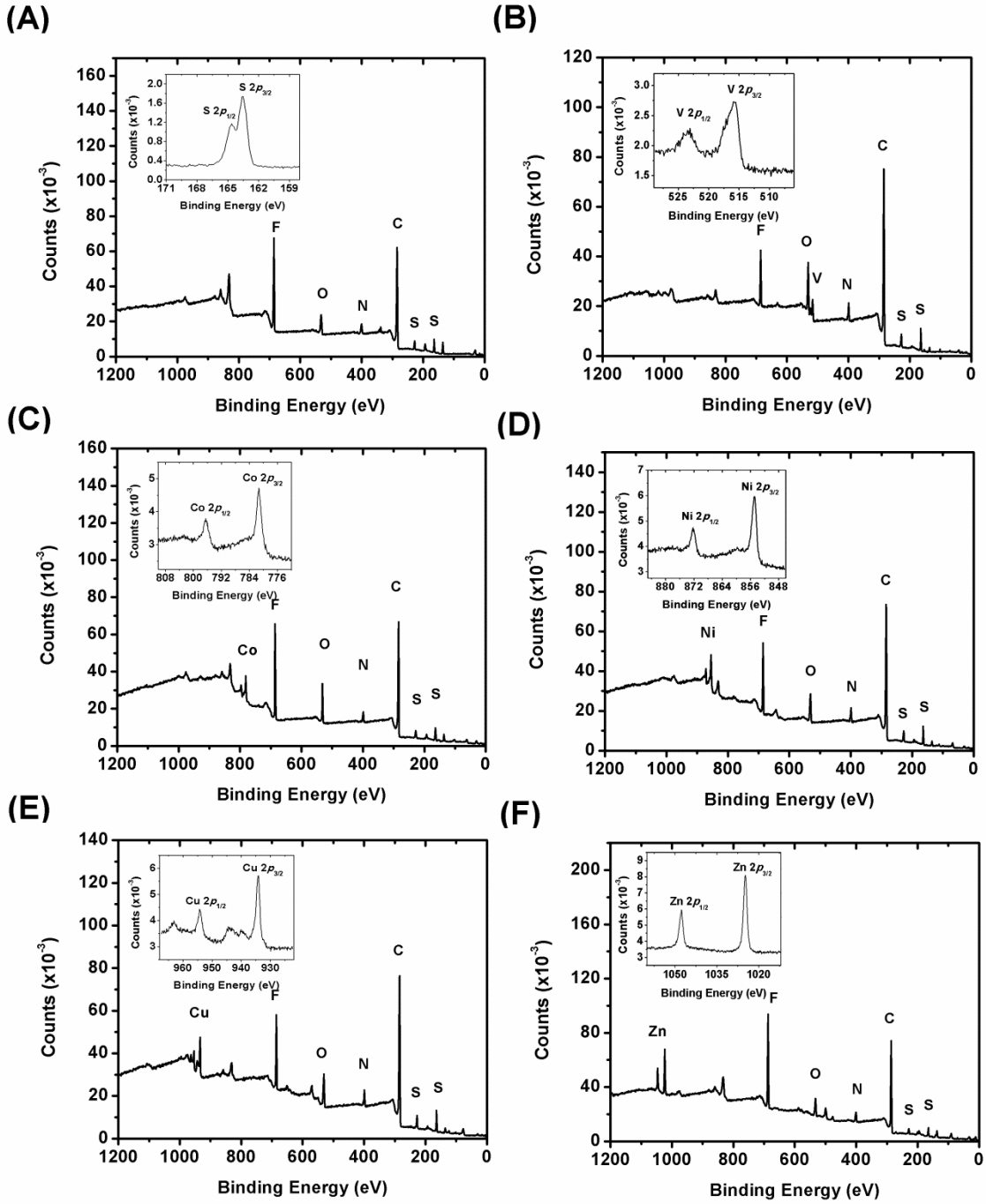

Figure 3.18. XPS survey scans of $\mathbf{ML^I}$ polymers: (A) poly-$\mathbf{H_2L^I}$, (B) poly-$\mathbf{VOL^I}$, (C) poly-$\mathbf{CoL^I}$, (D) poly-$\mathbf{NiL^I}$, (E) poly-$\mathbf{CuL^I}$, and (F) poly-$\mathbf{ZnL^I}$. Inset show the S *2p* peak for poly-$H_2\mathbf{L^I}$ and the metal peak for poly-$\mathbf{ML^I}$s.

Table 3.2. XPS and UV-Vis absorption data for **ML^{I}** polymer series.

polymer	XPS elemental analysis[a]		λ_{max} (nm) (α (cm^{-1}))[d]
	M : N : S ratio[b]	M peaks[c]	
poly-**VOL^{I}**	1.00 : 2.01 : 2.34	516.2 ($2p_{3/2}$)	403
	(1 : 2 : 2)	523.6 ($2p_{1/2}$)	(87400)
poly-**CoL^{I}**	1.00 : 2.26 : 2.18	782.0 ($2p_{3/2}$)	386
	(1 : 2 : 2)	797.2 ($2p_{1/2}$)	(93200)
poly-**NiL^{I}**	1.00 : 2.00 : 2.35	855.4 ($2p_{3/2}$)	401
	(1 : 2 : 2)	872.8 ($2p_{1/2}$)	(24600)
poly-**CuL^{I}**	1.00 : 1.85 : 2.02	934.7 ($2p_{3/2}$)	399
	(1 : 2 : 2)	954.9 ($2p_{1/2}$)	(60100)
poly-**ZnL^{I}**	1.00 : 2.04 : 1.90	1022.6 ($2p_{3/2}$)	384
	(1 : 2 : 2)	1045.4 ($2p_{1/2}$)	(20100)
poly-**H_2L^{I}**	0.00 : 1.00 : 0.91	-	402
	(0 : 1 : 1)	-	(5160)

[a] measured from thin film on ITO. [b] based on the total intergration of metal, nitrogen, and sulfur peaks; calculated values given in parentheses. [c] metal peaks are taken after correcting the C 1*s* peak to 284.8 eV. [d] absorption coefficient (α) was calculated from eq 1.

Metal complexes containing bithiophene and terthiophene as electropolymerizable groups also exhibit facile polymer growth upon electropolymerization. The resulting conducting metallopolymers exhibit consistent elemental composition when compared to the proposed structures as analyzed by quantitative XPS (Table 3.3).

Table 3.3. XPS data for **ML^{II}** and **ML^{IIIC4}** polymer series.

polymer	XPS elemental analysis[a]	
	M : N : S ratio[b]	M peaks[c]
poly-**VOL^{II}**	1.00 : 2.01 : 2.34	516.2 ($2p_{3/2}$)
	(1 : 2 : 2)	523.6 ($2p_{1/2}$)
poly-**CoL^{II}**	1.00 : 2.26 : 2.18	782.0 ($2p_{3/2}$)
	(1 : 2 : 2)	797.2 ($2p_{1/2}$)
poly-**NiL^{II}**	1.00 : 2.00 : 2.35	855.4 ($2p_{3/2}$)
	(1 : 2 : 2)	872.8 ($2p_{1/2}$)
poly-**CuL^{II}**	1.00 : 1.85 : 2.02	934.7 ($2p_{3/2}$)
	(1 : 2 : 2)	954.9 ($2p_{1/2}$)
poly-**VOL^{IIIC4}**	1.00 : 2.01 : 2.34	516.2 ($2p_{3/2}$)
	(1 : 2 : 2)	523.6 ($2p_{1/2}$)
poly-**CoL^{IIIC4}**	1.00 : 2.26 : 2.18	782.0 ($2p_{3/2}$)
	(1 : 2 : 2)	797.2 ($2p_{1/2}$)
poly-**NiL^{IIIC4}**	1.00 : 2.00 : 2.35	855.4 ($2p_{3/2}$)
	(1 : 2 : 2)	872.8 ($2p_{1/2}$)
poly-**CuL^{IIIC4}**	1.00 : 1.85 : 2.02	934.7 ($2p_{3/2}$)
	(1 : 2 : 2)	954.9 ($2p_{1/2}$)

[a] measured from thin film on ITO. [b] based on the total intergration of metal, nitrogen, and sulfur peaks; calculated values given in parentheses. [c] metal peaks are taken after correcting the C 1*s* peak to 284.8 eV.

3.2.4. Effect of Organic Backbone on Charge Delocalization and Charge Transport

3.2.4.1. Effects of Conjugated Backbone on Redox Conductivity

The charge transport properties of ligand polymers were studied by electrochemical scan-rate dependence and *in-situ* conductivity. CV studies of the three ligand polymers in pure electrolyte solution at different scan rates from 10 to 500 mV/s revealed a linear relationship of observed current with the scan rate (Figure 3.19). This

linear dependence is a characteristic observation of a strongly absorbed electroactive film in which electric current is not limited by the diffusion of counter ions and gives initial indications of the conductivity behavior of these polymers. By increasing the number of thiophene units in the ligand polymers, there is also an increase in the linearity of oxidative and reductive current versus scan rate curves revealing an increase in electroactivity of the polymer films.

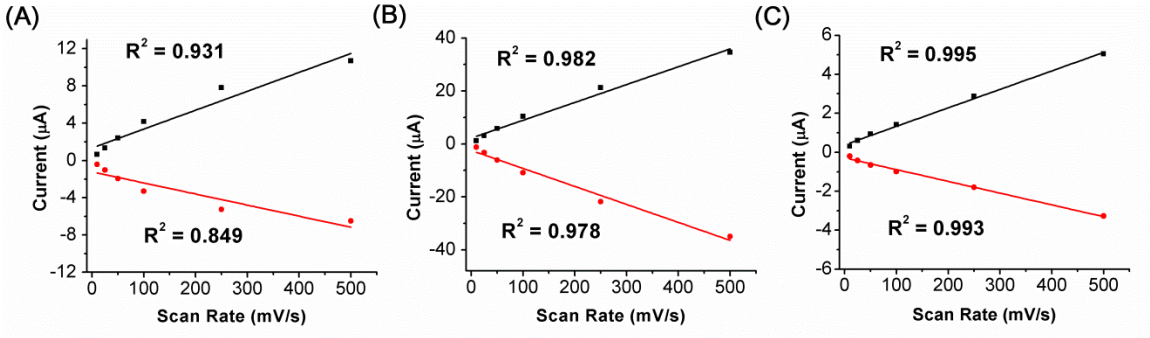

Figure 3.19. Linear relationships of oxidative (black) and reductive (red) peak current versus scan rate of ligand polymers in 0.1 M $TBAPF_6/CH_2Cl_2$ electrolyte solution. (A) $\mathbf{H_2L^I}$, (B) $\mathbf{H_2L^{II}}$, and (C) $\mathbf{H_2L^{III}}$.

The absolute conductivity of the polymers was then determined by *in-situ* conductivity using 10 μm Pt interdigitated electrode arrays (IDA). The method was first described by Wrighton and co-workers[19] to measure the conductivity of polypyrole and was then employed widely to determine the redox conductivity of conducting polymers such as polyanilines or polythiophenes by Murray[20-23] and Swager.[24-31] The basic principle of this measurement is based on the conductivity definition: when an electric field is applied inside one material, it will cause an electric current to flow. Conductivity (σ), which is the inverse of resistivity (ρ), is defined as the ratio of current density (J) to the applied electric field (E).

$$\sigma = 1/\rho = J/E \qquad (2)$$

In the redox conductivity measurement using an interdigitated array electrode (IDA), a conducting polymer was deposited on and in between the fingers of the two electrode arrays. CVs were then taken with a small offset potential (V_d) between the two electrode arrays. The magnitude of V_d is usually small (40 mV in our experiments) to ensure a linear function of the induced current by this voltage. The value of E in eq 2 is then determined as the voltage offset (V_d) divided by the distance (D) between the two arrays of electrode. The currents measured in the CVs, I_d, obtained from two electrode arrays is comprised of two components: the CV of the polymer and the current flowing between the two electrode arrays caused by the offset potential. In most cases, the later current, which reflects the conductivity of the polymer at certain doping states, is much higher than the current from the CV of the polymer. By approximation, the drain current I_d could be used to calculate the redox conductivity.[19,32] The current density is calculated from equation 3,

$$J = I_d/n \cdot L \cdot T \qquad (3)$$

where the denominator is the total cross-sectional area of polymer between two electrode arrays calculated from the area of one single cross-sectional gap determined by the multiplication of polymer thickness, T, to the length of one finger, and the total number of gaps, n, created by the two sets of electrodes. The redox conductivity is obtained by combining eq. 2 and eq. 3

$$\sigma = \frac{i_D}{V_D} \times \frac{D}{n \cdot T \cdot L} \qquad (4)$$

The results of *in-situ* conductivity of ligand polymers are listed in Table 3.4 . A plot of CV and *in-situ* conductivity versus applied potentials of poly- $\mathbf{H_2L^{III}}$ is shown in Figure 20A. As observed in other thiophene Schiff-base ligand polymers, the only

conductivity peak occurs with the formation of polarons on the oligothiophene backbone at 0.79 V vs Fc/Fc^{+}. A comparison in conductivity value of the ligand polymers with different conjugation length is shown in Figure 20B. As the conjugation length is increased, the conductivity increases over one order of magnitude from 0.1 mS/cm for poly- $\mathbf{H_2L^{I}}$ to 1.5 mS/cm for poly-$\mathbf{H_2L^{II}}$. The further increase in thiophene length increases the conductivity to 10.3 mS/cm for poly- $\mathbf{H_2L^{III}}$. This increase is less sensitive than the growth value that occurs when changing from one to two thiophene units in ligand monomers, but it is still significant. The results suggest that when the conjugation length of the thiophene backbone increases, the charge transport in the polymers becomes much more effective, indicating the role of charge delocalization and intra-chain interaction.

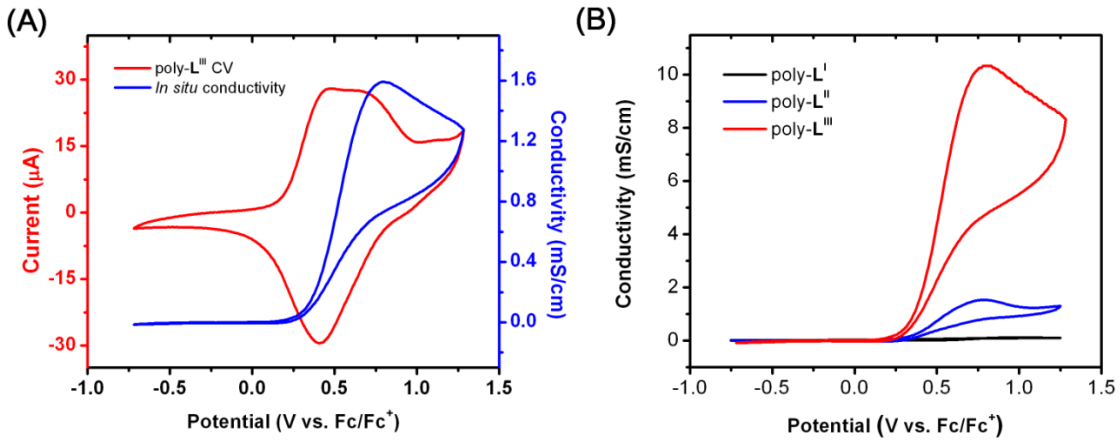

Figure 3.20. (A) Cyclic voltammetry (red) conductivity profile (blue) of poly- $\mathbf{H_2L^{II}}$. (B) Comparison of *in-situ* conductivity of ligand polymers with various conjugation length.

Table 3.4. Electrochemical and conductivity data of ligand polymers.

polymer	Cyclic voltammetry		Conductivity	
	$E_{p,a}$ (V)	$E_{p,c}$ (V)	E_{max} (V)	σ (mS/cm)
poly-$\mathbf{H_2L^I}$	0.56 0.97	0.32 0.61	0.94	0.11
poly-$\mathbf{H_2L^{II}}$	0.63 0.89	0.56 0.27	0.79	1.5
poly-$\mathbf{H_2L^{III}}$	0.46 0.67	0.41	0.79	10.3
poly-$\mathbf{H_2L^{IIIC4}}$	0.39 0.69	0.29 0.56	0.72	5.0

3.2.4.2. Effects of Conjugated Backbone on Charge Delocalization

We then investigated the charge delocalization of ligand polymers using UV-Vis-NIR spectroelectrochemistry. Polymer films were grown on ITO-coated glass and gradually oxidized by applying step potentials between -0.2 and 1.2 V vs. Fc/Fc^+. UV-Vis-NIR spectroscopy was then taken at each potential. The formation of polarons (radical cations) and bipolarons (dications) shown in the electronic absorption spectra provides information about charge delocalization in these polymers. Due to the low solubility of $\mathbf{H_2L^{III}}$, a sufficiently thick polymer film from this monomer could not be obtained for spectroelectrochemical study. Therefore, an analog of this polymer, poly-$\mathbf{H_2L^{IIIC4}}$, which contains the same number of thiophene units, was used to study the charge delocalization in the terthiophene series. Charge-transport properties of this alternative polymer may vary when compared to poly-$\mathbf{H_2L^{III}}$, however, the electronic features of the backbone should not have any major changes due to the same conjugation length. Figure 3.21 shows a 3D plot of different spectroelectrochemical spectra of the three polymer systems with various thiophene chains. Upon being gradually oxidized,

ligand polymers exhibit significant changes in their UV-Vis-NIR spectra. New absorption bands for polarons are found at 867, 1099, and 1307 nm for poly-$\mathbf{H_2L^I}$, poly-$\mathbf{H_2L^{II}}$, and poly-$\mathbf{H_2L^{IIIC4}}$, respectively. When further increasing the applied potential, bipolaron bands start to appear with maximum peak at 765, 951, and 1205 nm, respectively. Linear relationships between the polaron and bipolaron wavelength versus the number of thiophene units are found for those polymers (Figure 3.22). Spectroelectrochemical data show the correlation between charge delocalization and charge transport. By increasing the conjugation length, the conductivity of polymer increases dramatically.

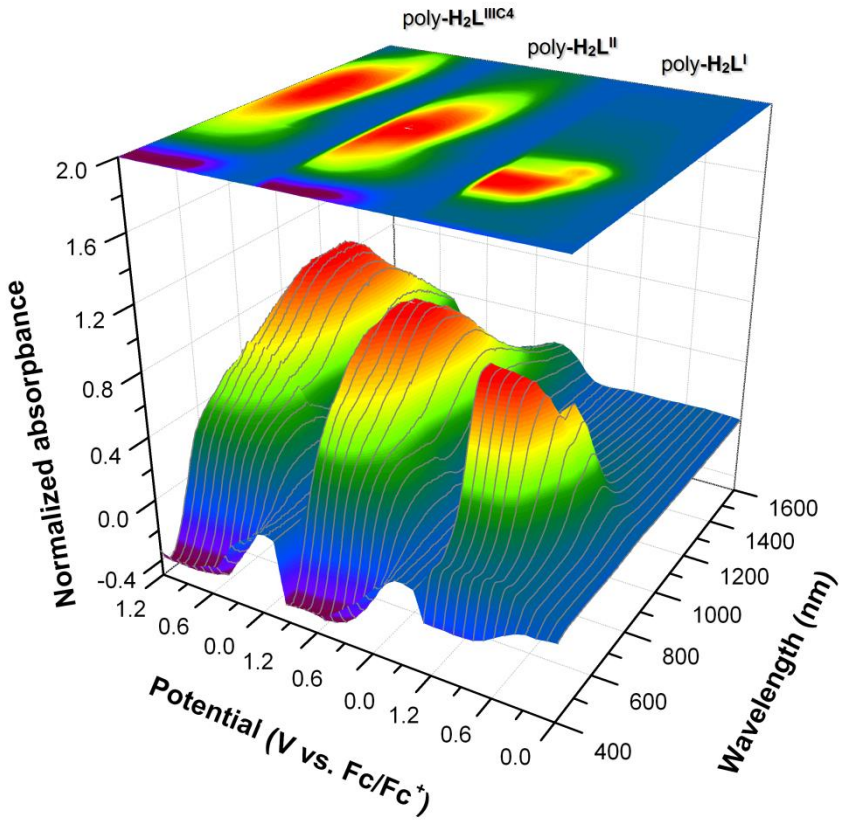

Figure 3.21. Different spectroelectrochemical spectra of poly-$\mathbf{H_2L^I}$, poly- $\mathbf{H_2L^{II}}$, and poly- $\mathbf{H_2L^{IIIC4}}$ on ITO-coated glass in 0.1 M $TBAPF_6$/DCM solution with applied potential between -02 and 1.2 V vs Fc/Fc^+.

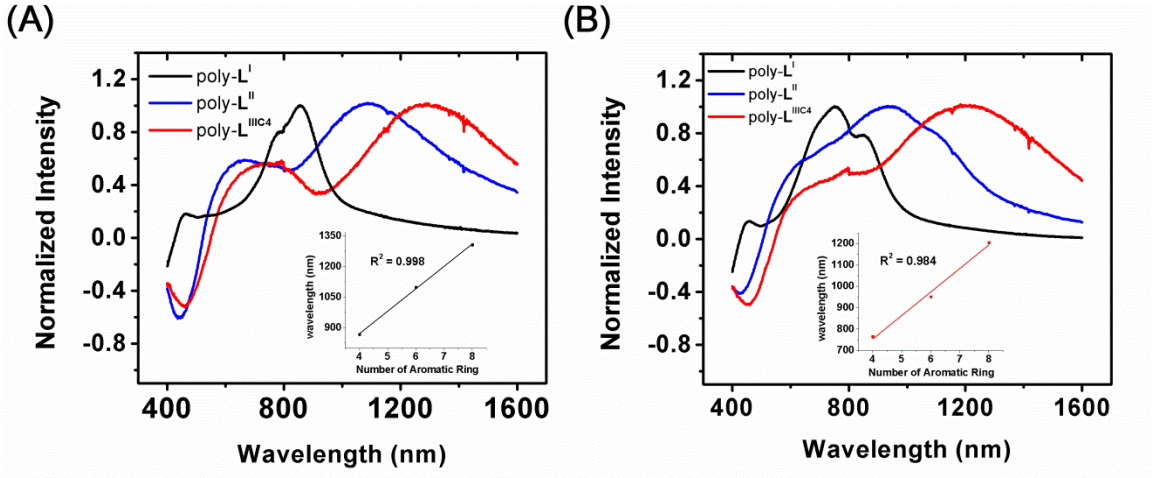

Figure 3.22. Different spectroelectrochemical spectra of poly-$\mathbf{H_2L^I}$, poly- $\mathbf{H_2L^{II}}$, and poly- $\mathbf{H_2L^{IIIC4}}$ showing absorption of polarons (A) and bipolarons (B) bands. Insets show the linear relationships between the wavelength at absorption maximum and the number of repeated aromatic rings in the three polymers.

3.2.5. Role of Metal Centers in Charge Delocalization and Transport of CMPs

3.2.5.1. Effects of Metal Centers to Redox Conductivity of CMPs

The electrochemical properties of the metallopolymers were investigated by cyclic voltammetry (CV). The CVs of poly-$\mathbf{NiL^I}$ in both DCM and ACN electrolyte solutions are shown in Figure 3.23. The CV taken in ACN seems to have more defined features than the one taken in DCM. A broad featureless peak at 0.52 V and a current increasing with no distinguished peak in the 1.00-1.25 V region were found in the CV of poly-$\mathbf{NiL^I}$ taken in DCM. The reversed scan gave three reductive events at 1.10, 0.50, and 0.29 V, which indicates that there should be three different electrochemical processes in the oxidative scan but there were not sufficiently defined. Cyclic voltammetry study of poly-$\mathbf{NiL^I}$ in ACN electrolyte helps to reveal more aspects of the electrochemical processes upon oxidizing this polymer. Three distinctive peaks are found in both oxidative and reductive scans. This could be due to the stabilization of oxidized species

by the high dielectric ACN solvent or the coordinating nature of ACN. From this observation, we have studied the CVs of ligand polymer and other metal complex polymers in ACN electrolyte and the results are summarized in Table 3.5.

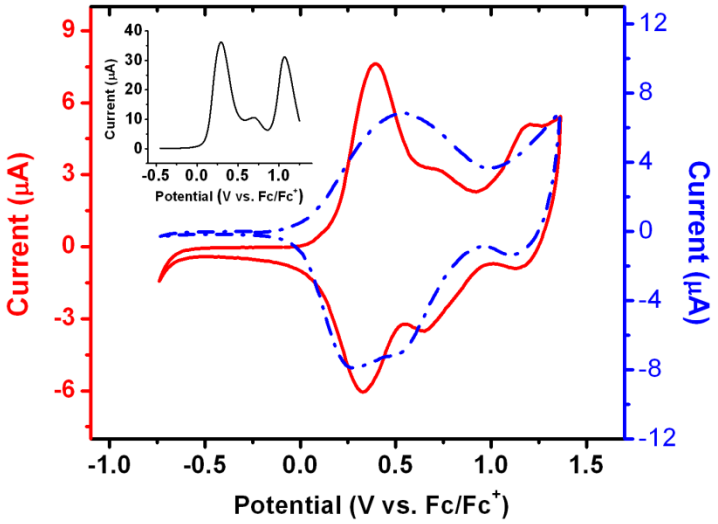

Figure 3.23. CVs of poly-**NiL**$^{\mathbf{I}}$ taken in ACN (solid, red) and in DCM (dotted, blue) with polymer film grown from 10 mM solution in DCM; scan rate = 50 mV/s. Inset shows differential pulse voltammogram of the same film in ACN electrolyte.

Cyclic voltammogram of the corresponding ligand polymer (poly-**L**$^{\mathbf{I}}$) in ACN shows two quasi-reversible oxidative peaks at 0.47 and 0.77 V, Figure 3.24A. We assign the first peak at 0.47 V to the formation of phenoxyl radical on the salen ligand, while the other peak at 0.77 V is assigned as the oxidation of the thiophene backbone to form radical cations or polarons. These two processes are observed in all corresponding metal complex polymers but at lower potentials for the first event except in poly-**CuL**$^{\mathbf{I}}$. The second electrochemical process occurs at about the same potential ca. 0.7 V for all polymers, an indication of little effect of the metal centers on the oxidation of thiophene backbone. A small but noticeable shoulder in 1.05-1.20 V range was observed in the CVs

of all polymers, which seems to belong to the formation of bipolarons on the thiophene backbone. Interestingly, a distinctive peak was found at 1.19 V in the CV of poly-**NiL^{I}**. The CVs in both DCM and ACN seem to reveal a one electron process for this wave. However, the differential pulse voltammetry (Figure 3.23) shows a 2 : 1 : 2 ratio of the 3 peaks at 0.39, 0.69, and 1.19, respectively, which indicates that there are probably more than one electron process at the 1.19 V wave. In conjunction with the conductivity studies, we assign this wave as the combination of the $Ni^{2+/3+}$ redox process and the formation of bipolarons on the thiophene backbone with major contribution from the former event.

Table 3.5. Electrochemical and conductivity data.

polymer	Cyclic voltammetry[a]		Conductivity[b]	
	$E_{p,a}$ (V)	$E_{p,c}$ (V)	E_{max} (V)	σ (mS/cm)
poly-**VOL^{I}**	0.29	0.22		6.7
	0.77	0.65	0.50	
poly-**CoL^{I}**	0.57	0.42		1.1
	0.67	0.59	0.77	
poly-**NiL^{I}**	0.39	0.33		
	0.69	0.65	0.57	27.0
	1.19	1.11	1.12	
poly-**CuL^{I}**	0.48	0.3	0.34	11.2
	0.65	0.62		
poly-**ZnL^{I}**	0.49	0.37	0.73	0.28
	0.69	0.58		
poly-**H_2L^{I}**	0.47	0.33	0.94	0.11
	0.77	0.65		

[a] Volts vs. Fc/Fc^{+}, Pt working electrode, ACN electrolyte. [b] E_{max} is potential at maximum conductivity. All conductivity is corrected to poly-(3-methylthiophene) which has a known value of 60 S/cm.[33]

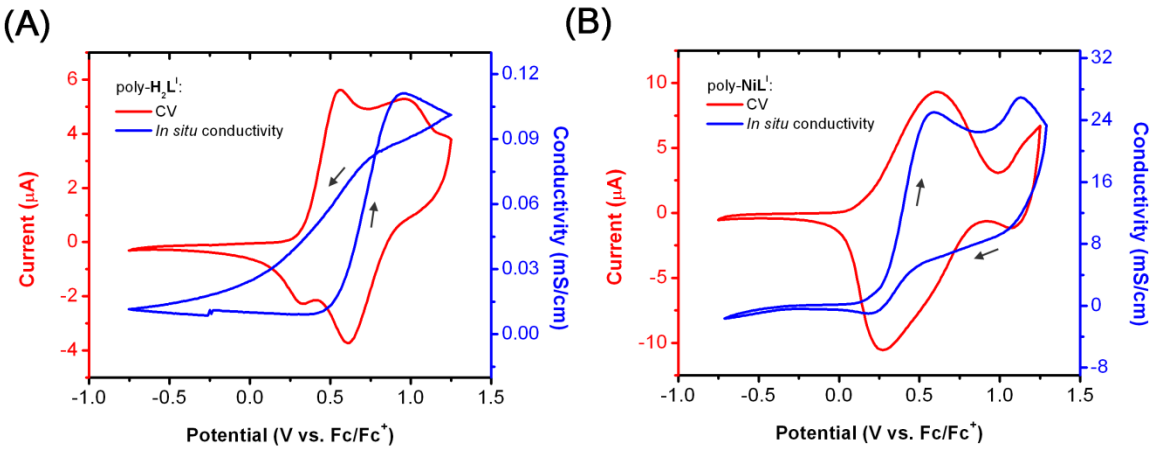

Figure 3.24. Cylic voltammetry (red) and *in-situ* conductivity profile (blue) of ligand polymer, poly-$\mathbf{H_2L^I}$ (A) and nickel complex polymer, poly-$\mathbf{NiL^I}$, in 0.1 M *n*-Bu_4NPF_6/CH_2Cl_2 solutions.

The electron transport of metallopolymers was studied by *in-situ* conductivity, and the results for poly-$\mathbf{ML^I}$ polymer series are summarized in Table 3.5. All polymers except poly-$\mathbf{NiL^I}$ have only one peak in the conductivity profile. This peak corresponds to the potential for the formation of polarons on the thiophene backbone. There are two peaks in the conductivity profile of poly-$\mathbf{NiL^I}$, appearing at the second and the third oxidative events in its CV (Figure 3.24B). The second peak in conductivity profile of poly-$\mathbf{NiL^I}$ is assigned to the redox event of $Ni^{2+/3+}$, which creates a mix-valence state of the metal center and electron transfer between two states causes the redox conductivity activity.

There are two processes which determine the conductivity of the ligand polymers and metallopolymers: the inter-chain and the intra-chain charge transport manners. Kingsborogh *et al.* observed that increasing the sterics of the metallopolymer backbone of copper(II) Schiff-base CMPs leads to the decrease of *in-situ* conductivity in these polymers due to the inter-chain interaction.[34] In this study, we utilized the same organic

backbone to prepare ligand and metallopolymers so that the inter-chain interaction could be minimized when comparing the relative conductivities. However, the inter-chain interactions need to be taken into account when polymer conformation varies in order to satisfy the coordination around metal centers, which will be discussed later. During the latter charge transport process, the intra-chain electron transfer, charge carriers migrate along the polymer chain and are affected by polymer conjugation and the interaction between metal centers and the conjugated organic backbone. This process reflects the behavior of metal centers and therefore reflective of the role of metal center in CMPs.

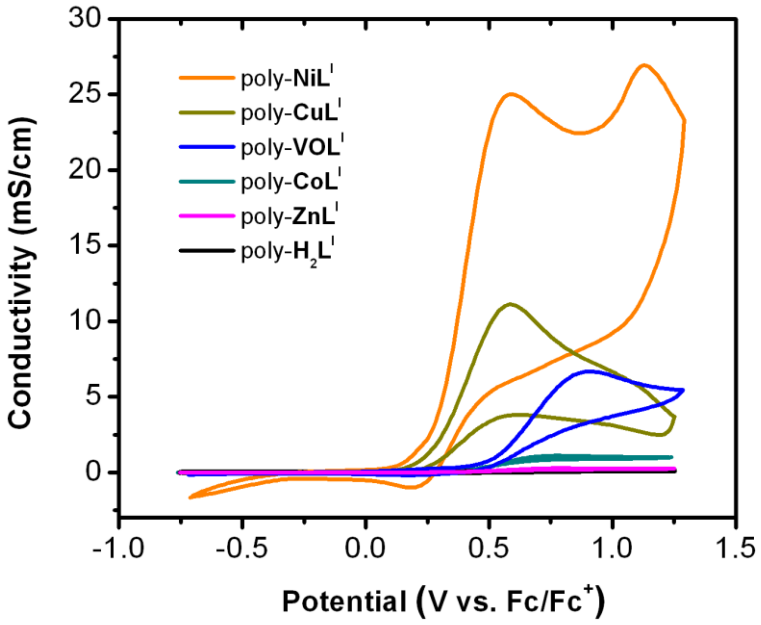

Figure 3.25. Conductivity profiles of ligand and metallo-polymers in DCM electrolyte. Scan rate 10 mV/s, 40 mV offset potential.

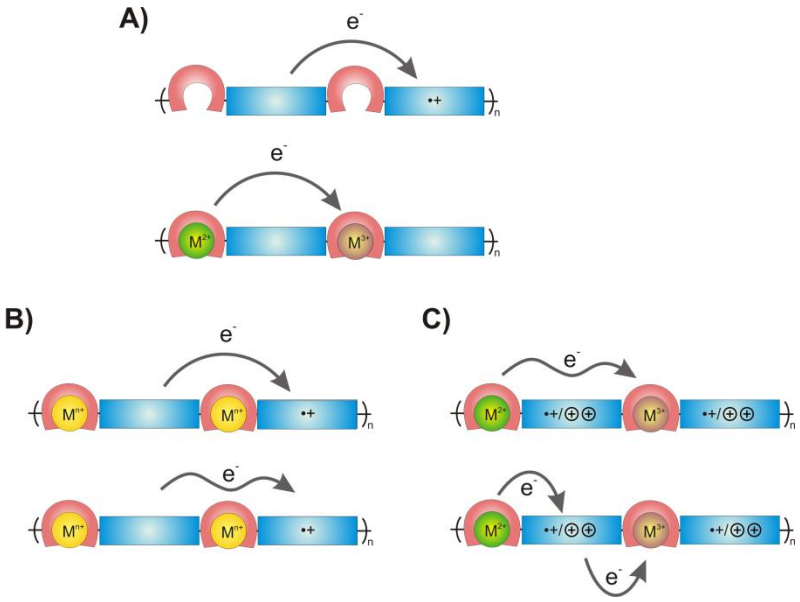

Figure 3.26. Mechanisms of intra-chain electron transfer in Wolf type II CMPs: A) charge transfer *via* hopping over insulated segments in ligand polymer and CMPs that have metal redox potential lower than that of the organic backbone; B) electron transfer in CMP with redox-inactive metals *via* hopping and super-exchange mechanisms; C) electron transfer *via* super-exchange and hopping between mix-valence states of metal centers with higher redox potential than that of the organic backbone.

The much higher conductivity of the metallopolymers in poly-**ML**$^{\mathbf{I}}$ series compare to the ligand polymer (poly-**H$_2$L**$^{\mathbf{I}}$) indicates the role of metal centers to the overall conductivity of CMPs (Figure 3.25). Based on the maxima of conductivity, these metallopolymers could be divided into three categories. Category I, including poly-**CoL**$^{\mathbf{I}}$ and poly-**ZnL**$^{\mathbf{I}}$, has conductivity of one order of magnitude higher than that of poly-**H$_2$L**$^{\mathbf{I}}$. Category II consist of poly-**CuL**$^{\mathbf{I}}$ and poly-**VOL**$^{\mathbf{I}}$ and has conductivity of two orders of magnitude higher that of ligand polymer. The last category, which only consists of poly-**NiL**$^{\mathbf{I}}$, shows the highest conductivity of about 3-fold higher than those in category II.

Base on the conductivity results, we have proposed the mechanism for electron transfer in the ligand polymer and metallopolymers (Figure 3.26). In the ligand polymer,

the only possible mean for electron transfer is the hopping of charge carriers from one conjugated segment to another over an insulated ligand binding site (Figure 3.26A). A less effective electron transfer and lower conductivity of the polymer results from an increased distance for the electron hop. This effect is more obvious in the conductivity profile of CMPs with redox potential of the metal center lower than that of organic backbone. There is no metal-based redox conductivity event found in these CMPs due to the long undoped insulated segments of organic backbone.

Metallopolymers that have only one peak in their *in-situ* conductivity contain either redox-inactive metal centers (Cu^{2+} and Zn^{2+}) or redox-active metals (Co^{2+} and VO^{2+}) with no redox matching to the redox potential of organic backbone.[5] The intra-chain charge transport in these CMPs follows the mechanism described in Figure 3.26B through electron hopping between organic segments as in ligand polymer and through super-exchange over the metal centers, which may have hyper-valent states.[35] In poly-**NiL^{I}**, the first conductivity peak is assigned to organic backbone oxidation as in other CMPs. This polymer, however, shows an additional conductivity peak at the metal-based redox potential. At this state, organic backbone is doped and could acts as a hopping station for charge transport between two metal centers (Figure 3.26C). The low conductivity of poly-**CoL^{I}** and poly-**ZnL^{I}** could also be due to the tendency of those two complexes to form a trinuclear complex as shown in the corresponding crystal structures to satisfy the coordination around the metal center, which may prevent an interchain interaction.

Higher conductivity in poly-**CuL^{I}** and poly-**VOL^{I}** in category II may result from the inter-chain interaction due to the planar molecular forms of monomers. Poly-**NiL^{I}**, in the other hand, has both strong inter-chain interaction and intra-chain charge transport due to the redox of $Ni^{2+/3+}$ event and possesses the highest conductivity among the series.

3.2.5.2. Contribution of Metal to Conjugation of CMPs

To further understand the electronic states of the ligand polymers upon oxidation, spectroelectrochemical analysis was conducted by doping the polymers to a certain state while taking the UV-Vis-NIR spectrum at that state. Figure 3.27 shows the spectroelectrochemical data of poly-$\mathbf{H_2L^I}$ and $\mathbf{ML^I}$s in 400-1200 nm region. Upon oxidation of poly-$\mathbf{H_2L^I}$, two peaks at 630 nm and 856 nm grow in and blue shifted at higher potential (Figure 3.27A). These two peaks are expected for the formation of radical cations on the thiophene backbone. The phenoxyl radical of the salen ligand is not expected to have an active transition in the 400-800 window.[36-39] Further oxidation of the polymer resulted in a new peak growing in at 770 nm and a decrease of the two peaks at 630 and 856 nm. The increase of the 770 nm band and the continuous decreasing of 856 nm band support the conversion of polarons to bipolarons.

In the spectroelctrochemical spectra of poly-$\mathbf{ZnL^I}$, shown in Figure 3.27F, polaron and bipolaron bands are red-shifted around 20 nm for both cases giving 877 and 795 nm peaks for polaron and bipolaron bands, respectively. The red-shifting in both bands reveals a contribution of metal centers to the overall conjugation of the polymer. These bands shift even more significantly in other CMPs (Figure 3.27B-E). However, since these are overlapping, they could not be distinguished from each other. For comparison, we use the well-defined bipolaron band at high potential, ca.1.2 V, for all polymers in the poly-$\mathbf{ML^I}$ series.

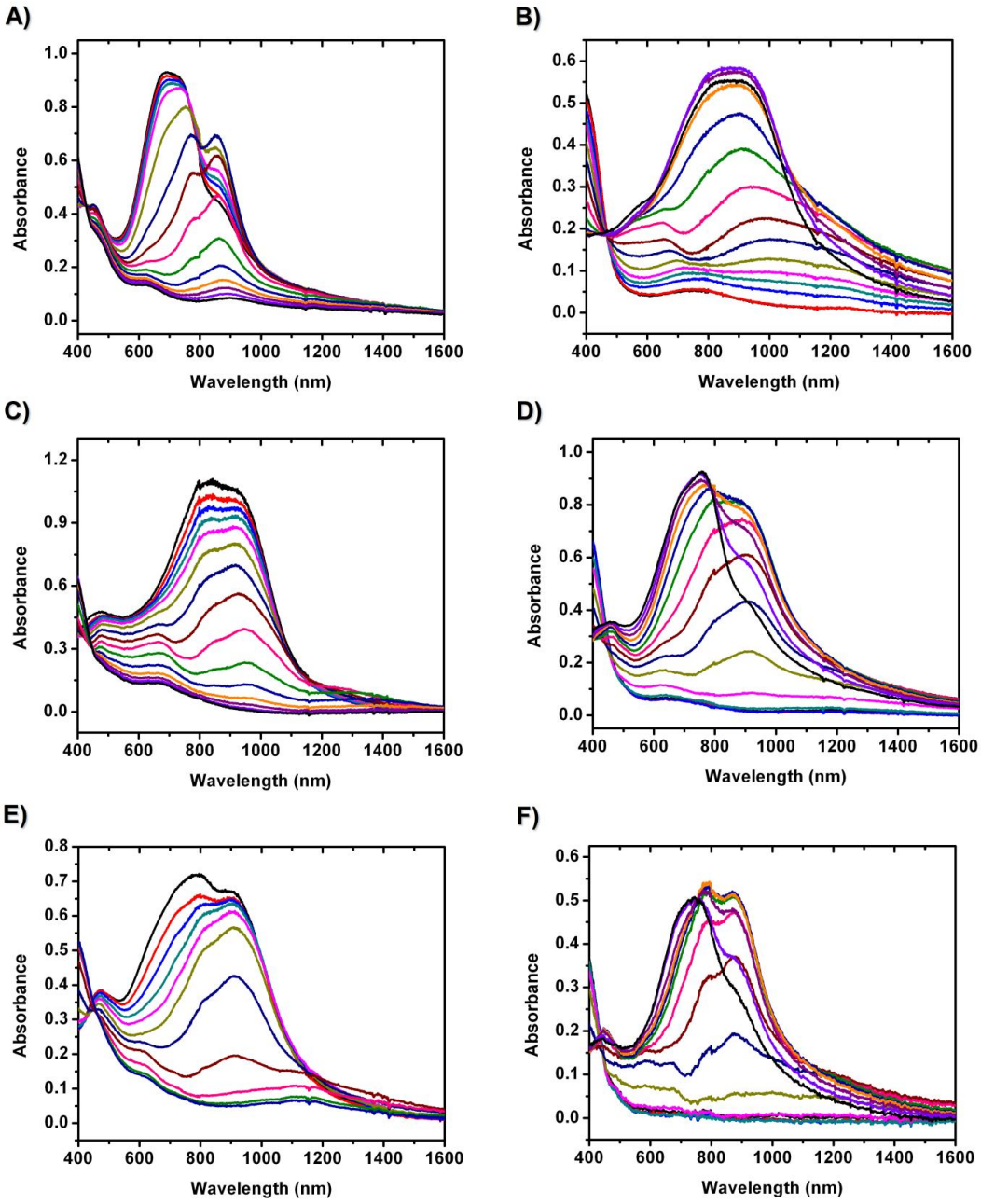

Figure 3.27. UV-Vis-NIR Spectroelectrochemistry of ligand polymer and metallopolymers measured on ITO-coated glass in 0.1 M $TBAPF_6/CH_2Cl_2$ electrolyte solution at -0.25 to 1.25 V vs Fc/Fc^+: (A) poly-$\mathbf{H_2L^I}$, (B) poly-$\mathbf{VOL^I}$, (C) poly-$\mathbf{CoL^I}$, (D) poly-$\mathbf{CuL^I}$, (E) poly-$\mathbf{NiL^I}$, and (F) poly-$\mathbf{ZnL^I}$.

Bipolaron bands of poly-**NiL^{I}**, poly-**CuL^{I}** and poly-**CoL^{I}** appear at an even longer wavelength (ca. 870 nm) and have a broader shape than that of poly-**ZnL^{I}**, which are indications of a highly delocalized charge carrier observed in a more extended conjugated system. The dramatical decrease in the intensity of the polaron band in the spectroelectrochemistry of poly-**NiL^{I}** and the change in shape of the bipolaron band, which becomes very sharp and narrow, could be evidence for the redox event of $Ni^{2+/3+}$. This electrochemical process occurs at potential near 1.1 V and induces more positive charges on the poly-**NiL^{I}** backbone causing Coulombic repulsion as well as a reduction of delocalized distances of the bipolarons. Spectroeletrochemistry of poly-**VOL^{I}**, shown in Figure 3.27B, has the most significant red-shifting of the bipolaron band (ca. 882 nm), which is likely due to the nature of the vanadyl group. The additional oxygen atom may cause a better mixing of the orbitals of the vanadium metal center to those of the organic backbone and give a longer extension of conjugation.

The contributions of the metal centers to the overall conjugation of metallopolymers is also observed in the second and the third polymer series with bithiophene and terthiophene as electropolymerizable groups. The different spectroelectrochemical spectra of the metallopolymers of vanadyl ion with the three ligands are shown in Figure 3.28. The bipolaron bands of poly-**VOL^{I}**, poly-**VO^{II}**, and poly-**VOL^{IIIC4}** are respectively found at 882, 1049, and 1337 nm, which are significantly red-shifted compared to those in ligand polymers (765, 951, and 1205 nm for poly-**H_2L^{I}**, poly-**H_2L^{II}**, and poly-**H_2L^{IIIC4}**, respectively (Figure 3.21). Again, these results confirm the role of metal in enhancing the conjugated system of metallopolymers over that of ligand polymers, which may account for the increase in redox conductivity of these metallopolymers.

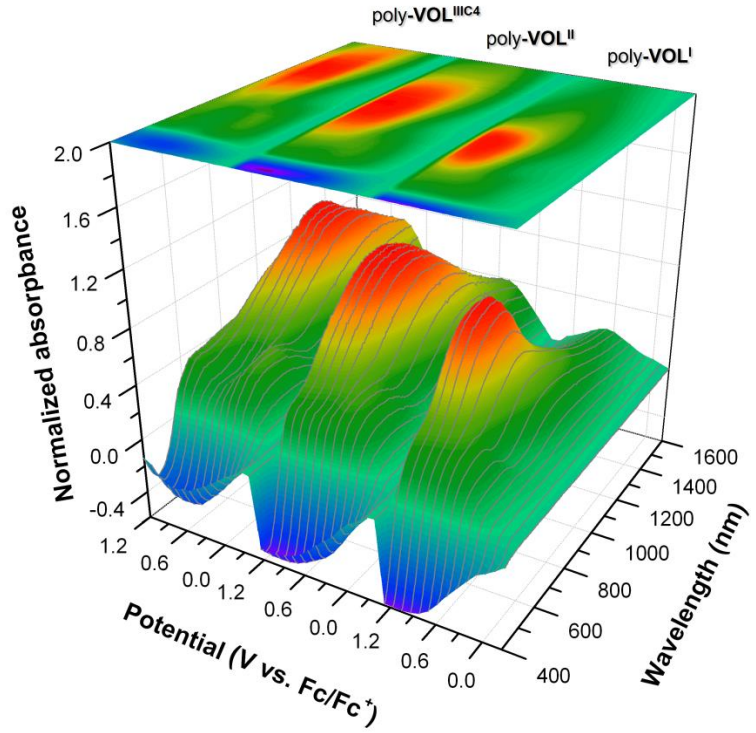

Figure 3.28. Different spectroelectrochemical spectra of poly-**VOL^{I}**, poly-**VOL^{II}**, and poly-**VOL^{IIIC4}** on ITO-coated glass in 0.1 M $TBAPF_6$/DCM solution with applied potential between -0.2 and 1.2 V vs. Fc/Fc^+.

In order to provide a deeper understanding of charge delocalization in the metallopolymer systems, DFT calculations were performed using the B3LYP/SDD basis set to calculate the optimized conformation and the spin distribution in neutral and one-electron-oxidized forms of the ligand and metal complex monomers. Figure 3.26 and 3.27 show the HOMOs/SOMOs and the LUMOs of neutral and 1+ forms of **ML^{I}** monomers. HOMOs of ligand molecule show a break in conjugation in both oxidized and neutral forms (Figure 3.29A) while continuous conjugation was found in metal complexes with contribution from the metal orbitals (Figure 3.29B-C and Figure 3.30). The incorporation of the metal center also helps to planarize the structure and supports conjugation extension, as observed in the red-shifting of the bipolaron bands in

spectroelectrochemistry of metallopolymers. The different features in the spectroelectrochemistry as well as the low redox conductivity of poly-**ZnL^{I}** are revealed in the molecular orbitals of this complex. Both the HOMO of the neutral form and the SOMO of 1^{+} form show the majority of electron density on the metal center and the imine-phenoxy group, supporting a highly localized radical cation when formed (Figure 3.29B). Unlike **ZnL^{I}** system, **VOL^{I}** shows the distribution of density of states from both vanadyl center and organic backbone in the SOMO and HOMO of its neutral and 1^{+} form, respectively (Figure 3.29C). A significant contribution from vanadium metal could explain the increased red-shifting in its UV-Vis-NIR spectroelectrochemistry compared with those in other metallopolymers.

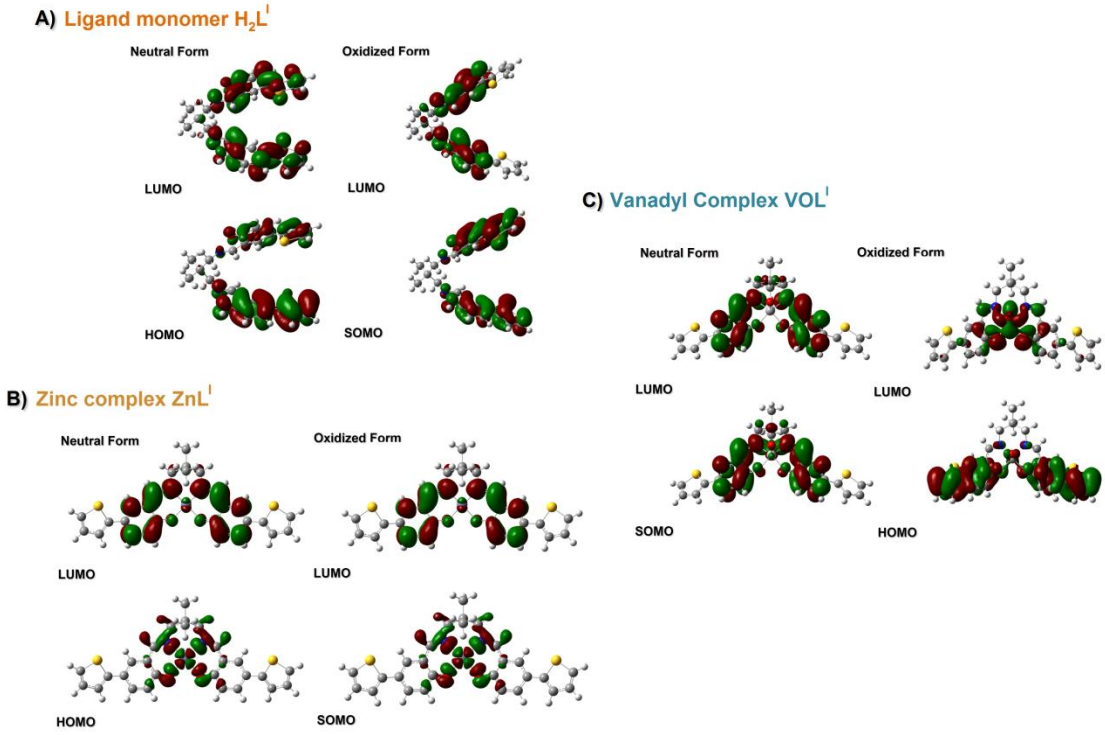

Figure 3.29. Calculated frontier molecular orbitals of neutral and one-electron-oxidized forms of **H$_2$L^{I}** (A), **ZnL^{I}** (B), and **VOL^{I}** (C).

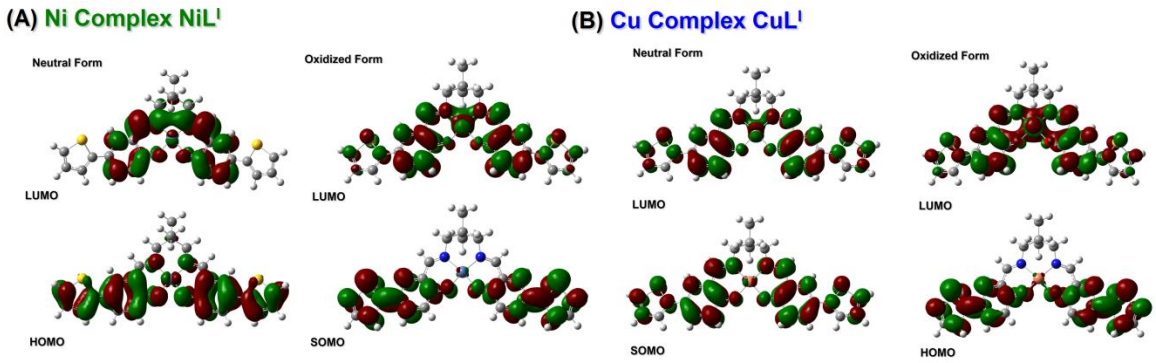

Figure 3.30. Calculated frontier molecular orbitals of neutral and one-electron-oxidized forms of **NiL^{I}** (A) and **CuL^{I}** (B).

3.2.6. Metal-Organic Backbone Interactions and the Effects on Properties of CMPs

The interaction between the metal centers and the organic backbone was implied when comparing the electrochemical properties and the *in-situ* conductivity of the metallopolymers of the same metal but with different length of organic conjugated backbone. The cyclic voltammograms and conductivity profile of metallopolymers from redox-inactive metals (e.g., Cu(II)) exhibit similar features with little difference for the three series, revealing two redox events in the CV and one conductivity maximum. The CV and conductivity profiles of metallopolymers with redox-active metals, on the other hand, are dramatically influenced by the change of conjugation length on the organic backbones. Cyclic voltammograms of poly-**H_2L^{IIIC4}** (Figure 3.31A) show two oxidation peaks at 0.30 V and 0.72 V, corresponding with the formation of phenoxy radicals on salen centers and the polarons on the thiophene backbone, respectively. The CV of poly-**VOL^{IIIC4}**, however, reveals three oxidation peaks at 0.22, 0.50, and 0.95 V (Figure 3.31B). The first two peaks are attributed to organic backbone oxidation-as observed in ligand polymer but at lower potentials-while the new peak at 0.95 V is assigned to be the redox potential of the vanadium center, corresponding to the $V^{4+/5+}$ redox process. It is

interesting that this third oxidation peak only appears in a polymer with a terthiophene backbone and was not observed in the shorter thiophene chain of bithiophene or monothiophene. This may be due to the Coulombic repulsion of the polarons on the organic backbone to the more-positive metal center when formed, making it harder to form in a short thiophene chain. When terthiophene is used, these positive charges can delocalize farther from the metal center and make the metal sites become more easily oxidized, and could be observed in the studied potential window. Moreover, *in-situ* conductivity of ligand and vanadyl complex polymer films were conducted using 10 μm Pt interdigitated microelectrode. There is only one conductivity peak in the conductivity profile of poly-$\mathbf{H_2L^{IIIC4}}$, which is found at the second oxidation peak (Figure 3.31A). This suggests that the first redox process of the polymer does not contribute to the overall conductivity. We believe that, as discussed before, this redox potential is attributed to the oxidation of phenoxy groups of the salen centers. The radical cations are highly localized on the iminophenol ring and are not involved in the conduction process. The conductivity caused by the second redox process is assigned to the formation of polarons on the thiophene backbone, which are highly mobile. The conductivity profile of poly-$\mathbf{VOL^{IIIC4}}$ is distinguished from poly-$\mathbf{H_2L^{IIIC4}}$ by two features: the appearance of a new peak and the magnitude of conductivity value. There are two peaks in the conductivity profile of poly-$\mathbf{VOL^{IIIC4}}$ (Figure 3.31B). The first peak appears at the potential for the second redox process, the formation of polarons as observed poly-$\mathbf{H_2L^{IIIC4}}$, while the second one occurs at the potential assigned to the $V^{4+/5+}$ redox couple. The appearance of the new peaks in poly-$\mathbf{VOL^{IIIC4}}$ conductivity profile is clear evidence of the contribution of metal centers to the polymer conductivity.

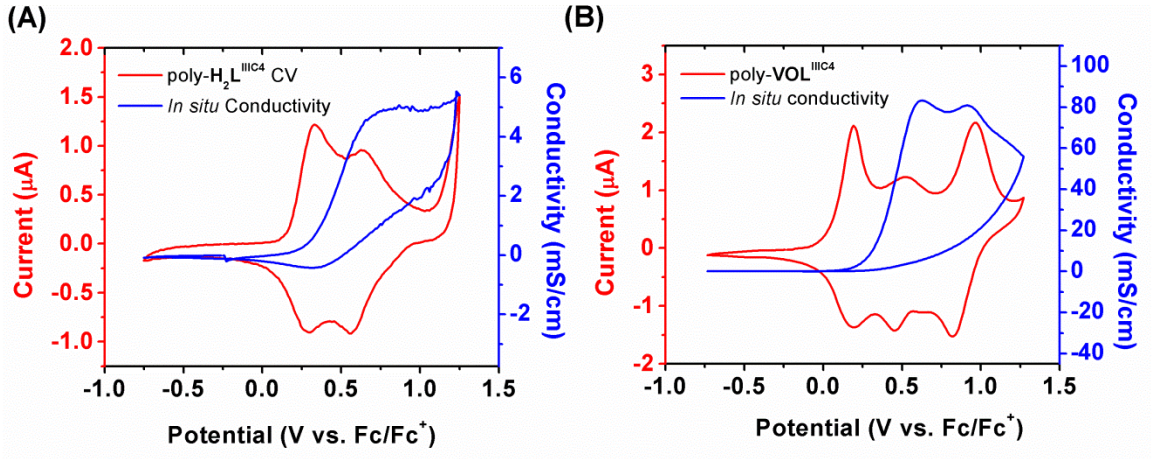

Figure 3.31. Cylic voltammetry (red) and *in-situ* conductivity profile (blue) of poly-$\mathbf{H_2L^{IIIC4}}$ (A) and poly-$\mathbf{VOL^{IIIC4}}$, in 0.1 M *n*-Bu_4NPF_6/CH_2Cl_2 electrolyte.

The interaction between the metal centers and the organic backbone are also observed in the CMPs of other redox-active metals including cobalt and nickel. The CV and conductivity profile of cobalt-containing CMPs of the mono-, bi-, and ter-thiophene series are presented in Figure 3.32A. The conductivity profile of poly-$\mathbf{CoL^{I}}$ reveals only one conductivity maximum (at 0.77 V) as found in ligand polymers and metallopolymers bearing redox-inactive metals (copper and zinc). When increasing the conjugation length of the organic backbone by adding one thiophene unit into the monomer, the resulting metallopolymer (poly-$\mathbf{CoL^{II}}$) exhibits two maxima in its conductivity profile at 0.62 and 1.16 V. The later peak at 1.16 V is attributed to the metal redox event $Co^{2+/3+}$. Also, further increasing the conjugation length of the organic backbone by using ter-thiophene as the electropolymerizable group in the monomer still reveals the two peaks in the conductivity profile but causes a shift to less positive potentials. This shows a decrease in the driving force for both organic backbone and metal oxidations. The two conductivity maxima are found at 0.57 and 0.89 V. The results support our hypothesis on the

Coulombic repulsion between positive charge on the metal centers and the polarons on the oligothiophene backbones. Increasing the conjugation length leads to less repulsion due to further delocalization of the polaron away from the metal centers, making it easier to oxidize the metal cations.

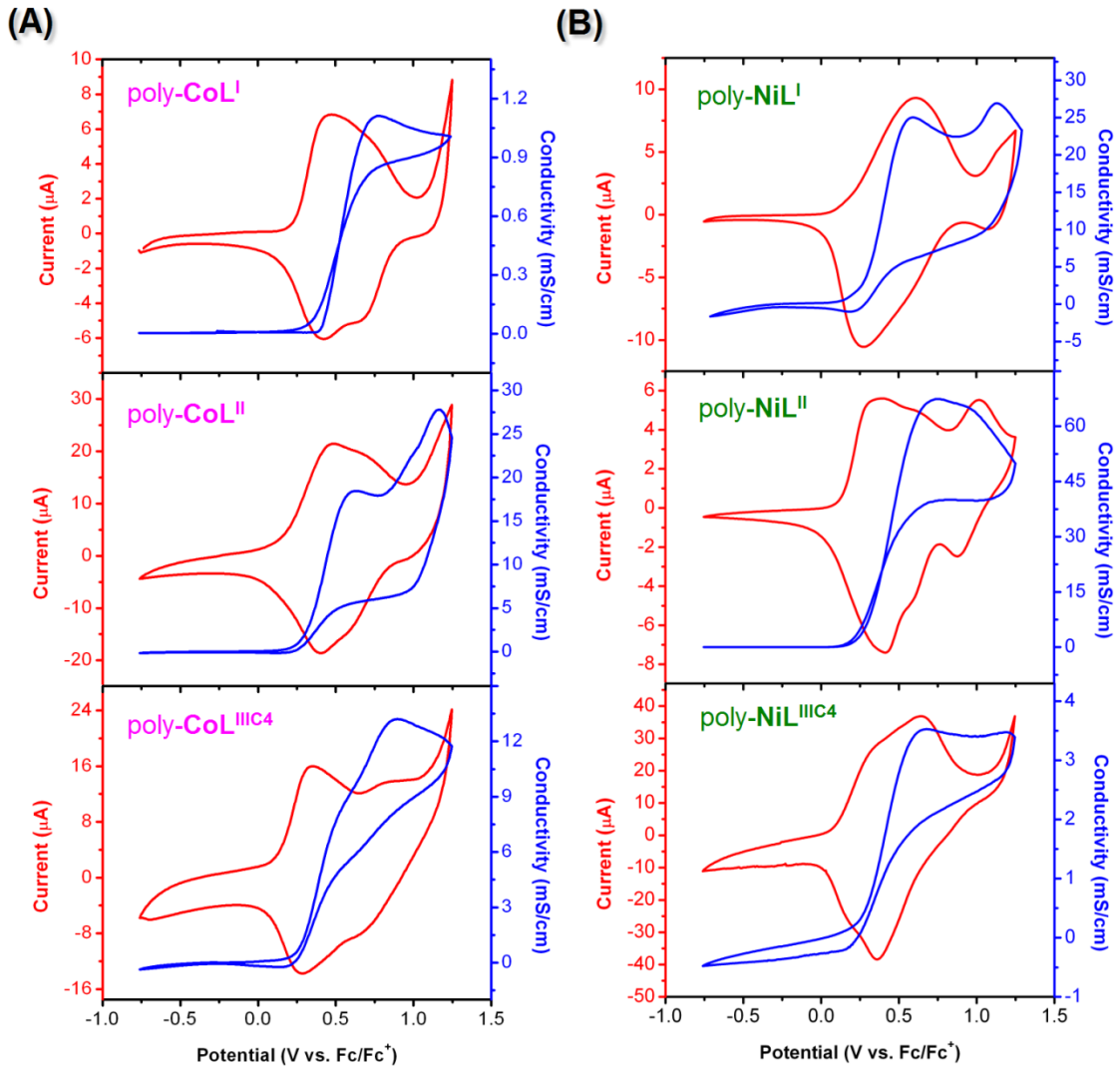

Figure 3.32. CV and conductivity profiles of Co(II) and Ni(II) CMPs in DCM electrolyte. Scan rate 10 mV/s, 40 mV offset potential.

Depending on the accessibility of the oxidation of the metal centers, the redox event of metal ions may be found in mono-, bi-, or ter-thiophene systems. For example, the redox of $Ni^{2+/3+}$ is found in the mono-thiophene series (Figure 3.32B) while $Co^{2+/3+}$ and $VO^{4+/5+}$ redox events only start to appear in the bi-, and ter-thiophene systems, respectively. There is a decrease in redox potential for metal oxidation when increasing the conjugation length of organic backbone, causing only one conductivity maximum for poly-**Ni^{IIIC4}**. This is due to the overlap of oxidation potentials for organic backbone and $Ni^{2+/3+}$ in this metallopolymer.

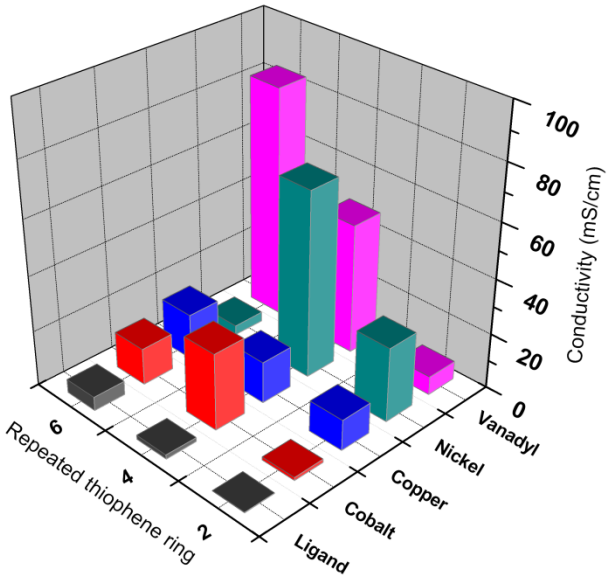

Figure 3.33. Comparison of maximum conductivity values of ligand polymers and metallopolymers of the three polymer series: monothiophene, bithiophene, and dibutylterthiophene as electropolymerizable groups.

The maximum conductivity of all ligand polymers and metallopolymers were then plotted as a function of repeated thiophene units in these polymers and presented in Figure 3.33. By extending the conjugation length of organic backbone ligand polymers, the conductivity increases significantly at almost one order of magnitude for every two

thiophene units in the backbone of the ligand polymers. In all cases, the incorporation of metal centers to ligand polymers raises the conductivity dramatically, indicating the contribution of these metal centers to the conductivity of metallopolymers. The influence of the metal centers to the conductivity is also dependent on the type of metals present. In metallopolymers with redox-inactive metals (i.e. copper), there are minimal changes in the conductivity for the three polymer series. The increase in conductivity in these metallopolymers compared to ligand polymers is primarily due to the extension of conjugation contributed from the metal centers. Conductivity of CMPs bearing redox-active metals, on the other hand, is strongly dependent upon the redox activity of metal centers. Polymer systems that have metal centers with redox potential higher than but similar to that of the organic backbone ($\Delta \sim 0.5$ V) exhibit highest conductivity in the series with the same metal (e.g., poly-**NiL^{II}**, poly-**CoL^{II}**, and poly-VO**L^{IIIC4}**). In these systems, charge transport is supported by the electron transfer between metal centers with the mixed-valence states through the conductive hopping mechanism through the organic backbone. The overlapping of redox potential of metal and organic backbone causes the decrease in conductivity as found in poly-**NiL^{IIIC4}** and poly-**CoL^{IIIC4}**, which is probably due to the loss of the electron transport pathway through metal-backbone-metal.

2.3. CONCLUSION

In summary, we have prepared and characterized a series of electropolymerizable monomers of Schiff-base ligands and metal complexes. Conducting polymers prepared from these monomers allows us to systematically study the charge transport and delocalization in this type of conducting metallopolymers using *in-situ* conductivity and UV-Vis-NIR spectroelectrochemistry. The successful synthesis of ligand polymers has created a direct comparison and enabled studies that elucidate the role of the metal

centers in Schiff-base CMPs. The extension of conjugation length of the organic backbone that occurs by increasing the number of thiophene rings in the repeating units leads to an increase in conjugation and conductivity of ligand polymers. We investigated intra-chain interaction between the metal center and organic backbone in CMPs by using metals with different redox properties. Our study revealed that the charge transport is most effective in CMPs with redox-active metals that have higher oxidation potential but still match that of the organic backbone. The redox-matching in such systems facilitates the electron transport process between conjugated organic segments in a metal-backbone-metal manner. Redox-inactive and redox-active metal without matching show similar electrochemical properties as the organic components are the only active element for charge transfer. In all cases, CMPs show much higher redox-conductivity than their ligand polymers (up to 240 fold for poly-$\mathbf{ML^I}$ series) due to the contribution of the metal center to the overall conjugation and the redox event for the oxidation of metal centers. Our results of charge transport studies in CMPs could possibly be extended to any general Wolf Type-III CMPs where the metal centers act as a part of conjugated backbone.

3.4. EXPERIMENTAL

3.4.1. General Methods

Air- and moisture-sensitive reactions were carried out in flame-dried glassware using standard Schlenk techniques under an inert nitrogen atmosphere. All chemicals were purchased from commercial sources and used as received. Dry solvents were dried using an Innovative Technology, Pure Solv solvent purifier with a double purifying column. ^{1}H NMR (400 MHz) and ^{13}C $\{^{1}$H$\}$ NMR (100 MHz) spectra were obtained on a Varian (400 MHz) spectrometer and were referenced to residual solvent peaks. All peak

positions are given in ppm and coupling constants are reported in Hz. Low-resolution and high-resolution mass spectrometry was carried out by a Thermo Finngan TSQ 700 and Waters Autospec Ultima, respectively. Melting points were recorded with an OptiMelt Automated Melting Point System with digital image processing technology from Stanford Research System (SRS, Sunnyvale, CA). Elemental analysis was performed by by Midwest Microlab, Indianapolis, IN (www.midwestlab.com). Infrared spectra were recorded using a Nicolet IR 200 FTIR spectrometer. X-ray photoelectron spectroscopy (XPS) was carried out on a PHI 5700 XPS system equipped with dual Mg X-ray source and monochromatic Al X-ray source complete with depth profile and angle-resolved capabilities. 2-(tributylstannyl)-3',4'-diehtyl-2,2':5',2''-terthiophene, 2-(tributylstannyl)-3',4'-dibutyl-2,2':5',2''-terthiophene,[40] **CuL^{II}**,[41] and **H$_2$L^{II}** [42] were prepared as reported in the literature. Commercially available reagents were used without further purification.

3.4.2. Crystal Structure Determination

The single–crystal diffraction data were collected on a AFC12 diffractometer with a Saturn 724+ CCD, a Nonius Kappa CCD diffractometer, or a Rigaku SCX-Mini diffractometer with a Mercury CCD using a graphite monochromator with MoKα radiation (λ = 0.71073 Å). Absorption corrections were applied using multi-scan technique using either Abscor for the Rigaku data.[43] Data reduction were performed using the Rigaku Americas Corporation's Crystal Clear version 1.40.[44] The structures were solved by direct methods and refined anisotropically using full-matrix least-squares methods with the SHELX 97 program package.[45] The coordinates of the non-hydrogen atoms were refined anisotropically, while hydrogen atoms were included in the calculation isotropically but not refined. Neutral atom scattering factors and values used to calculate the linear absorption coefficient are from the International Tables for X-ray

Crystallography (1992).[46] Crystal data collection and structure refinement details are given in Tables 3.6, 3.7, 3.8, 3.9, 3.10, and 3.11 for $\mathbf{H_2L^{I\text{-}IIIC4}}$, $\mathbf{NiL^{I\text{-}IIIC4}}$, $\mathbf{CuL^{I\text{-}II}}$, $\mathbf{VOL^{I\text{-}II}}$, $\mathbf{VOL^{I\text{-}II}}$, and $\mathbf{ZnL^{I}}$, respectively.

3.4.3. Electrochemistry

Electrochemical syntheses and studies were performed in a dry-box under an atmosphere of nitrogen using a GPES system from Eco. Chemie B. V. All the electrochemical experiments were carried out in a three-electrode cell with a $Ag/AgNO_3$ reference electrode (silver wire dipped in a 0.01 M silver nitrate solution with 0.1 M $[(n\text{-}Bu)_4N]^+[PF_6]^-$ in CH_3CN), a Pt working electrode, and a Pt wire coil counter electrode. Potentials were relative to this 0.01 M $Ag/AgNO_3$ reference electrode. Ferrocene was used as an external reference to calibrate the reference electrode before and after experiments were performed and that value was used to correct the measured potentials. All electrochemistry and electropolymerizations were performed in dichloromethane (DCM) or acetonitrile (ACN) solutions using 0.1 M $[(n\text{-}Bu)_4N]^+[PF_6]^-$ ($TBAPF_6$) as the supporting electrolyte. The $TBAPF_6$ was purified by recrystallization three times from hot ethanol before being dried for 3 days at 100-150 °C under active vacuum prior to use. Polymer films were prepared on Delta Technologies ITO-coated glass for spectroscopic measurement and on stainless steel for XPS. Electrosyntheses of the polymer films were performed from monomer solutions by continuous cycling between -0.5 and 1.5 V (vs. Fc/Fc^+) at a scan rate of 100 mV/s. The films obtained were then washed with copious amounts of fresh DCM before further experiments.

3.4.4. UV-Vis-NIR Spectroelectrochemistry

The spectroelectrochemical measurements were performed using the previously described cell arrangement on a polymer film deposited on ITO coated glass substrate as

working electrode, a platinum mesh as the counter electrode, and $Ag/AgNO_3$ as reference electrode. Experiments were carried out in an optical cuvette inside the glovebox. Absorption spectra were recorded on a Varian Cary 6000i UV-Vis-NIR spectrophotometer within the NIR/visible spectra ($1600 \geq \lambda \geq 400$ nm) under several applied potentials.

3.4.5. *In-situ* Conductivities

The conductivities of polymer films were determined from equation (4) using interdigitated array electrode (IDA) purchased from CH Instrument (CH 012126) with 10 μm interdigit spacing; 129 gaps; and 0.2 cm electrode length. Film thickness was obtained on a Dektak 3 surface profilometer. Conductivity profiles were carried at 0.04 V applied offset potential and a scan rate of 10 mV/s in DCM electrolyte.

3.4.6. Calculations

Geometry optimizations of neutral and 1^+ forms of ligand and metal complexes were performed with density functional theory (DFT) using the Gaussian 03 program,[47] employing the B3YLP functional in conjunction with the SDD basis set. All geometries were fully optimized using the default optimization criteria of the program. Orbital analyses were completed with GaussView 5.0 program.

3.4.7. Syntheses of Ligands and Metal Complex Monomers

Ligand L^I. To a solution of 5-(2-thiophenyl)-2-hydroxybenzaldehyde (0.64 g, 1.3 mmol) in 30 mL of $CHCl_3$/EtOH (v/v = 1/2) was added 1,3-diamino-2,2'-dimethylpropane (0.068 g, 0.66 mmol) in 10 ml EtOH. The reaction mixture was heated to 60 °C for 2 hrs, then cooled to room temperature, and $CHCl_3$ was removed in vacuo resulting in an yellow suspension in EtOH. The precipitate was collected by vacuum filtration to give 0.6 g (88%) of desired product (mp 131 ^oC). ^1H NMR (400 MHz,

$CDCl_3$): δ (ppm) = 13.57 (s, 2H), 8.37 (s, 2H), 7.56 (dd, 2H, *J* = 2.3, 8.6), 7.47 (d, 2H, *J* = 2.3), 7.20 (dd, 2H, *J* = 1.2, 5.1), 7.16 (dd, 2H, *J* = 1.2, 3.6), 7.02 (dd, 2H, *J* = 3.6, 5.1), 6.99 (d, 2H, *J* = 8.6), 3.52 (s, 4H), 1.09 (s, 6H); ^{13}C {^1H} NMR (100 MHz, $CDCl_3$): δ (ppm) = 165.6, 160.9, 143.7, 130.3, 128.7, 128.0, 125.6, 123.9, 122.1, 118.6, 117.6, 68.0, 36.3, 24.4. FTIR: 1633 cm^{-1}. UV-Vis (λ_{max} (ε), CH_2Cl_2): 345 nm (6,050 $cm^{-1}M^{-1}$), 294 nm (32,850 $cm^{-1}M^{-1}$). HRMS (CI^+) m/z calculated for $[C_{27}H_{24}N_2O_2S_2]^+$ ($[\mathbf{L^I}]^+$): 474.1436, found 474.1436. Elemental analysis calculated (found): C, 68.33(68.44); H, 5.52(5.67); N 5.90 (5.93).

VOL^I. Ligand **L^I** (0.125 g, 0.122 mmol) was dissolved in $CHCl_3$: EtOH = 1 : 1 (20 mL) and the solution was purged with nitrogen for 5 minutes. To this solution, a nitrogen-purged solution of vanadyl acetylacetonate (32.3 mg, 0.122 mmol) in 10 ml of EtOH was added. The reaction mixture was stirred under nitrogen at 60 °C for 1 hr, and then cooled to room temperature. $CHCl_3$ was removed in vacuo resulting in a suspension in EtOH. The light orange solid was isolated by vacuum filtration then further dried under vacuum to give 0.11 g yellow-orange solid (83%). mp > 250 ^oC. FTIR 1617 cm^{-1}. UV-Vis (λ_{max} (ε), CH_2Cl_2): 401 nm (6400 $cm^{-1}M^{-1}$), 313 nm (44,200 $cm^{-1}M^{-1}$), 282 nm (52,100 $cm^{-1}M^{-1}$). HRMS (CI^+) m/z calculated for $[C_{27}H_{24}N_2O_3S_2V]^+$ ($[\mathbf{VOL^I}]^+$): 539.0668, found 539.0663. Elemental analysis calculated (found): C, 60.10(59.92); H, 4.48(4.45); N, 5.19(5.08). Crystals suitable for X-ray analysis were grown *via* slow evaporation of dimethyl sulfoxide solution under nitrogen atmosphere.

CoL^I. This complex was prepared in a manner similar to VOL^I using $Co(OAc)_2 \cdot 4H_2O$. 73% yellow-brown solid, mp > 250 ^oC. FTIR: 1618 cm^{-1}. UV-Vis (λ_{max} (ε), CH_2Cl_2): 390 nm (4000 $cm^{-1}M^{-1}$), 315 nm (19,500 $cm^{-1}M^{-1}$), 269 nm (18,900 $cm^{-1}M^{-1}$). HRMS (CI^+) m/z calculated for $[C_{27}H_{24}N_2O_2S_2Co]^+$ ($[\mathbf{CoL^I}]^+$): 531.0611, found 531.0618. MS (CI) m/z calculated for $Co(AcO)_2$ 177, found 177. Elemental analysis

calculated (found) for $(CoL^I)_2 \cdot Co(AcO)_2$: C, 56.17(56.79); H, 4.34(4.53); N 4.52(4.46). Crystals suitable for X-ray analysis were grown *via* slow evaporation of *N,N*-dimethylformaldehyde solution.

NiL^I. This complex was prepared in a manner similar to VOL^I using $Ni(OAc)_2 \cdot 4H_2O$. 98% dark green solid, mp > 250 ^oC. ^1H NMR (400 MHz, $CDCl_3$): δ (ppm) = 8.35 (s, 2H), 7.56 (dd, 2H, *J* = 2.3, 8.6), 7.46 (d, 2H, *J* = 2.3), 7.18 (dd, 2H, *J* = 1.2, 5.1), 7.15 (dd, 2H, *J* = 1.2, 3.6), 7.04 (dd, 2H, *J* = 3.5, 5.1), 6.99 (d, 2H, *J* = 8.6), 3.51 (s, 4H), 1.09 (s, 6H). ^{13}C {^1H} NMR: compound is not sufficiently soluble in any common solvent to obtain a spectrum. FTIR 1610 cm^{-1}. UV-Vis (λ_{max} (ε), CH_2Cl_2): 434 nm (6440 $cm^{-1}M^{-1}$), 325 nm (48,400 $cm^{-1}M^{-1}$), 270 nm (49,000 $cm^{-1}M^{-1}$). HRMS (CI^+) m/z calculated for $[C_{27}H_{24}N_2O_2S_2Ni]^+$ ([**NiL^I**]$^+$): 530.0633, found 530.0636. Elemental analysis calculated (found): C, 61.04(59.98); H, 4.55(4.75); N 5.27(5.09). Crystals suitable for X-ray analysis were grown *via* slow evaporation of dichloromethane solution.

CuL^I. This complex was prepared in a manner similar to VOL^I using $Cu(OAc)_2$. 98% bright green solid, mp > 250 ^oC. FTIR 1616 cm^{-1}. UV-Vis (λ_{max} (ε), CH_2Cl_2): 400 nm (10,300 $cm^{-1}M^{-1}$), 320 nm (54,800 $cm^{-1}M^{-1}$), 274 nm (51,000 $cm^{-1}M^{-1}$). HRMS (CI^+) m/z calculated for $[C_{27}H_{24}N_2O_2S_2Cu]^+$ ([**CuL^I**]$^+$): 535.0575, found 535.0584. Elemental analysis calculated (found): C, 60.48(60.24); H, 4.51(4.62); N 5.22(5.26). Crystals suitable for X-ray analysis were grown *via* slow evaporation of dichloromethane solution.

ZnL^I. This complex was prepared in a manner similar to VOL^I using $Zn(OAc)_2 \cdot 2H_2O$. 77% bright yellow solid, mp > 250 ^oC. ^1H NMR (400 MHz, $CDCl_3$): δ (ppm) = 8.37 (s, 2H), 7.56 (dd, 2H, *J* = 2.3, 8.6), 7.47 (d, 2H, *J* = 2.3), 7.19 (dd, 2H, *J* = 1.2, 5.1), 7.16 (dd, 2H, *J* = 1.2, 3.6), 7.03 (dd, 2H, *J* = 3.5, 5.1), 6.98 (d, 2H, *J* = 8.6), 3.51 (s, 4H), 1.09 (s, 6H). ^{13}C {^1H} NMR: compound is not sufficiently soluble in any common solvent to obtain a spectrum. FTIR 1625 cm^{-1}. UV-Vis (λ_{max} (ε), CH_2Cl_2): 380

nm (7100 $cm^{-1}M^{-1}$), 311 nm (26,800 $cm^{-1}M^{-1}$), 269 nm (31,200 $cm^{-1}M^{-1}$). HRMS (CI^+) m/z calculated for $[C_{27}H_{24}N_2O_2S_2Zn]^+$ ($[\mathbf{ZnL^I}]^+$): 536.0571, found 536.0569. MS (CI) m/z calculated for $Zn(AcO)_2$ 182, found 182. Elemental analysis calculated (found) for $(ZnL^I)_2 \cdot Zn(AcO)_2$: C, 55.31(55.33); H, 4.32(4.44); N 4.45(4.31). Crystals suitable for X-ray analysis were grown *via* slow evaporation of *N,N*-dimethylformaldehyde solution.

VOL^{II}. This complex was prepared in a manner similar to VOL^I using ligand **H_2L^{II}**. 73% orange solid, mp > 250 ^oC.. UV-Vis (λ_{max} (ε), CH_2Cl_2): 390 nm (4000 $cm^{-1}M^{-1}$), 315 nm (19,500 $cm^{-1}M^{-1}$), 269 nm (18,900 $cm^{-1}M^{-1}$). HRMS (CI^+) m/z calculated for $[C_{35}H_{28}N_2O_3S_4V]^+$ ($[\mathbf{VOL^{II}}]^+$): 703.0422, found 703.0421. Elemental analysis calculated (found): C, 59.73(59.47); H, 4.01(4.09); N 3.98(3.90). Crystals suitable for X-ray analysis were grown *via* slow diffusion of acetonitrile to a dimethylformaldehyde solution.

CoL^{II}. This complex was prepared in a manner similar to **VOL^{II}** using $Co(OAc)_2 \cdot 4H_2O$. 73% yellow-brown solid, mp > 250 ^oC. UV-Vis (λ_{max} (ε), CH_2Cl_2): 390 nm (4000 $cm^{-1}M^{-1}$), 315 nm (19,500 $cm^{-1}M^{-1}$), 269 nm (18,900 $cm^{-1}M^{-1}$). HRMS (CI^+) m/z calculated for $[C_{35}H_{28}N_2O_2S_4Co]^+$ ($[\mathbf{CoL^{II}}]^+$): 695.0366, found 695.0370. MS (CI) m/z calculated for $Co(AcO)_2$ 177, found 177. Elemental analysis calculated (found) for $(CoL^{II})_2 \cdot 2H_2O$: C, 57.44(57.94); H, 4.41(4.20); N 3.83(3.68). Crystals suitable for X-ray analysis were grown *via* slow evaporation of a dichloromethane/ethanol solution.

NiL^{II}. This complex was prepared in a manner similar to **VOL^{II}** using $Ni(OAc)_2 \cdot 4H_2O$. 98% dark green solid, mp > 250 ^oC. 8.35 (s, 2H), 7.56 (dd, 2H, J = 2.3, 8.6), 7.46 (d, 2H, J = 2.3), 7.18 (dd, 2H, J = 1.2, 5.1), 7.15 (dd, 2H, J = 1.2, 3.6), 7.04 (dd, 2H, J = 3.5, 5.1), 6.99 (d, 2H, J = 8.6), 3.51 (s, 4H), 1.09 (s, 6H). ^{13}C $\{^1H\}$ NMR: compound is not sufficiently soluble in any common solvent to obtain a spectrum. FTIR 1610 cm^{-1}. UV-Vis (λ_{max} (ε), CH_2Cl_2): 434 nm (6440 $cm^{-1}M^{-1}$), 325 nm (48,400 $cm^{-1}M^{-1}$),

270 nm (49,000 $cm^{-1}M^{-1}$). HRMS (CI^+) m/z calculated for $[C_{35}H_{28}N_2O_2S_4Ni]^+$ ($[\mathbf{NiL^{II}}]^+$): 695.0387, found 695.0390. Elemental analysis calculated (found): C, 60.44(60.34); H, 4.06(4.31); N 4.03(3.90). Crystals suitable for X-ray analysis were grown *via* slow evaporation of a dichloromethane/ethanol solution.

5-(3',4'-diethyl-[2,2':5',2''-terthiophen]-5-yl)-2-hydroxybenzaldehyde (1). To a mixture of 5-bromosalicylaldehyde (1.00 g, 5 mmol), and $Pd(PPh_3)_2Cl_2$ (0.3 g, 0.88 mmol) in 60 mL of dry toluene was added 2-(tributylstannyl)-3',4'-diehtyl-2,2':5',2''-terthiophene[1] (2.97 g, 5 mmol). The reaction mixture was heated to 100 °C for 48 hours under nitrogen. The reaction was cooled and dried in vacuo. The mixture was dissolved in CH_2Cl_2, and then filtered through a silica gel plug. The filtrate was washed with dilute $NH_4Cl_{(aq)}$ (3 times, 80 mL), then dried over $MgSO_4$. Solvent was removed and the product was purified by column chromatography (silica gel, CH_2Cl_2 : hexanes = 50 : 50) to yield a light orange solid (1.23 g, 58%). ^{1}H NMR (400 MHz, $CDCl_3$): δ (ppm) = 11.02 (s, 1H), 9.90 (s, 1H), 7.72 (dd, 1H, *J* = 2.3, 8.4), 7.70 (d, 1H, *J* = 2.3), 7.30 (dd, 1H, *J* = 1.2, 5.1), 7.15 (d, 1H, *J* = 3.9), 7.14 (dd, 1H, *J* = 1.2, 3.6), 7.07 (d, 1H, *J* = 3.9), 7.06 (dd, 1H, *J* = 3.6, 5.1), 7.00 (d, 1H, *J* = 8.4), 2.79 (m, 4H), 1.23-1.30 (m, 6H); ^{13}C {^{1}H} NMR (100 MHz, $CDCl_3$): δ (ppm) = 196.4, 161.0, 141.9, 141.3, 141.2, 135.9, 135.4, 134.3, 130.3, 130.0, 129.6, 127.4, 126.6, 126.5, 125.9, 125.4, 123.1, 120.6, 118.4, 21.2, 21.0, 15.4, 15.3. HRMS (ESI) m/z calculated for $C_{23}H_{20}O_2S_3$ 424.0625, found 424.0629.

H_2L^{IIIC2}. To a solution of 5-(3',4'-diethyl-[2,2':5',2''-terthiophen]-5-yl)-2-hydroxybenzaldehyde (0.63 g, 1.48 mmol) in $CHCl_3$: EtOH = 1 : 2 (30 mL) was added 1,3-diamino-2,2'-dimethylpropane (0.076 g, 0.74 mmol) in 10 ml EtOH. The reaction mixture was stirred at overnight resulting in an orange suspension. The precipitate was collected by vacuum filtration to give the desired product (0.63 g, 91%). ^{1}H NMR (400 MHz, $CDCl_3$): δ (ppm) = 13.66 (s, 2H), 8.38 (s, 2H), 7.57 (dd, 2H, *J* = 2.3, 8.6), 7.47 (d,

2H, *J* = 2.3), 7.29 (dd, 2H, *J* = 1.2, 5.2), 7.12 (d, 2H, *J* = 3.7), 7.10 (d, 2H, *J* = 3.7), 7.06(dd, 2H, *J* = 3.7, 5.2), 7.04 (d, 2H, *J* = 3.7), 6.99 (d, 2H, *J* = 8.6), 3.51 (s, 4H), 2.75 (m, 8H), 1.22 (m, 12H), 1.09 (s, 6H); ^{13}C {^{1}H} NMR (100 MHz, $CDCl_3$): δ (ppm) = 165.6, 161.0, 143.1, 141.2, 140.9, 136.0, 134.5, 129.9, 129.8, 129.7, 128.4, 127.4, 126.6, 125.8, 125.3, 125.2, 122.4, 118.7, 117.7, 67.9, 36.3, 24.4, 21.1, 21.0, 15.4, 15.3. UV-Vis (λ_{max} (ε), CH_2Cl_2): 364 nm (59,300 $cm^{-1}M^{-1}$). HRMS (CI^+) m/z calculated for $[C_{51}H_{50}N_2O_3S_6]^+$ ($[\mathbf{H_2L^{IIIC2}}]^+$): 914.2197, found 914.2192. Elemental analysis calculated (found): C, 66.92(66.32); H, 5.51(5.39); N 3.06 (2.77). Crystals suitable for X-ray analysis were grown *via* slow evaporation of a dichloromethane/ethanol solution.

5-(3',4'-dibutyl-[2,2':5',2''-terthiophen]-5-yl)-2-hydroxybenzaldehyde (2). This compound was prepared in a similar procedure for **1** using 2-(tributylstannyl)-3',4'-dibutyl-2,2':5',2''-terthiophene. Orange solid (1.49 g, 62%). ^{1}H NMR (400 MHz, $CDCl_3$): δ (ppm) = 11.02 (s, 1H), 9.90 (s, 1H), 7.72 (dd, 1H, *J* = 2.3, 8.4), 7.70 (d, 1H, *J* = 2.3), 7.30 (dd, 1H, *J* = 1.2, 5.1), 7.15 (d, 1H, *J* = 3.9), 7.14 (dd, 1H, *J* = 1.2, 3.6), 7.07 (d, 1H, *J* = 3.9), 7.06 (dd, 1H, *J* = 3.6, 5.1), 7.00 (d, 1H, *J* = 8.4), 2.73 (m, 4H), 1.31-1.66 (m, 8H), 0.96 (m, 6H); ^{13}C {^{1}H} NMR (100 MHz, $CDCl_3$): δ (ppm) = 196.3, 160.8, 141.7, 140.1, 140.0, 139.5, 136.0, 135.5, 134.1, 130.1, 129.9, 129.5, 127.3, 126.5, 125.8, 125.3, 123.0, 120.5, 118.2, 32.8, 32.7, 27.8, 27.7, 23.0, 22.9, 13.8, 13.7. HRMS (ESI) m/z calculated for $[C_{27}H_{28}O_2S_3]^+$ ($[\mathbf{2}]^+$): 480.1211, found 480.1211.

$\mathbf{H_2L^{IIIC4}}$. This ligand was prepared in a manner similar to $\mathbf{H_2L^{IIIC2}}$ using **2** with a yield of 88% (0.60 g). ^{1}H NMR (400 MHz, $CDCl_3$): δ (ppm) = 13.68 (s, 2H), 8.35 (s, 2H), 7.56 (dd, 2H, *J* = 2.3, 8.6), 7.46 (d, 2H, *J* = 2.3), 7.28 (dd, 2H, *J* = 1.2, 5.2), 7.12 (d, 2H, *J* = 3.7), 7.10 (d, 2H, *J* = 3.7), 7.05 (dd, 2H, *J* = 3.7, 5.2), 7.04 (d, 2H, *J* = 3.7), 7.00 (d, 2H, *J* = 8.6), 3.50 (s, 4H), 2.71 (m, 8H), 1.56 (m, 8H), 1.44 (m, 8H), 1.09 (s, 6H), 0.96 (m, 12H); ^{13}C {^{1}H} NMR (100 MHz, $CDCl_3$): δ (ppm) = 165.5, 161.0, 143.1, 140.2,

139.8, 136.1, 134.6, 133.4, 129.9, 129.8, 129.6, 128.3, 127.3, 126.5, 125.7, 125.2, 122.3, 118.2, 117.63, 68.0, 36.17, 30.84, 27.8, 27.7, 24.3, 24.2, 23.0, 22.9, 13.8, 13.7. UV-Vis (λ_{max} (ε), CH_2Cl_2): 362 nm (56,900 $cm^{-1}M^{-1}$). HRMS (CI^+) m/z calculated for $[C_{59}H_{66}N_2O_2S_6]^+$ ($[\mathbf{H_2L^{IIIC4}}]^+$): 1026.3444, found 1026.3449. Elemental analysis calculated (found) for $C_{59}H_{66}N_2O_2S_6 \cdot CH_2Cl_2$: C, 64.78(65.63); H, 6.47(6.16); N 2.73 (2.52).

VOL^{IIIC2}. This complex was prepared in a manner similar to **VOL^{I}** using **H_2L^{IIIC2}** (0.21 g, 89%). UV-Vis (λ_{max} (ε), CH_2Cl_2): 379 nm (68,200 $cm^{-1}M^{-1}$). HRMS (CI^+) m/z calculated for $[C_{51}H_{48}N_2O_3S_6V]^+$ ($[\mathbf{VOL^{IIIC2}}]^+$): 979.1429, found 979.1440. Elemental analysis calculated (found): C, 62.49(62.36); H, 4.94(5.00); N 2.86(2.62).

VOL^{IIIC4}. This complex was prepared in a manner similar to VOL^{I} using **H_2L^{IIIC4}** (0.11 g, 83%). UV-Vis (λ_{max} (ε), CH_2Cl_2): 378 nm (64,700 $cm^{-1}M^{-1}$). HRMS (CI^+) m/z calculated for $[C_{59}H_{66}N_2O_3S_6V]^+$ ($[\mathbf{VOL^{IIIC4}}]^+$): 1091.2671, found 1091.2681. Elemental analysis calculated (found): C, 64.86(62.56); H, 5.90(5.08); N 2.56(2.70).

NiL^{IIIC4}. This complex was prepared in a manner similar to **VOL^{IIIC4}** using $Ni(OAc)_2 \cdot 4H_2O$. 73% yellow-brown solid. UV-Vis (λ_{max} (ε), CH_2Cl_2): 390 nm (72,400 $cm^{-1}M^{-1}$). HRMS (CI^+) m/z calculated for $[C_{59}H_{66}N_2O_3S_6Ni]^+$ ($[\mathbf{NiL^{IIIC4}}]^+$): 1091.2671, found 1091.2681. Elemental analysis calculated (found) for **NiL^{IIIC4}**$\cdot H_2O$: C, 64.29(62.23); H, 6.04(5.86); N 2.54(2.66). Crystals suitable for X-ray analysis were grown *via* slow diffusion of ethanol into a dichloromethane solution.

CuL^{IIIC4}. This complex was prepared in a manner similar to **VOL^{IIIC4}** using $Cu(OAc)_2$. 98% bright green solid. UV-Vis (λ_{max} (ε), CH_2Cl_2): 385 nm (76,500 $cm^{-1}M^{-1}$). HRMS (CI^+) m/z calculated for $[C_{59}H_{66}N_2O_3S_6Cu]^+$ ($[\mathbf{CuL^{IIIC4}}]^+$): 1091.2671, found 1091.2681. Elemental analysis calculated (found) for **CuL^{IIIC4}**$\cdot H_2O$: C, 64.01(64.04); H, 6.01(5.84); N 2.53(2.58). Crystals suitable for X-ray analysis were grown *via* slow

diffusion of ethanol into a dichloromethane solution.

CoL^{IIIC4}. This complex was prepared in a manner similar to **VOL^{IIIC4}** using $Co(OAc)_2 \cdot 4H_2O$. 73% yellow-brown solid. UV-Vis (λ_{max} (ε), CH_2Cl_2): 381 nm (54,700 $cm^{-1}M^{-1}$). HRMS (CI^+) m/z calculated for $[C_{59}H_{66}N_2O_3S_6Co]^+$ ([**CoL^{IIIC4}**]$^+$): 1091.2671, found 1091.2681. Elemental analysis calculated (found) for **CoL^{IIIC4}**$\cdot$(**$CHCl_3$**)(**H_2O**)$_2$: C, 61.49(61.1); H, 5.77(5.49); N 2.41(2.60).

CRYSTALLOGRAPHIC DATA

Table 3.6. Crystal data and structure refinement of $\mathbf{H_2L^I}$ and $\mathbf{H_2L^{IIIC2}}$

	$\mathbf{H_2L^I}$	$\mathbf{H_2L^{IIIC2}}$
Empirical formula	C27 H26 N2 O2 S2	C51 H50 N2 O2 S6
Formula weight	474.62	915.29
Temperature (K)	100(2)	100(2)
Wavelength (Å)	0.71073	0.71073
Crystal system	Orthorhombic	Monoclinic
Space group	P*212121*	*C*12/*c*1
a (Å)	5.723	37.215
b (Å)	12.338	14.101
c (Å)	33.143	9.619
α (deg)	90	90
β (deg)	90	96.59
γ (deg)	90	90
Volume ($Å^3$)	2340.2	5014.3
Z	4	4
ρ (mg/cm^3)	1.347	1.212
μ (mm^{-1})	0.256	0.312
F(000)	1000	1928
Crystal size (mm)	0.31 x 0.05 x 0.03	0.20 x 0.07 x 0.06
θ (deg)	1.76 to 25.00	3.09 to 24.89
Index ranges	$-6 \leq h \leq 6$	$-43 \leq h \leq 43$
	$-14 \leq k \leq 14$	$-16 \leq k \leq 16$
	$-39 \leq l \leq 39$	$-11 \leq l \leq 11$
Reflections collected	19521	21177
Max. and min. transmission	0.8918 and 0.7995	0.9815 and 0.9402
GOF on F^2	1.092	1.07
R1, wR2 [I>2σ(I)]	0.0567, 0.1347	0.0725, 0.1735
R1, wR2[all data]	0.0631, 0.1385	0.1168, 0.1948
Largest diff. peak and hole ($e.Å^{-3}$)	0.322 and -0.396	0.414 and -0.259

Table 3.7. Crystal data and structure refinement of **NiL^{I}**, **NiL^{II}**, **and NiL^{IIIC4}**.

	NiL^{I}	**NiL^{II}**	**NiL^{IIIC4}**
Empirical formula	C28 H26 Cl2 N2 Ni O2 S2	C35 H28 N2 Ni O2 S4	C60 H66 Cl2 N2 Ni O2 S6
Formula weight	616.24	695.54	1169.12
Temperature (K)	153(2)	100(2)	100(2)
Wavelength (Å)	0.71075	0.71073	0.71073
Crystal system	Monoclinic	Monoclinic	Monoclinic
Space group	P*21/c*	P*21/c*	P*21/c*
a (Å)	17.602	7.515	8.868(2)
b (Å)	8.31	35.334	19.809(5)
c (Å)	21.996	11.422	33.077(9)
α (deg)	90	90	90
β (deg)	125.22	90.44	102.154(7)
γ (deg)	90	90	90
Volume ($Å^3$)	2638	3032.8	5680(2)
Z	4	4	4
ρ (mg/cm^3)	1.551	1.523	1.367
μ (mm^{-1})	1.127	0.953	0.701
F(000)	1272	1440	2456
Crystal size (mm)	0.20 x 0.20 x 0.10	0.15 x 0.08 x 0.03	0.22 x 0.20 x 0.17
θ (deg)	2.27 to 27.53	3.22 to 25.03	1.63 to 25.00
Index ranges	$-22 \le h \le 22$	$-8 \le h \le 8$	$-10 \le h \le 10$
	$-9 \le k \le 10$	$-42 \le k \le 42$	$-23 \le k \le 23$
	$-28 \le l \le 28$	$-13 \le l \le 13$	$-39 \le l \le 39$
Reflections collected	22600	20776	101640
Max. and min. transmission	0.8957 and 0.8060	0.9720 and 0.8703	0.8901 and 0.8611
GOF on F^2	1.061	1.069	1.155
R1, wR2 [I>2σ(I)]	0.0536, 0.1262	0.0569, 0.1187	0.0906, 0.2359
R1, wR2[all data]	0.0753, 0.1408	0.0852, 0.1298	0.0920, 0.2372
Largest diff. peak and hole ($e.Å^{-3}$)	0.645 and -0.555	0.404 and -0.506	1.252 and -1.082

Table 3.8. Crystal data and structure refinement of $\mathbf{CuL^{I}}$ and $\mathbf{CuL^{IIIC4}}$.

	$\mathbf{CuL^{I}}$	$\mathbf{CuL^{IIIC4}}$
Empirical formula	C28 H26 Cl2 Cu N2 O2 S2	C59 H64 Cl0 Cu N2 O2 S6
Formula weight	621.07	1089.02
Temperature (K)	100(2)	100(2)
Wavelength (Å)	0.71073	0.71073
Crystal system	Monoclinic	Orthorhombic
Space group	*C*12/*c*1	P*bcn*
a (Å)	19.962	29.325(16)
b (Å)	12.997	20.484(11)
c (Å)	10.617	9.653(5)
α (deg)	90	90
β (deg)	94.52	90
γ (deg)	90	90
Volume ($Å^3$)	2746.0	5798(5)
Z	4	4
ρ (mg/cm^3)	1.502	1.247
μ (mm^{-1})	1.172	0.634
F(000)	1276	2292
Crystal size (mm)	0.20 x 0.20 x 0.10	0.20 x 0.05 x 0.04
θ (deg)	1.87 to 27.34	2.31 to 25.00
Index ranges	$-25 \le h \le 25$	$-34 \le h \le 34$
	$-13 \le k \le 16$	$-24 \le k \le 24$
	$-13 \le l \le 11$	$-11 \le l \le 11$
Reflections collected	9140	81863
Max. and min. transmission	0.8918 and 0.7995	0.9751 and 0.8836
GOF on F^2	1.118	1.365
R1, wR2 [I>2σ(I)]	0.0513, 0.1237	0.1924, 0.3260
R1, wR2[all data]	0.0662, 0.1337	0.1939, 0.3267
Largest diff. peak and hole ($e.Å^{-3}$)	0.555 and -0.687	0.657 and -0.485

Table 3.9. Crystal data and structure refinement of **VOL^{I}** and **VOL^{II}**.

	VOL^{I}	**VOL^{II}**
Empirical formula	C33 H42 N2 O6 S5 V	C40 H38 N4 O4 S4 V
Formula weight	773.93	817.92
Temperature (K)	100(2)	100(2)
Wavelength (Å)	0.71073	0.71073
Crystal system	Orthorhombic	Monoclinic
Space group	Pbca	P*21/n*
a (Å)	10.944	19.124
b (Å)	22.219	7.767
c (Å)	30.888	25.554
α (deg)	90	90
β (deg)	90	98.99
γ (deg)	90	90
Volume (Å^3)	7510.9	3749.0
Z	8	4
ρ (mg/cm^3)	1.369	1.449
μ (mm^{-1})	0.586	0.536
F(000)	3240	1700
Crystal size (mm)	0.20 x 0.20 x 0.10	0.19 x 0.13 x 0.06
θ (deg)	3.21 to 25.00	2.84 to 25.00
Index ranges	$-13 \leq h \leq 13$	$-22 \leq h \leq 22$
	$-26 \leq k \leq 26$	$-9 \leq k \leq 9$
	$-36 \leq l \leq 36$	$-30 \leq l \leq 30$
Reflections collected	127779	29463
Max. and min. transmission	0.8957 and 0.8060	0.9686 and 0.9051
GOF on F^2	1.065	1.032
R1, wR2 [I>2σ(I)]	0.0514, 0.1218	0.0900, 0.1928
R1, wR2[all data]	0.0568, 0.1289	0.1870, 0.2473
Largest diff. peak and hole (e.Å^{-3})	1.696 and -1.084	0.524 and -0.563

Table 3.10. Crystal data and structure refinement of **CoL^{I}** and **CoL^{II}**.

	CoL^{I}	**CoL^{II}**
Empirical formula	C70 H82 Co3 N8 O12 S4	C74 H62 Co2 N6 O6 S8
Formula weight	1532.51	1505.64
Temperature (K)	100(2)	100(2)
Wavelength (Å)	0.71075	0.71073
Crystal system	triclinic	Monoclinic
Space group	P-1	P*21/c*
a (Å)	12.140	8.9360(18)
b (Å)	13.081	11.6472(25)
c (Å)	13.230	31.5458(69)
α (deg)	61.24	90
β (deg)	79.55	93.753(3)
γ (deg)	79.13	90
Volume ($Å^3$)	1798.6	3276.22(10)
Z	1	2
ρ (mg/cm^3)	1.415	1.526
μ (mm^{-1})	0.865	0.823
F(000)	799	1556
Crystal size (mm)	0.20 x 0.20 x 0.10	0.23 x 0.17 x 0.11
θ (deg)	1.77 to 27.50	2.18 to 25.00
Index ranges	$-15 \leq h \leq 15$	$-10 \leq h \leq 10$
	$-16 \leq k \leq 16$	$-13 \leq k \leq 13$
	$-17 \leq l \leq 17$	$-37 \leq l \leq 37$
Reflections collected	33307	58109
Max. and min. transmission	0.8918 and 0.7995	0.9149 and 0.8333
GOF on F^2	1.025	1.261
R1, wR2 [I>2σ(I)]	0.0524, 0.1380	0.0630, 0.1427
R1, wR2[all data]	0.0710, 0.1511	0.0644, 0.1436
Largest diff. peak and hole ($e.Å^{-3}$)	0.763 and -0.763	0.764 and -0.865

Table 3.11. Crystal data and structure refinement of **ZnL^{I}** and **ZnL^{I}-trinuclear**.

	ZnL^{I}	**ZnL^{I}-trinuclear**
Empirical formula	C27 H26 N2 O3 S2 Zn	C35 H41 N4 O6 S2 Zn1.50
Formula weight	555.99	775.89
Temperature (K)	100(2)	100(2)
Wavelength (Å)	0.71073	0.71073
Crystal system	Monoclinic	Monoclinic
Space group	P21/n	P-1
a (Å)	19.399	10.943
b (Å)	6.289	11.786
c (Å)	19.974	15.837
α (deg)	90	97.68
β (deg)	93.49	102.40
γ (deg)	90	106.76
Volume ($Å^3$)	2432.3	1867.9
Z	4	2
ρ (mg/cm^3)	1.518	1.380
μ (mm^{-1})	1.215	1.130
F(000)	1152	808
Crystal size (mm)	0.29x 0.13 x 0.05	0.20 x 0.11 x 0.07
θ (deg)	3.02 to 27.49	3.04 to 25.00
Index ranges	$-25 \leq h \leq 25$	$-13 \leq h \leq 13$
	$-8 \leq k \leq 8$	$-14 \leq k \leq 14$
	$-25 \leq l \leq 25$	$-18 \leq l \leq 18$
Reflections collected	51333	20951
Max. and min. transmission	0.9418 and 0.7196	0.9251 and 0.8055
GOF on F^2	1.012	1.044
R1, wR2 [I>2σ(I)]	0.0516, 0.1105	0.0760, 0.1781
R1, wR2[all data]	0.0662, 0.1176	0.1268, 0.2113
Largest diff. peak and hole ($e.Å^{-3}$)	0.466 and -0.566	1.582 and -0.585

REFERENCES

(1) *Please see chapter 1 and references therein*.

(2) Friebe, C.; Hager, M. D.; Winter, A.; Schubert, U. S. *Adv. Mater.* **2012**, *24*, 332.

(3) Whittell, G. R.; Hager, M. D.; Schubert, U. S.; Manners, I. *Nat Mater* **2011**, *10*, 176.

(4) Wolf, M. *J. Inorg. Organomet. Polym. Mater.* **2006**, *16*, 189.

(5) Holliday, B. J.; Swager, T. M. *Chem. Commun.* **2005**, 23.

(6) Holliday, B. J.; Stanford, T. B.; Swager, T. M. *Chem. Mater.* **2006**, *18*, 5649.

(7) Shioya, T.; Swager, T. M. *Chem. Commun.* **2002**, 1364.

(8) Kingsborough, R. P.; Swager, T. M. *Adv. Mater.* **1998**, *10*, 1100.

(9) G. Pickup, P. *J. Mater. Chem.* **1999**, *9*, 1641.

(10) Pietrangelo, A.; Sih, B. C.; Boden, B. N.; Wang, Z.; Li, Q.; Chou, K. C.; MacLachlan, M. J.; Wolf, M. O. *Adv. Mater.* **2008**, *20*, 2280.

(11) You, Z.-L.; Zhu, H.-L.; Liu, W.-S. *Acta Cryst. E* **2004**, *60*, m1900.

(12) You, Z.-L.; Zhou, P. *Inorg. Chem. Commun.* **2007**, *10*, 1273.

(13) Gutiérrez, A.; Perpiñán, M. F.; Sánchez, A. E.; Torralba, M. C.; Torres, M. R. *Polyhedron* **2012**, *44*, 165.

(14) Yu, T.; Zhang, K.; Zhao, Y.; Yang, C.; Zhang, H.; Fan, D.; Dong, W. *Inorg. Chem. Commun.* **2007**, *10*, 401.

(15) Diao, Y.-P.; Huang, S.-S.; Zhang, H.-L.; Deng, S.; Liu, K.-X. *Acta Cryst. E* **2007**, *63*, m1694.

(16) Zulauf, A.; Hong, X.; Brisset, F.; Schulz, E.; Mellah, M. *New J. Chem.* **2012**, *36*, 1399.

(17) Schrebler, R.; Grez, P.; Cury, P.; Veas, C.; Merino, M.; Gómez, H.; Córdova, R.; del Valle, M. A. *J. Electroanal. Chem.* **1997**, *430*, 77.

(18) Berglund, S. P.; Flaherty, D. W.; Hahn, N. T.; Bard, A. J.; Mullins, C. B. *J. Phys. Chem. C* **2011**, *115*, 3794.

(19) Kittlesen, G. P.; White, H. S.; Wrighton, M. S. *J. Am. Chem. Soc.* **1984**, *106*, 7389.

(20) Pickup, P. G.; Kutner, W.; Leidner, C. R.; Murray, R. W. *J. Am. Chem. Soc.* **1984**, *106*, 1991.

(21) Chidsey, C. E. D.; Murray, R. W. *J. Phys. Chem.* **1986**, *90*, 1479.

(22) Chidsey, C. E.; Feldman, B. J.; Lundgren, C.; Murray, R. W. *Anal. Chem.* **1986**, *58*, 601.

(23) Wilbourn, K.; Murray, R. W. *J. Phys. Chem.* **1988**, *92*, 3642.

(24) Zhu, S. S.; Carroll, P. J.; Swager, T. M. *J. Am. Chem. Soc.* **1996**, *118*, 8713.

(25) Swager, T. M. *Acc. Chem. Res.* **1998**, *31*, 201.

(26) Simone, D. L.; Swager, T. M. *J. Am. Chem. Soc.* **2000**, *122*, 9300.

(27) Vigalok, A.; Zhu, Z.; Swager, T. M. *J. Am. Chem. Soc.* **2001**, *123*, 7917.

(28) Lee, D.; Swager, T. M. *J. Am. Chem. Soc.* **2003**, *125*, 6870.

(29) Ie, Y.; Han, A.; Otsubo, T.; Aso, Y. *Chem. Commun.* **2009**, 3020.

(30) Izuhara, D.; Swager, T. M. *J. Am. Chem. Soc.* **2009**, *131*, 17724.

(31) Rochat, S.; Swager, T. M. *J. Am. Chem. Soc.* **2013**, *135*, 17703.

(32) Gregg, B. A.; Cormier, R. A. *J. Phys. Chem. B* **1998**, *102*, 9952.

(33) Schiavon, G.; Sitran, S.; Zotti, G. *Synth. Met.* **1989**, *32*, 209.

(34) Kingsborough, R. P.; Swager, T. M. *J. Am. Chem. Soc.* **1999**, *121*, 8825.

(35) Liu, W.; Huang, W.; Chen, C.-H.; Pink, M.; Lee, D. *Chem. Mater.* **2012**, *24*, 3650.

(36) Storr, T.; Wasinger, E. C.; Pratt, R. C.; Stack, T. D. P. *Angew. Chem.* **2007**, *119*, 5290.

(37) Shimazaki, Y.; Stack, T. D. P.; Storr, T. *Inorg. Chem.* **2009**, *48*, 8383.

(38) Storr, T.; Verma, P.; Pratt, R. C.; Wasinger, E. C.; Shimazaki, Y.; Stack, T. D. P. *J. Am. Chem. Soc.* **2008**, *130*, 15448.

(39) Kurahashi, T.; Fujii, H. *J. Am. Chem. Soc.* **2011**, *133*, 8307.

(40) Chen, X. *PhD Dissertation* **2011**, The University of Texas at Austin.

(41) Mejia, M. L. *PhD Dissertation* **2010**, The University of Texas at Austin.

(42) Mejía, M. L.; Agapiou, K.; Yang, X.; Holliday, B. J. *J. Am. Chem. Soc.* **2009**, *131*, 18196.

(43) The Rigaku Corportation: Tokyo, Japan, 2001.

(44) *CrystalClear, 1.40*; Rigaku Americas Corporation: The Woodlands, Texas, USA, 2008.

(45) Sheldrick, G. M. *SHELX 97. A software package for the solution and refinement of X-ray data*; University of Gottingen: Gottingen, Germany, 1997.

(46) Cromer, D. T.; Waber, J. T. In *International Tables for X-ray Crystallography*; Kynoch Press: Birmingham, England, 1974; Vol. 4.

(47) Frisch, M. J.; Trucks, G. W.; Schlegel, H. B.; Scuseria, G. E.; Robb, M. A.; Cheeseman, J. R.; Montgomery Jr., J. A.; Vreven, T.; Kudin, K. N.; Burant, J. C.; Millam, J. M.; Iyengar, S. S.; Tomasi, J.; Barone, V.; Mennucci, B.; Cossi, M.; Scalmani, G.; Rega, N.; Petersson, G. A.; Nakatsuji, H.; Hada, M.; Ehara, M.; Toyota, K.; Fukuda, R.; Hasegawa, J.; Ishida, M.; Nakajima, T.; Honda, Y.; Kitao, O.; Nakai, H.; Klene, M.; Li, X.; Knox, J. E.; Hratchian, H. P.; Cross, J. B.; Bakken, V.; Adamo, C.; Jaramillo, J.; Gomperts, R.; Stratmann, R. E.; Yazyev, O.; Austin, A. J.; Cammi, R.; Pomelli, C.; Ochterski, J.; Ayala, P. Y.; Morokuma, K.; Voth, G. A.; Salvador, P.; Dannenberg, J. J.; Zakrzewski, V. G.; Dapprich, S.; Daniels, A. D.; Strain, M. C.; Farkas, O.; Malick, D. K.; Rabuck, A. D.; Raghavachari, K.; Foresman, J. B.; Ortiz, J. V.; Cui, Q.; Baboul, A. G.; Clifford, S.; Cioslowski, J.; Stefanov, B. B.; Liu, G.; Liashenko, A.; Piskorz, P.; Komaromi, I.; Martin, R. L.; Fox, D. J.; Keith, T.; Al-Laham, M. A.; Peng, C. Y.; Nanayakkara, A.; Challecombe, M.; Gill, P. M. W.; Johnson, B. G.; Chen, W.; Wong, M. W.; Gonzalez, C.; Pople, J. A.; Gaussian, Inc.: Wallingford, CT, 2004.

Chapter 4: Conducting Metallopolymers for Spin Crossover Applications

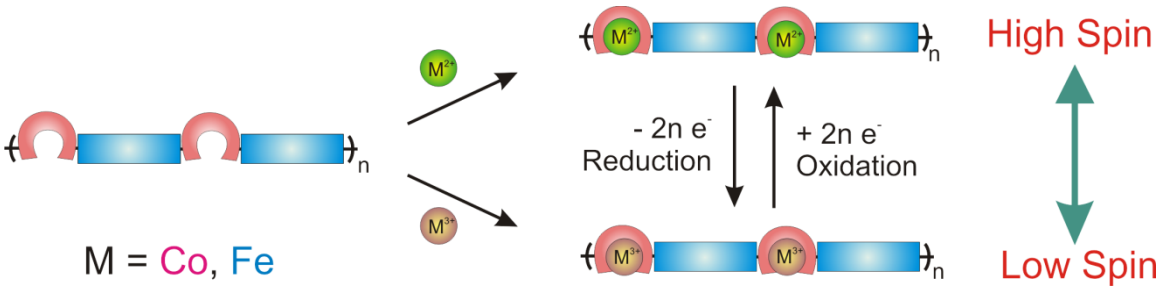

4.1. INTRODUCTION

Spin crossover (SCO) is a phenomenon in which the spin state of the metal center in a complex is switched between the low-spin (LS) and high-spin (HS) states. This phenomenon has been known for more than eight decades and is one of the most fascinating dynamic electronic changes in inorganic coordination chemistry.[1-4] SCO is expected to occur in octahedral complexes of first-row transition metals with an electronic configuration of d^4-d^7. The occurrence of SCO in metal complexes is governed by the relationship between the strength of the ligand field and the spin-pairing energy. Depending on whether the ligand field strength is weaker or stronger than the spin-pairing energy, the metal complexes are in HS or LS states, respectively. With a history of over 80 years, several hundreds of SCO compounds have been synthesized and characterized. Among these SCO systems, complexes of iron(II), iron(III), and cobalt(II) have been most commonly studied,[1,2] most likely due to the significant change in spin multiplicity (ΔS = 2, 2, and 1 for Fe(II), Fe(III), and Co(II), respectively) in SCO of complexes from these ions compared to those from other metals (Figure 4.1).

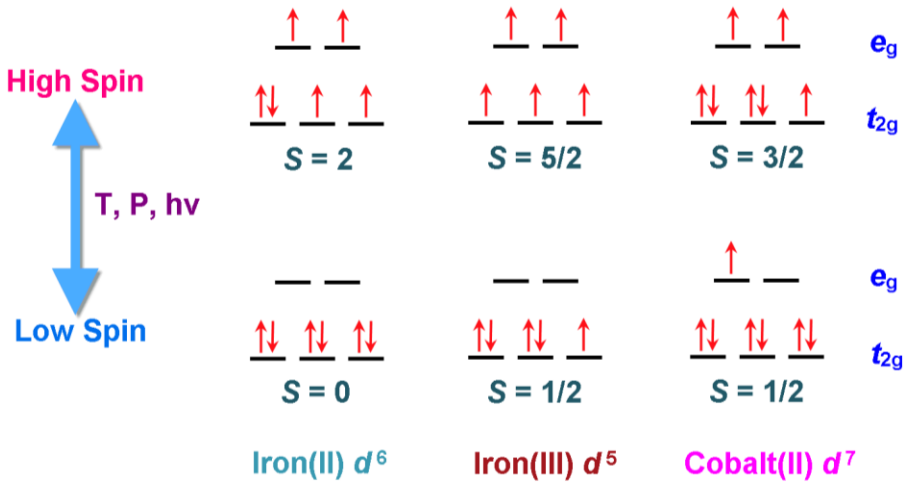

Figure 4.1. Schematic representation of the two possible spin states for iron(II), iron(III), and cobalt(II) complexes in an octahedral environment.

The change in spin states of SCO complexes is usually accompanied by physical changes in color, volume, and magnetic moment of the materials, enabling the use of SCO compounds for many applications such as displays, molecular switches, molecular attenuators, and memory devices.[1,5] The working principle for electronic devices using SCO compounds is based on the bistability behavior of the materials between the LS and HS states. The spin transition can be induced by the application of an external stimulus such as temperature, pressure, or light. Among these types of spin transitions, thermal SCOs are most commonly studied due to the structural complication of devices controlled by presure in addition to the fact that most SCO phenomenon triggered by light only occur at a very low temperature (< 150K).[1,6,7] Although electronic devices utilizing thermal SCO are less complicated than those with presure-induced SCO, device structures are still complicated. In addition, thermal SCO in many cases is too slow for use in some electronic applications such as memory devices. In addition, the requirement for SCO to be used in many applications is an abrupt, complete and hysteretic SCO occuring around room temperature, which could be only found in very limited numbers of SCO compounds. Considering these drawbacks of SCO induced by temperature, pressure and light as well as being motivated by interesting SCO phenomenon, we have designed systems in which the spin switching of the materials can be obtained by the application of electric current. Instead of relying on the search for an abrupt SCO with hysteresis near room temperature, the temperature hysteresis is obtained by the rational design of material structures and the spin switching is induced using electrochemistry.

In order for thermal SCO to occur, the difference in Gibb's free energies for the two spin states involved must be on the order of the thermal energy, $k_B T$.[8] At low temperatures, when the ligand field strength is higher than the spin pairing energy, the LS state of the SCO complexes is stable. However, when the temperature increases, the

repulsion between the two electrons in the same orbital increases, causing an increase in spin pairing energy while little change occurs in ligand field strength. The spin pairing energy continues increasing as the temperature increases until a certain value at which spin pairing energy becomes larger than the ligand field strength. At this temperature, the HS state of the complex is more stable, leading to a SCO in the complexes. As a result, the stronger the ligand field strength, the higher the temperature at which SCO occurs. This explains the fact that there are practically no SCO examples known for tetrahedral complexes of 3*d* metals and octahedral complexes of 4*d* and 5*d* transition elements.[4] The ligand field strength in tetrahedral complexes of 3*d* metals is only about half of octahedral complexes, thus favoring the HS state. In contrast, the ligand field strength of 4*d* and 5*d* transition metals is too strong (roughly 50% increase when changing from 3*d* to 4*d* and from 4*d* to 5*d* metals of the same group and same oxidation state). Therefore, octahedral complexes of these metals tend to adopt the LS state. SCO for these complexes, in principle, may occur but only at very high temperatures.

Similarily, increasing the oxidation state (OS) of the metal center in octahedral complexes while maintaining all other features also increases the ligand field strength (about 40-80%).[4] Consequently, the SCO temperature for complexes of metal with high OS should be higher than the SCO transition temperature for complexes of the same metal at low OS. This causes a resulting temperature range between the two SCO temperatures, in which changing oxidation states of the metal will result in the change of spin states (from the HS of the low-OS complex to the LS of the high-OS complex and *vice versa*). Figure 4.2 shows the possible spin switching when changing the oxidation states of metal centers between +2 and +3 for cobalt and iron complexes.

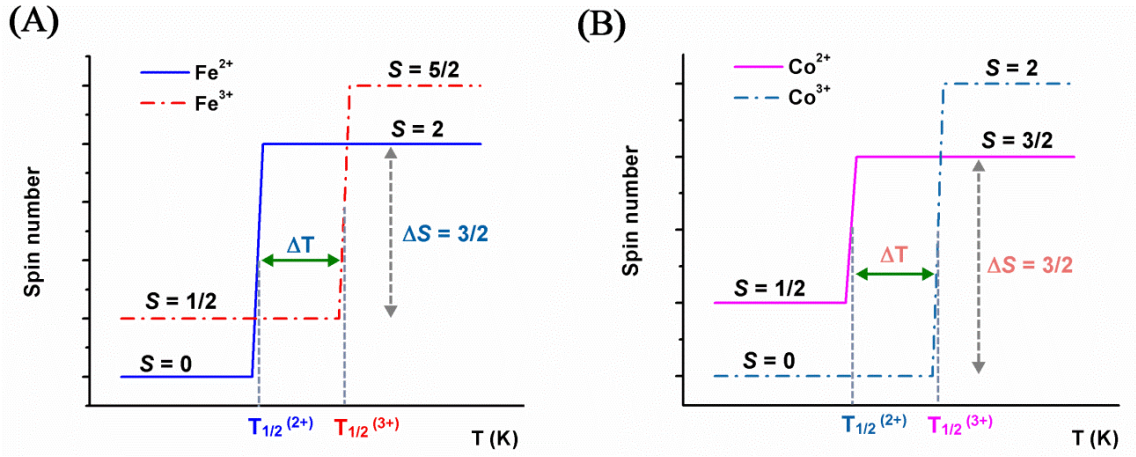

Figure 4.2. Schematic representation of the possible way of spin switching by changing the oxidation state of metal centers in iron (A) and cobalt (B) complexes.

In this work, we aim to synthesized "electrically spin-switchable" materials by taking advantage of the spin switching behavior of metal complexes and the electrical conductivity of conducting polymers. By incorporating SCO complexes of cobalt and iron into the backbone of conducting polymers, the resulting materials would have all the beneficial properties obtaining not only from the SCO phenomenon but also from the conducting polymers. Figure 4.3 shows the schematic representation of spin switching in the proposed conducting metalllopolymers. The appearance of a wide "hysteresis" as shown in Figure 4.2 is due to the difference in ligand field strength of metal ions at two oxidation states. Unlike conventional thermal SCO in which hysteresis is not predictable, the temperature hysteresis causing by the two SCO temperatures of low- and high-OS complexes in these polymers is consistently observed, even with a gradual SCO.

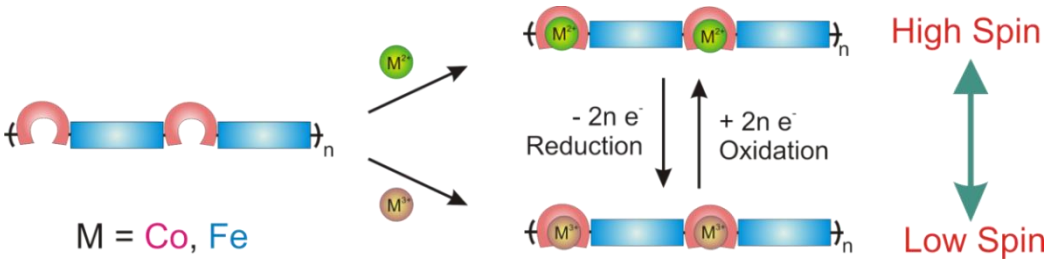

Figure 4.3. Schematic representation of the incorporation of metal centers at two oxidation states to obtain "electrically spin-switchable" conducting metallopolymers.

Herein, we report the synthesis and characterization of novel conducting metallopolymers bearing cobalt and iron complexes in both +2 and +3 oxidation states. These metallopolymers were obtained *via* electrochemical synthesis of electropolymerizable metal complex monomers. Three ligands systems: 4'-(2,2'-bithiophene-5-yl)-2,2':6',2' '-terpyridine (**L1**), 4'-(2,2'-bithiophene-5-yl)-2,6-*bis*(thiazol-2-yl)pyridine (**L2**), and 4'-(2,2'-bithiophene-5-yl)-2,6-*bis*(pyrazol-1-yl)pyridine (**L3**) have been used for coordinating environments as they are known to give SCO complexes with Co(II) and Fe(II) ions (Scheme 4.1). Bithiophene was used as the electropolymerizable groups to obtain the polymers.

Scheme 4.1. Molecular structures of **L1-L3**.

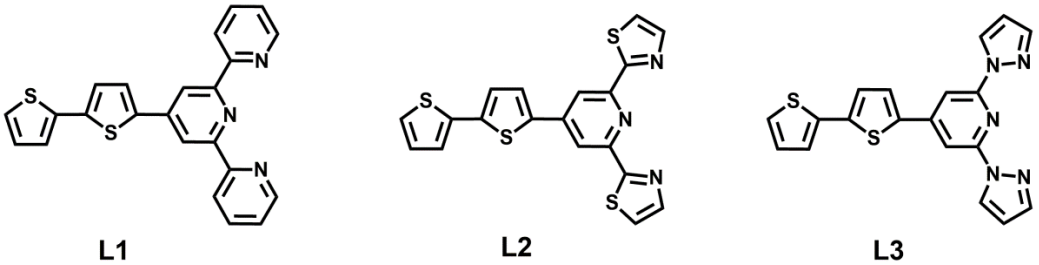

4.2. RESULTS AND DISCUSSION

4.2.1. Synthesis of Electropolymerizable SCO Metal Complex Monomers.

4.2.1.1. Cobalt(II) and Cobalt(III) Complexes

The synthesis of **L1** has been reported previously by Forster *et al.* (Scheme 4.2).[9] However, our effort in making **L1** using their synthetic route did not give a satisfactory product. Thus, we used a one-pot synthesis by modifying Forster's procedure to obtain **L1** in high yield (70%).[10] Cobalt(II) complexes from **L1** were prepared by reacting the ligand with cobalt(II) nitrate to give $\mathbf{Co(L1)_2(NO_3)_2}$ ($\mathbf{Co^{II}L1N}$), which was reacted with NH_4PF_6 through an anion exchange reaction to give $\mathbf{Co(L1)_2(PF_6)_2}$ ($\mathbf{Co^{II}L1P}$).

Scheme 4.2. Synthesis of ligand **L1**.

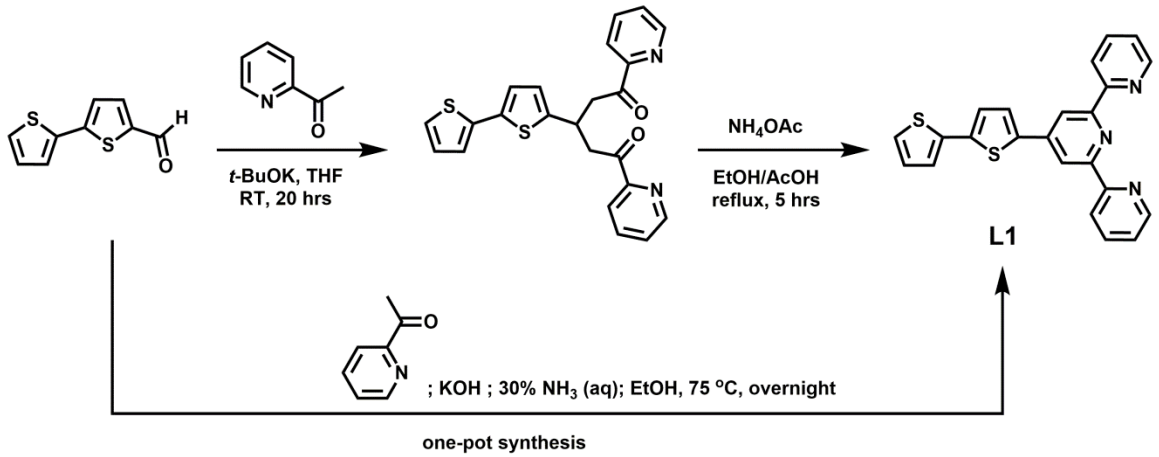

Cobalt(III) complexes were synthesized by oxidizing the $\mathbf{Co(L1)_2(NO_3)_2}$ complex with hydrogen peroxide (H_2O_2) in the presence of one equiv of HNO_3. The obtained complex, $\mathbf{Co(L1)_2(NO_3)_3}$ ($\mathbf{Co^{III}L1N}$), was also used in an anion exchange reaction with NH_4PF_6 to obtain the cobalt(III) hexafluorophosphate complex, $\mathbf{Co(L1)_2(PF_6)_3}$ ($\mathbf{Co^{III}L1P}$). Proposed structures for these complexes were confirmed by mass

spectrometry, nuclear magnetic resonance (NMR) spectroscopy, and single crystal X-ray diffraction.

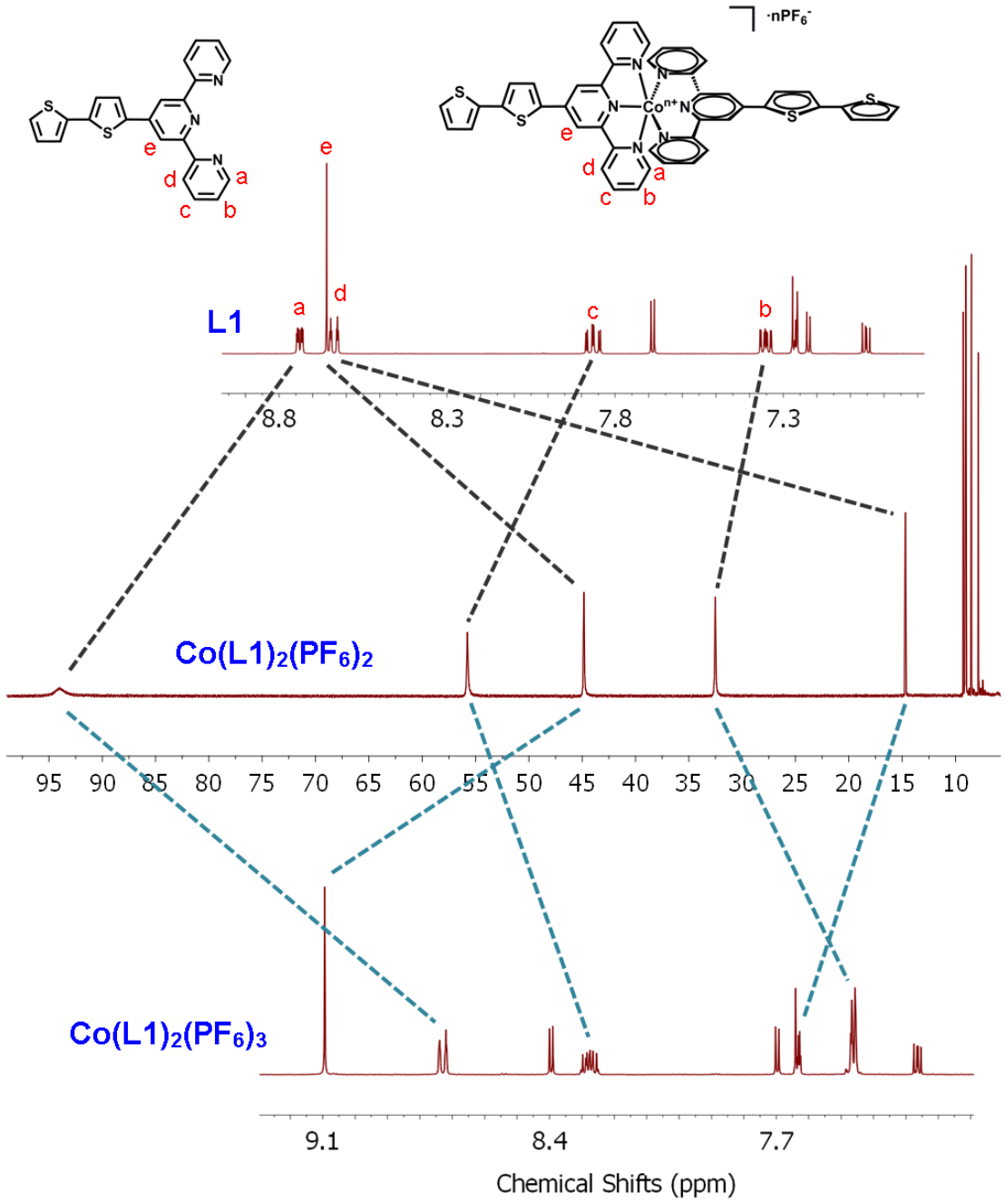

Figure 4.4. Molecular structures and proton NMR of ligand **L1** and the cobalt complexes of +2 and +3 oxidation states from this ligand.

Proton NMR spectra of **L1**, **Co^{II}L1P**, and **Co^{III}L1P** are presented in Figure 4.4. With a $3d^7$ electron configuration, octahedral complexes of cobalt(II) will possess at least one unpaired electron. The ^{1}H NMR spectra of cobalt(II) complexes are subjected to two effects associated with the paramagnetism of the metal centre. Firstly, the local magnetic field at the protons will be significantly different from the applied field due to the magnetic field caused by the unpaired electrons. Secondly, the signals will be broadened because of the coupling between electronic and magnetic spin. As a consequence of the combined effect, the ^{1}H NMR spectra of cobalt(II) complexes are paramagnetically shifted over a chemical shift range of several ten or hundred ppm and are typically broadened causing the loss of any *J* coupling information. As shown in Figure 4.4, the ^{1}H NMR spectrum of **Co^{II}L1P** in CD_3CN shows the significant shift in the signal of protons on terpyridine moiety, indicating the paramagnetic effect of Co(II) center. Complexes of Co(III) ion ($3d^6$), on the other hand, could be paramagnetic or diamagnetic depending on the electron configuration of the metal center. The ^{1}H NMR spectrum of **Co^{III}L1P** does not exhibit any significant shift from the normal chemical shift range for proton NMR suggesting a diamagnetic behavior for the low spin Co(III) center. The result is consistent with the fact that most Co(III) complexes are low spin at room temperature due to the strong ligand field strength caused by the high-oxidation-state ions.

In addition, another ligand system with 2,6-*bis*(thiazol-2-yl)pyrindine (**L2**) moiety was synthesized using the same synthetic procedure to prepare **L1** (Scheme 4.3) in order to explore the effect of ligand strength field caused by the coordination site on the ligand. A cobalt(II) complex with hexafluorophosphate as the counter anion, **$Co(L2)_2(PF_6)_2$** (**Co^{II}L2P**), was obtained in a similar manner to **Co^{II}L1P**. Our attempts to synthesize the cobalt(III) complex with **L2** were not successful.

Scheme 4.3. Synthesis of ligand **L2**.

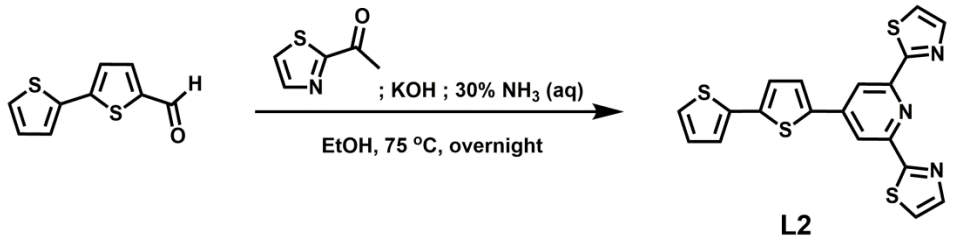

4.2.1.3. Iron(II) Complexes

2,6-*bis*(pyrazol-1-yl)pyridine was chosen for the coordination environment for iron(II) complexes as it has been shown to favor SCO for Fe(II) compounds.[11-13] Although the chemical skeleton of **L3** is similar to that of **L1** and **L2**, the synthetic route for this ligand is very different. Scheme 4.4 shows the synthesis of **L3** and its Fe(II) tertrafluoroborate complex, **$Fe(L3)_2(BF_4)_2$** (**Fe^{II}L3B**).

Scheme 4.4. Synthesis of ligand **L3** and its corresponding iron(II) complex.

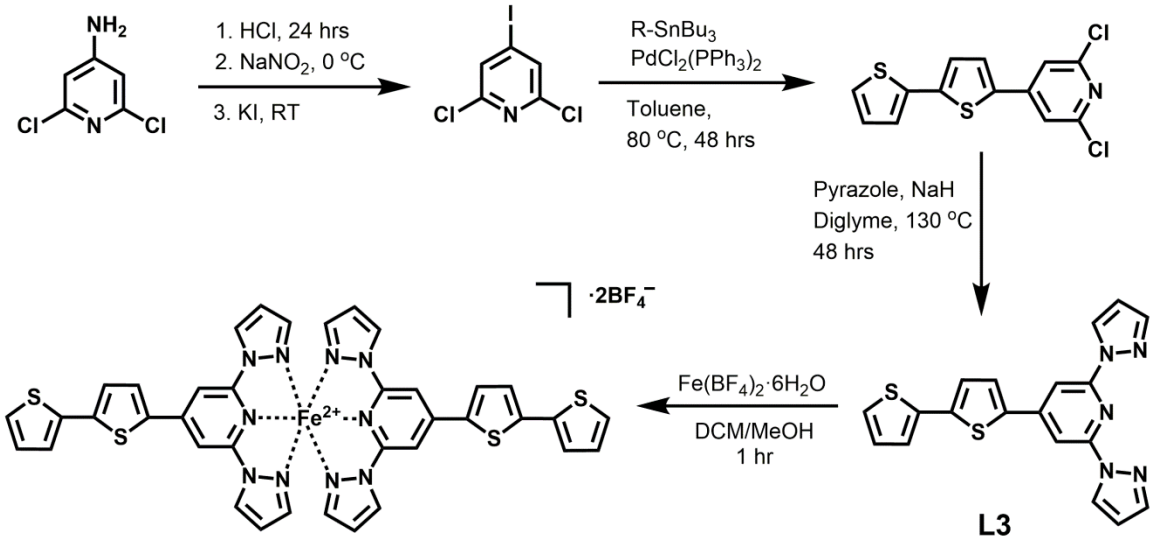

4.2.2. Structure Determination

4.2.2.1. Cobalt(II) Complexes

Crystals suitable for single-crystal X-ray diffraction study of **Co^{II}L1N** were obtained by the slow evaporation from a methanol solution. The crystal structure of **Co^{II}L1N** is shown in Figure 4.5 and is a representative example of the binding manner of the three ligands (**L1-L3**) in metal complexes. The structure of **Co^{II}L1N** contains the $[\mathbf{Co(L1)_2}]^{2+}$ cation and two nitrate anions, accompanied by one methanol solvate molecule. Two **L1** ligand molecules are bound to a Co(II) cation through the three nitrogen atoms of the terpyridine moiety and are perpendicular to each other. The Co–N average bond distance is 2.014 Å, which is in typical range observed for similar cobalt complexes.[14] The Co–N bond distance to the central pyridyl ring of the terpyridine moiety (1.902 Å) is slightly shorter than the other two pyridyl rings (2.070 Å).

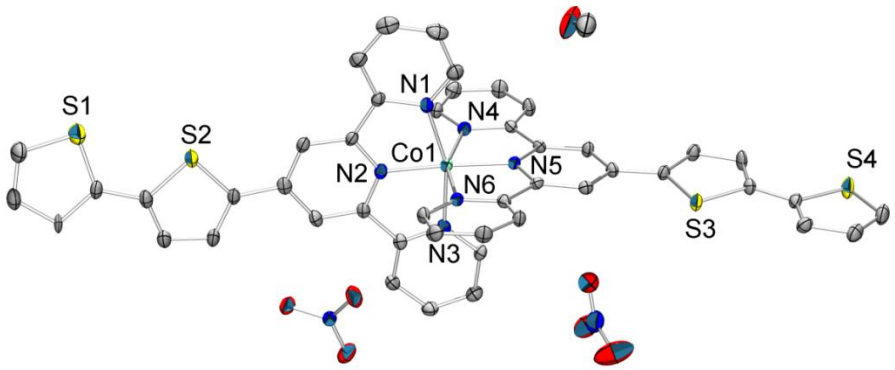

Figure 4.5. ORTEP view of molecule **$Co(L1)_2(NO_3)_2\cdot MeOH$**, drawn with the thermal ellipsoids at the 50% probability level. Hydrogen atoms have been omitted for clarity.

The solid-state structure of **Co^{II}L1P** is very similar to that of **Co^{II}L1N** except that there is no solvent within the crystal unit cell (Figure 4.6). This feature is favorable for our study since the solvents are shown to produce a significant effect on the SCO

behavior of metal complexes. Additionally, our ultimate goal is to synthesize SCO conducting metallopolymers, which is not likely to contain solvents. Therefore, the hexaflourophosphate complexes were chosen to prepare the metallopolymer and for further characterization and studies. The average distance for Co-N bonds in **Co^{II}L1P** (2.028 Å) is longer than in **Co^{II}L1N**. The Co–N bond distance to the central pyridyl ring of the terpyridine moiety (1.918 Å) is also shorter than the other two pyridyl rings (2.083 Å), which is likely due to the Jahn-Teller effect of Co(II) complexes.

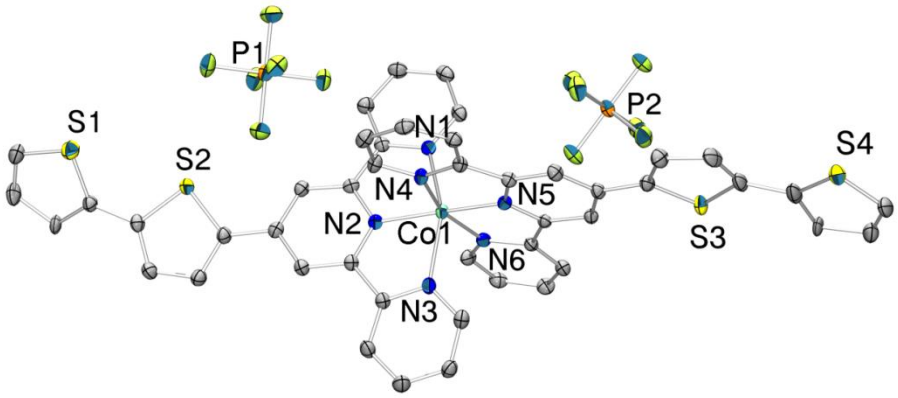

Figure 4.6. ORTEP view of molecule **$Co(L1)_2(PF_6)_2$**, drawn with the thermal ellipsoids at the 50% probability level. Hydrogen atoms have been omitted for clarity.

Slow evaporation of **Co^{II}L2P** in acetonitrile solution was used to grow single crystals suitable for X-ray diffraction. An ORTEP view of the crystal structure of **Co^{II}L2P** is presented in Figure 4.7, showing no solvent in the crystal lattice. The Co(II) center is six-coordinate in a distorted octahedral geometry. The Co(II) center is bound to two ligand molecules *via* two nitrogen atoms from the thiazole rings and one nitrogen atom from the pyridine ring. The Co-N distances involving the thiazole unit are longer (2.056 Å) than the pyridine one (2.170 Å).

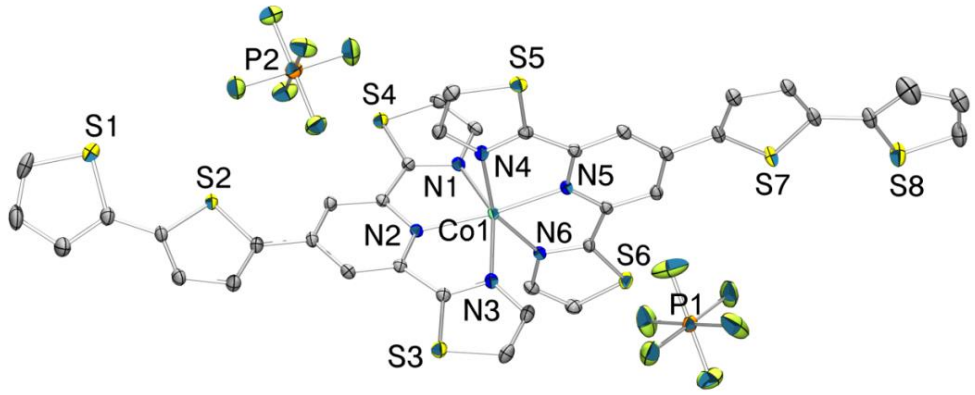

Figure 4.7. ORTEP view of molecule $\mathbf{Co(L2)_2(PF_6)_2}$, drawn with the thermal ellipsoids at the 50% probability level. Hydrogen atoms have been omitted for clarity.

4.2.2.2. Cobalt(III) Complexes

The solid-state structure of cobalt(III) complex $\mathbf{Co^{III}L1N}$ contains two tridentate chelating **L1** ligands as shown in Figure 4.8. The complex has a distorted octahedral geometry, and the two rigid tridentate chelating ligands are the main factors accounting for this distortion. The Co−N distances show the typical trend for Co(III) terpyridine complexes with bonds to the central pyridine ring (1.860 Å) being significantly shorter than those to the terminal rings (1.953 Å). The average Co–N distance for the complex is 1.922 Å, which is in agreement with the values reported for similar structures of Co(III). These shorter bond lengths in the cobalt(III) complex are expected because of the smaller radius of the Co^{3+} ion.

Crystals suitable for single-crystal X-ray diffraction study of $\mathbf{Co^{III}L1P}$ were obtained by the slow evaporation from a acetonitrile solution. Complex $\mathbf{Co^{III}L1P}$ crystallizes with a $[\mathbf{Co(L1)_2}]^{2+}$ cation, three hexafluorophosphate anions, and three acetonitrile solvate molecules (Figure 4.9, acetonitrile molecules are not shown). The molecular structure of this complex has the same cationic structure as that of $\mathbf{Co^{III}L1N}$. All bond lengths are normal with an average Co-N bond distance of 1.916 Å and with

shorter distances to central pyrindine rings than the terminal ones (1.858 Å versus 1.945 Å).

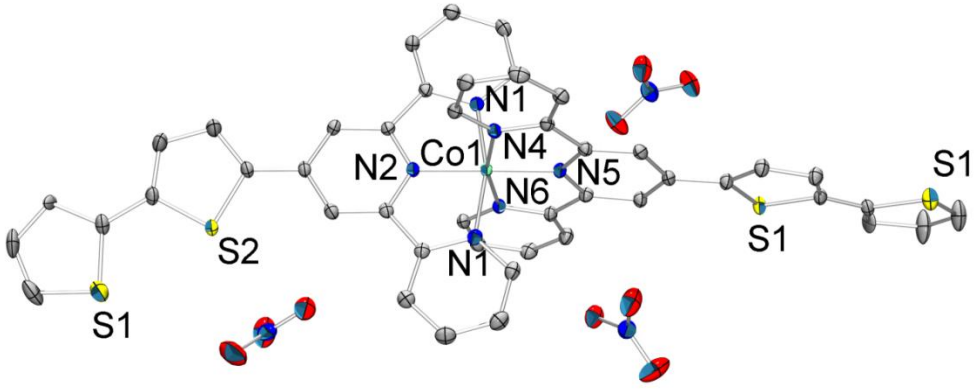

Figure 4.8. ORTEP view of molecule **$Co(L1)_2(NO_3)_3$**, drawn with the thermal ellipsoids at the 50% probability level. Hydrogen atoms and solvent molecules have been omitted for clarity.

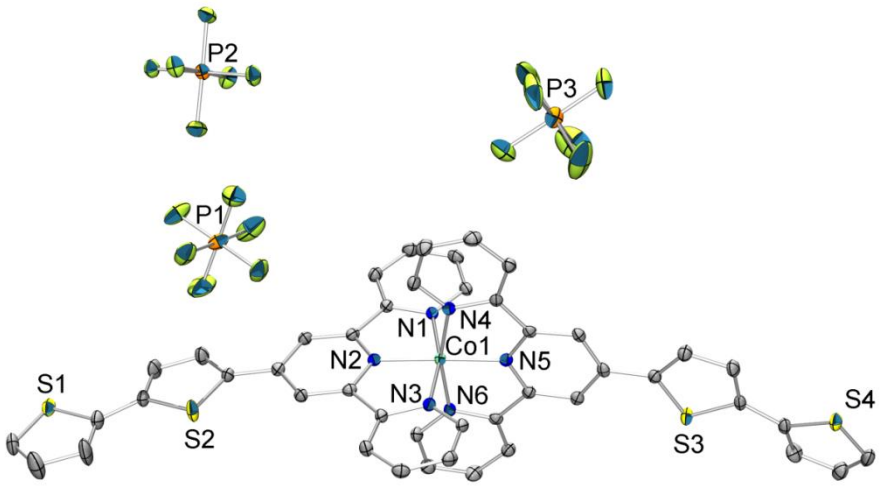

Figure 4.9. ORTEP view of molecule **$Co(L1)_2(PF_6)_3$**, drawn with the thermal ellipsoids at the 50% probability level. Hydrogen atoms and solvent molecules have been omitted for clarity.

4.2.2.3. Iron(II) Complexes

X-ray quality crystals were obtained by slow evaporation of a **Fe^{II}L3B** solution in acetone. The solid-state structure of **Fe^{II}L3B** shows a distorted octahedral geometry around Fe(II) center (Figure 4.10). The plane-plane angle between the two *bis*(pyrazol-1-yl)pyridine moieties is 101.56 ^{o}, which is significantly larger than that of the two tridentate ligand in cobalt complexes (98.80-91.24 ^{o}). The bond angle between nitrogen atoms of the two central pyridine rings with Fe(II) is 153.82 ^{o}. The Fe-N bond distances to the nitrogen atoms of pyridine rings (2.144 Å) are slightly shorter than the nitrogen atoms on the pyrazole rings (2.192 Å).

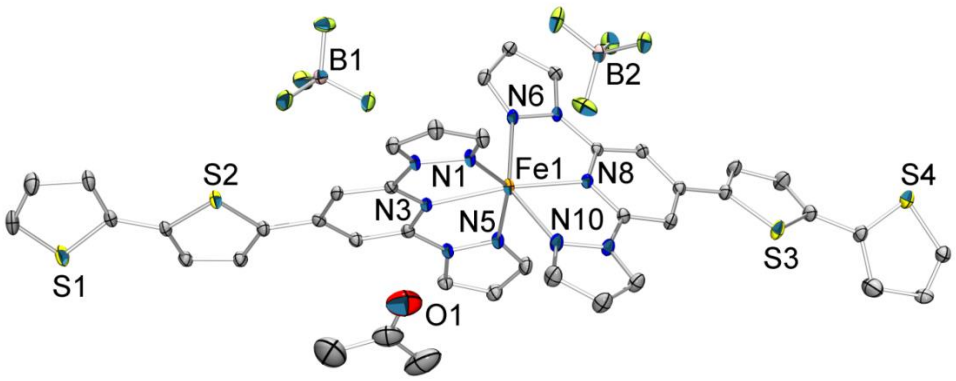

Figure 4.10. ORTEP view of molecule **$Fe(L3)_2(BF_4)_2$·acetone**, drawn with the thermal ellipsoids at the 50% probability level. Hydrogen atoms have been omitted for clarity.

4.2.3. Polymer Syntheses and Characterization

4.2.3.1. Cobalt(II) Metallopolymers

Electropolymerization of complex **Co^{II}L1P** was performed by continuous cycling the potential of working electrodes between -0.75 V and +1.10 V (Figure 4.11A). The first scan shows an oxidation peak at ca. -0.1 V for $Co^{2+/3+}$ redox couple and another peak

at 0.9 V for bithiophene oxidation. These peaks increase linearly with the increasing scans, indicating a continuous growth the polymer on the electrode surface. A reduction peak for $Co^{3+/2+}$ conversion is found at -0.2 V. Figure 4.11B shows the electrochemical scan rate dependence study of the electrode-confined film of poly-**Co^{II}L1P** in a monomer-free electrolyte solution. The inset for Figure 4.11B displays a linear relationship between the current of $Co^{2+/3+}$ in poly-**Co^{II}L1P** and the electrochemical scan rate, up to 500 mV/s. This linear relationship indicates that the electrode-confined film is an electroactive polymer that is not limited by the ionic flux of counter ions.

Scheme 4.5. Electrochemical polymerization of complex **Co^{II}L1P**.

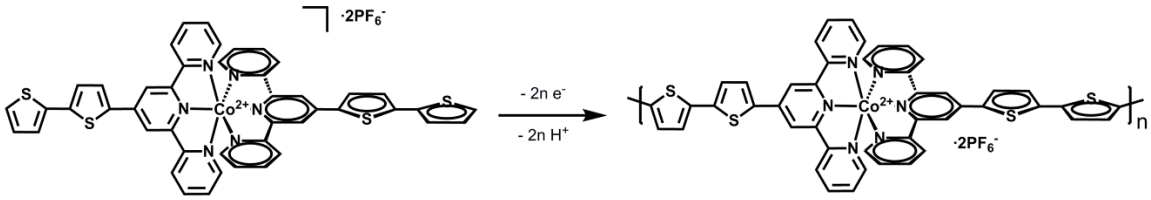

X-ray photoelectron spectroscopy (XPS) was used to determine the film composition and metal coordination environment for poly-**Co^{II}L1P**. Co $2p_{1/2}$ and $2p_{3/2}$ peaks are observed at 782.6 and 797.8 eV, respectively. The S 2*p* peak is found at 163.75 eV. Quantitative XPS analysis reveals that poly-**Co^{II}L1P** film has an atomic ratio of Co : S = 1 : 4.26, which is in agreement with the stoichiometric molar ratio of the proposed polymer structure (Co : S = 1 : 4, Scheme 4.5).

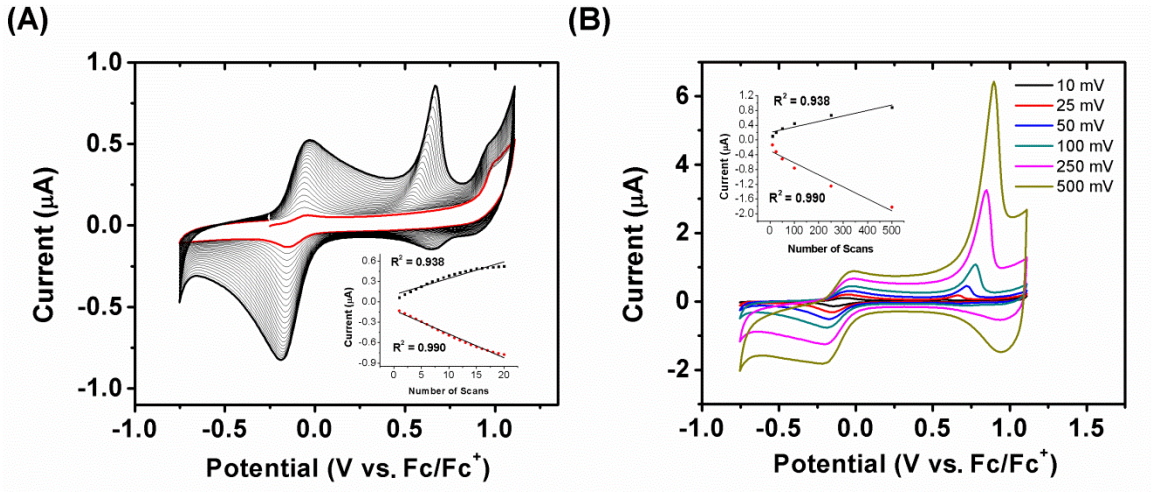

Figure 4.11. (A) Cyclic voltammogram of **Co^{II}L1P** . Insets show the linear relationship between peak polymer oxidation/reduction currents and number of scans. (B) Scan rate dependence study of **poly- Co^{II}L1P**. Inset: plot of current *versus* scan rate.

Cobalt(II) complex monomer **Co^{II}L2P** was used for electrochemical synthesis of poly-**Co^{II}L2P** in similar conditions to poly-**Co^{II}L1P** (Scheme 4.6). A typical electropolymerization of **Co^{II}L2P** onto a Pt button electrode is shown in Figure 4.12A. The linear increase in the polymer oxidation peak corresponding with the increase of number of CV scans indicates the growing progress of the metallopolymer after each electrochemical cycle. The composition of poly-**Co^{II}L2P** was determined by XPS, and the data plots for poly-**Co^{II}L2P** films are shown in Figure 4.12B-D. Co $2p_{1/2}$ and $2p_{3/2}$ peaks are observed at 782.6 and 797.8 eV, respectively. The S 2*p* peak is found at 163.75 eV showing multiple peaks and is deconvoluted into two different signals, which is consistent with the two types of sulfur found in thiophene and thiazol rings in **Co^{II}L2P**. Quantitative XPS analysis of poly-**Co^{II}L2P** yields an atomic ratio of Co : S = 1 : 8.08. This is consistent with the predicted stochiometric ratio of 1 : 8 in the proposed polymer structure.

Scheme 4.6. Electrochemical polymerization of complex **Co^{II}L2P**.

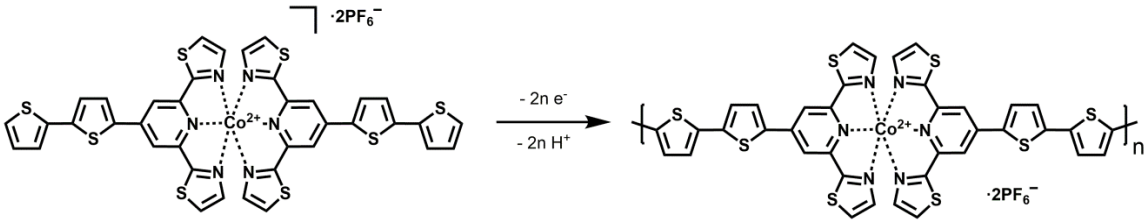

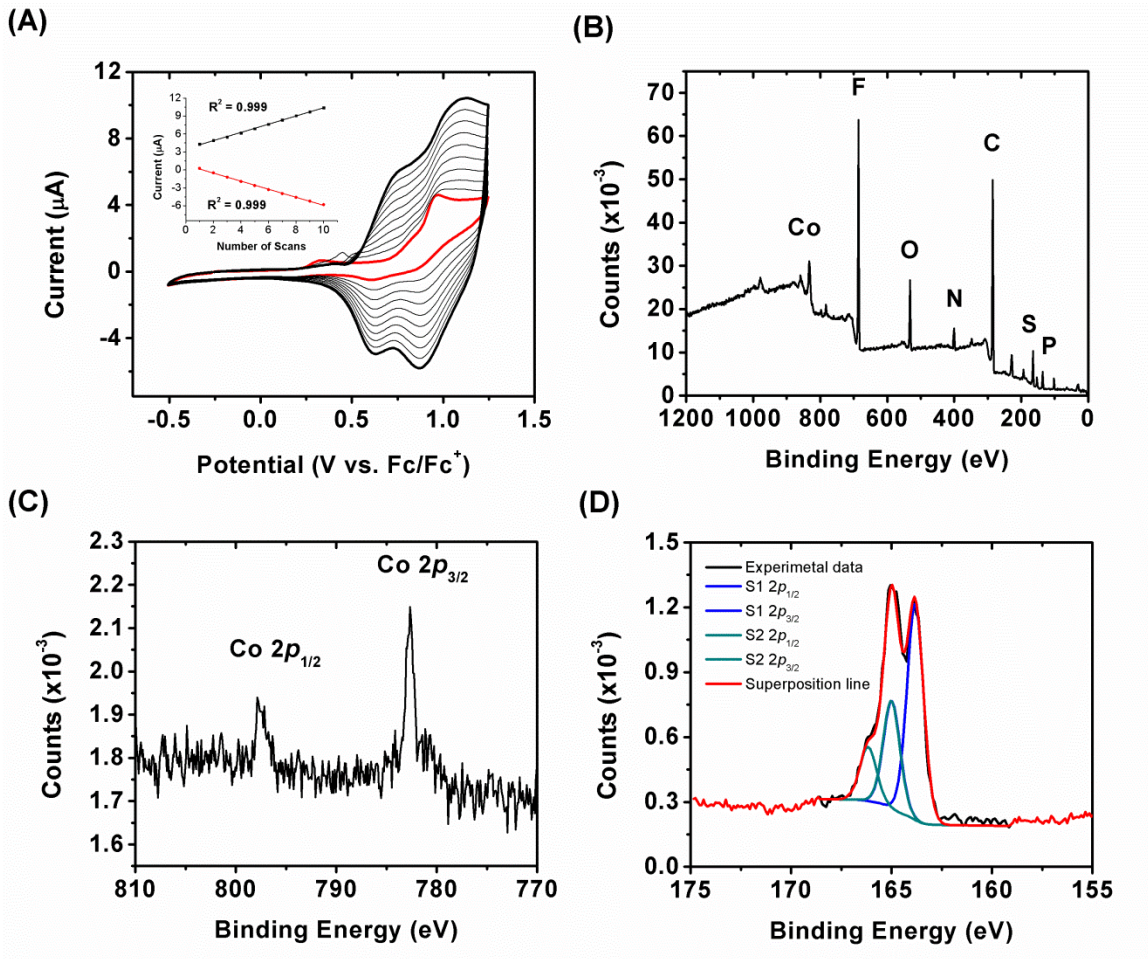

Figure 4.12. (A) Electropolymerization of **Co^{II}L2P**. Insets show the linear relationship between peak polymer oxidation/reduction currents and number of scans. (B) XPS survey scan, (C) Co *2p* XS spectra, and (D) S *2p* XS spectra of poly-**Co^{II}L2P**. Note: S1 $2p_{1/2}$ and S2 $2p_{3/2}$ peaks are not resolved.

4.2.3.2. Iron(II) Metallopolymers

Cyclic voltammetry of **Fe^{II}L3B** over a potential window of -0.75 to 1.25 V resulted in the growth of a polymer film (Figure 4.13). The first scan has oxidation peaks around 0.8 and 1.1 V, and reduction peaks at 0.74 and 0.49 V. As the number of scans is increased, the peak corresponding to monomer oxidation steadily becomes more positive and grows linearly with increasing scans. The inset of Figure 4.13A shows a linear relationship between the oxidative and reduction current and the number of scans, indicating that uniform polymer growth occurs up to 10 electrochemical scans. A study of the electrochemical scan-rate dependence of the polymer films (Figure 4.13B) in pure electrolyte solution revealed a linear relationship of observed current with the scan rate in the range of 10-500 mV/s. This linear dependence is a characteristic observation of a strongly absorbed electroactive film in which current is not limited by the diffusion of counter ions.

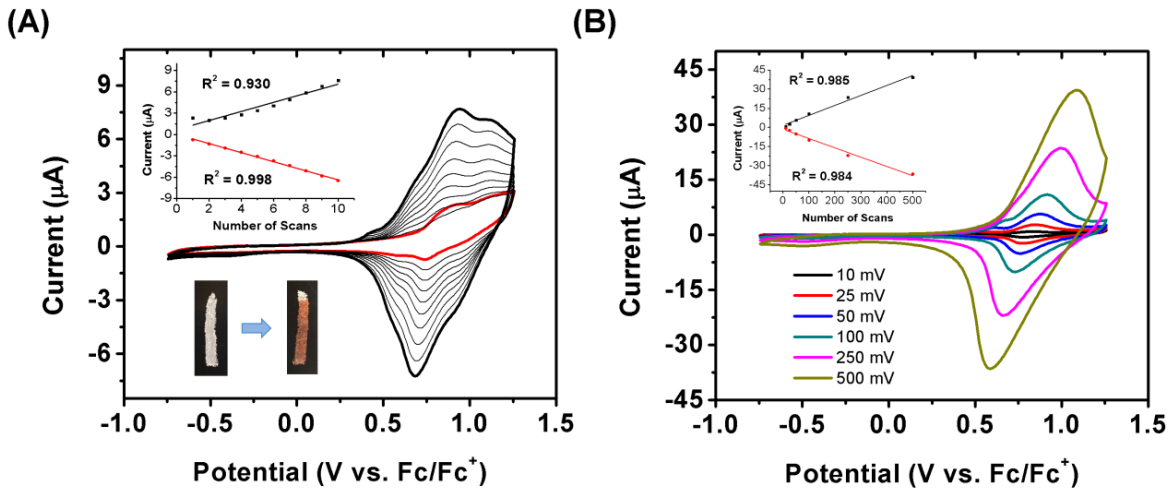

Figure 4.13. (A) Cyclic voltammogram of **Fe^{II}L3B**. Insets show the linear relationship between peak polymer oxidation/reduction currents and number of scans and a photograph of poly-**Fe^{II}L3B** on Pt mesh. (B) Scan rate dependence study of poly-**Fe^{II}L3B**. Inset: plot of current *versus* scan rate.

Scheme 4.7. Electrochemical polymerization of complex **Fe^{II}L3B**.

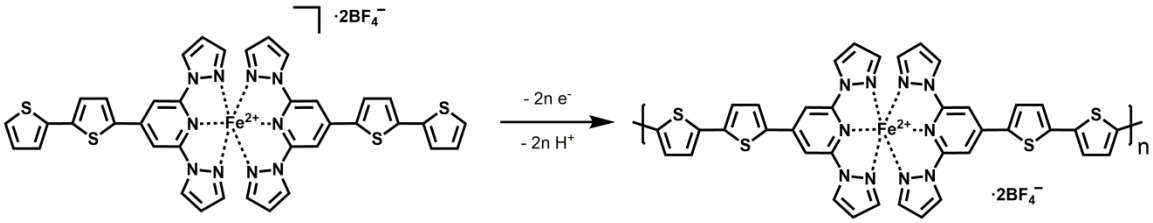

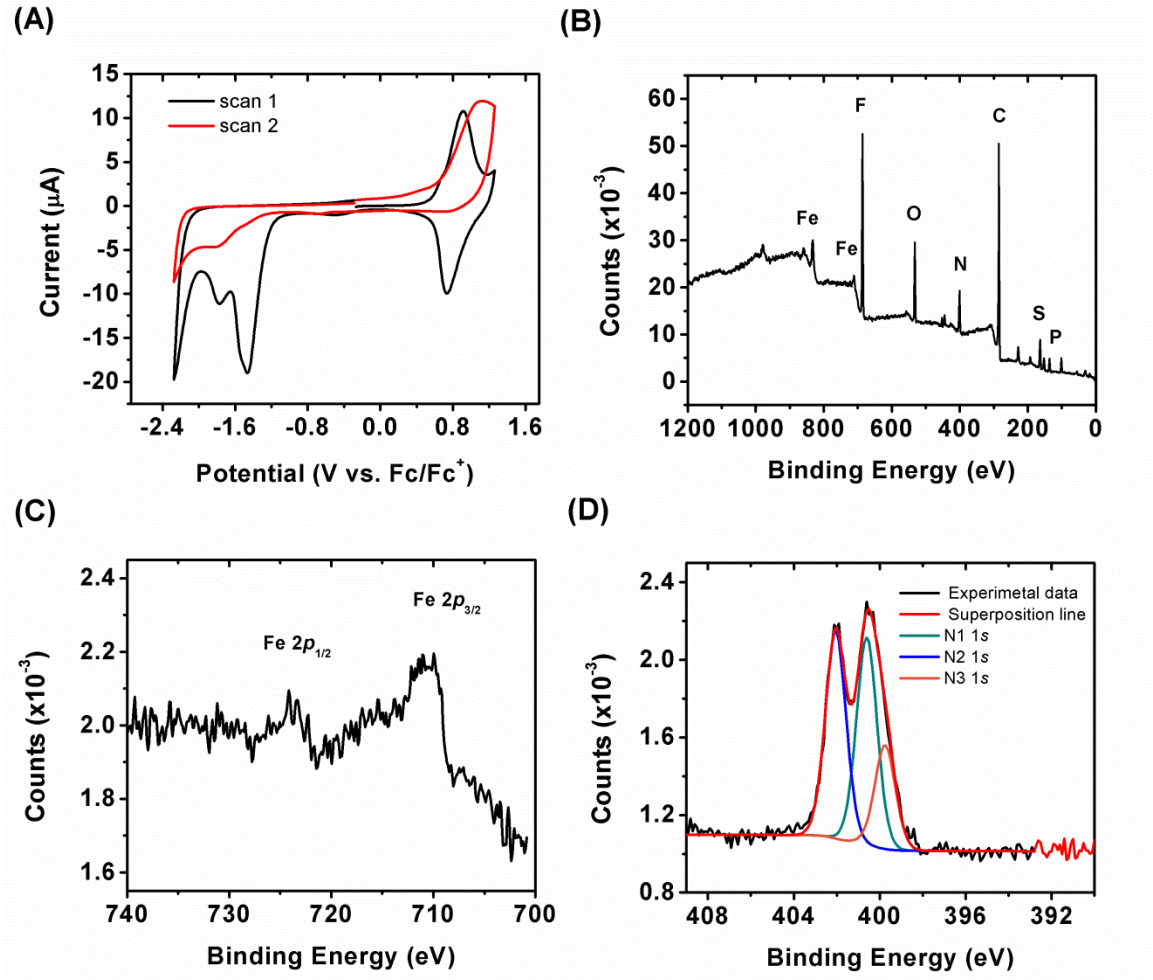

Figure 4.14. (A) Cyclic voltammogram of poly-**Fe^{II}L3B** in 0.1 M $TBAPF_6$ in CH_2Cl_2. (B) XPS survey scan, (C) Fe *2p* XS spectra, and (D) N 1*s* XS spectra of poly-**Fe^{II}L3B**.

Cyclic voltammogram of poly-**Fe^{II}L3B** reveals that this polymer is decomposed when sweeping the potential on the working electrode to the far negative potential, ca. -2.2 V (Figure 4.14A). However, the polymer is highly stable at a potential window from -0.75 V to 1.25 V with no loss in oxidation current of polymer up to 5 CV scans. The result suggests that reduction of the ligand may facilitate the cleavage of the pyrazole rings therefore causing the polymer degradation. The XPS data were used to determine the film composition and metal coordination environment of poly-**Fe^{II}L3B** (Figure 4.14B-D). Fe $2p_{1/2}$ and $2p_{3/2}$ peaks are observed at 723.6 and 710.7 eV, respectively. The S 2*p* peak is found at 163.75 eV while the N 1*s* peak is observed in the 398-404 eV region revealing multiple peaks and is deconvoluted into three different signals with an atomic ratio of 2 : 2 : 1. The deconvoltion of the N 1*s* peak is in high agreement with the three different types of nitrogen atoms and the present relative ratio found in poly-**Fe^{II}L3B** (Scheme 4.7). Quantitative XPS analysis of poly-**Fe^{II}L3B** films yields an atomic ratio of Fe : S : N = 1 : 4.30 : 10.11, which is consistent with the predicted stochiometric ratio of 1 : 4 : 10 in the proposed polymer structure.

UV-Vis-NIR spectroelectrochemistry was then performed to investigate the redox-dependent electronic states of poly-**Fe^{II}L3B**. As shown in Figure 4.15, upon electrochemical oxidation of the polymer film, two new peaks at 725 nm and 1170 nm appear in the absorption spectra of poly-**Fe^{II}L3B** films due to the formation of polarons (radical cations) within the polymer backbone (Figure 4.15). Further oxidation of the polymer resulted in the diminishment of these two bands and the growth of a new band at 832 nm. This can be attributed to the conversion of the polarons to bipolarons (dications).

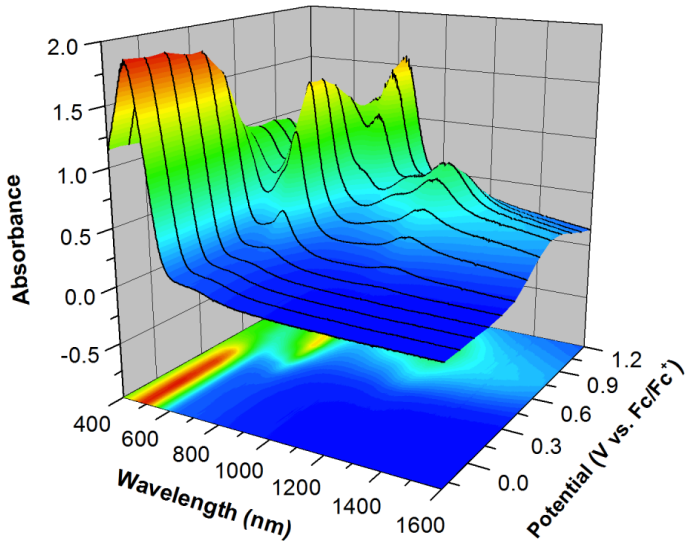

Figure 4.15. Spectroelectrochemistry of poly-**Fe^{II}L3B** measured on ITO-coated glass in 0.1 M $TBAPF_6/CH_2Cl_2$ electrolyte solution at -0.25 to 1.25 V vs. Fc/Fc^+.

4.2.4. Magnetic Property Studies

Magnetic properties of cobalt and iron complexes were obtained by superconducting quantum interference device (SQUID) measurements. Variable-temperature magnetic susceptibility of cobalt(II) complexes, **Co^{II}L1P** and **Co^{II}L2P**, are shown in Figure 4.16. At 300 K, the $\chi_m T$ product of 1.75 cm^3 K mol^{-1} (3.73 μ_B) effective is observed for **Co^{II}L1P**, which is consistent with HS cobalt(II) (S = 1/2) in an octahedral environment. Upon cooling, a gradual spin transition is observed ca. 270 K. At 70 K the $\chi_m T$ product for **Co^{II}L1P** is 0.37 cm^3 K mol^{-1} (1.72 μ_B), which is in good agreement with the spin-only value (1.73 μ_B) expected for a LS cobalt(II) center (S = 1/2). This value remains relatively constant down to 5 K. Upon heating again, a gradual increase in magnetic moment starting from 70 K is observed and SCO transition reached nearly complete at 300 K (Figure 4.16A). Three consecutive thermal cycles were performed revealing that the magnetic behavior is reproducible and hence fully reversible. No thermal hysteresis was observed in the SCO for this complex.

A magnetic study for **Co^{II}L2P**, on the other hand, shows that only the HS state is found for the Co(II) center in the entire temperature range of 5-300 K. the $\chi_m T$ product of 2.1 cm^3 K mol^{-1} (4.1 μ_B) was observed at 300 K for **Co^{II}L2P**. This value only decreases to a 1.6 cm^3 K mol^{-1} (3.5 μ_B) at 5 K, indicating the majority of the complex is still in the HS state (Figure 4.16).

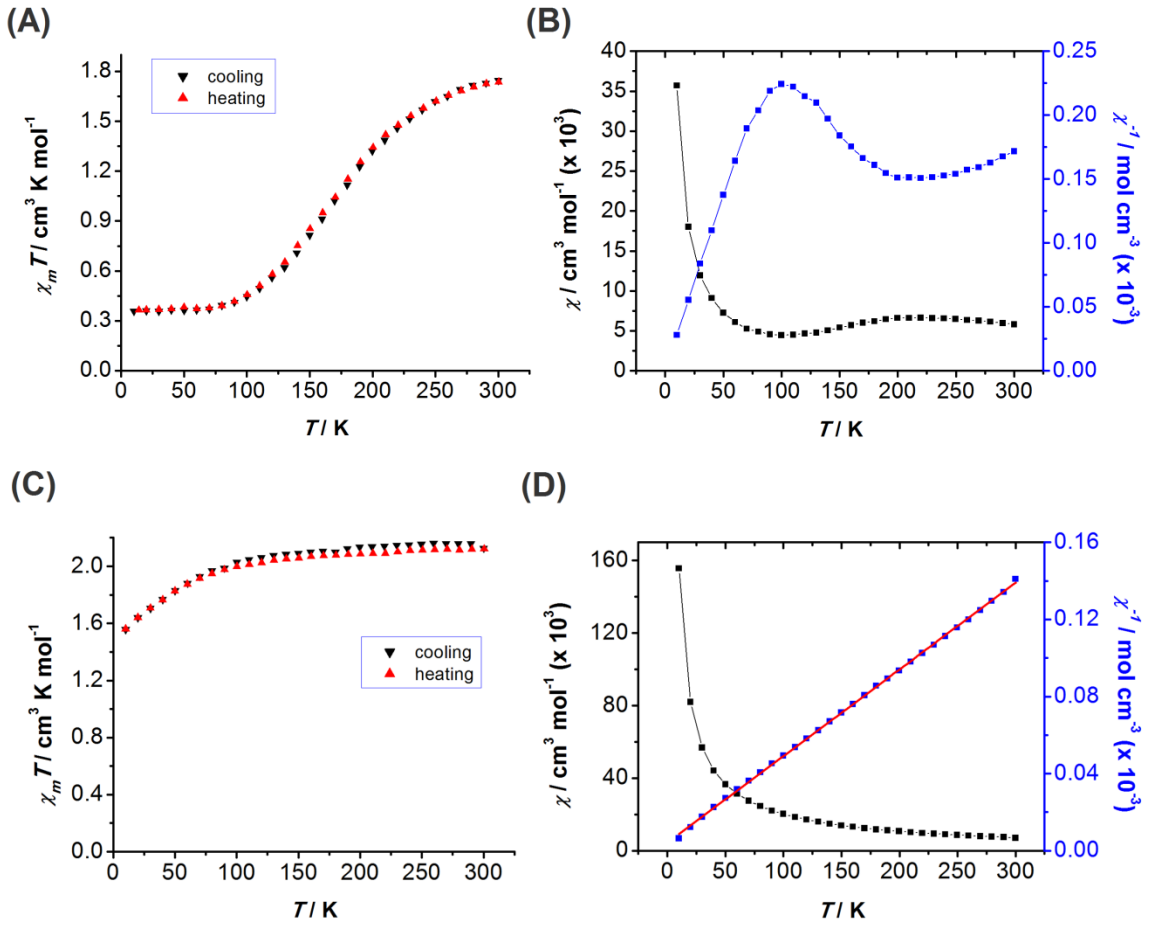

Figure 4.16. (A) Plots of observed $\chi_m T$ vs. T for **Co^{II}L1P**. (B) Plots of χ_m vs. T (black) and χ_m^{-1} vs. T (blue) for **Co^{II}L1P**. (C) Plots of observed $\chi_m T$ vs. T for **Co^{II}L2P**. (D) Plots of χ_m vs. T (black) and χ_m^{-1} vs. T (blue) for **Co^{II}L2P**.

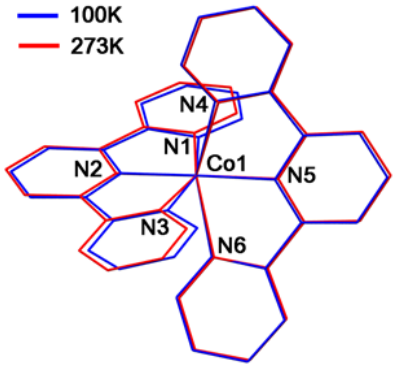

Bond Length (Å)	100 K	273 K
Co-N1	2.002	2.123
Co-N2	1.848	2.019
Co-N3	2.009	2.151
Co-N4	2.158	2.170
Co-N5	1.949	2.026
Co-N6	2.163	2.157

Figure 4.17. Overlay of the core structures and Co-N bond distances of **Co^{II}L1P** crystal structures measured at 100 K and 273 K.

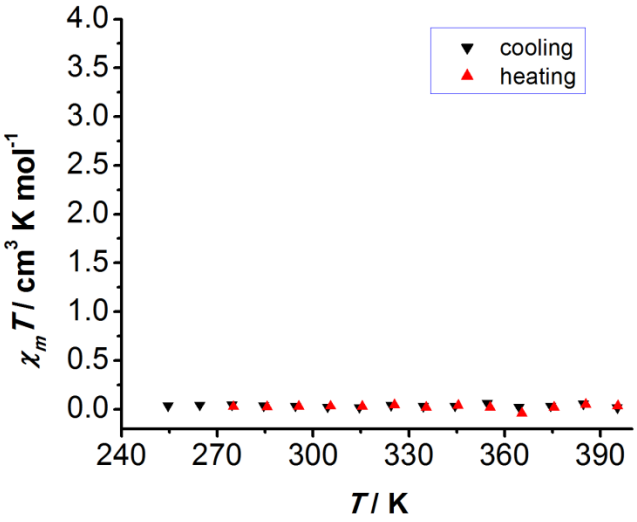

Figure 4.18. Plots of observed $\chi_m T$ vs. T for **Co^{III}L1P**.

In order to investigate the structural changes due to the SCO in **Co^{II}L1P**, we performed the variable-temperature X-ray single-crystal studies. An overlay of the core structures of **Co^{II}L1P**, Co(II) center and the two terpyridine moieties, at 100 K and 273 K is shown in Figure 4.17. The magnetic data illustrate the presence of complex **Co^{II}L1P** in LS and HS states at 100 K and 273 K, respectively. The SCO in **Co^{II}L1P** induces a Jahn-

Teller-influenced change from compressed (at 273 K) to elongated (at 100 K) octahedral coordination of cobalt(II). The X-ray analysis data show an increase of 4.8% in the volume of crystal unit cells accompanied by the spin transition from LS to HS states. This volume change is less significant than observed for other SCO complexes (~ 10%), which is likely due to the large portion occupied by the organic ligands.

Due to the LS behavior at room temperature of **Co^{III}L1P**, observed by NMR spectroscopy, the magnetic moment study for this complex was measured from 250 K to 400 K. As shown in Figure 4.18, **Co^{III}L1P** exhibits a LS behavior up to 400 K with no SCO found. The results reveal that at room temperature (ca. 300 K), changing metal oxidation states (from Co^{+2} to Co^{+3}) leads to the change of the magnetic property from a paragmagnetic to a diamagnetic behavior. This result is in agreement with what we proposed in Figure 4.2B. Current efforts in this study are focused on investigating the change in magnetic moment when altering the oxidation of conducting metallopolymers synthesized from these two cobalt complexes.

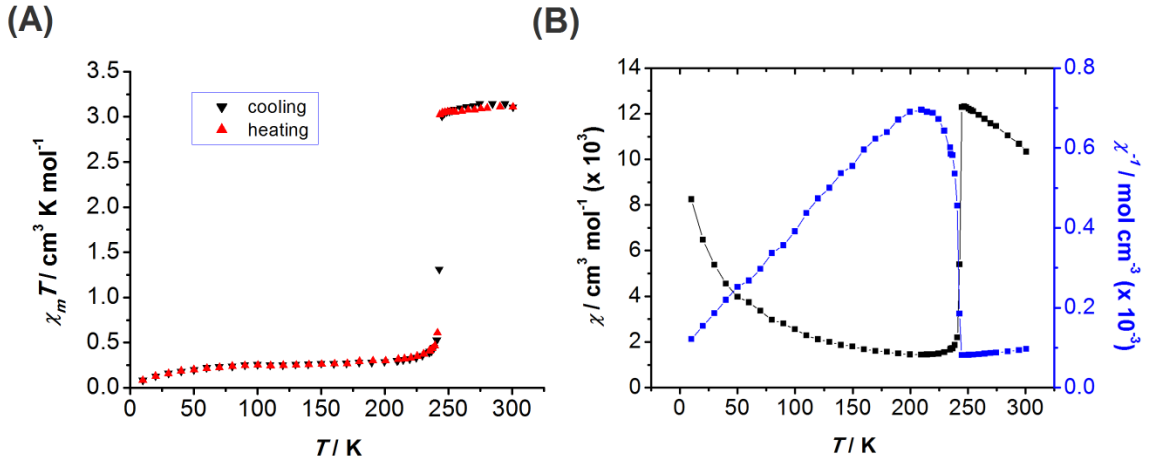

Figure 4.19. Plots of observed (A) $\chi_m T$ vs. T and (B) χ_m vs. T (black) and χ_m^{-1} vs. T (blue) for **Fe^{II}L3B**.

The SCO transition is also observed in the iron(II) complex from **L3**. The $\chi_m T$ product of a **Fe^{II}L3B·actetone** microcrystalline sample at 300 K is 1.75 cm^3 K mol^{-1} (5.0 μ_B), in agreement with the spin-only magnetic moment of 4.90 μ_B for the high spin iron(II) (S = 2). Upon cooling, the compound undergoes an abrupt SCO transition to a low-spin state (S = 0) with the $T_{1/2}$ = 242.7 K. No thermal hysteresis loop is observed for this SCO transition. The $\chi_m T$ value of 0.08 (0.78 μ_B) at 5 K indicates the almost complete SCO of the iron(II) centers (Figure 4.19). Interestingly, the SCO was only observed for acetone-solvated complex with a change from yellow crystals to brown-yellow samples. Crystals grown from a solution of other solvents (e.g., acetonitrile) or the unsolvated powder form of **Fe^{II}L3B**, which appear brown in color, do not undergo any spin transition and are in an LS state. The effect of solvents on SCO behavior of metal complexes can be explained by the influence of solvent molecules on the packing mode of meal complexes in the unit cell, thereby affecting the intermolecular interaction and magnetic properties. Ozaka *et al.* also observed similar behavior of iron(II) complexes with *bis*(pyrazol-1-yl) ligand.[13]

Our attempts on the magnetic moment studies of the conducting metallopolymers (section 4.2.3) were not successful due to the small amount of metallopolymers obtained from electropolymerization method (< 0.1 mg) and the large effect of conductive substrate. Current efforts are focused on synthesizing these metallopolymers by chemical methods so that a sufficient quantity of samples can be obtained for SQUID measurements.

4.4. CONCLUSION

We reported the synthesis and characterization of novel cobalt(II), cobalt(III), and iron(II) complexes from one known (**L1**) and two novel ligands (**L2** and **L3**). A magnetic

moment study of these compounds, investigated by SQUID measurements, reveals a gradual spin transition for Co(II) complex from **L1** and an abrupt SCO transition for the compound from Fe(II) and **L3**. Moreover, all complexes show facile polymer growth under electropolymerization conditions. Our approach to achieve an "electrically spin-switchable" metallopolymer was supported by the magnetic moment studies of the monomer forms, $\mathbf{Co^{II}L1P}$ and $\mathbf{Co^{III}L1P}$ complexes. Current efforts are focusing on the metallopolymer synthesis *via* chemical method in order to obtain sufficient quantity of sample for further investigation.

4.4. EXPERIMENTAL

4.4.1. General Methods

Air- and moisture-sensitive reactions were carried out in flame-dried glassware using standard Schlenk techniques under an inert nitrogen atmosphere. All chemicals were purchased from commercial sources and used as received. Dry solvents were dried using an Innovative Technology, Pure Solv solvent purifier with a double purifying column. ^{1}H NMR (400 MHz) and ^{13}C $\{^{1}$H$\}$ NMR (100 MHz) spectra were obtained on a Varian (400 MHz) spectrometer and were referenced to residual solvent peaks. All peak positions are given in ppm and coupling constants are reported in Hz. Low-resolution and high-resolution mass spectrometry was carried out by a Thermo Finngan TSQ 700 and Waters Autospec Ultima, respectively. Melting points were recorded with an OptiMelt Automated Melting Point System with digital image processing technology from Stanford Research System (SRS, Sunnyvale, CA). Elemental analysis was performed by Midwest Microlab, Indianapolis, IN (www.midwestlab.com). Infrared spectra were recorded using a Nicolet IR 200 FTIR spectrometer. X-ray photoelectron spectroscopy (XPS) was carried out on a PHI 5700 XPS system equipped with dual Mg X-ray source

and monochromatic Al X-ray source complete with depth profile and angle-resolved capabilities. The DC magnetization was measured with a commercial superconducting quantum interference device (SQUID) magnetometer. 2,6-dichloro-4-iodopyridine was prepared as reported in the literature.[15] 5-formyl-2,2‘-bithiophene, 2-acetyl pyridine, 2-acetyl thiazole, and commercially available reagents were used without further purification.

4.4.2. Crystal Structure Determination

The single–crystal diffraction data were collected on a AFC12 diffractometer with a Saturn 724+ CCD, a Nonius Kappa CCD diffractometer, or a Rigaku SCX-Mini diffractometer with a Mercury CCD using a graphite monochromator with MoKα radiation (λ = 0.71073 Å). Absorption corrections were applied using multi-scan technique using either Abscor[16] for the Rigaku data or Scalepack[17] for the Nonius data. Data reduction were performed using the Rigaku Americas Corporation’s Crystal Clear version 1.40.[18] The structures were solved by direct methods and refined anisotropically using full-matrix least-squares methods with the SHELX 97 program package.[19] The coordinates of the non-hydrogen atoms were refined anisotropically, while hydrogen atoms were included in the calculation isotropically but not refined. Neutral atom scattering factors and values used to calculate the linear absorption coefficient are from the International Tables for X-ray Crystallography (1992).[20] Crystal data collection and structure refinement details are given in Tables 4.1, 4.2, 4.3, and 4.4.

4.4.3. Electrochemistry

Electrochemical syntheses and studies were performed in a dry-box under an atmosphere of nitrogen using a GPES system from Eco. Chemie B. V. All the electrochemical experiments were carried out in a three-electrode cell with a $Ag/AgNO_3$

reference electrode (silver wire dipped in a 0.01 M silver nitrate solution with 0.1 M [(*n*-Bu)$_4$N]$^+$[PF$_6$]$^-$ in CH$_3$CN), a Pt working electrode, and a Pt wire coil counter electrode. Potentials were relative to this 0.01 M Ag/AgNO$_3$ reference electrode. Ferrocene was used as an external reference to calibrate the reference electrode before and after experiments were performed and that value was used to correct the measured potentials. All electrochemistry and electropolymerizations were performed in dichloromethane (DCM) or acetonitrile (ACN) solutions using 0.1 M [(*n*-Bu)$_4$N]$^+$[PF$_6$]$^-$ (TBAPF$_6$) as the supporting electrolyte. The TBAPF$_6$ was purified by recrystallization three times from hot ethanol before being dried for 3 days at 100-150 °C under active vacuum prior to use. Polymer films were prepared on Delta Technologies ITO-coated glass for spectroscopic measurement and on stainless steel for XPS. Electrosyntheses of the polymer films were performed from monomer solutions by continuous cycling between -0.5 and 1.5 V (vs. Fc/Fc$^+$) at a scan rate of 100 mV/s. The films obtained were then washed with copious amounts of fresh DCM before further experiments.

4.4.4. UV-Vis-NIR Spectroelectrochemistry

The spectroelectrochemical measurements were performed using the previously described cell arrangement on a polymer film deposited on ITO coated glass substrate as working electrode, a platinum mesh as the counter electrode, and Ag/AgNO$_3$ as reference electrode. Experiments were carried out in an optical cuvette inside the glovebox. Absorption spectra were recorded on a Varian Cary 6000i UV-Vis-NIR spectrophotometer within the NIR/visible spectra ($1600 \geq \lambda \geq 400$ nm) under several applied potentials.

4.4.5. Syntheses of Ligands and Metal Complexes

Ligand L1. To a solution of 5-formyl-2,2‘-bithiophene (0.56 g, 3.3 mmol) in ethanol (50 mL), the 2-acetyl pyridine (0.75 mL, 6.7 mmol), potassium hydroxide (0.37 g, 6.6 mmol) were added successively. The solution became yellow. Then, an aqueous solution of ammonia (30 mL, 28%) was added. The mixture was refluxed overnight. A yellow precipitate appeared was filtered and washed with ethanol. Yield: 60% (0.56 g)-yellow powder. ^{1}H NMR spectrum show a pure product with matching features to literature reported compound.[9] Therefore, this ligand was used for the next step without any further purification.

Ligand L2. This compound was prepared in a manner similar to **L1** using 2-acetyl thiazole. 59% green-yellow solid. ^{1}H NMR (400 MHz, $CDCl_3$): δ (ppm) = 8.33 (s, 2H), 7.95 (d, 2H, *J* = 3.2), 7.62 (d, 2H, *J* = 3.9), 7.48 (d, 2H, *J* = 3.2), 7.27 (dd, 2H, *J* = 1.2, 5.1), 7.24 (dd, 2H, *J* = 1.2, 3.6), 7.20 (d, 2H, *J* = 3.9), 7.04 (dd, 2H, *J* = 3.6, 5.1); ^{13}C {^{1}H} NMR (100 MHz, $CDCl_3$): δ (ppm) = 168.5, 151.5, 144.1, 143.4, 140.0, 138.7, 136.6, 128.1, 127.2, 125.4, 124.8, 124.5, 122.0, 115.4, 110.0. HRMS (CI^+) m/z calculated for $[C_{19}H_{11}N_3S_4]^+$ ([**L2**]$^+$): 408.9869, found 408.9861.

4-(2,2‘-bithiophene-5-yl)-2,6-dichloropyridine. To a mixture of 2,6-dichloro-4-iodopyridine (0.808 g, 2.95 mmol), and $Pd(PPh_3)_2Cl_2$ (0.207 g, 0.3 mmol) in 60 mL of dry toluene was added 5-(tributylstannyl)-2,2‘-bithiophene[21] (1.343 g, 2.95 mmol). The reaction mixture was heated to 100 °C for 48 hours under nitrogen. The reaction was cooled and dried in vacuo. The mixture was dissolved in CH_2Cl_2, and then filtered through a silica gel plug. The filtrate was washed with dilute $NH_4Cl_{(aq)}$ (3 times, 80 mL), then dried over $MgSO_4$. Solvent was removed and the product was purified by column chromatography (silica gel, CH_2Cl_2 : hexanes = 70 : 30) to yield a yellow solid (0.545 g, 59%). ^{1}H NMR (400 MHz, $CDCl_3$): δ (ppm) = 7.44 (d, 1H, *J* = 3.9), 7.40 (s, 2H), 7.31

(dd, 1H, *J* = 1.2, 5.1), 7.27 (dd, 2H, *J* = 1.2, 3.6), 7.20 (d, 2H, *J* = 3.9), 7.04 (dd, 2H, *J* = 3.6, 5.1); ^{13}C {^{1}H} NMR (100 MHz, $CDCl_3$): δ (ppm) = 151.2, 128.2, 127.8, 125.9, 125.0, 124.8, 118.2. HRMS (CI^+) m/z calculated for $[C_{13}H_7Cl_2NS_2]^+$: 310.9397, found 310.9392.

Ligand L3. Sodium hydride (86.4 mg, 3.6 mmol) was added to a 250 mL schlenk flask. Dry *bis*(2-methoxyethyl) ether (diglyme) (50 mL) was added to the flask. Pyrazole (0.2 g, 3 mmol) was slowly added to the above solution under N_2. The mixture was stirred at room temperature for 30 min until all bubbles evolved and the solution became clear. After the addition of 4-(2,2‘-bithiophene-5-yl)-2,6-dichloropyridine (0.31 g, 1 mmol), the mixture was stirred at 130 °C overnight. Solvent was removed and the product was purified by column chromatography (silica gel, CH_2Cl_2 : hexanes = 70 : 30) to yield a bright yellow solid (Yield = 80%). ^{1}H NMR (400 MHz, $CDCl_3$): δ (ppm) = 8.58 (dd, 2H, *J* = 0.6, 2.6), 8.04 (s, 2H), 7.80 (dd, 2H, *J* = 0.6, 1.7), 7.62 (d, 2H, *J* = 3.9), 7.28 (dd, 2H, *J* = 1.1, 5.1), 7.26 (dd, 2H, *J* = 1.1, 3.6), 7.22 (d, 2H, *J* = 3.9), 7.06 (dd, 2H, *J* = 3.6, 5.1), 6.51 (dd, 2H, *J* = 1.7, 2.6); ^{13}C {^{1}H} NMR (100 MHz, $CDCl_3$): δ (ppm) = 150.7, 146.4, 142.4, 140.0, 138.7, 136.6, 128.0, 127.3, 127.2, 125.4, 124.6, 124.5, 108.0, 104.9. HRMS (CI^+) m/z calculated for $[C_{19}H_{13}N_5S_2]^+$ ([**L3**]$^+$): 375.0612, found 375.0610.

$Co(L1)_2(NO_3)_2$. Cobalt(II) nitrate hexahydrate (15 mg, 0.05 mmol) dissolved in MeOH (5 mL) was added to **L1** (40 mg, 0.10 mmol) solution in CH_2Cl_2 (10 mL). The resulting brown solution was stirred at room temperature under N_2 for 30 min. The solvents were removed under vacuum, yielding a dark brown solid of the desired product with unity yield. ^{1}H NMR (400 MHz, CD_3CN): δ (ppm) = 93.93 (s, 4H, terpy), 55.75 (s, 4H, terpy), 44.84 (s, 4H, terpy), 32.52 (s, 4H, terpy), 14.70 (s, 4H, terpy), 9.27 (dd, 2H, *J* = 0.9, 3.2); 9.07 (s, 2H), 9.04 (s, 2H), 8.51 (dd, 2H, *J* = 0.9, 5.2), 7.85 (dd, 2H, *J* = 3.2, 5.2). Crystals suitable for X-ray analysis were grown *via* slow evaporation of a methanol

solution.

$Co(L1)_2(PF_6)_2$. A solution of **$Co(L1)_2(NO_3)_2$** in acetonitrile was added to a saturated aqueous solution of ammonium hexafluorophosphate. The orange precipitate was filtered and washed with diethyl ether. ^{1}H NMR (400 MHz, CD_3CN): δ (ppm) = 93.93 (s, 4H, terpy), 55.75 (s, 4H, terpy), 44.84 (s, 4H, terpy), 32.52 (s, 4H, terpy), 14.70 (s, 4H, terpy), 9.27 (dd, 2H, *J* = 0.9, 3.2); 9.07 (s, 2H), 9.04 (s, 2H), 8.51 (dd, 2H, *J* = 0.9, 5.2), 7.85 (dd, 2H, *J* = 3.2, 5.2). Crystals suitable for X-ray analysis were grown *via* slow evaporation of an acetonitrile solution.

$Co(L2)_2(PF_6)_2$. Cobalt(II) tetrafluoroborate hexahydrate (85 mg, 0.25 mmol) dissolved in MeOH (10 mL) was added to **L2** (0. 205 g, 0.50 mmol) solution in CH_2Cl_2 (20 mL). The resulting brown solution was stirred at room temperature under N_2 for 2 hours. The solvents were removed under vacuum, yielding a dark brown solid of the desired product with unity yield. ^{1}H NMR (400 MHz, CD_3CN): δ (ppm) = 83.93 (s, 4H, terpy), 55.75 (s, 4H, terpy), 44.84 (s, 4H, terpy), 32.52 (s, 4H, terpy), 14.70 (s, 4H, terpy), 9.27 (dd, 2H, *J* = 0.9, 3.2); 9.07 (s, 2H), 9.04 (s, 2H), 8.51 (dd, 2H, *J* = 0.9, 5.2), 7.85 (dd, 2H, *J* = 3.2, 5.2). Crystals suitable for X-ray analysis were grown *via* slow evaporation of a methanol solution.

$Co(L1)_2(NO_3)_3$. To a solution of **L1** (40 mg, 0.10 mmol) in DCM (4 mL) was added a solution of $Co(NO_3)_2 \cdot 6H_2O$ (14.6 mg, 0.05 mmol) in methanol (10 mL). Then, 1 equiv of 1 M aqueous nitric acid and 30% hydrogen peroxide was added successively. The reaction was stirred at 60 ^{o}C for 2 days. The mixture was cooled to room temperature and all solvents were removed under vacuum. The residue was recrystallized from methanol–acetonitrile 1:1 mixture to give the desired product (64%). ^{1}H NMR (400 MHz, $CDCl_3$): δ (ppm) = 9.09 (s, 4H), 8.73 (d, 2H, *J* = 7.9), 8.73 (d, 1H, *J* = 4.2), 8.28 (m, 2H), 7.70 (d, 1H, *J* = 4.19), 7.63 (m, 2H), 7.46 (m, 4H), 7.26 (dd, 2H, *J* = 3.7, 5.0). Crystals

suitable for X-ray analysis were grown *via* slow evaporation of an acetonitrile solution.

$Co(L1)_2(PF_6)_3$. This complex was prepared in a manner similar to **$Co(L2)_2(PF_6)_2$** from **$Co(L1)_2(NO_3)_3$** using an anion exchange reaction. ^{1}H NMR (400 MHz, CD_3CN): δ (ppm) = 9.09 (s, 4H), 8.73 (d, 2H, *J* = 7.9), 8.73 (d, 1H, *J* = 4.2), 8.28 (m, 2H), 7.70 (d, 1H, *J* = 4.19), 7.63 (m, 2H), 7.46 (m, 4H), 7.26 (dd, 2H, *J* = 3.7, 5.0). Crystals suitable for X-ray analysis were grown *via* slow evaporation of an acetonitrile solution.

$Fe(L3)_2(BF_4)_2$. Ferrous tetrafluoroborate hexahydrate (56 mg, 0.17 mol) in acetone (5 mL) was added into the **L3** (125 mg, 0.33 mmol) solution in CH_2Cl_2 (10 mL). The mixture was stirred under N_2 for 1 hour. The solvents were removed *in vacuo*, yielding a dark brown solid of the desired product. Yellow crystals suitable for X-ray diffraction analysis were obtained after a few days (30.7 mg, 26%). ^{1}H NMR (400 MHz, CD_3CN): δ (ppm) = 66.42 (s, 4H), 56.97 (s, 4H), 39.74 (s, 4H), 39.25 (s, 4H), 7.20 (br, 4H), 6.80 (br, 6H); UV-Vis (λ_{max} (ε), CH_2Cl_2): 250 nm (38,450 $cm^{-1}M^{-1}$), 266 nm (35,550 $cm^{-1}M^{-1}$), 376 (35,550 $cm^{-1}M^{-1}$). Crystals suitable for X-ray analysis were grown *via* slow evaporation of an acetone solution.

CRYSTALLOGRAPHIC DATA

Table 4.1. Crystal data and structure refinement of $Co(L1)_2(NO_3)_2$ and $Co(L2)_2(PF_6)_2$.

	$Co(L1)_2(NO_3)_2$	$Co(L2)_2(PF_6)_2$
Empirical formula	C47 H34 Co N8 O7 S4	C38 H22 Co F12 N6 P2 S8
Formula weight	1009.99	1167.96
Temperature (K)	100(2)	100(2)
Wavelength (Å)	0.71073	0.71073
Crystal system	Triclinic	Monoclinic
Space group	P-1	P *21/c*
a (Å)	12.624	19.972
b (Å)	13.386	15.219
c (Å)	14.003	15.503
α (deg)	90.48	90
β (deg)	96.76	109.47
γ (deg)	112.37	90
Volume ($Å^3$)	2169.3	4313.9
Z	2	4
ρ (mg/cm^3)	1.546	1.798
μ (mm^{-1})	0.653	0.952
F(000)	1038	2340
Crystal size (mm)	0.31 x 0.05 x 0.03	0.22 x 0.19 x 0.12
θ (deg)	1.47 to 27.47	3.02 to 27.60
Index ranges	$-16 \leq h \leq 16$	$-25 \leq h \leq 25$
	$-17 \leq k \leq 17$	$-19 \leq k \leq 19$
	$-18 \leq l \leq 18$	$-19 \leq l \leq 18$
Reflections collected	40373	94884
Max. and min. transmission	0.8918 and 0.7995	0.9815 and 0.9402
GOF on F^2	1.233	1.055
R1, wR2 [I>2σ(I)]	0.0888, 0.1545	0.0324, 0.0781
R1, wR2[all data]	0.1009, 0.1597	0.0381, 0.0807
Largest diff. peak and hole ($e.Å^{-3}$)	0.946 and -0.806	0.931 and -0.567

Table 4.2. Crystal data and structure refinement of $\mathbf{Co(L1)_2(PF_6)_2}$.

	100 K	**273 K**
Empirical formula	C46 H30 Co F12 N6 P2 S4	C46 H30 Co F12 N6 P2 S4
Formula weight	1143.87	1143.87
Temperature (K)	100(2)	273(2)
Wavelength (Å)	0.71073	0.71073
Crystal system	Monoclinic	Monoclinic
Space group	P *21/c*	P *21/c*
a (Å)	19.227	19.653
b (Å)	15.521	15.750
c (Å)	15.870	16.904
α (deg)	90	90
β (deg)	110.56	111.14
γ (deg)	90	90
Volume ($Å^3$)	4434.4	4646.4
Z	4	4
ρ (mg/cm^3)	1.713	1.635
μ (mm^{-1})	0.743	0.709
F(000)	2308	2308
Crystal size (mm)	0.31 x 0.05 x 0.03	0.31 x 0.05 x 0.03
θ (deg)	1.90 to 27.53	3.01 to 27.48
Index ranges	$-24 \leq h \leq 24$ $-19 \leq k \leq 20$ $-20 \leq l \leq 20$	$-25 \leq h \leq 25$ $-20 \leq k \leq 20$ $-20 \leq l \leq 20$
Reflections collected	46693	47660
Max. and min. transmission	0.8918 and 0.7995	0.8918 and 0.7995
GOF on F^2	1.063	1.124
R1, wR2 [I>2σ(I)]	0.0425, 0.1010	0.0631, 0.1316
R1, wR2[all data]	0.0522, 0.1077	0.1060, 0.1500
Largest diff. peak and hole ($e.Å^{-3}$)	0.477 and -0.618	0.651 and -0.766

Table 4.3. Crystal data and structure refinement of $Co(L1)_2(NO_3)_3$ and $Co(L2)_2(PF_6)_3$.

	$Co(L1)_2(NO_3)_3$	$Co(L1)_2(PF_6)_3$
Empirical formula	C46 H29 Co N9 O14 S4	C52 H39 Co F18 N9 P3 S4
Formula weight	1118.95	1412.00
Temperature (K)	100(2)	100(2)
Wavelength (Å)	0.71073	0.71073
Crystal system	Triclinic	Triclinic
Space group	P-1	P-1
a (Å)	12.217	11.557
b (Å)	12.452	13.254
c (Å)	16.919	20.049
α (deg)	94.39	102.40
β (deg)	96.86	105.66
γ (deg)	109.54	93.34
Volume ($Å^3$)	2389.4	2866.0
Z	2	2
ρ (mg/cm^3)	1.555	1.636
μ (mm^{-1})	0.612	0.635
F(000)	1142	1424
Crystal size (mm)	0.21 x 0.05 x 0.08	0.31 x 0.05 x 0.03
θ (deg)	1.09 to 25.00	1.09 to 25.00
Index ranges	$-15 \leq h \leq 15$ $-16 \leq k \leq 16$ $-21 \leq l \leq 21$	$-13 \leq h \leq 13$ $-15 \leq k \leq 15$ $-23 \leq l \leq 23$
Reflections collected	25493	45049
Max. and min. transmission	0.9153 and 0.8236	0.8918 and 0.7995
GOF on F^2	1.460	1.077
R1, wR2 [I>2σ(I)]	0.0649, 0.1885	0.0422, 0.1069
R1, wR2[all data]	0.0711, 0.1936	0.0445, 0.1113
Largest diff. peak and hole ($e.Å^{-3}$)	1.150 and -0.618	0.858 and -0.761

Table 4.4. Crystal data and structure refinement of **$Fe(L3)_2(BF_4)_2$**.

	$Fe(L3)_2(BF_4)_2$
Empirical formula	C38 H26 B2 F8 Fe N10 O1 S4
Formula weight	1038.48
Temperature (K)	100(2)
Wavelength (Å)	0.71073
Crystal system	Triclinic
Space group	P-1
a (Å)	13.198
b (Å)	13.786
c (Å)	14.457
α (deg)	67.50
β (deg)	65.49
γ (deg)	79.64
Volume ($Å^3$)	2209.1
Z	2
ρ (mg/cm^3)	1.486
μ (mm^{-1})	0.607
F(000)	1000
Crystal size (mm)	0.32 x 0.07 x 0.05
θ (deg)	3.05 to 27.43
Index ranges	$-17 \leq h \leq 17$
	$-17 \leq k \leq 17$
	$-18 \leq l \leq 18$
Reflections collected	48984
Max. and min. transmission	0.9153 and 0.8236
GOF on F^2	1.063
R1, wR2 [I>2σ(I)]	0.0363, 0.0840
R1, wR2[all data]	0.0438, 0.0875
Largest diff. peak and hole ($e.Å^{-3}$)	0.406 and -0.374

REFERENCES

(1) Gülichi, P.; Goodwin, H. A. *Spin Crossover in Transition Metal Compounds I–III, Top. Curr. Chem.* **2004**.

(2) Halcrow, M. A. *Spin-Crossover Materials: Properties and Applications* **2013**.

(3) Gütlich, P.; Gaspar, A. B.; Garcia, Y. *Beilstein J. Org. Chem.* **2013**, *9*, 342.

(4) Gütlich, P. *Eur. J. Inorg. Chem.* **2013**, *2013*, 581.

(5) Gamez, P.; Costa, J. S.; Quesada, M.; Aromi, G. *Dalton Trans.* **2009**, 7845.

(6) Hayami, S.; Gu, Z.-z.; Einaga, Y.; Kobayasi, Y.; Ishikawa, Y.; Yamada, Y.; Fujishima, A.; Sato, O. *Inorg. Chem.* **2001**, *40*, 3240.

(7) Mathonière, C.; Lin, H.-J.; Siretanu, D.; Clérac, R.; Smith, J. M. *J. Am. Chem. Soc.* **2013**, *135*, 19083.

(8) Gütlich, P.; Hauser, A.; Spiering, H. *Angew. Chem. Int. Ed.* **1994**, *33*, 2024.

(9) Hjelm, J.; Handel, R. W.; Hagfeldt, A.; Constable, E. C.; Housecroft, C. E.; Forster, R. J. *J. Phys. Chem. B* **2003**, *107*, 10431.

(10) Fillaud, L.; Trippé-Allard, G.; Lacroix, J. C. *Org. Lett.* **2013**, *15*, 1028.

(11) Buchen, T.; Gütlich, P.; Sugiyarto, K. H.; Goodwin, H. A. *Chem. Eur. J.* **1996**, *2*, 1134.

(12) Šalitroš, I.; Fuhr, O.; Kruk, R.; Pavlik, J.; Pogány, L.; Schäfer, B.; Tatarko, M.; Boča, R.; Linert, W.; Ruben, M. *Eur. J. Inorg. Chem.* **2013**, *2013*, 1049.

(13) Hasegawa, Y.; Sakamoto, R.; Takahashi, K.; Nishihara, H. *Inorg. Chem.* **2013**, *52*, 1658.

(14) Nemati Kharat, A.; Bakhoda, A.; Tamaddoni Jahromi, B. *Polyhedron* **2011**, *30*, 2768.

(15) Mello, J. V.; Finney, N. S. *Org. Lett.* **2001**, *3*, 4263.

(16) The Rigaku Corportation: Tokyo, Japan, 2001.

(17) Otwinoski, Z.; Minor, W. In *Macromolecular Crystallography, Part A*; Carter Jr., C. W., Sweets, R. M., Eds.; Academic Press 1997, p 307.

(18) *CrystalClear, 1.40*; Rigaku Americas Corporation: The Woodlands, Texas, USA, 2008.

(19) Sheldrick, G. M. *SHELX 97. A software package for the solution and refinement of X-ray data*; University of Gottingen: Gottingen, Germany, 1997.

(20) Cromer, D. T.; Waber, J. T. In *International Tables for X-ray Crystallography*; Kynoch Press: Birmingham, England, 1974; Vol. 4.

(21) Zhu, S. S.; Swager, T. M. *J. Am. Chem. Soc.* **1997**, *119*, 12568.

Chapter 5: Self-Assembly Behavior of Perylene Diimide Pendant Groups Appended to Polynorbornene Chains[a]

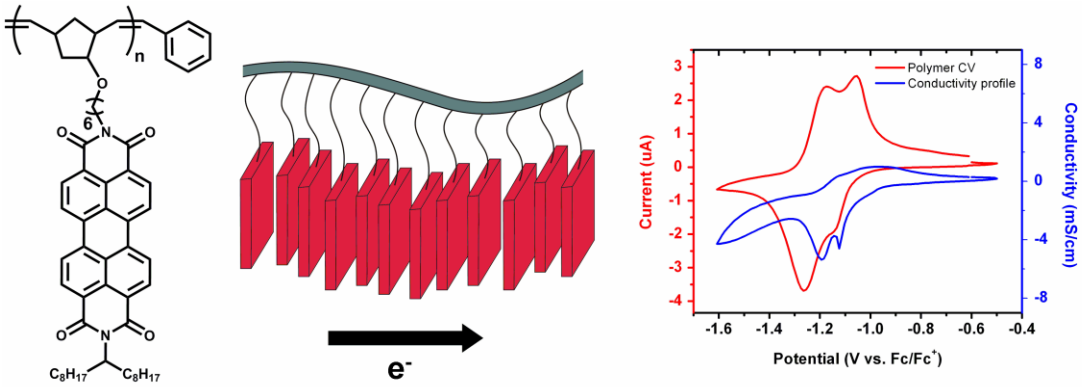

[a] prior publication: Glaz, M. S.; Biberdorf, J. D.; Nguyen, M. T.; Travis, J. J.; Holliday, B. J.; Vanden Bout, D. A."Perylene diimide functionalized polynorbornene: a macromolecular scaffold for supramolecular self-assembly," *J. Mater. Chem. C*, **2013**, *1*, 8060-8065. The polymer was synthesized and characterized M.T.N and J.D.B. Spectroscopic experiments were conducted by S.M.G. and J.J.T. The manuscript was written by all authors.

5.1. INTRODUCTION

Perylene diimide and its derivatives (PDIs), first known as industrial pigments with high thermal and photo stability, have recently been extensively studied as electron transporting materials due to their attractive photophysical and electronic properties.[1] Much research has been focused on harnessing the n-type semiconductor behavior of this class of molecules, specifically in organic field-effect transistors (OFETs),[2] light-emitting diodes (LEDs),[3] and organic photovoltaics (OPVs).[4] PDI is an attractive component in these devices because of high electron mobilities, up to 2.1 $cm^2/V \cdot s$, demonstrated in small molecule studies.[5] One important feature of PDI that contributes to the electronic properties of the material, e.g., high charge-carrier mobilities, is the ability to form highly ordered π-stacked structures. From these π-stacks, electron transport can occur in a 1D direction *via* a hopping mechanism from one PDI unit to another. There have been several studies on PDI self-assembly behavior obtained *via* π-stacking at the molecular level.[1,6,7] Zang and co-workers reported the formation of nanobelts obtained from the self-assembly of disubstituted PDI molecules. The observation of increased conductivity shows promise for the use of these PDI materials in optoelectronic devices.[6] Although there have been many studies on the stacking of PDI derivatives at the molecular level, there are very few reports on the stacking mode in polymeric systems, which have high potential for applications due to more desirable properties of polymers over small molecules. Thelakkat and co-workers have prepared block copolymers with PDI pendant groups on the backbone of the polymer.[8,9] The use of such copolymers creates self-assembled domains with sizes ideal for charge transport in photovoltaic applications. However, the manner in which PDI units stack within polymeric systems has not been investigated.

Herein, we report a study of the self-assembly behavior of PDI pendant groups appended to polynorbornene chains. By creating polymeric materials that incorporate PDI functionalities, the desirable properties of polymers, such as pendant group preorganization and ease of processing into thin films, can be combined with the electronic and photophysical properties inherent to PDI small molecules. The PDI pendant groups along the polymer backbone show evidence of aggregation with neighboring groups, forming pathways for efficient electron transport from one PDI group to another. Among other advantages, these types of polymeric materials will increase the ability to control the morphology of devices on a much more rigorous basis, enabling easier refinement in an effort to obtain optimal electronic and material performance.

5.2. RESULTS AND DISCUSSION

5.2.1 Synthesis of Monomer and Polymer

Scheme 5.1 illustrates the synthetic steps starting with the literature-reported compound *exo*-5-norbornene-2-ol (**1**).[10] The deprotonation of this material allows its use as a powerful nucleophile for substitution type reactions. In this case, after deprotonation, the anion is exposed to 6-chloro-1-hexyl *p*-toluenesulfonate. The resulting substitution reaction yields an alkyl halide norbornene monomer (**2**). The Gabriel amine synthesis is then utilized to result in, 6-amino-1-(*exo*-5-norbornene-2-oxy)hexane (**3**). When beginning with 3,4,9,10-Perylenetetracarboxylic acid dianhydride, the addition of alkyl groups to provide solubility is a required first step. Through a reaction in molten imidazole, with a simple secondary amine, the *N,N'-bis*(1-nonyloctyl)perylene-3,4,9,10-tetracarboxylic diimide (**4**) is obtained and easily purified. Then through hydrolysis of one end of the molecule, it is possible to obtain *N*-(1-nonyloctyl)perylene-3,4,9,10-

tetracarboxy-3,4-anhydride-9-10-imide (**5**).[11] Finally, **5** is condensed with **3** through a short reflux in toluene resulting in the final PDI containing monomer (**6**). Polymerization of **6** using 1st generation Grubbs' catalyst in $CHCl_3$ resulted in a ring-opened metathesis polymer (**poly-PDI**) (Scheme 5.1).

Scheme 5.1. Synthesis of monomer and polymer with PDI pendant moieties.

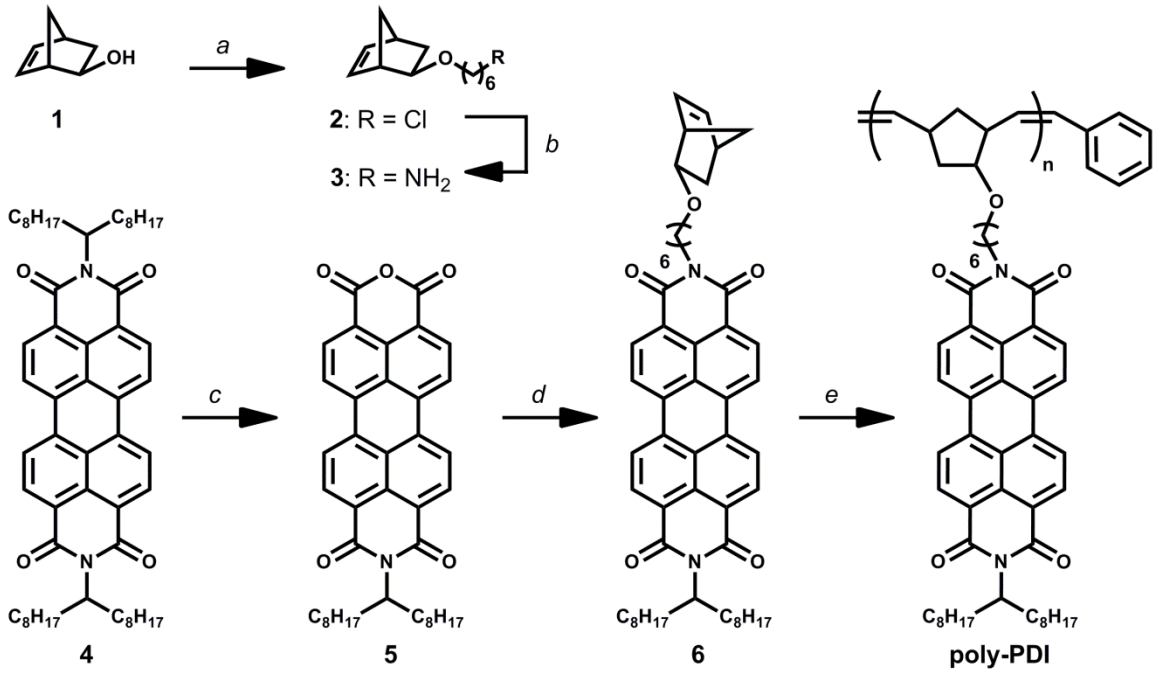

Reagents: (a) 1) Na, THF, reflux, 2) 6-chloro-1-hexyl *p*-toluenesulfonate, THF, reflux; (b) 1) potassium phthalimide, DMF, 100 ^oC, 2) hydrazine monohydrate, EtOH, 60 ^oC; (c) KOH, *t*-BuOH, reflux; (d) **3**, toluene, reflux; (e) 1) $Cl_2Ru(PCy_3)_2$=CHPh, $CHCl_3$, 25 ^oC, 2) ethyl vinyl ether.

By varying the initial mole % catalyst in five separate polymerizations (Figure 5.1), a linear relationship was found between the initial monomer to catalyst ratio and molecular weight demonstrating the "living" nature of this polymerization. This is essential for the use of this monomer as a building block in more complex architectures

involving multi-block polymers. The polymer used in the studies herein had an M_n of 31,200 g/mole and was obtained using 1 mol% catalyst in the polymerization. Differential scanning calorimetry (DSC) and thermogravimetric analysis were performed on samples of **poly-PDI**. Between -50 and 275 °C a weak glass transition was observed with an onset of 117 °C. The polymer is highly thermally stable. Decomposition of the polymer reached 1 wt% at 357 °C.

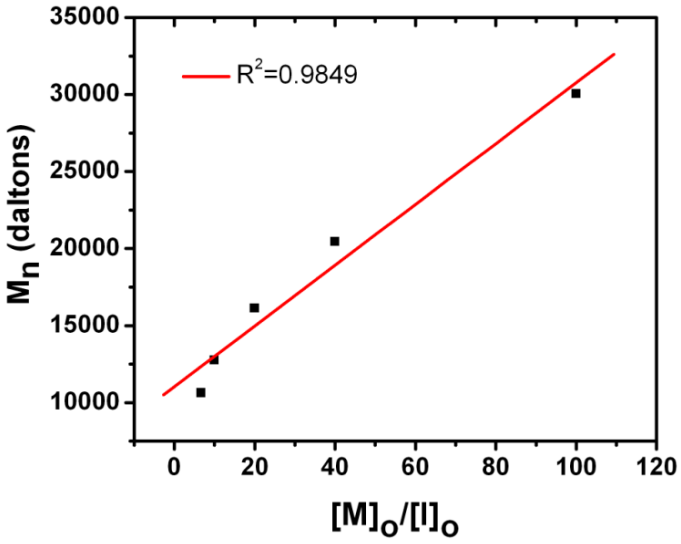

Figure 5.1. Initial monomer to catalyst ratio vs. molecular weight of resulting polymers for five separate polymerization trials.

5.2.2. Photophysical Properties of PDI Polymer

Photophysical properties of the monomer and polymer were studied and shown in Figure 5.2. The renowned photophysics of perylene diimides are generally unaffected upon substitution with simple alkyl groups, as observed in the absorption and emission spectra of the monomer (Figure 5.2A). The absorption spectrum of **6** exhibits three absorption peaks at 457, 488, and 526 nm. The emission spectrum of **6** shows the expected well-resolved vibronic structure for disubstituted perylene diimides and is the

mirror image of the absorption spectrum with peaks at 534, 570, and 620 nm. The quantum yield of **6**, when calculated versus *N,N'-bis*(1-octylnonyl)-perylene-3,4,9,10-tetracarboxylic diimide (**PDI-C9**), a known standard, is near unity. The absorption spectrum of **poly-PDI** shows a similar band structure to that of the monomer with an apparent difference in the decrease in oscillator strength of the 0-0 vibronic transition relative to the 0-1 and 0-2 bands. This observed change is indicative of electronic coupling interactions between PDI moieties when self-assembly materials or aggregates are formed in either solution or in solid thin films.[12-15] When compared to the monomer, the emission of **poly-PDI** contains a large featureless, red-shifted peak centered at 633 nm. This type of emission is typical of molecules which form eximers, suggesting that the perylene pendant groups interact with one another in the excited state. A detailed spectroscopic study on the aggregation of PDI pendant groups of this polymer can be found elsewhere.[16]

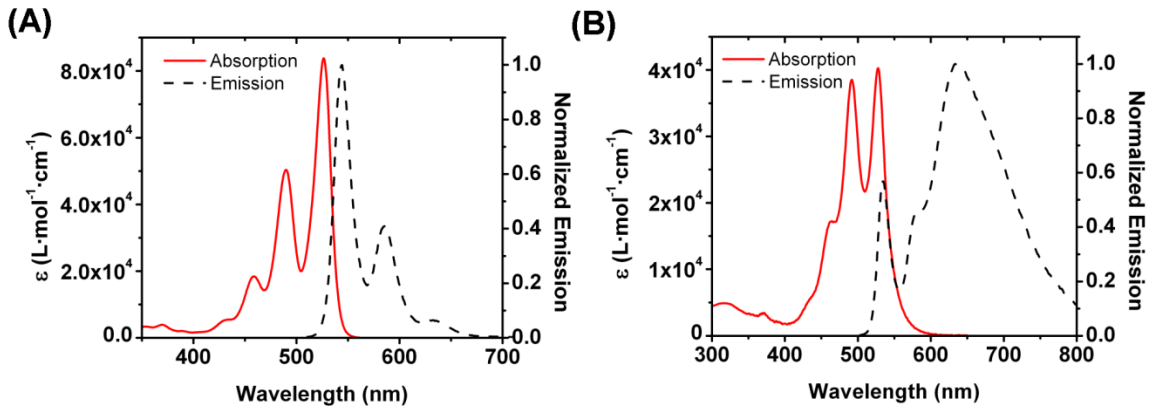

Figure 5.2. Absorption and normalized fluorescence emission spectra of monomer **6** (A) and polymer **poly-DPI** (B) in $CHCl_3$ at room temperature.

5.2.3. Electrochemistry of Polymer in Solution

Cyclic voltammetry (CV) was used to study the electrochemical behavior and determine the relative HOMO and LUMO energy levels of **6** and **poly-PDI**. The resulting values for reduction potentials, band gaps, and estimated HOMO and LUMO levels for **6** and **poly-PDI**, as well as **PDI-C9**, are shown in Table 5.1. There are only slight differences in the band gap and band levels between the monomer and polymer. However, the difference in reduction potentials between the polymer and monomer is mainly caused by the difference in the reduction and oxidation potentials of the radical anion species (Figure 5.3). The less negative reduction potential as well as the less positive oxidation potential of the radical anions on **poly-PDI** are indicative of electron delocalization among the PDI moieties along the polymer chain. This seems only to occur with radical anions rather than neutral states or the dianions.

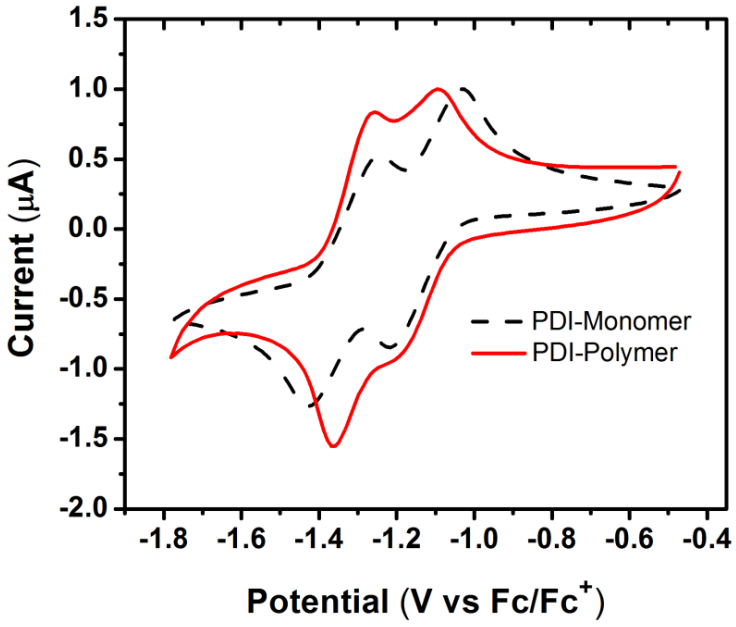

Figure 5.3. Solution cyclic voltammograms of monomer **6** and polymer **poly-PDI** in 0.1 M $TBAPF_6/CH_2Cl_2$ electrolyte solutions.

Table 5.1. Electrochemical data and estimated MO energies.

Compounds	$E_{1/2}^{-1}$	$E_{1/2}^{-2}$	Optical band gap	HOMO	LUMO
monomer **6**	-1.12	-1.35	2.07	5.75	3.68
poly-PDI	-1.17	-1.32	2.06	5.69	3.63
PDI-C9	-1.11	-1.37	2.13	5.82	3.69

5.2.4. EPR Studies of Radical Anions of Monomer 6 and Polymer poly-PDI

To further understand the behavior of these radical anion species on the monomer and polymer, electron paramagnetic resonance (EPR) studies were conducted. Due to the difference in solubility of the polymer and monomer in organic solvents, the radical anion species were generated electrochemically and chemically with sodium dithionite, respectively. Figure 5.4 shows the formation of radical anions monitored by UV-Vis-NIR and EPR spectroscopies. The EPR spectrum of the radical anions of **6** shows well-defined hyperfine couplings. Simulation of the spectrum shows good agreement with experimental data and gives coupling contants of 1.78, 1.2, and 0.6 G for 4H in the bay positions, 4H in core position, and 2N, respectively (Figure 5.4C). EPR studies of the polymer radical anions gave a distorted spectrum with hyperfine couplings similar to those of the monomer. Attempts to simulate this spectrum with hyperfine coupling caused by one single radical species did not give a spectrum with good agreement with the experimental data (Figure 5.5A). As discussed above, photophysical and electrochemical studies show electronic coupling between the PDI moieties; we speculate that the EPR signal of the polymer radical anions is comprised of multiple components resulting from radicals on independent PDI moieties and from radicals delocalized on PDI moieties that couple with each other. Due to the delocalization of the unpaired electrons, the EPR signal from the radicals on the PDI moieties experiencing such

coupling will be broad and lack well-defined features. This signal is simulated as one broad line (Figure 5.5B) and was added to monomer-like signal with varying ratio (5x for best fit) to match the experimental data of the polymer radical anions (Figure 5.5C). Figure 5.4D shows the experimental and simulated (as multiple component) spectra of the radical anions of **poly-PDI**. Quantification of the monomer-like signal and the broad polymer signal gave a ratio of 3.5% between the independent PDI moieties and the PDI moieties in electronic coupling (Figure 5.5D and 5.5E). This result is consistent with the ratio obtained from UV-Vis and fluorescence data, which indicate less than 5% of PDI moieties are in monomer-like states.[16]

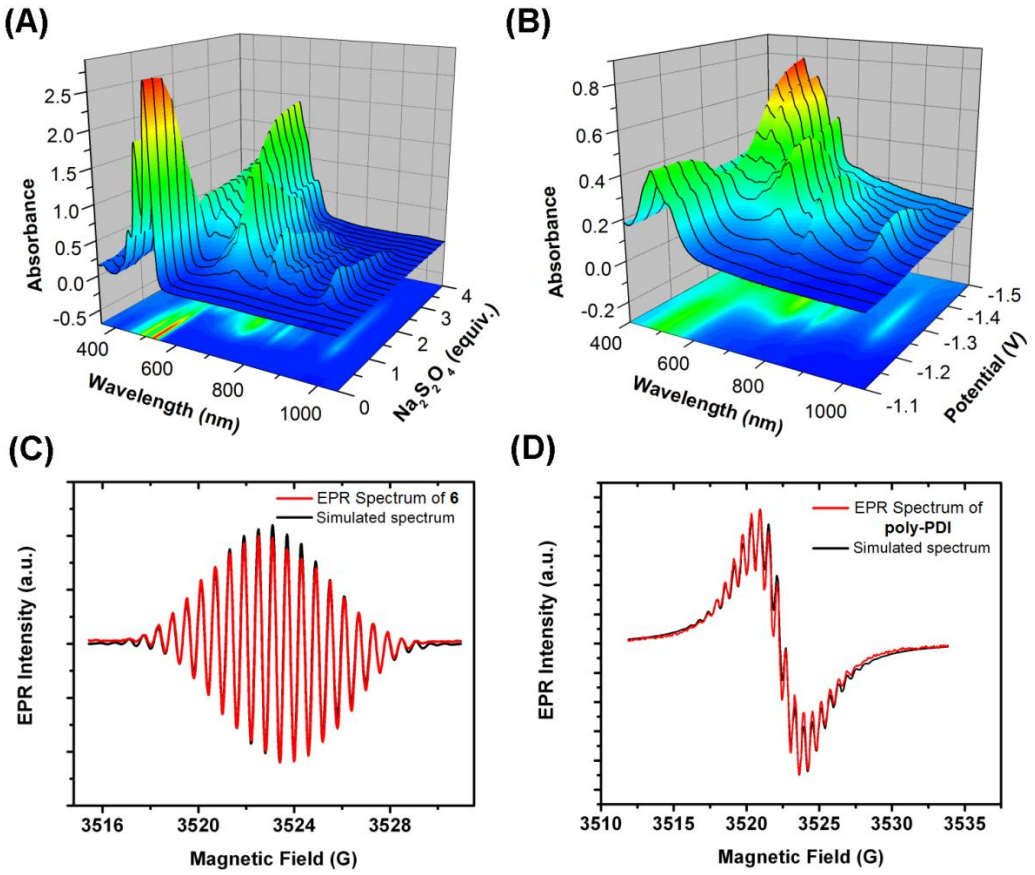

Figure 5.4. (A) UV-Vis titration of momomer **6**. (B) Spectroelectrochemical spectra of **poly-PDI**. EPR spectra of radical anions generated from **6** (C) and **poly-PDI** (D). red line: experimental data, black line: simulated spectra.

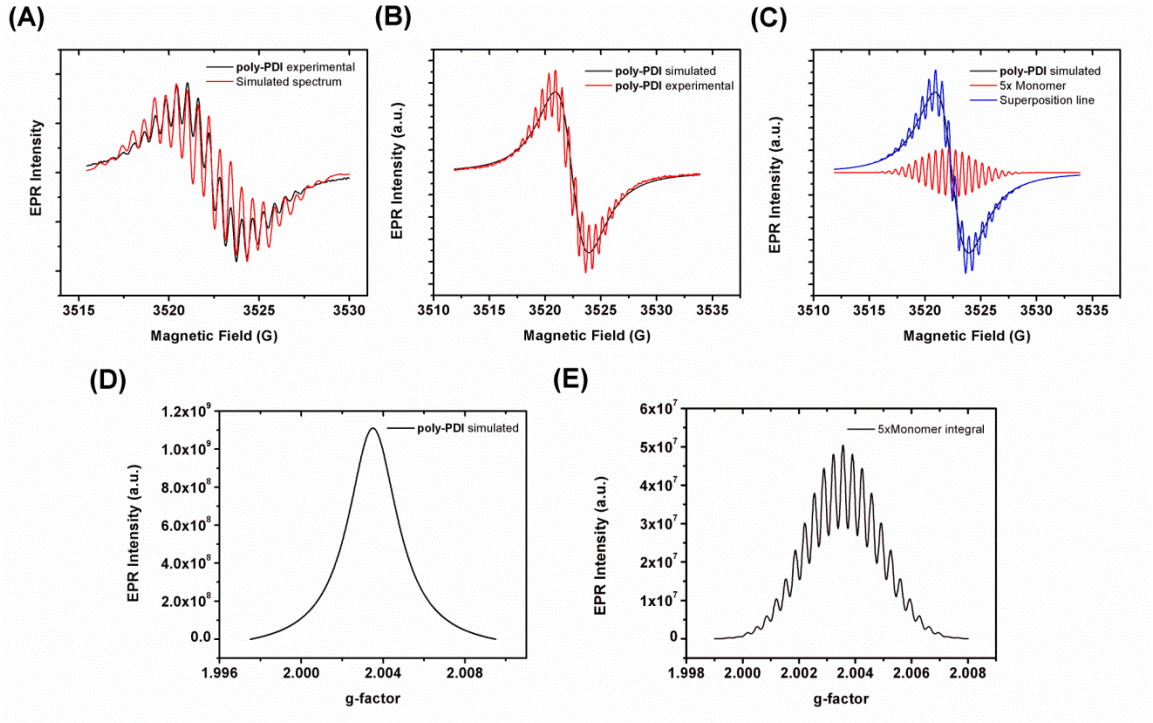

Figure 5.5. Simulated spectra of the **poly-PDI** radical anions as (A) single species, (B) a broad line due to electron delocalization, and (C) multiple components of monomer signal and polymer broad line signal. Integration of broad line simulated spectrum poly-PDI (D) and 5x signal from spectrum of **6** (E).

5.2.5. Self-Assembly of PDI Moieties in Polymer Aggregates

In addition to the aggregation of the PDI moieties along the polymer chain in solution, the PDI moieties also further aggregate when polymer aggregates are formed. When a polymer solution in chloroform was injected into DMF, a poor solvent for the polymer, a new absorption band at 550 nm was found, which is indicative of formation of a new chromophore upon aggregation (Figure 5.6). Aging the sample for two weeks leads to a reorganization of the PDI moieties aggregates and forms higher order aggregates along the chain, revealed by the further red shifting of the 550 nm absorption band.

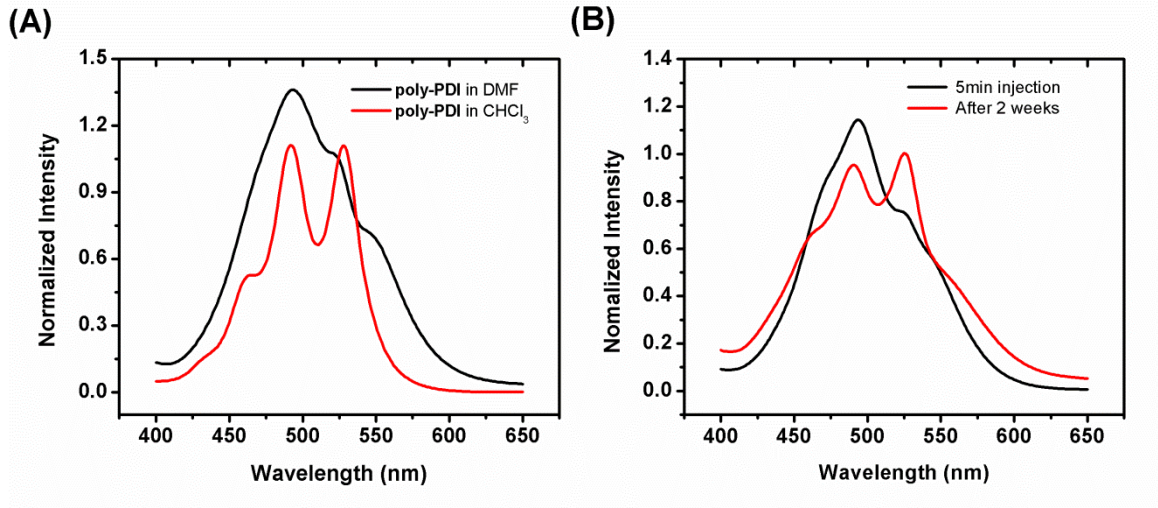

Figure 5.6. (A) UV-Vis spectra of polymer solution in $CHCl_3$ and aggregates in DMF (B) UV-Vis spectra of polymer aggregates in DMF upon aging for 2 weeks.

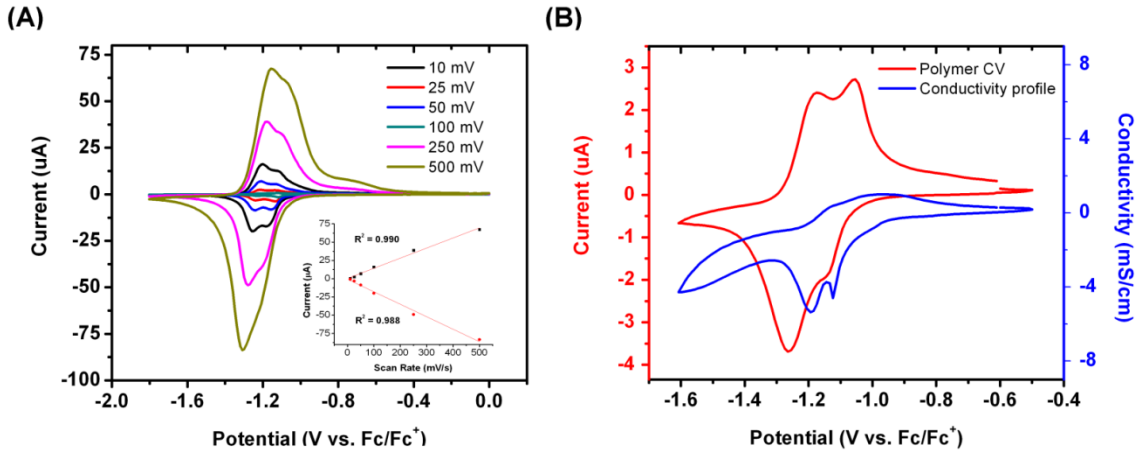

Figure 5.7. (A) Scan rate dependence of **poly-PDI** film on a Pt button electrode. Inset: current vs. scan rate (B) Cyclic voltammogram and conductivity profile of a 50 nm **poly-PDI** film on a Pt interdigitated electrode.

5.2.4. Electrochemistry and Redox Conductivity of Polymer in the Solid State

Electrochemical properties of the polymer were studied as solid thin films. Due to the exceptional solubility of the polymer in $CHCl_3$, thin films compared *via* solution processing of $CHCl_3$ solution and can be characterized electrochemically in other

solvents. Figure 5.7A shows the scan rate dependence study of a **poly-PDI** thin film drop cast from a $CHCl_3$ solution onto a Pt button electrode. The CV of the polymer film was then taken in a polymer-free electrolyte solution in acetonitrile at scan rates ranging from 10-500 mV/s (Figure 5.7A). The linear relationship between the current of the oxidation and reduction peaks and the scan rates reveals that the polymer films are highly electroactive. The diffusion of charges is not limited by the polymer film, which is a desirable property for use in organic electronics. The conductivity of the polymer film was then studied using Pt interdigitated electrode arrays. Films of varying thickness, determined by profilometry, were made by spin coating from a $CHCl_3$ solution. The conductivity of the film was calculated using the formula as reported.[17] Figure 5.7B shows the CV and the conductivity profile of a 50 nm thick polymer film. There were two peaks observed in the conductivity profile; The first peak appears +0.02 V from the first reduction peak in the CV, while the second conductivity peak (the maximum one) appears at -0.05 V from the first reduction peak but +0.07 V from the second reduction peak in the CV. This result is consistent with the fact that the conductivity of organic materials usually reaches a maximum at partial oxidation or reduction, where more free charges are created but do not repel each other as strongly as when fully oxidized or reduced.[18] The second and largest conductivity peak was seen at a potential that is slightly more negative than the first reduction potential, which correlates to a large number of free charges with relatively small repulsion forces. This scenario occurs when the PDI moieties are not yet fully reduced to the dianions. The maximum conductivity was found to be 5.4×10^{-3} S/cm which is comparable to other reported values of crystaline PDI or PDI in self-assembly materials.[19,20] This value is one order of magnitude smaller than liquid crystal films with 3-5 μm in diameter crystallinities reported by Cormier and co-workers using the same conductivity measuring technique.[19]

Chen *et al.* also reported a conductivity of 3.3 x 10^{-3} S/cm for small molecule nanobelts which were also spin coated onto interdigitated electrodes.[20] Our conductivity value shows that the polymer films exhibit good electrical conductivity and show promise for use in organic electronics.

5.3. CONCLUSION

In summary, we reported the synthesis and characterization of a novel brush polymer that has perylene diimide moieties appended to a polynorbornene chain. Our synthetic design allows for a simple route to monomers with attractive functionalities for use in block copolymers containing numerous types of pendant groups. The pre-organization of PDI moieties helps the facile formation of PDI aggregates along the polymer chains in solution as well as in polymer aggregates. Spectroscopic studies support the existence of electronic coupling between PDI moieties along polymer chains in neutral forms as well as when reduced to radical anion form. Electron delocalization between PDI moieties was confirmed by EPR and resulted in high electrical redox conductivity. This conductivity is comparable to other PDI crystalline structures indicating that this material is a good candidate for use in organic electronics. Photovolatic and field effect transistor devices made from this material are currently being investigated.

5.4. EXPERIMENTAL

5.4.1. General Methods

Air- and moisture-sensitive reactions were carried out in oven-dried glassware using standard Schlenk techniques under an inert atmosphere of dry nitrogen. Solvents were dried using a double-column anhydrous solvent system (Innovative Technologies, Newburyport, MA) and further degassed *via* nitrogen purge prior to use. Column

chromatography was carried out on Silicyle® SiliaFlash® F60, 40-63 μm 60Å. Visualization of TLCs involving non-fluorescent/non-quenching molecules was done in an I_2 chamber or through a potassium permanganate dip. ^1H (300 MHz) and ^{13}C $\{^1H\}$ (75 MHz) NMR spectra were obtained on a Varian Unity+ 300 and were referenced to the residual solvent peaks. Low-res and high-res mass spectrometry were carried out by Thermo Finngan TSQ 700 and Waters Autospec Ultima, respectively. UV-Vis spectra were recorded on a Varian Cary 6000i UV-Vis-NIR spectrophotometer with Stanna Quartz fluorometer cells with a pathlength on 10 mm. Spectrophotometer with Starna Quartz Fluorometer Cells with a pathlength of 10 mm. Luminescent measurements were recorded on a Photon Technology International QM 4 spectrophotometer equipped with a 6-inch diameter K Sphere-B integrating sphere. For quantum yield measurements, the integrating sphere was used. Quantum yield was calculated by dividing the area under the emission peak of the complex by the difference between the area under the excitation peak of the sample and that of a blank solution ($A_{em\ sample}/(A_{ex\ blank}-A_{ex\ sample})$, where A = area under peak). The compounds 9-aminoheptadecane[21], 6-chloro-1-hexyl *p*-toluenesulfonate[22], *exo*-5-norbornene-2-ol (**1**)[10], and *N*-(1-octylnonyl)perylene-3,4,9,10-tetracarboxy-3,4-anhydride-9-10-imide (**5**)[11] were prepared according to literature procedures. All other chemicals were purchased from commercial suppliers and were used as received.

5.4.2. Electrochemistry

Electrochemical studies were performed in a dry-box under a nitrogen atmosphere using a GPES system from Eco. Chemie B. V. All electrochemical experiments were carried out in a three-electrode cell with a $Ag/AgNO_3$ reference electrode (silver wire dipped in a 0.01 M silver nitrate solution with 0.1 M $[(n\text{-}Bu)_4N][PF_6]$ ($TBAPF_6$) in

CH_3CN), a Pt button working electrode, and a Pt wire coil counter electrode. Potentials were referenced relative to the 0.01 M $Ag/AgNO_3$ reference electrode. Ferrocene was used as an external reference to calibrate the reference electrode before and after experiments were performed, and that value was used to correct the measured potentials. The supporting electrolyte was 0.1 M $TBAPF_6$ that was purified by recrystallization three times from hot ethanol before being dried for 3 days at 100-150 ^oC under active vacuum.

5.4.3. UV-Vis-NIR Spectroelectrochemistry

The spectroelectrochemical measurements were performed using the previously described cell arrangement on a polymer film deposited on ITO coated glass substrate as working electrode, a platinum mesh as the counter electrode, and $Ag/AgNO_3$ as reference electrode. Experiments were carried out in an optical cuvette inside the glovebox. Absorption spectra were recorded on a Varian Cary 6000i UV-Vis-NIR spectrophotometer within the NIR/visible spectra ($1600 \geq \lambda \geq 400$ nm) under several applied potentials.

5.4.4. Electron Paramagnetic Resonance Spectroscopy (EPR)

Monomer radical anions were generated in a nitrogen filled glove bag by reducing the monomer in a DMF solution with an aqueous sodium dithionite solution. The monomer radical anion solution was then transferred to a 1.4 mm outer diameter (o.d.) quartz tube and sealed carefully with vacuum grease and paraffin film. Polymer radical anions were generated by electrochemical reduction of the polymer film in a blank solution of electrolyte in acetonitrile. The films were then washed with acetonitrile, dried, and dissolved in DMF. This solution was transferred to a 1.4 mm o.d. quartz tube and sealed carefully as described above. EPR experiments were recorded on a Bruker EMX-Plus X-band spectrometer at 293 K with 4 mW microwave power and 0.1 G modulation

amplitude. Spectral integration was performed by Bruker WinEPR Processing software and simulated spectra were obtained using SimFonia software.

5.4.5. Synthesis of poly-PDI Polymer

6-chloro-1-(*exo*-5-norbornene-2-oxy)hexane (2). In an inert atmosphere glovebox, **1** (1.02 g, 9.09 mmol) was weighed into a 100 mL schlenk flask. THF (50 mL) was added, and the solution was stirred while oil free Na metal (300 mg, 13.04 mmol) was added. The reaction was then refluxed under inert atmosphere for 12 hours and allowed to cool to room temperature. In a separate 100 mL flask, 6-chloro-1-hexyl *p*-toluenesulfonate (2.51 g, 8.62 mmol) was dissolved in dry THF. The cooled solution of deprotonated **1**, was then cannula transferred to the 6-chloro-1-hexyl *p*-toluenesulfonate solution. The new mixture was then refluxed for an additional 12 hours. Upon cooling, the mixture was poured into ether and washed with H_2O, 0.1 M NaOH, 1.0 M HCl, and brine. The organic layer was then dried over magnesium sulfate, filtered, and concentrated under vacuum. Chromatography (silica gel, 30% CH_2Cl_2 in hexanes) gave pale yellow oil (yield = 1.55 g, 79%). ^{1}H NMR δ **(**$CDCl_3$) 6.15 (1H, dd, *J* = 5.7, 2.8 Hz), 5.94 (1H, dd, *J* = 5.8, 3.2 Hz), 3.51 (2H, t, *J* = 6.7 Hz), 3.47-3.31 (3H, m), 2.84 (1H, br s), 2.76 (1H, br s), 1.77 (2H, p, *J* = 6.8 Hz), 1.68-1.22 (10H, m). ^{13}C {^{1}H} NMR δ **(**$CDCl_3$) 140.50, 133.18, 80.15, 68.93, 46.33, 45.87, 44.98, 40.29, 34.37, 32.51, 29.83, 26.65, 25.59. LRMS (CI^+ m/z) (%): Calc. 228, Found 228.

6-amino-1-(*exo*-5-norbornene-2-oxy)hexane (3). To a schlenk flask, **2** (0.672 g, 2.95 mmol) and potassium phthalimide (0.602 g, 3.25 mmol) were added. The flasked was placed under an inert atmosphere and degassed DMF (40 mL) was added. The flask was equipped with a condenser and the reaction was heated at 100 °C for 24 hours. Upon cooling, the mixture was poured into water and extracted with ether (3x). The organic fractions were collected, washed with water (4x) and brine, dried over magnesium sulfate

and filtered. The solvent was removed under vacuum. Chromatography (silica gel, 30% CH_2Cl_2 in hexanes) gave a clear liquid, 2-[6-bicyclo[2.21]hept-5-en-2-*exo*-yloxy)hexyl]-1*H*-isoindole-1,3(2*H*)-dione as the isolatable intermediate **2a** (yield = 0.912 mg, 91%). ^{1}H NMR δ **(**$CDCl_3$) 7.80 (2H, m), 7.65 (2H, m) 6.12 (1H, dd, *J* = 5.8, 2.8 Hz), 5.86 (1H, dd, *J* = 5.8, 3.1 Hz), 3.62 (2H, t, *J* = 6.6 Hz), 3.49-3.27 (3H, m), 2.81 (1H, br s), 2.76 (1H, br s), 1.78-1.19 (12H, m). ^{13}C {^{1}H} NMR δ **(**$CDCl_3$) 168.11, 140.27, 133.60, 133.00, 13.89, 122.87, 79.91, 68.78, 46.14, 45.68, 40.09, 37.71, 34.17, 29.64, 28.32, 26.46, 25.69. LRMS (CI^+ m/z) (%): Calc. 339, Found 339.

2a (905 mg) was added into a schlenk flask under inert atmosphere. Degassed EtOH (40 mL) was added *via* cannula, followed by an injection of hydrazine monohydrate (1.0 mL). After equipping with a reflux condenser the mixture was heated at 60 °C for 8 h under inert atmosphere. Upon cooling, the mixture was poured into water and the ethanol removed through vacuum. Concentrated HCl (5 mL) was added to the solution while cooled in an ice bath. The resulting white precipitate was removed and the filtrate was extracted with diethyl ether (3x, ~200 mL total volume). The organic fractions were collected and washed with water and brine, then dried over magnesium sulfate and filtered. The solvent was removed under vacuum to give **4** as a clear liquid (yield: 0.491 g, 54%). ^{1}H NMR δ **(**$CDCl_3$) 6.19 (1H, dd, *J* = 6.0, 2.9 Hz), 5.65 (1H, dd, *J* = 5.9, 3.1 Hz), 3.42-3.27 (3H, m), 2.81 (1H, br s), 2.72 (1H, br s), 2.61 (2H, t, *J* = 6.8 Hz), 1.62-1.18 (14H, m). ^{13}C {^{1}H} NMR δ **(**$CDCl_3$) 140.32, 133.04, 79.967, 68.95, 46.18, 45.71, 41.93, 40.12, 34.21, 33.53, 29.84, 26.54, 25.99. LRMS (CI^+ m/z) (%): Calc. 209, Found 209.

***N,N'*-Bis(1-octylnonyl)-perylene-3,4,9,10-tetracarboxylic diimide (4)**. A mixture of 3,4,9,10-Perylenetetracarboxylic acid dianhydride (9.012 g, 22.9 mmol), 9-aminoheptadecane (13.115 g, 50.9 mmol), and imidazole (45 g) was heated with stirring

for 2 h at 160 °C. Upon cooling, hexanes was added to the mixture and the entire flask was sonicated. Extraction of the soluble alkylated species continued with additional hexanes until no additional color is seen when fresh hexanes is sonicated. The remaining solid is dissolved in the minimal amount of ethanol. This solution was then poured into an excess of 2N HCl. The resulting precipitate is filtered and combined with the residue remaining after removing the hexanes under vacuum. Chromatography (silica gel, $CHCl_3$) gave the lead fraction as a red solid (yield = 15.23 g, 76%). ^{1}H NMR δ **(**$CDCl_3$) 8.68-8.45 (8H, br m), 5.16 (2H, m), 2.24 (4H, m), 1.83 (4H, m), 1.39-1.17 (48H, m), 0.79 (12H, t, J = 6.6 Hz). ^{13}C {^{1}H} NMR δ **(**$CDCl_3$) 164.51, 163.41, 134.30, 131.70, 130.96, 129.46, 126.27, 123.89, 122.85, 54.74, 32.34, 31.79, 29.49, 29.22, 26.97, 22.59, 14.04. LRMS (CI^+ m/z) (%): Calc. 866, Found 866.

***N*-(1-octylnonyl)perylene-3,4,9,10-tetracarboxy-3,4-anhydride-9-10-imide (5)**. **4** (5.109 g, 5.90 mmol) and KOH (0.410 g, 7.32 mmol) were added to *t*-BuOH (60 mL). The mixture was refluxed for 30 min. If at 30 min starting material was visible through TLC analysis, small amount of additional KOH was added. Upon disappearance of starting material, the reaction was allowed to cool and was poured into 2M HCl (50 mL) with 50 mL AcOH and stirring. The resulting precipitate was filtered and rinsed with water until neutral. Chromatography (silica gel, $CHCl_3$) gave a reddish-brown powder (yield = 1.536 g, 41%). ^{1}H NMR δ **(**$CDCl_3$) 8.65 (8H, m), 5.20 (1H, m), 2.25 (2H, m), 1.88 (2H, m), 1.33-1.22 (24H, m), 0.85 (6H, t, J = 6.6 Hz). ^{13}C {^{1}H} NMR δ **(**$CDCl_3$) 164.42, 163.31, 135.31, 133.77, 131.92, 129.56, 126.52, 126.32, 124.28, 123.91, 123.01, 55.03, 32.51, 32.08, 29.67, 29.36, 27.05, 22.78, 14.14. LRMS (CI^+ m/z) (%): Calc. 629, Found 629.

Perylene containing monomer (6). **5** (102 mg, 0.16 mmol) and **3** (135 mg, 0.645 mmol) were placed into a schlenk flask with toluene (7 mL). The reaction was brought to

reflux for 2 h, or until TLC showed the disappearance of starting material **5**. Upon cooling the solvent was evaporated to leave a crude product. Chromatography (silica gel, 75% $CHCl_3$ in hexanes) gave red crystals (yield = 111 mg, 83%). ^{1}H NMR δ **(**$CDCl_3$) 8.62-8.21 (8H, br m), 6.12 (1H, dd, *J* = 5.6, 2.9 Hz), 5.88 (1H, dd, *J* = 5.7, 3.2 Hz), 5.16 (1H, m), 4.15 (2H, t, *J* = 7.5 Hz), 3.41 (3H, m), 2.84 (1H, br s), 2.74 (1H, br s), 2.25 (2H, m), 1.89 (2H, m), 1.78-1.12 (36H, m) 0.82 (6H, t, *J* = 6.7 Hz). ^{13}C {^{1}H} NMR δ **(**$CDCl_3$) 162.95, 140.51, 134.12, 133.24, 130.92, 80.14, 69.11, 54.82, 46.37, 45.90, 40.31, 34.38, 32.34, 31.81, 29.95, 29.57, 29.25, 28.03, 27.00, 26.06, 22.61, 14.05. UV-Vis ($CHCl_3$) λ_{max} (ε): 525 nm (84,600±500 $M^{-1}cm^{-1}$) Φ_F 487 nm ($CHCl_3$): 0.99±0.04 vs. *N,N'*-Di(9-octylnonyl)-perylene-3,4,9,10-bis(dicarboximide). LRMS (CI^+ m/z) (%): Calc. 822, Found 822. HRMS (CI^+ CH_4) calcd. 821.4893, Found 821.4894.

Polymerization of 6 (poly-PDI). $Cl_2Ru(PCy_3)_2$=CHPh, 1st generation Grubbs' catalyst, (11 mg, 0.012 mmol) was dissolved in $CHCl_3$ (1 mL) in an inert atmosphere glove box. This was added to a $CHCl_3$ solution (2 mL) of **6** (220 mg, 0.268 mmol) with stirring. After 2 h, TLC showed the disappearance of **6**. The reaction was then quenched with addition of ethyl vinyl ether (1 mL) and allowed to stir for an additional 30 minutes. The solution was then poured into excess MeOH to precipitate the red polymer. The polymer was washed successively with MeOH (3x) and hexanes untill washings were colorless to yield **poly-PDI** (yield = 195 mg, 89%).

REFERENCES

(1) Wurthner, F. *Chem. Commun.* **2004**, 1564.

(2) Horowitz, G.; Kouki, F.; Spearman, P.; Fichou, D.; Nogues, C.; Pan, X.; Garnier, F. *Adv. Mater.* **1996**, *8*, 242.

(3) Ego, C.; Marsitzky, D.; Becker, S.; Zhang, J.; Grimsdale, A. C.; Müllen, K.; MacKenzie, J. D.; Silva, C.; Friend, R. H. *J. Am. Chem. Soc.* **2002**, *125*, 437.

(4) Li, C.; Wonneberger, H. *Adv. Mater.* **2012**, *24*, 613.

(5) Tatemichi, S.; Ichikawa, M.; Koyama, T.; Taniguchi, Y. *Appl. Phys. Lett.* **2006**, *89*.

(6) Balakrishnan, K.; Datar, A.; Oitker, R.; Chen, H.; Zuo, J.; Zang, L. *J. Am. Chem. Soc.* **2005**, *127*, 10496.

(7) Che, Y.; Datar, A.; Yang, X.; Naddo, T.; Zhao, J.; Zang, L. *J. Am. Chem. Soc.* **2007**, *129*, 6354.

(8) Lindner, S. M.; Hüttner, S.; Chiche, A.; Thelakkat, M.; Krausch, G. *Angew. Chem. Int. Ed.* **2006**, *45*, 3364.

(9) Sommer, M.; Lindner, S. M.; Thelakkat, M. *Adv. Funct. Mater.* **2007**, *17*, 1493.

(10) Davies, D. I.; Pearce, D. J. A.; Dart, E. C. *J. Chem. Soc., Perkin Trans. 1* **1973**, 433.

(11) Langhals, H.; Jona, W. *Chem. Eur. J.* **1998**, *4*, 2110.

(12) Shanks, D.; Preus, S.; Qvortrup, K.; Hassenkam, T.; Nielsen, M. B.; Kilsa, K. *New J. Chem.* **2009**, *33*, 507.

(13) Albert-Seifried, S.; Finlayson, C. E.; Laquai, F.; Friend, R. H.; Swager, T. M.; Kouwer, P. H. J.; Juríček, M.; Kitto, H. J.; Valster, S.; Nolte, R. J. M.; Rowan, A. E. *Chem. Eur. J.* **2010**, *16*, 10021.

(14) Zhou, Z.; Brusso, J. L.; Holdcroft, S. *Chem. Mater.* **2010**, *22*, 2287.

(15) Tolkki, A.; Vuorimaa, E.; Chukharev, V.; Lemmetyinen, H.; Ihalainen, P.; Peltonen, J.; Dehm, V.; Würthner, F. *Langmuir* **2009**, *26*, 6630.

(16) Glaz, M. S.; Biberdorf, J. D.; Nguyen, M. T.; Travis, J. J.; Holliday, B. J.; Vanden Bout, D. A. *J. Mater. Chem. C* **2013**, *1*, 8060.

(17) Simone, D. L.; Swager, T. M. *J. Am. Chem. Soc.* **2000**, *122*, 9300.

(18) Marks, T. J. *Angew. Chem. Int. Ed.* **1990**, *29*, 857.

(19) Gregg, B. A.; Cormier, R. A. *J. Phys. Chem. B* **1998**, *102*, 9952.

(20) Chen, Y.; Feng, Y.; Gao, J.; Bouvet, M. *J. Colloid Interface Sci.* **2012**, *368*, 387.

(21) Wescott, L. D.; Mattern, D. L. *J. Org. Chem.* **2003**, *68*, 10058.

(22) Tomohiro, T.; Avval, P. A.; Okuno, H. Y. *Synthesis* **1992**, 639.

References

Chapter One

(1) Skotheim, T. A.; Reynolds, J. *Handbook of Conducting Polymers, Third Edition* **2007**.

(2) Hadziioannou, G.; Malliaras, G. G. *Semiconducting Polymers: Chemistry, Physics and Engineering, 2nd Edition* **2006**.

(3) Savéant, J.-M. *Chem. Rev.* **2008**, *108*, 2348.

(4) Rogers, C. W.; Wolf, M. O. *Coord. Chem. Rev.* **2002**, *233–234*, 341.

(5) Kido, J.; Okamoto, Y. *Chem. Rev.* **2002**, *102*, 2357.

(6) Holliday, B. J.; Swager, T. M. *Chem. Commun.* **2005**, 23.

(7) Wolf, M. O. *Adv. Mater.* **2001**, *13*, 545.

(8) Wolf, M. *J. Inorg. Organomet. Polym. Mater.* **2006**, *16*, 189.

(9) Wu, P.-T.; Bull, T.; Kim, F. S.; Luscombe, C. K.; Jenekhe, S. A. *Macromolecules* **2009**, *42*, 671.

(10) Peng, Q.; Xie, M.; Huang, Y.; Lu, Z.; Cao, Y. *Macromol. Chem. Phys.* **2005**, *206*, 2373.

(11) Hjelm, J.; Handel, R. W.; Hagfeldt, A.; Constable, E. C.; Housecroft, C. E.; Forster, R. J. *Inorg. Chem.* **2005**, *44*, 1073.

(12) Pizzoferrato, R.; Ziller, T.; Paolesse, R.; Mandoj, F.; Micozzi, A.; Ricci, A.; Lo Sterzo, C. *Chem. Phys. Lett.* **2006**, *426*, 124.

(13) Mellah, M.; Ansel, B.; Patureau, F.; Voituriez, A.; Schulz, E. *J. Mol. Catal. A: Chem.* **2007**, *272*, 20.

(14) Heinze, J.; Frontana-Uribe, B. A.; Ludwigs, S. *Chem. Rev.* **2010**, *110*, 4724.

(15) Friebe, C.; Hager, M. D.; Winter, A.; Schubert, U. S. *Adv. Mater.* **2012**, *24*, 332.

(16) Whittell, G. R.; Hager, M. D.; Schubert, U. S.; Manners, I. *Nat Mater* **2011**, *10*, 176.

(17) G. Pickup, P. *J. Mater. Chem.* **1999**, *9*, 1641.

(18) Whittell, G. R.; Manners, I. *Adv. Mater.* **2007**, *19*, 3439.

(19) Eloi, J.-C.; Chabanne, L.; Whittell, G. R.; Manners, I. *Mater. Today* **2008**, *11*, 28.

(20) Ho, C.-L.; Wong, W.-Y. *Coord. Chem. Rev.* **2011**, *255*, 2469.

(21) Zhao, Q.; Liu, S.-J.; Huang, W. *Macromol. Rapid Commun.* **2010**, *31*, 794.

(22) Stanley, J. M.; Holliday, B. J. *Coord. Chem. Rev.* **2012**, *256*, 1520.

(23) Fan, L.-J.; Zhang, Y.; Murphy, C. B.; Angell, S. E.; Parker, M. F. L.; Flynn, B. R.; Jones Jr, W. E. *Coord. Chem. Rev.* **2009**, *253*, 410.

(24) Lodeiro, C.; Capelo, J. L.; Mejuto, J. C.; Oliveira, E.; Santos, H. M.; Pedras, B.; Nunez, C. *Chem. Soc. Rev.* **2010**, *39*, 2948.

(25) Smith, R. C.; Tennyson, A. G.; Lim, M. H.; Lippard, S. J. *Org. Lett.* **2005**, *7*, 3573.

(26) Smith, R. C.; Tennyson, A. G.; Won, A. C.; Lippard, S. J. *Inorg. Chem.* **2006**, *45*, 9367.

(27) Bryan, N. S.; Grisham, M. B. *Free Radical Biol. Med.* **2007**, *43*, 645.

(28) Do, L.; Smith, R. C.; Tennyson, A. G.; Lippard, S. J. *Inorg. Chem.* **2006**, *45*, 8998.

(29) Tennyson, A. G.; Do, L.; Smith, R. C.; Lippard, S. J. *Polyhedron* **2007**, *26*, 4625.

(30) Xing, C.; Yu, M.; Wang, S.; Shi, Z.; Li, Y.; Zhu, D. *Macromol. Rapid Commun.* **2007**, *28*, 241.

(31) Papkovsky, D.; Zhdanov, A. V.; Fercher, A.; Dmitriev, R. I.; Hynes, J. *Phosphorescent Oxygen-Sensitive Probes* **2012**.

(32) Thomas Iii, S. W.; Yagi, S.; Swager, T. M. *J. Mater. Chem.* **2005**, *15*, 2829.

(33) Shi, H.; Ma, X.; Zhao, Q.; Liu, B.; Qu, Q.; An, Z.; Zhao, Y.; Huang, W. *Adv. Funct. Mater.* **2014**, *24*, 4823.

(34) Li, Z. a.; Lou, X.; Yu, H.; Li, Z.; Qin, J. *Macromolecules* **2008**, *41*, 7433.

(35) Huang, Y.; Ou, D.; Wang, C.; Huang, C.; Li, Q.; Li, Z. *Polym. Chem.* **2014**, *5*, 2041.

(36) Bao, Y.; Wang, H.; Li, Q.; Liu, B.; Li, Q.; Bai, W.; Jin, B.; Bai, R. *Macromolecules* **2012**, *45*, 3394.

(37) Ogawa, K.; Guo, F.; Schanze, K. S. *J. Photochem. Photobiol. A: Chem.* **2009**, *207*, 79.

(38) Sun, S.; Tong, W.-L.; Chan, M. C. W. *Macromol. Rapid Commun.* **2010**, *31*, 1965.

(39) Shi, H.-F.; Liu, S.-J.; Sun, H.-B.; Xu, W.-J.; An, Z.-F.; Chen, J.; Sun, S.; Lu, X.-M.; Zhao, Q.; Huang, W. *Chem. Eur. J.* **2010**, *16*, 12158.

(40) Qin, C.; Wong, W.-Y.; Wang, L. *Macromolecules* **2010**, *44*, 483.

(41) Sugiyasu, K.; Swager, T. M. *Bull. Chem. Soc. Jpn.* **2007**, *80*, 2074.

(42) Holliday, B. J.; Stanford, T. B.; Swager, T. M. *Chem. Mater.* **2006**, *18*, 5649.

(43) Reddinger, J. L.; Reynolds, J. R. *Chem. Mater.* **1998**, *10*, 3.

(44) Lin, W.-P.; Liu, S.-J.; Gong, T.; Zhao, Q.; Huang, W. *Adv. Mater.* **2014**, *26*, 570.

(45) Liu, S.-J.; Lin, W.-P.; Yi, M.-D.; Xu, W.-J.; Tang, C.; Zhao, Q.; Ye, S.-H.; Liu, X.-M.; Huang, W. *J. Mater. Chem.* **2012**, *22*, 22964.

(46) Wang, P.; Liu, S.-J.; Lin, Z.-H.; Dong, X.-C.; Zhao, Q.; Lin, W.-P.; Yi, M.-D.; Ye, S.-H.; Zhu, C.-X.; Huang, W. *J. Mater. Chem.* **2012**, *22*, 9576.

(47) Liu, S.-J.; Lin, Z.-H.; Zhao, Q.; Ma, Y.; Shi, H.-F.; Yi, M.-D.; Ling, Q.-D.; Fan, Q.-L.; Zhu, C.-X.; Kang, E.-T.; Huang, W. *Adv. Funct. Mater.* **2011**, *21*, 979.

(48) Lin, W.; Sun, H.; Liu, S.; Yang, H.; Ye, S.; Xu, W.; Zhao, Q.; Liu, X.; Huang, W. *Macromol. Chem. Phys.* **2012**, *213*, 2472.

(49) Ling, Q.-D.; Song, Y.; Teo, E. Y. H.; Lim, S.-L.; Zhu, C.; Chan, D. S. H.; Kwong, D.-L.; Kang, E.-T.; Neoh, K.-G. *Electrochem. Solid-State Lett.* **2006**, *9*, G268.

(50) Song, Y.; Tan, Y. P.; Teo, E. Y. H.; Zhu, C.; Chan, D. S. H.; Ling, Q. D.; Neoh, K. G.; Kang, E. T. *J. Appl. Phys.* **2006**, *100*.

(51) Li, L.; Ling, Q.-D.; Lim, S.-L.; Tan, Y.-P.; Zhu, C.; Chan, D. S. H.; Kang, E.-T.; Neoh, K.-G. *Org. Electron.* **2007**, *8*, 401.

(52) Choi, T.-L.; Lee, K.-H.; Joo, W.-J.; Lee, S.; Lee, T.-W.; Chae, M. Y. *J. Am. Chem. Soc.* **2007**, *129*, 9842.

(53) Bandyopadhyay, A.; Sahu, S.; Higuchi, M. *J. Am. Chem. Soc.* **2011**, *133*, 1168.

(54) Gülichi, P.; Goodwin, H. A. *Spin Crossover in Transition Metal Compounds I–III, Top. Curr. Chem.* **2004**.

(55) Halcrow, M. A. *Spin-Crossover Materials: Properties and Applications* **2013**.

(56) Djukic, B.; Lemaire, M. T. *Inorg. Chem.* **2009**, *48*, 10489.

(57) O'Sullivan, T. J.; Djukic, B.; Dube, P. A.; Lemaire, M. T. *Chem. Commun.* **2009**, 1903.

(58) Djukic, B.; Seda, T.; Gorelsky, S. I.; Lough, A. J.; Lemaire, M. T. *Inorg. Chem.* **2011**, *50*, 7334.

(59) Baleizão, C.; Garcia, H. *Chem. Rev.* **2006**, *106*, 3987.

(60) Zulauf, A.; Mellah, M.; Guillot, R.; Schulz, E. *Eur. J. Org. Chem.* **2008**, *2008*, 2118.

(61) Zulauf, A.; Mellah, M.; Schulz, E. *Chem. Commun.* **2009**, 6574.

(62) Zulauf, A.; Hong, X.; Brisset, F.; Schulz, E.; Mellah, M. *New J. Chem.* **2012**, *36*, 1399.

(63) Hong, X.; Mellah, M.; Bordier, F.; Guillot, R.; Schulz, E. *ChemCatChem* **2012**, *4*, 1115.

(64) Hong, X.; Billon, L.; Mellah, M.; Schulz, E. *Catal. Sci. Technol.* **2013**, *3*, 723.

(65) Koper, M. T. M.; Iwasawa, Y. *PCCP* **2014**, *16*, 13567.

(66) Marković, N. M.; Schmidt, T. J.; Stamenković, V.; Ross, P. N. *Fuel Cells* **2001**, *1*, 105.

(67) Kingsborough, R. P.; Swager, T. M. *Chem. Mater.* **2000**, *12*, 872.

(68) Edelman, K. R.; Stevenson, K. J.; Holliday, B. J. *Macromol. Rapid Commun.* **2012**, *33*, 610.

(69) Sullivan, B. P.; Krist, K.; Guard, H. E. *Electrochemical and Electrocatalytic Reaction of Carbon Dioxide*; Elsevier: New York, 1993.

(70) Halman, M. M.; Steinberg, M. *Greenhouse Gas Carbon Dioxide Mitigation: Science and Technology*; CRC Press LLC: Boca Raton, 1999.

(71) Underwood, A. J. V. *Ind. Eng. Chem.* **1940**, *32*, 449.

(72) Benson, E. E.; Kubiak, C. P.; Sathrum, A. J.; Smieja, J. M. *Chem. Soc. Rev.* **2009**, *38*, 89.

(73) O'Toole, T. R.; Margerum, L. D.; Westmoreland, T. D.; Vining, W. J.; Murray, R. W.; Meyer, T. J. *J. Chem. Soc., Chem. Commun.* **1985**, 1416.

(74) O'Toole, T. R.; Sullivan, B. P.; Bruce, M. R. M.; Margerum, L. D.; Murray, R. W.; Meyer, T. J. *J. Electroanal. Chem. Interfacial Electrochem.* **1989**, *259*, 217.

(75) Portenkirchner, E.; Gasiorowski, J.; Oppelt, K.; Schlager, S.; Schwarzinger, C.; Neugebauer, H.; Knör, G.; Sariciftci, N. S. *ChemCatChem* **2013**, *5*, 1790.

(76) Portenkirchner, E.; Oppelt, K.; Ulbricht, C.; Egbe, D. A. M.; Neugebauer, H.; Knör, G.; Sariciftci, N. S. *J. Organomet. Chem.* **2012**, *716*, 19.

(77) Cheung, K.-C.; Guo, P.; So, M.-H.; Lee, L. Y. S.; Ho, K.-P.; Wong, W.-L.; Lee, K.-H.; Wong, W.-T.; Zhou, Z.-Y.; Wong, K.-Y. *J. Organomet. Chem.* **2009**, *694*, 2842.

(78) Cao, W.; Xue, J. *Energy Environ. Sci.* **2014**, *7*, 2123.

(79) Cao, H.; He, W.; Mao, Y.; Lin, X.; Ishikawa, K.; Dickerson, J. H.; Hess, W. P. *J. Power Sources* **2014**, *264*, 168.

(80) Jørgensen, M.; Norrman, K.; Gevorgyan, S. A.; Tromholt, T.; Andreasen, B.; Krebs, F. C. *Adv. Mater.* **2012**, *24*, 580.

(81) Kietzke, T. *Adv. OptoElectronics* **2007**, *2007*, 15.

(82) Ewbank, P. C.; Laird, D.; McCullough, R. D. *Organic photovoltaics* **2009**.

(83) Guo, F.; Kim, Y.-G.; Reynolds, J. R.; Schanze, K. S. *Chem. Commun.* **2006**, 1887.

(84) Kularatne, R. S.; Magurudeniya, H. D.; Sista, P.; Biewer, M. C.; Stefan, M. C. *J. Polym. Sci., Part A: Polym. Chem.* **2013**, *51*, 743.

(85) Mak, C. S. K.; Chan, W. K. In *Macromolecules Containing Metal and Metal-Like Elements*; John Wiley & Sons, Inc.: 2010, p 159.

(86) Liu, S.-J.; Chen, Y.; Xu, W.-J.; Zhao, Q.; Huang, W. *Macromol. Rapid Commun.* **2012**, *33*, 461.

(87) Xu, H.; Chen, R.; Sun, Q.; Lai, W.; Su, Q.; Huang, W.; Liu, X. *Chem. Soc. Rev.* **2014**, *43*, 3259.

(88) Asatkar, A. K.; Bedi, A.; Zade, S. S. *Isr. J. Chem.* **2014**, *54*, 467.

(89) Wong, W.-Y.; Wang, X.-Z.; He, Z.; Djurisic, A. B.; Yip, C.-T.; Cheung, K.-Y.; Wang, H.; Mak, C. S. K.; Chan, W.-K. *Nat. Mater.* **2007**, *6*, 521.

(90) Gilot, J.; Wienk, M. M.; Janssen, R. A. J. *Nat. Mater.* **2007**, *6*, 704.

(91) Wong, W.-Y.; Wang, X.-Z.; He, Z.; Chan, K.-K.; Djurišić, A. B.; Cheung, K.-Y.; Yip, C.-T.; Ng, A. M.-C.; Xi, Y. Y.; Mak, C. S. K.; Chan, W.-K. *J. Am. Chem. Soc.* **2007**, *129*, 14372.

(92) Wang, Q.; Wong, W.-Y. *Polym. Chem.* **2011**, *2*, 432.

(93) Liu, S.; Zhang, K.; Lu, J.; Zhang, J.; Yip, H.-L.; Huang, F.; Cao, Y. *J. Am. Chem. Soc.* **2013**, *135*, 15326.

(94) *poly[4,8-bis(2-ethylhexyloxyl)benzo[1,2-b:4,5-b']dithiophene-2,6-diyl-alt-ethylhexyl-3-uorothithieno[3,4-b]thiophene-2-carboxylate-4,6-diyl]*.

(95) Shi, S.; Jiang, P.; Chen, S.; Sun, Y.; Wang, X.; Wang, K.; Shen, S.; Li, X.; Li, Y.; Wang, H. *Macromolecules* **2012**, *45*, 7806.

(96) Zhan, H.; Lamare, S.; Ng, A.; Kenny, T.; Guernon, H.; Chan, W.-K.; Djurišić, A. B.; Harvey, P. D.; Wong, W.-Y. *Macromolecules* **2011**, *44*, 5155.

(97) Chao, Y. I. H.; Jheng, J.-F.; Wu, J.-S.; Wu, K.-Y.; Peng, H.-H.; Tsai, M.-C.; Wang, C.-L.; Hsiao, Y.-N.; Wang, C.-L.; Lin, C.-Y.; Hsu, C.-S. *Adv. Mater.* **2014**, *26*, 5205.

(98) Clem, T. A.; Kavulak, D. F. J.; Westling, E. J.; Fréchet, J. M. J. *Chem. Mater.* **2009**, *22*, 1977.

(99) Liao, C.-Y.; Chen, C.-P.; Chang, C.-C.; Hwang, G.-W.; Chou, H.-H.; Cheng, C.-H. *Sol. Energy Mater. Sol. Cells* **2013**, *109*, 111.

(100) Feng, K.; Shen, X.; Li, Y.; He, Y.; Huang, D.; Peng, Q. *Polym. Chem.* **2013**, *4*, 5701.

Chapter Two

(1) Huynh, W. U.; Dittmer, J. J.; Alivisatos, A. P. *Science* **2002**, *295*, 2425.

(2) Sun, B.; Marx, E.; Greenham, N. C. *Nano Letters* **2003**, *3*, 961.

(3) Sun, B.; Snaith, H. J.; Dhoot, A. S.; Westenhoff, S.; Greenham, N. C. *J. Appl. Phys.* **2005**, *97*, 014914.

(4) Gur, I.; Fromer, N. A.; Chen, C.-P.; Kanaras, A. G.; Alivisatos, A. P. *Nano Lett.* **2006**, *7*, 409.

(5) Dayal, S.; Kopidakis, N.; Olson, D. C.; Ginley, D. S.; Rumbles, G. *Nano Letters* **2009**, *10*, 239.

(6) Borchert, H. *Energy Environ. Sci.* **2010**, *3*, 1682.

(7) Kusum, K.; Umesh, K.; Shailesh, N. S.; Suresh, C.; Rita, K.; Vankar, V. D.; Vikram, K. *J. Phys. D: Appl. Phys.* **2008**, *41*, 235409.

(8) Lek, J. Y.; Xi, L.; Kardynal, B. E.; Wong, L. H.; Lam, Y. M. *ACS Appl. Mater. Interfaces* **2011**, *3*, 287.

(9) Lokteva, I.; Radychev, N.; Witt, F.; Borchert, H.; Parisi, J. r.; Kolny-Olesiak, J. *J. Phys. Chem. C* **2010**, *114*, 12784.

(10) Seo, J.; Kim, W. J.; Kim, S. J.; Lee, K.-S.; Cartwright, A. N.; Prasad, P. N. *Appl. Phys. Lett.* **2009**, *94*.

(11) Olson, J. D.; Gray, G. P.; Carter, S. A. *Sol. Energy Mater. Sol. Cells* **2009**, *93*, 519.

(12) Zhou, Y.; Riehle, F. S.; Yuan, Y.; Schleiermacher, H.-F.; Niggemann, M.; Urban, G. A.; Krüger, M. *Appl. Phys. Lett.* **2010**, *96*.

(13) Liu, J.; Tanaka, T.; Sivula, K.; Alivisatos, A. P.; Fréchet, J. M. J. *J. Am. Chem. Soc.* **2004**, *126*, 6550.

(14) Liao, H.-C.; Chen, S.-Y.; Liu, D.-M. *Macromolecules* **2009**, *42*, 6558.

(15) Dayal, S.; Kopidakis, N.; Olson, D. C.; Ginley, D. S.; Rumbles, G. *J. Am. Chem. Soc.* **2009**, *131*, 17726.

(16) Mejía, M. L.; Agapiou, K.; Yang, X.; Holliday, B. J. *J. Am. Chem. Soc.* **2009**, *131*, 18196.

(17) Mejia, M. L.; Reeske, G.; Holliday, B. J. *Chem. Commun.* **2010**, *46*, 5355.

(18) Wolf, M. O. *Adv. Mater.* **2001**, *13*, 545.

(19) Wolf, M. *J. Inorg. Organomet. Polym. Mater.* **2006**, *16*, 189.

(20) Reddinger, J. L.; Reynolds, J. R. *Macromolecules* **1997**, *30*, 673.

(21) Harima, Y.; Eguchi, T.; Yamashita, K.; Kojima, K.; Shiotani, M. *Synth. Met.* **1999**, *105*, 121.

(22) Zykwinska, A.; Domagala, W.; Czardybon, A.; Pilawa, B.; Lapkowski, M. *Chem. Phys.* **2003**, *292*, 31.

(23) Lee, H.; Wang, M.; Chen, P.; Gamelin, D. R.; Zakeeruddin, S. M.; Grätzel, M.; Nazeeruddin, M. K. *Nano Lett.* **2009**, *9*, 4221.

(24) Heinemann, M. D.; von Maydell, K.; Zutz, F.; Kolny-Olesiak, J.; Borchert, H.; Riedel, I.; Parisi, J. *Adv. Funct. Mater.* **2009**, *19*, 3788.

(25) Witt, F.; Kruszynska, M.; Borchert, H.; Parisi, J. *J. Phys. Chem. Lett.* **2010**, *1*, 2999.

(26) Kitamura, C.; Tanaka, S.; Yamashita, Y. *Chem. Mater.* **1996**, *8*, 570.

Chapter Three

(1) *Please see chapter 1 and references therein.*

(2) Friebe, C.; Hager, M. D.; Winter, A.; Schubert, U. S. *Adv. Mater.* **2012**, *24*, 332.

(3) Whittell, G. R.; Hager, M. D.; Schubert, U. S.; Manners, I. *Nat Mater* **2011**, *10*, 176.

(4) Wolf, M. *J. Inorg. Organomet. Polym. Mater.* **2006**, *16*, 189.

(5) Holliday, B. J.; Swager, T. M. *Chem. Commun.* **2005**, 23.

(6) Holliday, B. J.; Stanford, T. B.; Swager, T. M. *Chem. Mater.* **2006**, *18*, 5649.

(7) Shioya, T.; Swager, T. M. *Chem. Commun.* **2002**, 1364.

(8) Kingsborough, R. P.; Swager, T. M. *Adv. Mater.* **1998**, *10*, 1100.

(9) G. Pickup, P. *J. Mater. Chem.* **1999**, *9*, 1641.

(10) Pietrangelo, A.; Sih, B. C.; Boden, B. N.; Wang, Z.; Li, Q.; Chou, K. C.; MacLachlan, M. J.; Wolf, M. O. *Adv. Mater.* **2008**, *20*, 2280.

(11) You, Z.-L.; Zhu, H.-L.; Liu, W.-S. *Acta Cryst. E* **2004**, *60*, m1900.

(12) You, Z.-L.; Zhou, P. *Inorg. Chem. Commun.* **2007**, *10*, 1273.

(13) Gutiérrez, A.; Perpiñán, M. F.; Sánchez, A. E.; Torralba, M. C.; Torres, M. R. *Polyhedron* **2012**, *44*, 165.

(14) Yu, T.; Zhang, K.; Zhao, Y.; Yang, C.; Zhang, H.; Fan, D.; Dong, W. *Inorg. Chem. Commun.* **2007**, *10*, 401.

(15) Diao, Y.-P.; Huang, S.-S.; Zhang, H.-L.; Deng, S.; Liu, K.-X. *Acta Cryst. E* **2007**, *63*, m1694.

(16) Zulauf, A.; Hong, X.; Brisset, F.; Schulz, E.; Mellah, M. *New J. Chem.* **2012**, *36*, 1399.

(17) Schrebler, R.; Grez, P.; Cury, P.; Veas, C.; Merino, M.; Gómez, H.; Córdova, R.; del Valle, M. A. *J. Electroanal. Chem.* **1997**, *430*, 77.

(18) Berglund, S. P.; Flaherty, D. W.; Hahn, N. T.; Bard, A. J.; Mullins, C. B. *J. Phys. Chem. C* **2011**, *115*, 3794.

(19) Kittlesen, G. P.; White, H. S.; Wrighton, M. S. *J. Am. Chem. Soc.* **1984**, *106*, 7389.

(20) Pickup, P. G.; Kutner, W.; Leidner, C. R.; Murray, R. W. *J. Am. Chem. Soc.* **1984**, *106*, 1991.

(21) Chidsey, C. E. D.; Murray, R. W. *J. Phys. Chem.* **1986**, *90*, 1479.

(22) Chidsey, C. E.; Feldman, B. J.; Lundgren, C.; Murray, R. W. *Anal. Chem.* **1986**, *58*, 601.

(23) Wilbourn, K.; Murray, R. W. *J. Phys. Chem.* **1988**, *92*, 3642.

(24) Zhu, S. S.; Carroll, P. J.; Swager, T. M. *J. Am. Chem. Soc.* **1996**, *118*, 8713.

(25) Swager, T. M. *Acc. Chem. Res.* **1998**, *31*, 201.

(26) Simone, D. L.; Swager, T. M. *J. Am. Chem. Soc.* **2000**, *122*, 9300.

(27) Vigalok, A.; Zhu, Z.; Swager, T. M. *J. Am. Chem. Soc.* **2001**, *123*, 7917.

(28) Lee, D.; Swager, T. M. *J. Am. Chem. Soc.* **2003**, *125*, 6870.

(29) Ie, Y.; Han, A.; Otsubo, T.; Aso, Y. *Chem. Commun.* **2009**, 3020.

(30) Izuhara, D.; Swager, T. M. *J. Am. Chem. Soc.* **2009**, *131*, 17724.

(31) Rochat, S.; Swager, T. M. *J. Am. Chem. Soc.* **2013**, *135*, 17703.

(32) Gregg, B. A.; Cormier, R. A. *J. Phys. Chem. B* **1998**, *102*, 9952.

(33) Schiavon, G.; Sitran, S.; Zotti, G. *Synth. Met.* **1989**, *32*, 209.

(34) Kingsborough, R. P.; Swager, T. M. *J. Am. Chem. Soc.* **1999**, *121*, 8825.

(35) Liu, W.; Huang, W.; Chen, C.-H.; Pink, M.; Lee, D. *Chem. Mater.* **2012**, *24*, 3650.

(36) Storr, T.; Wasinger, E. C.; Pratt, R. C.; Stack, T. D. P. *Angew. Chem.* **2007**, *119*, 5290.

(37) Shimazaki, Y.; Stack, T. D. P.; Storr, T. *Inorg. Chem.* **2009**, *48*, 8383.

(38) Storr, T.; Verma, P.; Pratt, R. C.; Wasinger, E. C.; Shimazaki, Y.; Stack, T. D. P. *J. Am. Chem. Soc.* **2008**, *130*, 15448.

(39) Kurahashi, T.; Fujii, H. *J. Am. Chem. Soc.* **2011**, *133*, 8307.

(40) Chen, X. *PhD Dissertation* **2011**, The University of Texas at Austin.

(41) Mejia, M. L. *PhD Dissertation* **2010**, The University of Texas at Austin.

(42) Mejía, M. L.; Agapiou, K.; Yang, X.; Holliday, B. J. *J. Am. Chem. Soc.* **2009**, *131*, 18196.

(43) The Rigaku Corportation: Tokyo, Japan, 2001.

(44) *CrystalClear, 1.40*; Rigaku Americas Corporation: The Woodlands, Texas, USA, 2008.

(45) Sheldrick, G. M. *SHELX 97. A software package for the solution and refinement of X-ray data*; University of Gottingen: Gottingen, Germany, 1997.

(46) Cromer, D. T.; Waber, J. T. In *International Tables for X-ray Crystallography*; Kynoch Press: Birmingham, England, 1974; Vol. 4.

(47) Frisch, M. J.; Trucks, G. W.; Schlegel, H. B.; Scuseria, G. E.; Robb, M. A.; Cheeseman, J. R.; Montgomery Jr., J. A.; Vreven, T.; Kudin, K. N.; Burant, J. C.; Millam, J. M.; Iyengar, S. S.; Tomasi, J.; Barone, V.; Mennucci, B.; Cossi, M.; Scalmani, G.; Rega, N.; Petersson, G. A.; Nakatsuji, H.; Hada, M.; Ehara, M.; Toyota, K.; Fukuda, R.; Hasegawa, J.; Ishida, M.; Nakajima, T.; Honda, Y.; Kitao, O.; Nakai, H.; Klene, M.; Li, X.; Knox, J. E.; Hratchian, H. P.; Cross, J. B.; Bakken, V.; Adamo, C.; Jaramillo, J.; Gomperts, R.; Stratmann, R. E.; Yazyev, O.; Austin, A. J.; Cammi, R.; Pomelli, C.; Ochterski, J.; Ayala, P. Y.; Morokuma, K.; Voth, G. A.; Salvador, P.; Dannenberg, J. J.; Zakrzewski, V. G.; Dapprich, S.; Daniels, A. D.; Strain, M. C.; Farkas, O.; Malick, D. K.; Rabuck, A. D.; Raghavachari, K.; Foresman, J. B.; Ortiz, J. V.; Cui, Q.; Baboul, A. G.; Clifford, S.; Cioslowski, J.; Stefanov, B. B.; Liu, G.; Liashenko, A.; Piskorz, P.; Komaromi, I.; Martin, R. L.; Fox, D. J.; Keith, T.; Al-Laham, M. A.; Peng, C. Y.; Nanayakkara, A.; Challecombe, M.; Gill, P. M. W.; Johnson, B. G.; Chen, W.; Wong, M. W.; Gonzalez, C.; Pople, J. A.; Gaussian, Inc.: Wallingford, CT, 2004.

Chapter Four

(1) Gülichi, P.; Goodwin, H. A. *Spin Crossover in Transition Metal Compounds I–III, Top. Curr. Chem.* **2004**.

(2) Halcrow, M. A. *Spin-Crossover Materials: Properties and Applications* **2013**.

(3) Gütlich, P.; Gaspar, A. B.; Garcia, Y. *Beilstein J. Org. Chem.* **2013**, *9*, 342.

(4) Gütlich, P. *Eur. J. Inorg. Chem.* **2013**, *2013*, 581.

(5) Gamez, P.; Costa, J. S.; Quesada, M.; Aromi, G. *Dalton Trans.* **2009**, 7845.

(6) Hayami, S.; Gu, Z.-z.; Einaga, Y.; Kobayasi, Y.; Ishikawa, Y.; Yamada, Y.; Fujishima, A.; Sato, O. *Inorg. Chem.* **2001**, *40*, 3240.

(7) Mathonière, C.; Lin, H.-J.; Siretanu, D.; Clérac, R.; Smith, J. M. *J. Am. Chem. Soc.* **2013**, *135*, 19083.

(8) Gütlich, P.; Hauser, A.; Spiering, H. *Angew. Chem. Int. Ed.* **1994**, *33*, 2024.

(9) Hjelm, J.; Handel, R. W.; Hagfeldt, A.; Constable, E. C.; Housecroft, C. E.; Forster, R. J. *J. Phys. Chem. B* **2003**, *107*, 10431.

(10) Fillaud, L.; Trippé-Allard, G.; Lacroix, J. C. *Org. Lett.* **2013**, *15*, 1028.

(11) Buchen, T.; Gütlich, P.; Sugiyarto, K. H.; Goodwin, H. A. *Chem. Eur. J.* **1996**, *2*, 1134.

(12) Šalitroš, I.; Fuhr, O.; Kruk, R.; Pavlik, J.; Pogány, L.; Schäfer, B.; Tatarko, M.; Boča, R.; Linert, W.; Ruben, M. *Eur. J. Inorg. Chem.* **2013**, *2013*, 1049.

(13) Hasegawa, Y.; Sakamoto, R.; Takahashi, K.; Nishihara, H. *Inorg. Chem.* **2013**, *52*, 1658.

(14) Nemati Kharat, A.; Bakhoda, A.; Tamaddoni Jahromi, B. *Polyhedron* **2011**, *30*, 2768.

(15) Mello, J. V.; Finney, N. S. *Org. Lett.* **2001**, *3*, 4263.

(16) The Rigaku Corportation: Tokyo, Japan, 2001.

(17) Otwinoski, Z.; Minor, W. In *Macromolecular Crystallography, Part A*; Carter Jr., C. W., Sweets, R. M., Eds.; Academic Press 1997, p 307.

(18) *CrystalClear, 1.40*; Rigaku Americas Corporation: The Woodlands, Texas, USA, 2008.

(19) Sheldrick, G. M. *SHELX 97. A software package for the solution and refinement of X-ray data*; University of Gottingen: Gottingen, Germany, 1997.

(20) Cromer, D. T.; Waber, J. T. In *International Tables for X-ray Crystallography*; Kynoch Press: Birmingham, England, 1974; Vol. 4.

(21) Zhu, S. S.; Swager, T. M. *J. Am. Chem. Soc.* **1997**, *119*, 12568.

Chapter Five

(1) Wurthner, F. *Chem. Commun.* **2004**, 1564.

(2) Horowitz, G.; Kouki, F.; Spearman, P.; Fichou, D.; Nogues, C.; Pan, X.; Garnier, F. *Adv. Mater.* **1996**, *8*, 242.

(3) Ego, C.; Marsitzky, D.; Becker, S.; Zhang, J.; Grimsdale, A. C.; Müllen, K.; MacKenzie, J. D.; Silva, C.; Friend, R. H. *J. Am. Chem. Soc.* **2002**, *125*, 437.

(4) Li, C.; Wonneberger, H. *Adv. Mater.* **2012**, *24*, 613.

(5) Tatemichi, S.; Ichikawa, M.; Koyama, T.; Taniguchi, Y. *Appl. Phys. Lett.* **2006**, *89*.

(6) Balakrishnan, K.; Datar, A.; Oitker, R.; Chen, H.; Zuo, J.; Zang, L. *J. Am. Chem. Soc.* **2005**, *127*, 10496.

(7) Che, Y.; Datar, A.; Yang, X.; Naddo, T.; Zhao, J.; Zang, L. *J. Am. Chem. Soc.* **2007**, *129*, 6354.

(8) Lindner, S. M.; Hüttner, S.; Chiche, A.; Thelakkat, M.; Krausch, G. *Angew. Chem. Int. Ed.* **2006**, *45*, 3364.

(9) Sommer, M.; Lindner, S. M.; Thelakkat, M. *Adv. Funct. Mater.* **2007**, *17*, 1493.

(10) Davies, D. I.; Pearce, D. J. A.; Dart, E. C. *J. Chem. Soc., Perkin Trans. 1* **1973**, 433.

(11) Langhals, H.; Jona, W. *Chem. Eur. J.* **1998**, *4*, 2110.

(12) Shanks, D.; Preus, S.; Qvortrup, K.; Hassenkam, T.; Nielsen, M. B.; Kilsa, K. *New J. Chem.* **2009**, *33*, 507.

(13) Albert-Seifried, S.; Finlayson, C. E.; Laquai, F.; Friend, R. H.; Swager, T. M.; Kouwer, P. H. J.; Juríček, M.; Kitto, H. J.; Valster, S.; Nolte, R. J. M.; Rowan, A. E. *Chem. Eur. J.* **2010**, *16*, 10021.

(14) Zhou, Z.; Brusso, J. L.; Holdcroft, S. *Chem. Mater.* **2010**, *22*, 2287.

(15) Tolkki, A.; Vuorimaa, E.; Chukharev, V.; Lemmetyinen, H.; Ihalainen, P.; Peltonen, J.; Dehm, V.; Würthner, F. *Langmuir* **2009**, *26*, 6630.

(16) Glaz, M. S.; Biberdorf, J. D.; Nguyen, M. T.; Travis, J. J.; Holliday, B. J.; Vanden Bout, D. A. *J. Mater. Chem. C* **2013**, *1*, 8060.

(17) Simone, D. L.; Swager, T. M. *J. Am. Chem. Soc.* **2000**, *122*, 9300.

(18) Marks, T. J. *Angew. Chem. Int. Ed.* **1990**, *29*, 857.

(19) Gregg, B. A.; Cormier, R. A. *J. Phys. Chem. B* **1998**, *102*, 9952.

(20) Chen, Y.; Feng, Y.; Gao, J.; Bouvet, M. *J. Colloid Interface Sci.* **2012**, *368*, 387.

(21) Wescott, L. D.; Mattern, D. L. *J. Org. Chem.* **2003**, *68*, 10058.

(22) Tomohiro, T.; Avval, P. A.; Okuno, H. Y. *Synthesis* **1992**, 639.